Alma Mater Studiorum – Università di Bologna

DOTTORATO DI RICERCA IN

FISICA

Ciclo XXXII

Settore Concorsuale: 02/B1

Settore Scientifico Disciplinare: FIS/03

Semiconducting Polymers for Electronic Biosensors and Biological Interfaces

Presentata da: Francesco Decataldo

Coordinatore Dottorato **Supervisore**

Prof. Silvia Arcelli **Prof. Beatrice Fraboni**

Esame finale anno 2020

To my family.

Contents

Abstract

Bioeletronics is a scientific branch that aims at the direct coupling of biomolecular function units with standard electronic or optical devices. As often occurs for new research disciplines, the main limitations of this field are the material needed to interface soft living entities, mainly regulated by ionic current or chemical reactions, with hard inorganic devices, which mainly transmit signals through hole or electron currents. The development of conducting polymers enabled the bridging of the inherent gap between these two separate worlds: owing to their biocompatibility, tunable conductivity, soft nature, ease of fabrication and low temperature processability, together with their capability to resist to corrosion in liquid environments and be tailored according to the required application, conducting polymers replaced the traditional inorganic electronic materials.

Among several conducting polymers, the intrinsically conductive poly(3,4-ethylenedioxythiophene) (PEDOT), doped with poly(styrenesulfonic acid) (PSS), or PEDOT:PSS, is one of the most representative and used, having an excellent chemical and thermal stability, reversible doping state and high conductivity.

This thesis work relies on the use of PEDOT:PSS as semiconducting material for biological interfaces and biosensors. All PEDOT:PSS-based Organic Electrochemical Transistors have been realized to study cell tissue integrity, the amount of oxygen dissolved in solution and cytokines/analytes released from stem cells undergoing osteogenic differentiation. On the other hand, PEDOT:PSS thin films have been employed as gold electrode coatings for *in-vivo*, chronic recordings of the spiking activity of peripheral nerves.

In detail, it was demonstrated that OECTs have the potential to real-time monitor growth and detachment of both strong-barrier and no-barrier cell lines, according to the patterning of the active area of the device, influenced by the cell tissue: the comparison of the implemented vertical and planar configurations proved that, in the latter, ions cross twice the cell layer forming on the device, thus doubling the cell effect on the OECT response time and enabling the detection of even no-barrier cells, such as human embryonic fibroblast (NIH-3T3). Planar OECTs were then employed to assess silver nanoparticles (AgNPs) toxicity effects on human colorectal epithelial cells (Caco-2) and NIH-3T3, representing the intestinal and skin barrier, respectively, since AgNPs are commonly found in food packaging and cosmetics. The real-time monitoring of citrate-coated AgNPs (toxic) and the passivated (11-mercaptoundecyl)hexa(ethylene glycol) (EG_6OH)-coated ones (non-toxic) allowed further insights and informations of citrate-coated AgNPs uptake by the cells and their toxic actions. On the contrary, EG_6OH-coated AgNPs were demonstrated to be non-toxic towards both cell lines, showing a response comparable to untreated samples.

Moreover, PEDOT:PSS OECTs were also been employed as oxygen sensors, demonstrating their capability to detect oxygen amount dissolved in KCl or even cell culture medium solutions, in the oxygen partial pressure (above the solution) range of 0-5%. This paves the way for sensors able to study cell culture grown in hypoxia conditions or analyse tumour properties related to different tissue oxygen partial pressures (that are in the range between 10% and 0%).

Furthermore, the gate of PEDOT:PSS OECTs were biofunctionalized to impart specificity on the OECT sensing capabilities: in detail, a chemical functionalization strategy, involving (3-Aminopropyl)triethoxysilane (APTES) molecules, biotin units, streptavidin proteins and a final biotinylated capture antibody towards the selected analyte/cytokine, was developed and characterized. The resulting device showed a proof of concept detection of a fundamental cytokine for cells undergoing osteogenic differentiation (namely, Bone Morphogenic Protein 2), thus introducing the possibility for real-time monitoring of cell differentiation process.

Besides, PEDOT:PSS thickness-controlled films were electrodeposited on gold electrodes as biocompatible, low-impedance and soft interface between the animal nerve and the metallic layer. In detail, the introduction of the plasticizer polyethylene glycol (PEG) enhanced the elasticity of the final film while keeping good conductivity and low-impedance properties, as highlighted by electrochemical impedance and atomic force microscopy measurements under tensile strain. A final *in-vivo* chronic recording of the renal sympathetic nerve activity of a rat was performed, proving the efficiency of the device.

List of acronyms

AA – ascorbic acid
AFM – Atomic Force Microscopy
AgNPs – silver nanoparticles
ALP – alkaline phosphatase
AP – Arterial blood pressure
APTES – (3-Aminopropyl)triethoxysilane
ATR – Attenuated Total Reflectance
BMP-2 – Bone Morphogenic Protein 2
BMSC – Bone marrow stromal cells
bpm – beats per minute
C- AFM – Conductive Atomic Force Microscopy
C2C12 – myoblast cells
Caco-2 – human colorectal epithelial cell
CE – counter electrode
CEA – conductivity enhancing agents
CM-OFET – Charge Modulated Organic Field Effect Transistor
COL1 – collagene type 1
CP – Conducting Polymers
CPE – constant phase element
CTR or Ctrl – control
CV – cyclic voltammogram (or cyclic voltammetry)
CVD – Chemical Vapor Deposition
DAPI – 4,6-diamidin-2-phenylindole
DBSA – dodecylbenzenesulfonate
DI – distilled
DMEM – Dulbecco's modified Eagle medium
DMSO – dimethyl sulfoxide
DNA- deoxyriboNucleic Acid
DPBS – Dulbecco's phosphate buffered saline
DPPH – 2,2.diphenyl-1-picrylhydrazyl
ECG – electrocardiogram
ECM – extracellular matrix
ECoG – electrocorticography
EDL – Electrical Double Layer
EDOT – 3,4-ethylenedioxythiophene
EDTA – Ethylenediaminetetraacetic Acid
EG – ethylene glycol
EG_6OH – (11-mercaptoundecyl)hexa(ethylene glycol)
EGOFET – electrolyte-gated field effect transistor
EGTA – Ethylene Glycol Tetraacetic Acid
EIS – Electrochemical Impedance Spectroscopy
ELISA – enzyme-linked immunosorbent assay
EMG – electromyography or electromyogram
FBS – fetal bovine serum
FS – feedback mechanism

FTIR Spectroscopy – Fourier Transform Infrared Spectroscopy
FTO – fluorine doped tin oxide
GOPS – 3-glycidoxypropyltrimethoxysilane
GOx – glucose oxidase
GP – gelatin-g and PANI
H9c2 – cardiac cells(cardiomyoblasts)
hDF – primary human dermal fibroblasts
HEC-1-B – human endometrium epithelial cells
Hela – immortalized human epithelial tumour cells
HFIP - 1,1,1,3,3,3-hexafluoro- 2-propanol
HHFC – height-height correlation function
HOMO – highest occupied molecular orbital
HPE – host polyelectrolyte
HR – heart rate
HRP – horseradish peroxidase
ISOFET – ion-selective organic field effect transistors
ITO – indium tin oxide
LOD – limit of detection
LUMO – lowest unoccupied molecular orbital
MC3T3-E1 – preosteoblast cells
MDCK I – Madin-Darby canine kidney renal epithelial cells
mRNA – messenger RiboNucleic Acid
MTT – 3-(4,5-di-methyl-2-thiazolyl)-2,5-diphenylttetrazolium) bromide
NaDBS – sodium dodecylbenzenesulfonate
NEAA – nonessential amino acids
NIhH-3T3 – mouse embryonic fibroblast
NP – nanoparticle
OD – Optical density
OECT – organic electrochemical transistors
OEG – oligo(ethylene glycol)
OEIP – organic electronic ion pump
OFET – organic field effect transistor
OLED - Organic Light-Emitting Diode
OPV – Organic Photovoltaic
OSC – organic semiconductor
OTFT – Organic Thin Film Transistor
P3HT – poly(3-hexylthiophene)
PAA – Polyacrylic acid
PAc – polyacetylene
PANI – Polyaniline
PBST – 0.05% of Tween® 20 in Phosphate Buffer Saline solution
PC12 – rat phaeochromocytoma cells
PCB – printed circuit board
PCL – polycaprolactone
PCTC – polycaprolactone-block-polytetrahydrofuran-blick-polycaprolactone
PDLLA – poly(D,L-lactic acid)
PDMS – Polydimethylsiloxane

PEDOT - Poly(3,4-ethylenedioxythiophene)
PEDOT – Poly(ethylenedioxithiophene)
PEEK – polyether ether ketone
PEG – polyethylene glycol
PEGS-FA – poly(ethylene glycol)-co-poly(glycerol sebacate)
PET – Polyethylene terephthalate
PFu – Polyfuran
PLA – polylactide
PLGA – poly(lactic-co-glycolic acid)
PPP – polyparaphenylene
PPV – polyparaphenylene vinylene
PPy – Polypirrole
PSS - Poly(styrenesulfonate)
PTh – Polythiophene
PTTA – alkyl-substituted triphenylamine polymers
QCM – quartz crystal microbalance
QCM-D – quartz crystal microbalance with dissipation monitoring
QCSP – quaternized chitosan-g-PANI
RE – reference electrode
rH – relative humidity
RIgG – antibody anti-rabbit IgG
RPM – round per minute
RSC96 – Schwann cells
RSNA – renal sympathetic nerve activity
Runx2 – run-related transcription factor 2
S – Soaking
SaOS-2 sarcoma osteogenic cells
SCE – saturated calomel electrode
SLB – supported lipid bilayer
SMU – Source Meter Units
SPM – Scanning Probe Microscopy
T98G – human gliobastoma multiforme cells
TCAP – carboxylterthiophene monomer
TECH-OECT – Tissue Engineering Cell Holder for Organic Electrochemical Transistor
TEER – Transepithelial Electrical Resistance
TGA – thermogravimetrical analysis
TJ – Tight Junction
TMS – trimethylsilyl
UV – ultraviolet
UV – ultraviolet
VRH – variable range hopping
WE – working electrode
XRD – x-ray diffraction
α6T – α-sexithiophene

Introduction

Bioelectronics is a scientific branch which aims at the interfacing of the electronic world of sensors, actuators, transistors and logic circuits, with the biological systems, consisting of cells, tissues, proteins, bacteria. The capability to interact with biology using electrical signals as a mean to investigate or stimulate living organisms allows for infinite possibilities to gain further insights on, as well as to control, biological events. This paves the way to the development of a broad range of powerful and interesting biomedical applications, such as smart prostheses, neural implants, biosensors, wearable electronics and many others, having the potential to improve the quality of life of millions of people.

However, the difficult interfacing of the biological and electronic worlds relies on the communication between "soft" living biological entities, which transmit signals using ion concentration gradients or chemical reactions in liquid environment, and the "hard" electronic elements, that usually interact via electron and hole currents. Materials are then the main limitations for the development of these new technologies. The rising of semiconducting polymers, with their ability to conduct both electronic and ionic (bio)signals, thus bridging the gap between these two diverse worlds,[1] spread completely new possibilities, leading to the growth of Organic Bioelectronics.

Among the different conducting polymers used, the commercially available poly(3,4-ethylenedioxythiophene) doped with poly(styrenesulfonate) (PEDOT:PSS), is the gold standard material for bioelectronic studies and applications, due to its properties: in detail, PEDOT:PSS presents high electrochemical and thermal stability, water dispersibility, good and tunable conductivity and good film-forming properties.[2–4] For these reasons, several powerful and potentially commerciable applications have been developed with this polymer, such as organic electrochemical transistors (OECT), biosensors, organic electronic ion pump (OEIP), implantable electrodes.[2,5]

The aim of this thesis is to employ PEDOT:PSS features towards the realization of new smart biosensing devices, characterizing their electrical and electrochemical performances. In particular, organic electrochemical transistors and electrodes have been fabricated and studied in which the PEDOT:PSS behave as soft and biocompatible interface between the biological element and the electronic device.

This work has been carried out at the Department of Physics and Astronomy of the University of Bologna, and in part at the Institute for the Study of Nanostructured Material of the National Centre of Research in Bologna and, during a secondment, at the Department of Chemical Engineering and Biotechnology at the University of Cambridge, in the United Kingdom. Moreover, fruitful collaborations with the Department of Industrial Chemistry of the University of Bologna, The Department of Biomedical and Neuromotor Sciences in Bologna, the Florey Institute of Neuroscience and Mental Health of the University of Melbourne in Australia, the Department of Physics and centre for Plastic Electronics of the Imperial College in London (UK), the Biological and Environmental Science and Engineering Division of the King Abdullah University of Science and Technology in Thuwal (Saudi Arabia) helped to realize these studies.

In the first Chapter, an overview on Organic Bioelectronics is reported, focusing on its development and the rise of conducting polymer as smart interfacing material for several bioelectronic applications (surfaces, scaffolds, biosensors, electrodes for sensing and stimulations).

In the second Chapter, conjugated polymers and their properties are introduced and, in particular, PEDOT:PSS features and its technological applications in the bioelectronic field are explained: organic electrochemical transistor working principles, biosensors and electrodes are summarized.

Materials, fabrication and characterization technique, together with the experimental setups and the biological components are explained in detail in the third Chapter.

Last three Chapters report the results obtained in this thesis.
In the fourth Chapter, PEDOT:PSS-based organic electrochemical transistors (OECTs) were investigate as smart devices for cell tissue integrity monitoring. In detail, the Chapter starts with the fabrication of a sample holder for OECTs, which mimic cell culture Petri dishes, enabling to perform real-time measurements inside the incubator, sequentially over several devices. Then, vitality tests on the cell cultures are reported. Finally, OECTs are employed to continuously study both barrier and non-barrier cell layer formation and disruption, showing how the geometry influence the chosen cell monitoring. Furthermore, the OECT ability to assess cell health conditions when stressed by the introduction of nanoparticles in the cell media was investigated.
In the fifth Chapter, PEDOT:PSS coated stretchable electrodes are studied as a means to record neural activity from a peripheral nerve. In detail, the plasticizer polyethylene glycol (PEG) was introduced in the PEDOT:PSS, testing the elastic and electrical properties of the new composite compared to the pristine PEDOT:PSS ones. Moreover, also the electrode features and long-term stability were evaluated. In the end, the electrode was implanted and used to measure *in vivo* chronic nerve spiking activity in a free-moving rat.
OECTs as sensors were investigated in the sixth and last Chapter. The first Section reports the characterization of an all PEDOT:PSS OECT for sensing oxygen dissolved in solution, together with a first preliminary measurement in a biological liquid environment. The second Section is instead focused on the functionalization strategy of the gate of an OECT, in order to realize a biocompatible electrical device able to monitor cytokines or analytes released from stem cell undergoing osteogenic differentiation. Several techniques and electrical characterizations are employed to study the biofunctionalization unit, with a final proof of concept experiment for Bone Morphogenic Protein 2 (a cytokine crucial at earlier stage of the differentiation process)[6] detection.

Chapter 1

Organic Bioelectronics

1.1 Development of organic bioelectronic

Electrical signals to investigate biological systems are currently used to obtain further and usefull insights on signaling principles of living organisms.[7] What is now considered a powerfull but standard tool, has its origins in the experiment of Luigi Galvani, at the University of Bologna. He performed various experiments in the 18th century, electrically inducing muscular activities on a detached leg of a frog, that represent a starting point of Bioelectronics. Indeed, he was a pioneer in using bioelectricity to investigate tissue of living organism.[7]

Bioelectronic is a scientific branch that IUPAC defines as "the application of biomolecular principles to microelectronics such as biosensors and biochips".[8] In other word, as wrote Wolfgang Göpel (another hystorical bioelectronic pioneer) in 1998 "Bioelectronics is aimed at the direct coupling of biomolecular function units of high molecular weight and extremely complicated molecular structure with electronic or optical transducer devices". [9] This definition introduces two key point of this field, namely "direct couplig" and "high molecular weight": the first highlights the intimate integration between electronic and biomolecular principles in this field, while the latter reports the complicated biological structures this scientific branch has to deal with (i.e. proteins, cells, bacteria).[10] Indeed, biological systems are regulated by multiple chemical, electrical and electrochemical signals, that control life cycle of individual cells but also the behaviour of multicellular systems, for example organs or tissues. These signals can be carried inside the organism by the blood stream, along neurons or transported by cluster of cells, linked one another.[7] Usually a broad range of proteins or ions allow for the transmission of signals along these pathways, further confirming the complexity of biological systems. Bioelectronic aims at measuring and stimulating these multiple biological signals.

Nowadays, different electronic and electrochemical devices offer improved healthcare, enviromental protection and accelerate scientific research.[11] Among them, there are biosensors for glucose (or other interesting analytes) monitoring, pacemakers and defibrillators that helped saving unncountable lives and biomedical instruments providing insights on cell communication among each other and with the external enviroment.

As often happens with emerging technologies or disciplines, materials are the main limitation for the development of new bioelectronic devices[12], due to the need of softness, biocompatibility, biostability at the biological interface, together with the properties to transduce signal across biotic/abiotic interface.[11] As an example, neural interfaces require low invasive and long-term electrodes to record and stimulate brain/nerve activity. For this purpose, conducting polymer coatings have been used to endow metallic electrodes with many advantages, such as electrical impedance reduction, better mechanical properties and the possibility to deliver drugs. These features contributed in better stimulation/recording ability, improved life-time and reeduced inflammation response of the implanted area.[13] The next paragraph will focus on organic materials properties and features, needed for bioelectronic applications, while conjugated polymer (and in particular Poly(3,4-ethylenedioxythiophene) poly(styrenesulfonate), PEDOT:PSS), will be discussed in Chapter 2. In

particular, conjugated polymer properties led to the development of the Organic Bioelectronics, which deals with the use of carbon-based semiconductors (in form of polymer or small molecules) into electronic or optoelectronic devices at the interface with biology.[14]

Owing to the powerfull applications and the great potential in scientific researches, sanitary and biomedical field together with the economic opportunities related, research interest in bioelectronics and organic bioelectronics field ia growing at increasing rate. Figure 1.1a reports the number of pubblication per year regarding these topics from 1985 to 2015 in the Web of Science™ Core Collection Database. It should be noted the huge amount of absolute pubblications in bioelectronic topic, starting from 1990, while organic bioelectronic field started to gain interest quite recently, in 2005. This year could be seen a threshold also for bioelectronics in general, whose pubblication almost doubled and started having an exponential trend in the new millenium, due to the diffusion of organic semiconductors for different applications, such as organic light-emitting diodes (OLEDs), organic thin film transistors (OTFTs) and organic photovoltaics (OPVs) (Figure 1.1b).

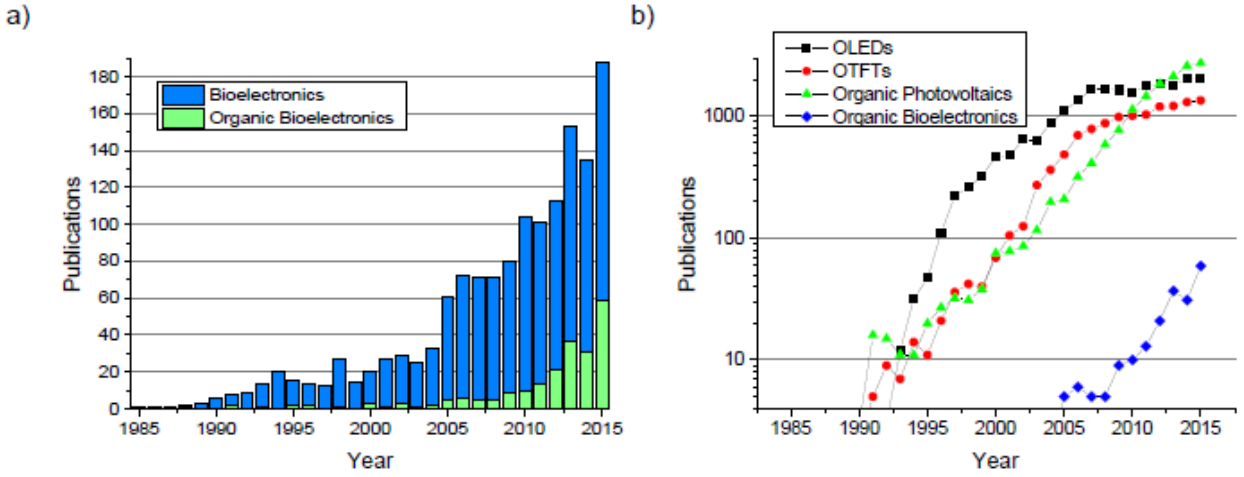

Figura 1.1: Pubblication per year regarding (a) Bioelectronics (the reported ones, plus the ones published without explicitily using the word bioelectronics) and (b) Organic Electronics from 1985 to 2015. Source: Web of Science™ Core Collection Database.

1.2 Organic Materials: Conducting Polymers

As reported above, materials are often the main limitation for new technologies development. This is the case for Bioelectronics: there is a mechanical and electrical mismatch between standard inorganic electronic devices and living biological systems. Electronic devices, such as transistors, electrodes and so on, are our way to measure and transmit signals or information, using electron and hole currents. On the other hand, the biological world, i.e. cells, DNA, neurons and microorganisms, usually communicate throught ionic current or chemical reactions, making interaction with known electronics quite difficult. In addition, even in presence of devices able to transduce the signals across the biotic/abiotic interface, currently used inorganic semiconductors or electronic devices have limited conversion in acqueous environment due to the Debye screening effect caused by the formation of an electrical double layer on the sensing material surface.[15] Indeed, electrostatic interactions in a liquid media are known to extend up to the Debye's screening length, reducing the distance at which the detector can probe a target analyte and limiting its application in biomedical analysis.[16] Moreover, there is a big difference in the mechanical properties of silicon-based devices and the biological systems: for example, human brain Young's modulus (0.1MPa) is 6-order of magnitude smaller than silicon one (170 GPa), which may lead to strain and mismatch between the surfaces in chronic implants.[17]

The gap between inorganic electronic and the biological living entitites needs to be filled by materials whose properties are able to interface these two separate worlds, such have proved to be conducting polymers. Indeed, as it will be further discussed in the next chapter, conducting polymers have a broad range of physical and chemical design space influencing parameters that can impact on cell growth and function: thus, an appropriate fabrication can ensure that the supporting/interfacing material do not adversely affect (but maybe improve, sustain or enhance) biological standard behavior.[18]

1.2.1 Properties of Conducting Polymers

Conducting polymers (CPs) (also called synthetic metals or conjugated polmers) are organic polymers, typically containing a linear backbone with repeated units of conjugated monomers, with highly reversible redox behavior and properties resembling both metal and plastic ones. The most commonly diffused are polyaniline (PANI), polypirrole (PPy), poly(ethylenedioxithiophene) (PEDOT), polythiophene (PTh) and polyfuran (PFu).[19] The great interest and popularity gained by bioelectronic field in last years is also due to the powerfull electrical and optical features owned by this class of materials, which were previously only seen in inorganic ones. Among the different properties, one of the most remarkable is their ability to be nanostructurally tailored depending on the required application, using innovative synthetic transformations or deposition techniques.[19] Other interesting features are their biocompatibility and "soft" nature, in contrast with the "hard" one for standard inorganic material for electronic applications, easy and low temperature processability, the possibility to control chemical structures and film morphology, together with their tunable conductivity and the corrosion resistance (biological interfacing often means the need to work in acqueous environment).[3,20,21] These features enable conducting polymers to have a better mechanical compatibility and structural tunability with biological living systems, an easy and wide range control over physical or chemical properties, using surface functionalizations or doping techniques, and the capability to be assembled or deposited resembling biological structures (fibrous, comformable, 3D porous).[3,7,21–24] This resulted in the replacement of traditional inorganic electronic materials with conducting polymers, having a variety of meaningfull applications in a broad range of fields, including energy storage, enviromental remediation, medical and biomedical applications.[25,26] In particular, conducting polymers have especially spread in biolectronic owing their promising biointerfacing capabilities:[3] as a matter of fact, electrodes coated with doped CPs are used to record neural activity,[27–29] and polymer-based devices are exploited as biosensors,[30–32] in form of electrodes or transistors, as tissue engineering films[33] and scaffolds[34,35] and as drug delivery systems.[36] Further insights and examples on CP bioelectronic applications will be covered in paragraph 1.3.

It might be usefull to introduce a comparison between two main representing materials of inorganic semiconductors and conducting polymers: inorganic silicon (Si) and the conjugated polymer poly(3,4-ethylenedioxythiophene) (PEDOT), both p-type doped (silicon with boron (Si:B) and PEDOT with poly(styrene sulfonate) (PEDOT:PSS)) and in contact with an electrolyte solution. Figure 1.2 shows a schematic of the suggested scenario, where a solvated ion is reported to have a relative scale. Silicon is composed by a network of covalent bonds, each atoms sharing valence electrons with four neightbors; on the other hand, PEDOT:PSS has covalently bounded (macro-)molecular blocks (typically planar, rigid aromatic repeated units that create a macromolecular conformation) which are held together by weak van der Waals intermolecular associations, together with dipolar and electrostatic interactions (for doped materials). These forces are reponsible of organic material "soft" nature and represent the main difference with inorganic silicon "hard" one.

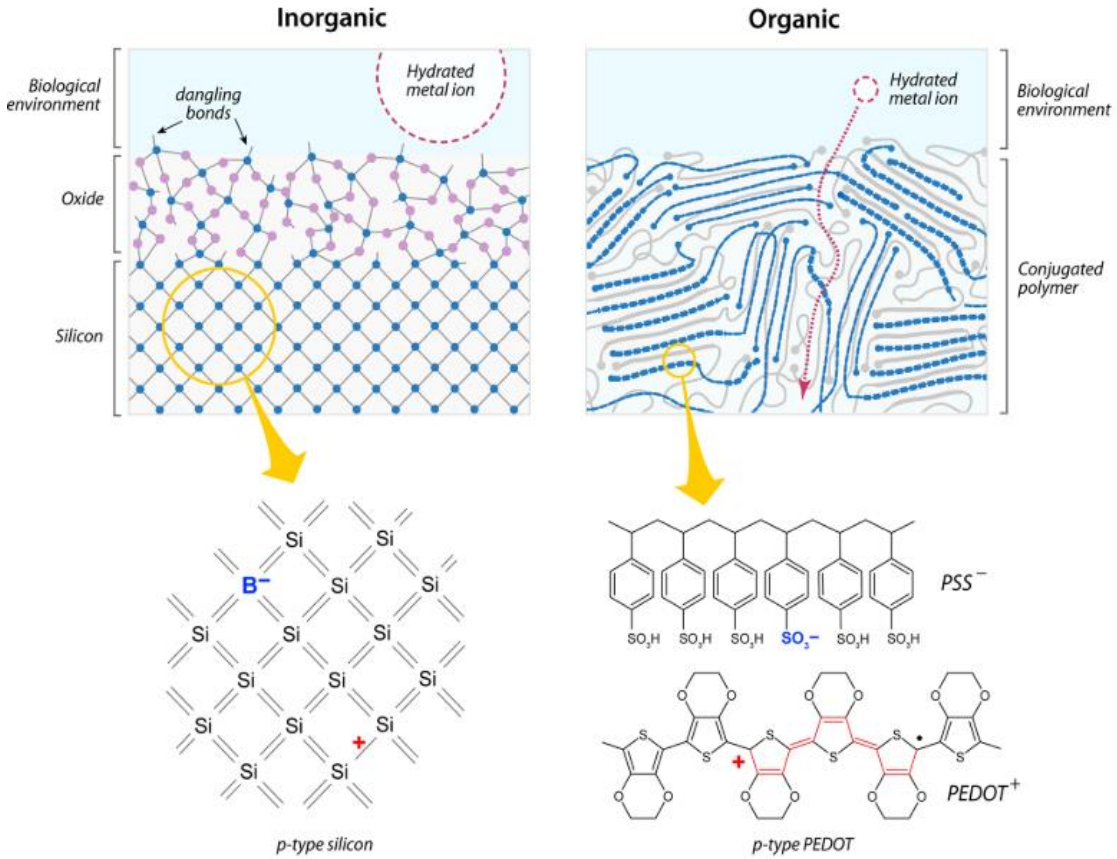

Figura 1.2: Schematic representation of boron-doped inorganic silicon (left) and organic PEDOT:PSS (right) at the interface with an aqueous enviroment. A hydrated metal ion is reported as a relative scale, highlighting the compact and rigid covalently bound silicon structure compared to the "softer" and less dense (relatively larger space are present betwen molecules) organic one.[11]

Stemming from this bondings are also the main features of CPs, that can be summarized as: [3,11,20]

- CPs allow a facile chemical and film morphology modification to reach the required features, dependent on the material application. Basic polymers can be considered blank canvas, using organic chemistry to tailor molecular design with several possibilities, since altering the π-conjugated backbone or the side groups, one can modify (opto-)electronic, mechanical or biological properties. For example, by adding biomolecules into the backbone or choosing selected materials at the starting point of the systhesis, it is possibile to further improve the compatibility between biological systems and the resulting final organic material. Moreover, thin film morphology and transport properties can be modified changing the size and/or shape of the side chains, while their composition can influence aqueous and ionic uptake.
- Doping. Organic materials can be either p-type or n-type doped, thus being able to achieve a broad range of conductivity (from insulating material almost towards metallic behavior). Differentely from their inorganic counterparts, doping mechanism relies on redox processes (oxidation/reduction) leading to charge carrier formation, upon charge transfer. The doping process produces charge carriers in the form of positive or negative polarons (radical ions), bipolarons (dications or dianions) or soliton in the CP. The latter are present only in degenerate polymers, which have two identical identical structures in the ground state, while polarons and bipolarons are observed in both degenerate and non-degenerate (having different structures, i.e. quinoid and benzoid, with different energy at the ground state) polymers. Upon doping, changes occur in the geometric structure of CPs (e.g., from benzoid to quinoid). For example, Figure 1.2 shows that removing an electron from the PEDOT thiophene chain leads

to the modification of part of the chain from an aromatic to a quinoid structure (as will be further explained in Chapter 2). Polarons and bipolarons are delocalized on the polymer chain, allowing the electronic conductivity. Since n-doping is not as stable as the positively charged form for CPs, p-doping is more commonly found in reasearch field (for example PPy or PEDOT).

- Once doped, organic materials can support hole (p-type) or electron (n-type) transport at room temperature, or even be classified as ambipolar (being able to support both). Noteworthy, they can transport also ions, which is allowed by the large space between molecules in their structure (due to van der Waals interactions). Additionally, the hydrophilic nature of CPs permits water uptaking and swelling, enhancing ion transport. Moreover, the high polaron density of CP systems increases ion penetration close to the polymer backbone thanks to the Coulombic attraction.

- Swelling abilities. CPs can undergo swelling/de-swelling, according to changing in their redox state. Electrochemical driven expansion/reduction of CP dimensions has been investigated with the aim of the development of a new generation of actuators, whose two different mechanisms are illustrated and explained in Figure 1.3. Oxidazing the conducting polymer, thus extracting electrons from its polymer chain, leads to the introduction of small anions in its matrix to keep the neutrality, which can be later expelled applying negative voltages (electrochemical reduction). Anion-driven actuation allows swelling (expansion in volume) upon oxidation and de-swelling (dimension decresing) upon reduction, as reported in Figure 1.3 a-c. On the contrary, if anions incorporated during polymerization in the CP matrix are large enough, they are immobilized and trapped inside the polymer structure. In this case, swelling may occur when cations move from solution into the conducting polymer upon reduction to compensate the charge (cation-driven actuation).

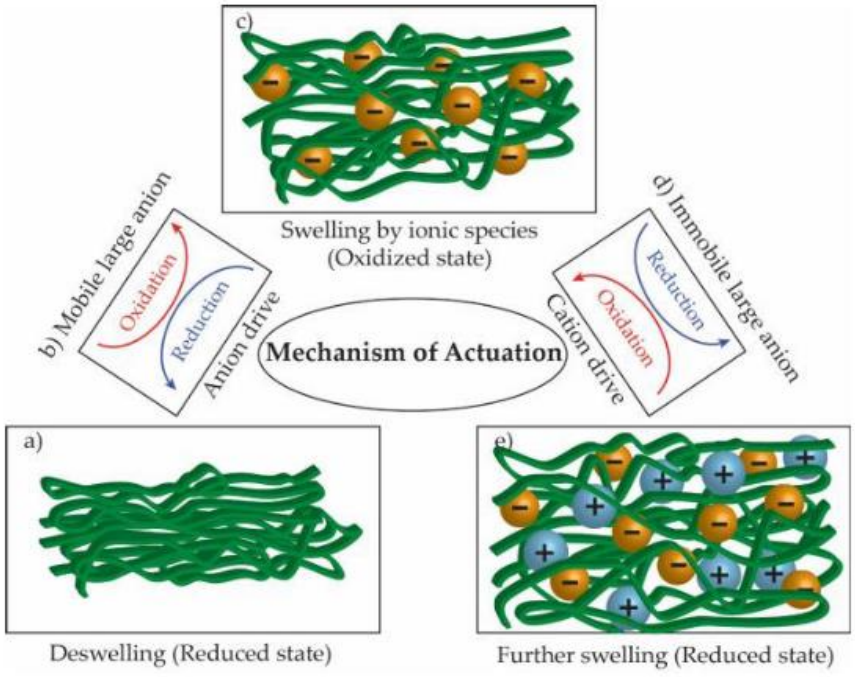

Figura 1.3: Schematic representation of the electrochemo-mechanical mechanism, regulating actuation in CPs (swelling/de-swelling capabilities). (a, c, e) Redox pathway leading to increase/reduce CP volumes (b, d).[20]

- CPs can be processed at low temperature, exploiting the weak interactions that keep molecular blocks together. Indeed, a mild heating or the addition of a solvent can overcome these forces,

thus depositing a film from vapour or solution on different selected substrates (i.e. glass, plastic, textile yarns) using low cost techiniques and materials.

- Reversible Electrochemical Oxidation/Reduction. This clearly represents one of the main features for organic materials, allowing for the development of a wide range of applications. Since geometric structure changes occur in the polymer upon charge carrier formation (benzoid to quinoid modifications), the original structure can be recovered electrochemically reducing it to its undoped state (driving ions in the semiconducting material film). This electrochemical doping/dedoping capability (within the electrochemical window given by the electrolyte) is based on electrochemical-driven ion uptaking and can be used to affect its electronic conductivity and, subsequently, film morphology and microstructure, together with optical and mechanical properties. Conversely, in silicon, the presence or creation of electronic charges do not change lattice structure, in which atoms are strongly bonded one another in a 3D template. Owing to the reversible electrochemical features, CPs have been employed for biosensors,[37–39] electrochromic devices,[40] and actuators for artifical muscles.[41]
- Organic materials allow for oxide-free interfaces with the electrolyte. As can be seen from Figure 1.2, on silicon, cleaved and exposed to the atmosphere, is present an oxide layer, while for CPs, van der Waals interactions lead to a well-defined and intimate interface with the aqueous environment, without dangling bonds or oxides. This enables direct contact and ion exchange between liquid biological environment and the material, while oxide acts as a physical 2D barrier, leading to an ion accumulation at the electrolye/oxide interface in silicon.
- Stricly connected to the previous feature, is the ability of CPs to bulky interact with the biological environment, since not only the surface, but the whole volume of the polymer film is involved in the ion exchange with the electrolyte, enabling a 3D interaction between them.
- As we stated above, they have better mechanical biocompatibility with biological surfaces, due to their "soft" nature, compared to the inorganic material "hard" one.
- Finally, they are often transparent, allowing for optical transmission imaging and microscopy-based techniques to study interactions between biological species and devices/films.

1.2.2 Interaction with biology

Humankind's endeavor to interface biological living systems with modern electronics started with Galvani's experiment in the 18th century, as we stated above, and now impacts on a wide range of fields, including philosophy, biology, chemistry, physics and medicine. Indeed, new tools for treating deseases or disabilities have been developed in the latter discipline, improving human health conditions (pacemakers, cochlear implant, deep-brain stimulation). Moreover, electrical experiments on living tissues, cells and brain/nerve have shed light on biological system behaviors and properties, previously unrevealed. Furthermore, together with *in vitro* studies using electronics interfaces with cell coltures for drug screening and preclinical tests, the pharmaceutical industries are exploring "bioelectronic medicines", with the aim to exploit electrical stimulation from implanted devices instead of traditional drug administration.

Clearly, these applications require high-quality, biocompatible and reliable interfaces between living tissues and inorganic electronics, provided by the conducting polymers. As previously explained, "Organic Bioelectronics", term coined by Berggren and Tichter-Dahlfors in their review,[7] is the discipline that bridges the electronic world of organic-semiconductor-based devices with the world

of biology. This crosstalk works in two directions, as depicted in Figure 1.4: on one side, a biological process or reaction can transfer a signal to an organic electronic device (for example an enzimatic reaction that leads to a current modulation in a polymeric transistor); on the opposite, an organic electronic device can stimulate a biochemical reaction or process (i.e. the polarization of a conducting polymer electrode stimulates a neural potential action).[3,24] In the former, the device acts as a sensor, transducing an analyte/ion/chemical variation in an electric output, while in the latter it behaves as an actuator, electrically stimulating a biological response.

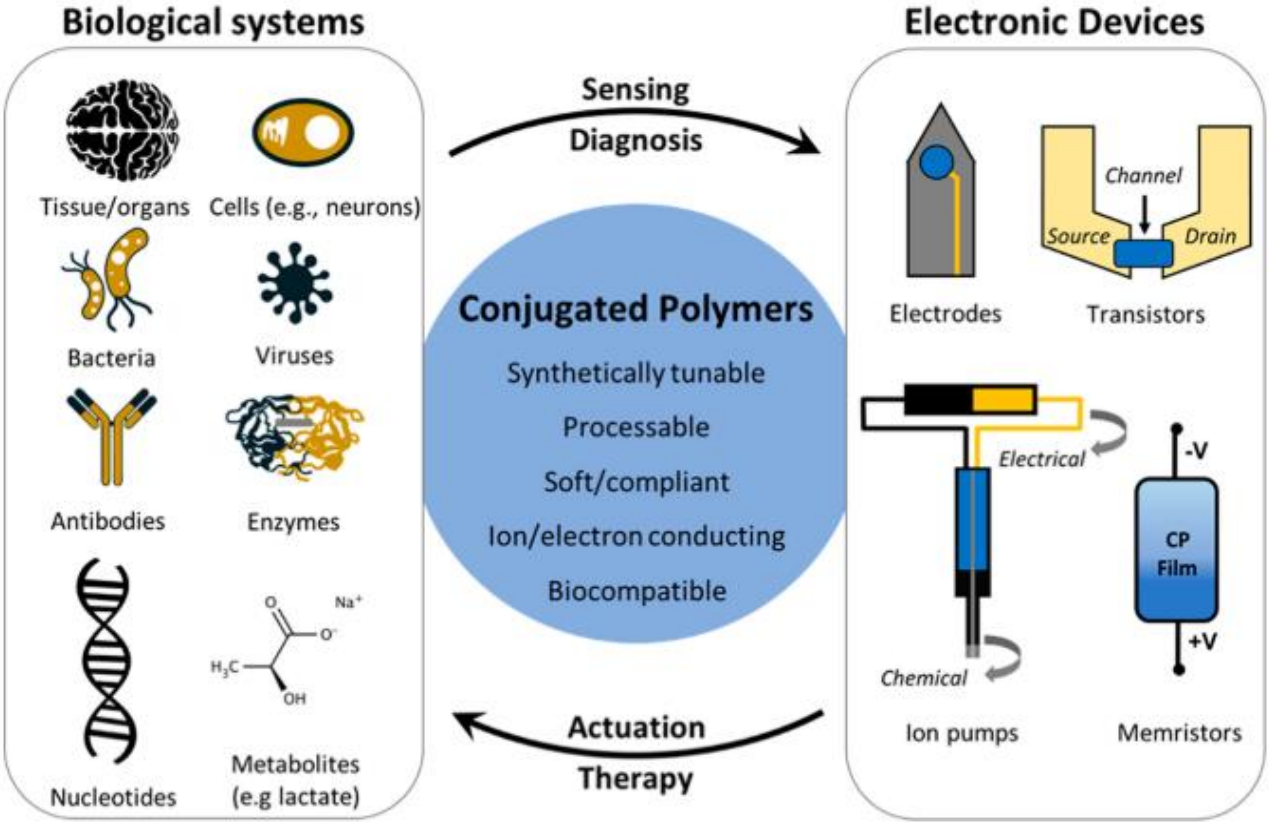

Figura 1.4: Scheme representing the bidirectional interaction between electronic devices and biological systems in bioelectronics. The gap between the two different worlds is bridged by conducting (conjugated) polymers, whose unique features allow the development of state-of the-art devices used for sensing and actuation in biomedical, reasearch and sanitary fields.[3]

Regarding the sensing, several natural biomaterials proved to be able to "recognize" one another, for example enzimes that metabolized substrates, antigens that specifically bind with antibodies or oligonucleotides hybridizing with complementary strands. Commonly, such biomaterials are exploited as transducers, coupled with electronic devices to built biosensors: thus, the biochemical interactions between the recognition element and the ligand are used to provide specificity, while the devices allow for the translation of the binding event into an electronic measurable output.[24,42] The main challenge in this coupling is to maximize the information transfer between the two elements, which is the reason for the conducting polymer wide-spread use in this field, being able to interact with these biomaterials. Biosensors will be further explained in paragraph 1.3.2, providing also different examples. At the same time, sensing can stand for "probe": semiconducting polymers have been indeed used as interface in electrophysiology between rigid inorganic electronics and soft neural tissue, in order to improve the quality of neural signal recording,[43,44] with the final aim to also stimulate neural systems. Indeed, as introduced above, electronic devices can be used to stimulate biological events: in particular, conducting polymers have attracted great interest for such "active"

applications.[3,24] In paragraphs 1.3.1 and 1.3.3 two main applications of CPs for stimulation will be discussed, i.e. substrates for tissue engineering control and electrodes for neural stimulation.
When interfacing biological systems with conducting polymers, the main important feature that needs to be taken into account is the biocompatibility of the material, which can differ vastly, due to the synthesis route of the organic polymer and the overall characteristic of the polymer itself, such as acidity, surface charge, roughness and chemical composition.[7] The route of synthesis of the choosen material can leave residuals inside the polymer (monomers, solvents, detergents, or excessive doping-ions), that, seeping out from the film ,may lead toxic effects on cells during experiments. Regarding the polymer characteristics, surface topography, which can range from micrometer to nanometer, may influence cell-surface interaction.[45] Moreover, this interaction, as well as cell adhesion and interfacing properties can be affected also by the absorption and organization of proteins on the surface.
A wide range of biocompatible studies have been done, using various kinds of vitality tests, in order to assess the biocompatibility of different pristinely doped or undoped conducting polymers.[46–48] Moreover, the biocompatibility of the surface can be dramaticcaly altered by coating the polymer surface with matrix proteins, which was proved by Langer and Ingber in 1994,[49] as well as changing the structure of the polymer in order to mimick and match tissue and organs. Strategies towards carefully designed nanopatterned surfaces[50] and 3D scaffold with porous structures[34,51] have been explored and are currently investigated to further improve cell-polymer matching and biocompatibility.

1.3 Applications

In this Section some of the most innovative and efficient applications, brought by organic materials, will be discussed.

1.3.1 Biocompatible surfaces and scaffolds for active cell tissue engineering

Tissue engineering or regenerative medicine is a discipline that aims at developing functional biological substitutes able to restore, maintain or even improve tissue functions and features, combining polymer films or scaffolds, with cells and biological molecules.[3,21,22,52,53] Indeed, polymers have several interesting properties desired for tissue enginering, such as processing flexibility, better mechanical compatibility, redox stability, reversible oxidation, biodegradability (often tunable) and biocompatibility. Moreover, in the form of scaffold, polymers can better resemble biomedical tissue or embed cells during their growth, having mechanical strenght and suitable porosity for the transportation of nutrients and waste.[54] However, it is still a challenge to combine such properties with the ability to enhance cell proliferation or guide cell differentiation. For this purpose, conducting polymers have been investigated since their conductivity allows to subject cells to an electrical stimulation, being thus able to promote cellular activities. For this reason, CPs are especially usefull to interface with electrical-sensitive cells/tissues, i.e skeletal muscle, nerves, cardiac muscles, skins and bones: for example, it was discovered that biomaterial with CPs can enhance cell adhesion and proliferation of C2C12 myoblasts, H9c2 cardiac cells, RSC96 Schwann cells and mesenchymal stem cells.[4,21,55,56] The broad range of applications of such organic materials will be discussed later in this paragraph, focusing formerly on various kind of conducting biomaterials fabricated by different techniques: a brief summary is reported in Figure 1.5.

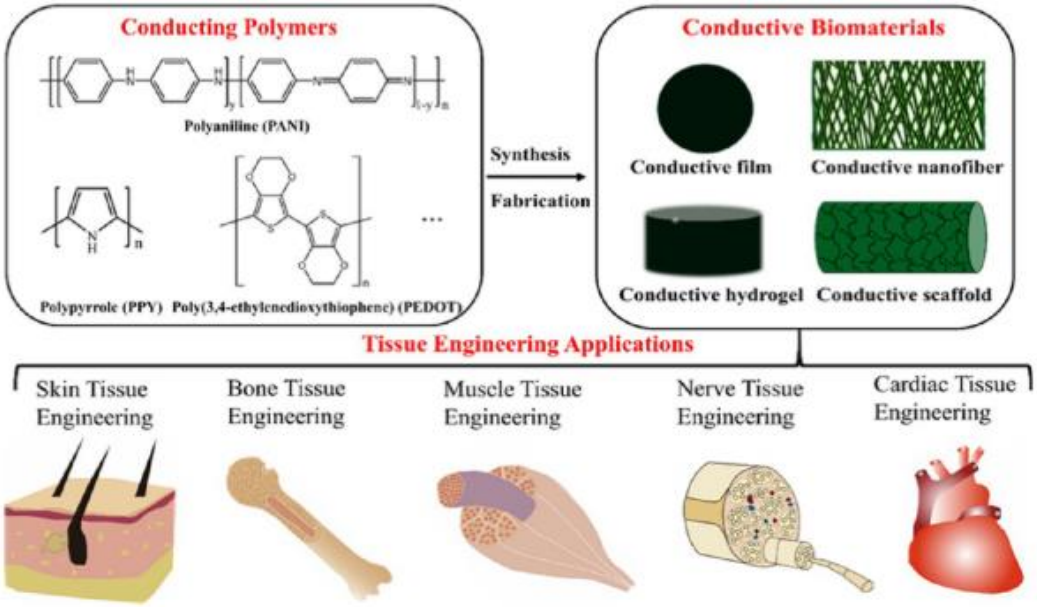

Figura 1.5: Schematic of conductive polymers and related biomaterials, with their possible tissue engineering applications.[21]

The first main example that redox-induced modifications of surface properties can control cell behavior was reported by Langer and co-workers in 1994.[49] They observed that aortic endothelial cells spread normally and synthesized DNA when cultured on fibronectin-coated oxidized polypirrole, while their extension and DNA synthesis were inhibited switching the polymer to its neutral state. Since the application of the same potential to cells cultured on indium tin oxide substrates had no effects on their behavior and shape, they conclude that conducting polymers can provide non-invasive substrates to control adherent cells.

Nowadays, PANI, PPy, PTh, PEDOT and their derivatives are the most attractive and used conducting polymers for tissue engineering purposes, due to their further ability to electronically control physical and chemical properties by surface functionalization or using molecules that can be entrapped or inserted as dopants in the polymer.[22,23] Noteworthy, different conducting biomaterials can be created starting from this pristine conducting polymers, which can be grouped in 6 main categories, namely thin films, blends or composite films, copolymer films, nanofibers, hydrogels, composite 3D scaffold.[21]

Thin films

CPs can be used for *in vitro* culture due to their ability to support adhesion, proliferation and differentiation of different cell types,[4,57] proving their cytocompatibility.[58] Moreover, biocompatibility was also confirmed in animal models, as demonstrated by no tissue response or inflammation in *in vivo* studies.[59,60] Conducting polymer can be synthesized chemically or electrochemically, with the latter method usually leading to a conducting film over an electrode. As an example, PPy nanoparticles were electrically deposited on an indium-tin oxide glass slide and preosteoblast MC3T3-E1 cells were cultured on top of it. It was proved that combined electrical and mechanical stimulation promoted MC3T3-E1 proliferation and differentiation, highlighting that nano-PPy membrane allow for bone tissue repair stimulation.[61] On the other hand, in situ polymerization was exploited to create a layer-by-layer PANI copolymer on polyethylene teraphtalate film, used to show that electrical stimulation increased the mineralization of both bone marrow stromal cells (BMSCs) and preosteoblast cells (MC3T3-E1).[62]

Blends or composite films

It is often difficult to fabricate pure conducting polymer film from pristine CPs, due to their brittleness.[63] Therefore, conducting polymer blends using other degradable polymers are widely exploited to develope biomaterials for tissue engineeering. An example is provided by the work of Marzocchi et al.,[33] in which PEDOT:PSS was simply spin coated or an additional electrodeposited layer was added onto the previously spin coated one: these films were then used under different oxidation states as cell growth substrates, for human gliobastoma multiforme cells (T98G) and primary human dermal fibroblasts (hDF). They found that the cell growth rate was influenced by the electrochemical state of the polymer and that this effect was cell-dependent. Indeed, T98G growth was enhanced in reduced samples, while hDF growth was improved on the oxidized substrates, indipendentely of the substrate preparation. Other common blending are created mixing synthetic and natural polymers, such as polylactide (PLA), poly(lactic-co-glycolic acid) (PLGA), polycaprolactone (PCL), chitosan and silk fibroin, with CPs like PANI and PPy. For example, conductive PPy/poly(D,L-lactic acid) (PDLLA) composite films and nerve conduits were made with emulsion polymerization and dip-coating methods for nerve regeneration studies, as will be shown later in this paragraph.[64]

Copolymer films

Conducting polymer nondegradability often limits in-vivo applications,[65] thus aniline/pyrrole-based copolymer were functionalized with hydrolyzable groups to develop conducting biomaterials that were both electroactive and erodible (biodegradable).[66] For example, Gharibi et al. realized electroactive polyurethane/siloxane/aniline tetramer composite films, with enhanced mechanical properties thanks to the siloxane introduction, together with electroactivity and antioxidant properties given by aniline tetramer.[67]

Nanofibers

Collagen, one of the main proteins of extracellular matrix (ECM), takes the form of nanofiber. In order to mimic the ECM structure, nanofibrous polymeric scaffolds have been realized throughout many techniques, including electrospinning, molecular assembly and phase separation.[68,69] Electrospinning is the most widely used technique for such purpose: the resulting fibers show high surface area and porosity, with tunable diameter between nanometers or micrometers.[70,71]

Ku et al. show that myoblast and neurons can be guided by fibrous strucure: aligned structure were able to enhance their proliferation and guide cells towards differentiation. Thus, well-ordered, alligned conductive nanofibers were fabricated, such for example PCL/PANI nanofibers, using a magnetic field-assisted electrospinning process for a blend of PCL and camphor sulfonic acid-doped PANI, mixed in 1,1,1,3,3,3-hexafluoro- 2-propanol (HFIP).[72]

Hydrogels

Several kind of hydrogel with different structures and properties have been made,[73–75] due to their rubbery nature (that closely resemble soft organic tissues), tunable properties and excellent biocompatibility.[76,77] Furthermore, injectable hydrogels have been strongly used in tissue engineering field owing to their ability to encapsulate cells,[78,79] such the ones based on gelatin-g and PANI (GP), realized by Li and co-workers.[80] Unfortunately, chemical gelatination-based hydrogels often contain monomers, initiators or agents that can be toxic for cells (such as glutaraldehyde or isocyanate).[81] Therefore, physical cross-linked hydrogels are more suitable for cellular applications since they undergo mild gelation processing without any cross-linking agents.[82,83] For example, an injectable electroactive hydrogel was synthetized by thermosensitive gelation, one of the most popular synthesis method for physical consuctive hydrogels,[84] chemically grafting an electroactive tetraanline segment onto the chain end of a thermosensitive Pluronic F127 (PF127-tetraanline hydrogel).[82]

Composite 3D scaffold

In the past decade, concerns regarding the physiological and biological relevance of 2D cell-culture model lead to the development of 3D models in tissue engineering to replace 2D planar substrates. The ECM organizes cells into a functional tissue, providing a physical scaffold with its topography, structure and composition, that regulates cell functions supplying the necessary biochemical cues. When processed in scaffolds with a porous architecture, CPs have the ability to better support 3D cell growth, mimicking the ECM behavior.[3] In particular, skeletal and cardiac muscle cells with aligned structure can strongly benefit from designing scaffolds that resemble native issues and are able to guide their 3D alignment. For example, Wang et al.,[85] realized scaffolds composed of an aligned nanofiber yarn (NFY) core and a photocurable hydrogel shell mimicking native skeletal muscle structure. They successfully demonstrated that aligned NFY guided C2C12 myoblast (seeded within the core-shell scaffolds) alignment, elongation and differentiation, while a suitable 3D environment for nutrition exchange and mechanical protection was provided by the hydrogel shell.
Conductive biomaterials allow for a broad range of applications, being able to electrically stimulate and improve specific cell functions: they have been widely exploited in the regeneration of electrical signal-responsive cells, including bone, cardiac, muscle, nerve and skin.

Bone tissue engineering

Conducting biomaterials were shown to enhance the adhesion and proliferation of MC3T3-E1 cells, osteoblast-like SaOS-2 cells, C2C12 cells, and mesenchymal stem cells.[65,86] PEDOT:PSS scaffolds with pore diameter of 50 μm allow cell growth and matrix deposition within the void spaces (Figure 1.6a-b), permit to enhance gene expression levels (ALP, COL1 and Runx2), promote osteocalcin deposition and increase extracellular matrix mineralization of MC3T3-E1 cells (as shown in Figure 1.6b), being able to induce the differentiation of osteogenic precursor cell into osteoblasts. Moreover, among the benefits of the CPs scaffolds, there is the capability of electrical stimulation of the tissue engineered substrates: for this purpose a heparin-doped PPy/PLLA conducting film have been used for osteoblast-like SaSO2 growth, using electrical stimulation to promote osteogenic differentiation, which was proved by higher calcium and phospate level than the control group and by the regulation of the osteoblast-specific markers espression level (BMP-2, ALP and Runx2).[87]

Cardiac tissue engineering

Heart excitation-contractions coupling works thanks to the propagation of electrical signals by means of cardiac cells in a synchronized fashion.[88] Wang and co-workers realized (by electrospinning) PLA/PANI conductive nanofibrous sheets that showed high cell viability and the capability to promote differentiation of H9c2 cardiomyoblasts, favoring cell–cell interaction, maturation with more secreted proteins and spontaneous beating of primary cardiomyocytes.[89]

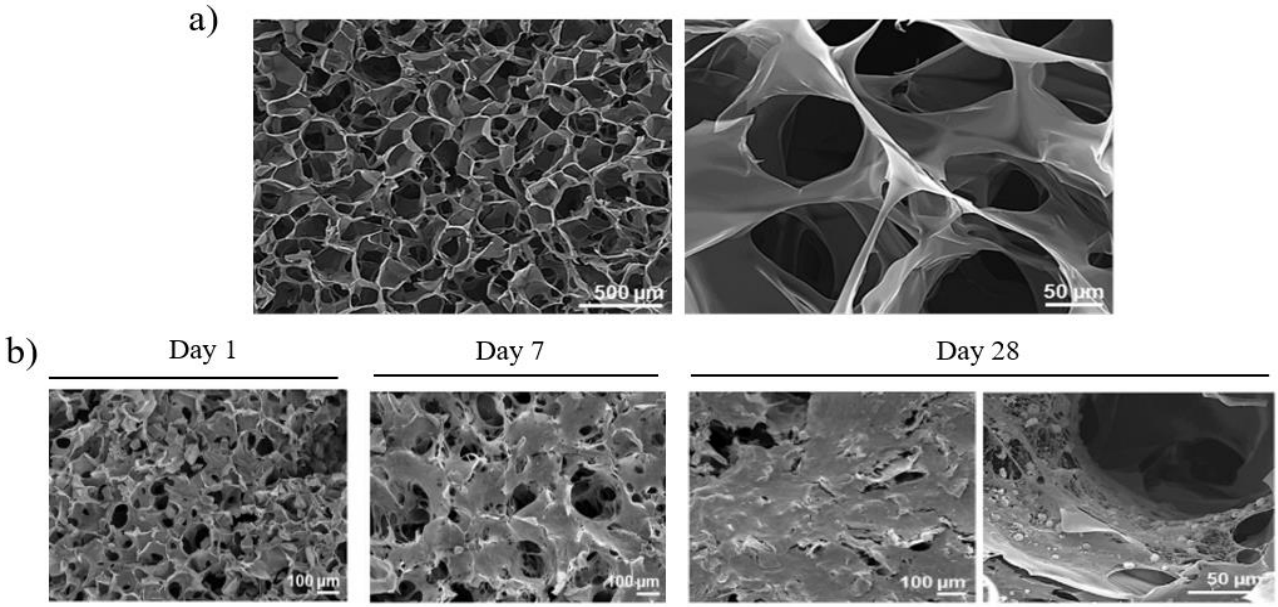

Figura 1.6: a) Scanning electron microscopy (SEM) images of PEDOT:PSS cunductive scaffolds with 50µm size pores, obtained through ice template. [90] b) SEM images of PEDOT:PSS scaffolds with MC3T3-E1 cells cultured within, after 1, 7 and 28 days after the seeding: it can be noted that cell number and matrix deposition were increased over the time, finally forming a tissue after 28 days.[90]

Skeletal muscle tissue engineering

Even though muscles have the ability to regenerate, under severe conditions, such as strong trauma, muscle function can be lost. Skeletal muscles tissue engineering, aiming to restore these functions, consists in the *in vitro* prefabrication of muscle tissues through differentiation of muscle precursor cells or stem cells, using a supporting scaffold.[91] Moreover, the typical anisotropic structure of elongated myofibers can be mimicked by the aligned structure of scaffolds composed by nanofibers. For example, Chen *et al* demonstrated that conductive and highly aligned PCL/PANI nanofibers were able to guide myoblast orientation and promote myotube formation and maturation, much more than nonconductive PCL fiber and random-aligned conductive PCL/PANI, as shown in Figure 1.7.[72]
Myofibers are the fundamental structural units of skeletal muscles and are formed by myoblast fused together in an elongated and multinucleated myotube (Figure 1.8a). For this purpose, as cited before, Wang *et al* designed core-shell composite scaffolds of aligned NYFs (Figure 1.8b), demonstrating that cultivated C2C12 myblasts were guided to align and elongate towards myotube formation, also for long-term cultivation (Figure 1.8c).[85]

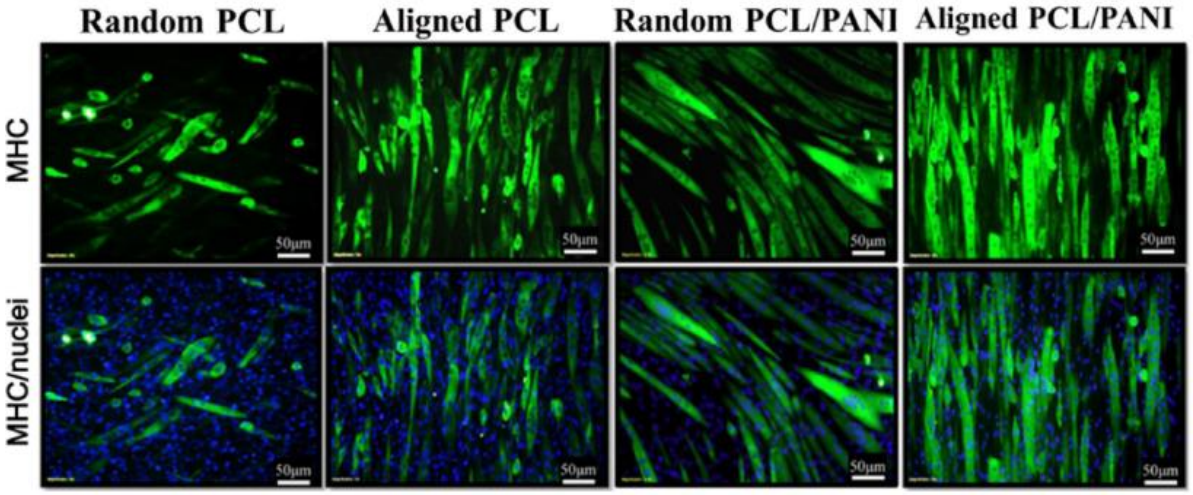

Figure 1.7: Immunofluorescence images of myotubes differentiated after 5 days on random-aligned PCL fibers, aligned PCL fibers, random-aligned PCL/PANI3 fibers and aligned PCL/PANI3 fibers, where MHC and nuclei were immunostained green and blue, respectively.[72]

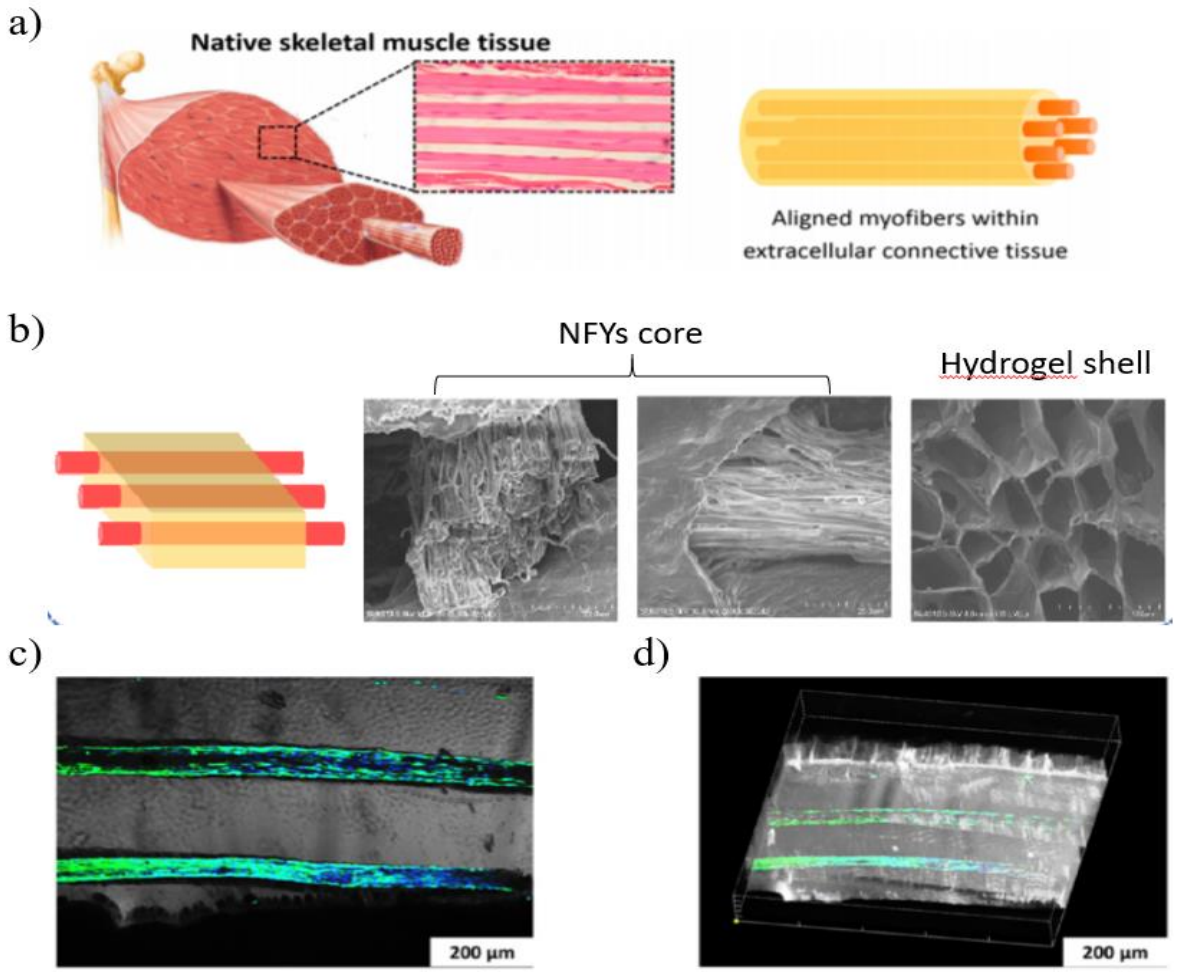

Figure 1.8: a) The native structure of skeletal muscle tissue, consisting in aligned myofibers surrounded by extracellular connective tissue. b) Core-shell sheet scaffold, resembling the extracellular connective tissue, made with aligned nanofiber yarns (NFYs). SEM images of NFYs core and shell of the scaffold. c) Merged image of NFY cores with cultured and aligned C2C12 cells, organizing into myotubes, inside the hydrogel sheet. d) 3D side view of the realized core-shell scaffold containing myotubes.[85]

Nerve tissue engineering

Neurons are electrically excitable cells able to transmit signals at a quick pace.[92] Different conducting polymer, such as PPy and PANI, have been developed as conductive scaffolds to improve and guide nerve tissue regeneration.[93,94] Furthermore, electrical stimulation was shown to be effective for nerve regeneration and neuronal function.[95,96] Indeed, PC12 cells seeded onto conductive PPY/PDLLA conduits showed enhanced percentage of neurite-bearing cells and median neurite length, upon the increase in PPy content and the application of electrical stimulation (100mV for 2h), as could be seen from the Figure1.9a-h. Thus, a PPY(5%)/PDLLA nerve conduit was implanted in rat to bridge a 10mm defect of the sciatic nerve, presenting functional recovering with performances similar to the autologous graft gold standard.[64] Finally, also template alignment plays an important role: aligned conductive PPy nanofibers presented neurites oriented along one direction with longer maximum length compared to the ones cultured on random-aligned counterparts. Again, it was shown that for both aligned and random nanofibers the electrical stimulation enhanceed maximum neurite length.[97]

Skin tissue engineering

Human body is protected from external damage and microbial invasion by the skin. Among the different biomaterials that have been used for wound dressing owing their antibacterial properties,[98] conductive materials have been demonstrated to promote cellular activities, including fibroblast and keratinocytes.[36,99] Moreover, some conducting polymers also presented antibacterial properties, such as PANI, thus rendering them suitable for wound healing applications.[100,101] For example,

antibacterial and conductive injectable benzaldehyde-functionalized poly(ethylene glycol)-co-poly(glycerol sebacate) (PEGS-FA)/quaternized chitosan-g-PANI (QCSP) hydrogels were developed and used for wound healing: such hydrogels, with 1.5% of cross-linker, showed *in vivo* excellent blood clotting capacity and enhanced wound healing.[102]
Conducting polymers clearly demonstrated to be suitable smart materials that may be used to restore electrical-sensitive cells and tissues, thus more researches on the synthesis and functionalization of these biomaterials is continuely carried on.

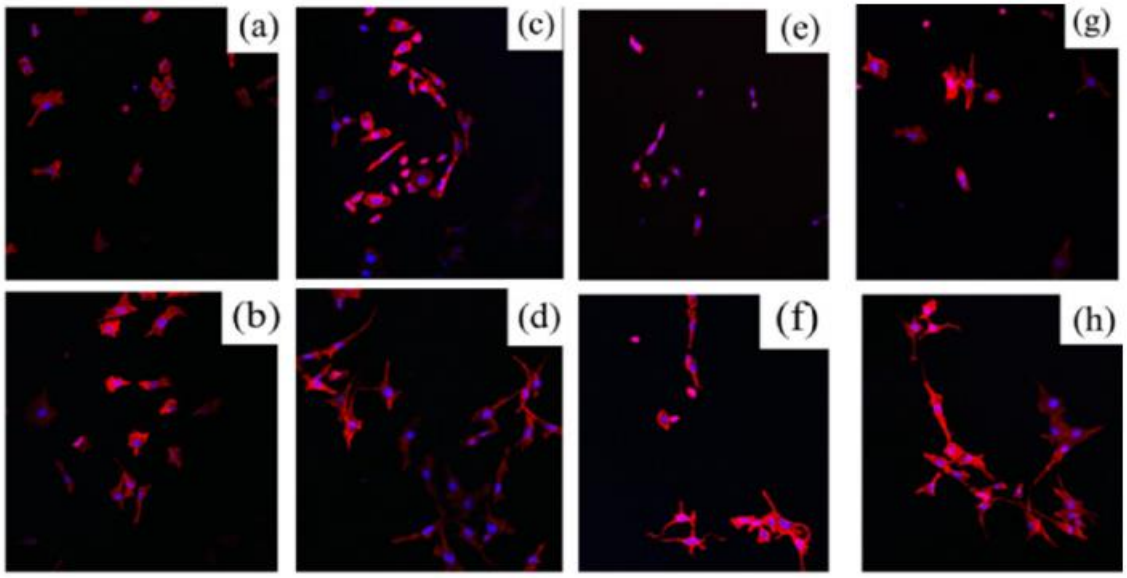

Figure 1.9: Fluorescent images of PC12 cells stained for actin (red) and nuclei (blue) seeded into PDLLA(a), 5% PPY/PDLLA (c), 10% PPY/PDLLA (e), and 15% PPY/PDLLA (g) conduits without electrical stimulations and into PDLLA(b), 5% PPY/PDLLA (d), 10% PPY/PDLLA (f), and 15% PPY/PDLLA (h) conduits with electrical stimulations of 100mV for 2h. Scale bar:200nm.[64]

1.3.2 Biosensors

The first biosensor was developed by L. C. Clark and C. Lyons in 1962,[103] that succeeded in continuously recording blood chemistry in surgical patients for hundreds of hours. Indeed, a system with external electrodes was used to study blood pH, oxygen and carbon dioxide tensions, together with intravascular electrodes capable to detect hydrogen, sense oxygen tension changes and to indicate ascorbate dilution curves. Since that year, many other steps and studies have been made monitoring metabolites (such as glucose, neurotransmitters, antibodies, hormones, antigens) or other biological analytes, exploiting biosensors for different applications in medical diagnosis, drug discovery, environmental and food safety fields.[23,104]
Biosensors are devices composed of biological sensing elements, capable of producing sensitive and selective analytical signals. More precisely, IUPAC defines a biosensor as "a device that uses specific biochemical reactions mediated by isolated enzymes, immunosystems, tissues, organelles or whole cells to detect chemical compounds, usually by electrical, thermal or optical signals". This definition highlights the two main components of a biosensor, i.e. (1) a biological sensing element, that interacts with the the bioanalyte/molecule/chemical of interest producing a chemical signal, connected to (2) a transducer, which converts the response into a measurable output, that should be proportional to the concentration of that target bionalyte/molecule/chemical (Figure 1.10a).
1) The former, also called "biocomponent", is the recognition elements which imparts selectivity to the sensor but could be vulnerable to harsh environmental condition (temperature, pH, ionic strength).[105] For this reason, they are often fixed in a suitable matrix, such as membranes, gels, carbon or polymeric films, exploiting different techniques such as physical adsorption, cross-linking, gel entrapment, covalent coupling, etc.[106–110] The final activity and behaviour of the immobilized

molecules will depend on the reaction condition and method chosen for the immobilization, but also on surface area, porosity, hydrophilic character of the matrix.[105] Great interests have been directed towards conducting polymers as suitable matrix, looking for rapid electron transfer at the electrode surface, enhanced speed, sensitivity and versatility of the biosensors for a broad range of analytes.[105]
2) The transducer, which converts the biochemical signal into an electronic output, usually responds in a way that the signal can then be electronically amplified, stored or displayed. The appropriate transducing system, which can be an electrochemical, spectroscopic, thermal, piezoelectric or surface acustic wave technology,[111,112] can be introduced in the sensor structure depending on the nature of the biochemical interaction with the biological elements.[105]
As stated above, CPs are extensively coupled with biological elements to build biosensors, acting as matrix to entrap/immobilized biological molecules (thus coupled with a biorecognition element) or working as transducer to integrate the signal produced by the biochemical sensing mechanism. Indeed, CP electrical and optical properties may change upon the specific binding between the recognition element and the target molecules.[113] Moreover, sometimes they can act both as biorecognition and transduction element, giving a continuous and selective detection of bio-interaction.[18,114,115] Their wide-spread use for biosensing is due to their inherent properties that render CPs suitable for interfacing with biological active elements: flexibility in the available chemical structures (modulating, in accordance, chemical and physical features of the polymer); the possibility to modify the polymer binding protein molecules (even during the electrochemical synthesis, thus controlling film thickness, the distribution of immobilized molecules and molecules activity); biocompatibility with biological molecules in neutral acqueous solutions; the capability of being reversibly doped and undoped (that leads to conductivity and/or spectroscopic variations); the ability to efficiently transfer charges produced by biochemical reactions to an external electronic circuit; the ease of deposition. In particular, electrodeposition has been widely used to deposit thin polymeric films due to the possibility of immobilyze enzymes,[116] that provide good detectability and fast response with the redox reaction occurring in the bulk of the polymer matrix. Figure 1.10b reports a schematic of the electron pathway for an amperometric biosensors, where an appropriate enzyme catalyzes the biochemical reaction.
A first division of biosensors made of CPs can be made according to the transducing system they provide for the sensing and transmitting of the starting chemical signal related to the analyte detection. There are different categories: amperometric (measures current), potentiometric (potential), conductometric (change in conductivity), optical (light absorbance or emission), calorimetric (change in enthalpy), and piezoelectric (mechanical stress). The most important and diffused biosensor categories will be discussed below, together with some examples.[23,105,116]

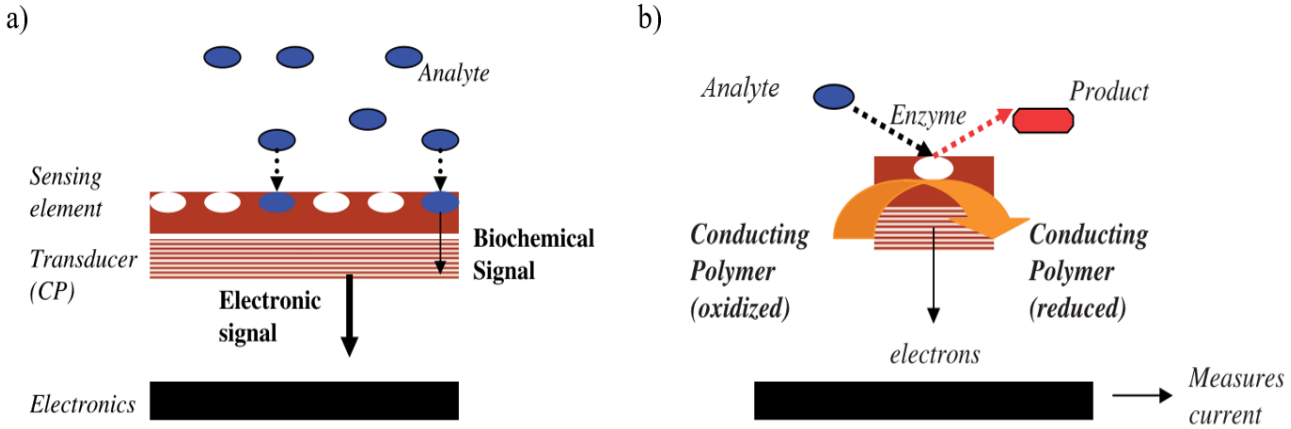

Figure 1.10: a) Biosensor representative schematic, reporting its two main components: a biological sensing element (i.e. enzyme, antibody) and a transducer. b) Electron transfer schematic for an enzyme-based amperometric sensors. The entrapped enzyme is used

to catalyse a redox reaction for a specific analyte, transferring an electron to the CP, which leads to the its reduction. A current can be measured as electronic output at the polymer edges. [23]

Electrochemical Biosensors

Electrochemical biosensors usually convert a biochemical reaction of target species into an electrical signal, which exhibits changes in current, potential or conductivity.[37] Thus, this type of biosensors can be divided in 3 main categories, which are voltammetric/amperometric, potentiometric and conductometric/impedimetric biosensors, further described below. Electrochemical methods are interesting due to the very low detection limits they offer, the high selectivity and the small amount of volume required for the detection part. Electrochemical devices usually consist in two or three electrode systems: a typical three electrode cell is formed by a working electrode (WE), where the detection occurs; a reference electrode (RE), usually a silver-silver chloride one (Ag/AgCl); and a platinum wire as a counter electrode (CE). A potential is applied relative to the RE, while a current flows between CE and WE, affected by the electrochemical reaction that occurs on the WE surface and by the electrode/electrolyte interface layer. This allow for the target species detection.

Amperometric/Voltammetric Method

An amperometric (voltammetric) biosensor measures the current flow produced upon the oxidation or reduction of a product or a reactant (for example the redox reaction of a substrate in an anzyme, such as shown previously in Figure 1.10b), usually under a contant (sweeped) applied potential. The main factor affecting amperometric sensor performances is the electron transfer between the catalytic molecule (usually oxidase or dehydrogenase) and the electrode surface, often exploiting a mediation or a conducting polymer.[105] The polymer matrix partecipates in the electron transfer process allowing the design of reagentless biosensors, thus operating in the absence of natural cosubstrates. However, the role of CPs in not fully understood. Several polymers have been used for enzyme or molecule immobilization and their presence and deposition can affect biosensor sensitivity and response. Redox mediators, such as ferrocene, Prussian Blue, viologen or derivatives have been introduced to improve electron transfer or reduce interferences, thus improving sensor sensitivity and selectivity.[23,116] These are incorporated as dopants, entrapped, or chemically conjugated to the monomer.[117–120]

An example of amperometric biosensor using conducting polymers is the cholesterol biosensor of S. Singh et al,[32] who co-immobilized (using covalent linkage through glutaraldehyde) cholesterol oxidase, cholesterol esterase and peroxidase onto electrochemically fabricated polyaniline films. On the other hand, an example of an enzyme-free amperometric biosensor using CPs is reported in the work of Prof. Fraboni's group: a full PEDOT:PSS-based organic electrochemical transistor has been developed as ascorbic acid (AA) sensor, using the transistor inherent amplification to further increase the amperometric output.[39] In this case, AA oxidation takes place at the PEDOT:PSS gate or channel (depending on the applied electrical potential on the gate: on the gate for positive potential and on the channel for negative one) reducing in both cases the current flowing in the channel, which is linearly dependent to the logarithm of the concentration, allowing the sensor calibration.

Potentiometric Method

Potentiometric biosensors often use ion-selective electrodes as physical transducers and are based on the measurement of the potential while drawing negligible (almost zero) current.[121] Even if potentiometry is a less used detection method for biosensors with enzymes immobilized in electrodeposited polymer, they provide some advantages over amperometric detection. Indeed, potentiometric method seems to be less affected by the aging process of the polymer layers that contain the entrapped enzyme. For example, a polypyrrole-based electrode with glucose oxidases (GOx) bound on top have been demonstrated to have a reduced rate of degradation of polymer matrix.

Potentiometric biosensors made of CPs can also be fabricated exploiting pH sensitivity of polymers, such as the interaction of ammonia (NH_3) with PPy, that was used to built an urea biosensor, with urease immobilized in the polymer layer.[122]

Conductometric and Impedimetric Method

Conductometric biosensors rely on the measurement of the conductance variation of the biological element arising between two metal electrodes. Conductivity biosensors with conducting polymers were fabricated for penicillin[123] and also for glucose, lipids, urea and hemoglobin, following the concept that the enzyme-catalyzed reaction of the biomolecule changes the pH and/or redox potential of the polymer matrix environment, triggering an electrical conductivity variation.[124] For example, urease immobilized on PPy layer, deposited on gold film electrodes, was used to sense urea concentration in the mM range, measuring conductance, capacitance and admittance.

Regarding the impedimetric biosensors the experimental approach is to perturbate the system with a small-amplitude AC potential, observing the AC current response of the system (using only one frequency or sweeping on a broad range): the impedance is thus calculated dividing the potential by the current. Then, depending on the presence or absence of specific recognition elements, two types of biosensors are obtained: in the first one, the impedance change relies on the binding of targets to receptors, such as antibodies and nucleic acids, previously immobilized on the electrode surface; in the second one, adsorption or desorption of target species, as a result of growth, leads to surface and, consquentely, impedance variations.[37,125] Electrochemical impedance spectroscopy technique will be better explained in Materials and Methods Section.

Optical Biosensors

Optical biosensors rely on the measurement of adsorbed or emitted light due to a certain biochemical reaction. In these sensors, light waves are often guided using optical fibers toward suitable detectors for the signal quantification. Optical biosensors have been exploited for the detection of O_2, pH and CO_2. Moreover, also glucose sensing was performed with optical method: Sinhal et al. developed an optical glucose sensor, using UV-visible spectroscopy after the immobilization of GOx on polyhexylthiophene by Langmuir-Blodgett technique.[126]

Calorimeric Biosensors

Calorimeric biosensors are based on the principle that all biochemical reactions involve an enthalpy variation, which can be detected and measured by the biosensor. For example, Mosbach and Danielsson in 1981 realized an enzyme thermistor in which a thermistor device measured the temperature change occurred after an enzyme reaction.[127]

Piezoelectric Biosensors

When an anisotropic natural crystal is subjected to mechanical stress there is the generation of electric dipoles. Once an analyte is adsorbed on a crystal, the total mass increases, thus altering the oscillation frequency. This is the principle on which piezoelectric biosensors are based. Such kind of method have been utilized for ammonia, methane, carbon monoxide, nitrous oxide, hydrogen and other organophosphorous compounds sensing.

Since conducting polymer-based biosensors have been widely used for different purposes and research fields, several device classes/configurations have been developed, according for the required features and the final application. In this thesis, some of the main biosensing devices will be discussed and shown: electrodes, organic field effect transistors (OFETs), ion-selective organic field effect transistors (ISOFETs), electrolyte-gated field effect transistors (EGOFETs) and organic electrochemical transistors (OECTs).[1,3,7,128]

Electrodes

Electrodes coated with CPs are commonly used as biointerface, in most cases to record local electrical potential changes, especially for neural implants (non-specific electrical sensing). Noteworthy, they are also capable of sense, in amperometric[129] or potentiometric[130] mode, a variety of biologically relevant analytes, and record potential-dependent oxidation or reduction of biomolecular species (for example via the fast-scan cyclic voltammetry). CP coating resembles the standard polymer coating introduced for neural recording electrodes (as it will be discussed in paragraph 1.3.3), whereby specificity can be imparted adding a transduction or a functinalization layer, as an ion-selective membrane or an antibody towards a specific antigen. Moreover, the use of CP coating allows for an effective capacitance that is 2 order of magnitude higher compared to the one of metallic electrode, since ionic species can penetrate in the film bulk and electronic carriers can be transported inside it.
Among several applications, immunosensors have gained great interest for many years due to the possibility to provide quick, selective, reliable and sensitive immunological responses. In these systems, antibodies are used to impart specificity towards the selected antigen in the sensing mechanism: the common approach is the so-called enzyme-linked immunosorbent assay (ELISA). Then, several chromatographic and/or photometric techniques are added in order to combine analyte sensing with the signal recording. As a matter of fact, ELISA has been coupled with amperometric electrodes, using the enzymes to amplify the primary signal and detecting at the electrode the enzymatic reaction species. Enzyme conjugates, commonly horseradish peroxidase (HRP), glucose oxidase (GOx) and catalase, are immobilized either in the bulk or at the surface of the polymer.[131]
One problem in the use of mediators, antibodies and enzymes is their leakage into the analyte solution. To face this problem Darain *et al* polymerized carboxylterthiophene monomer (TCAP) on screen-printed carbon electrodes, using carboxyl grous as immobilizing sites for HRP via amide bonds.[131] Then, the electrode was functionalized with streptavidin (covalently bound to TCAP), biotin and the selected antibody anti-rabbit IgG (RIgG). The analyte contained known concentration of RIgG-GOx, glucose and RIgG molecule. H_2O_2 (produced by RIgG-GOx) oxidizes HRP to different extent, depending on RIgG concentration. The HRP oxidation level (reduction of HRP at cathodic potentials) is then recorded at the electrode and the catalytic current is thus used as sensing parameter.

Organic Field-Effect Transistors (OFETs)

Whereas electrodes can be considered as passive devices for biosensing, transistors have been evaluated for their ability to amplify and transduce biological signals.[3]
OFETs were first introduced in 1980s by Nara's group[132] and are now reaching performances and interest levels comparable with their inorganic conterparts.[133] Typical organic p-type or n-type semiconducting materials (with different chemical and physical properties) that have been used for OFET include polymers such as poly(3-hexylthiophene) (P3HT) and alkyl-substituted triphenylamine polymers (PTAA), but also some oligomers like pentacene and its soluble derivatives, as well as α-sexithiophene (α6T).[134]
OFETs are three terminal devices, with contacts usually made in metal, named source (S), drain (D) and gate (G) and with an organic semiconductor (OSC) film connecting S and D, representing the channel of the device (with the length L being the distance between S ad D pads, while the width W is the geometrical width of the pad itself), while the gate is separated from the channel by an insulator. A representative schematic is shown in Figure 1.11. Different dieletrics have been used such as vacuum, oxides, polymers or self-assembled monolayers,[128] usally having high capacitance either due to a high dielectric constant or because it was in the form of a thin film.[133]

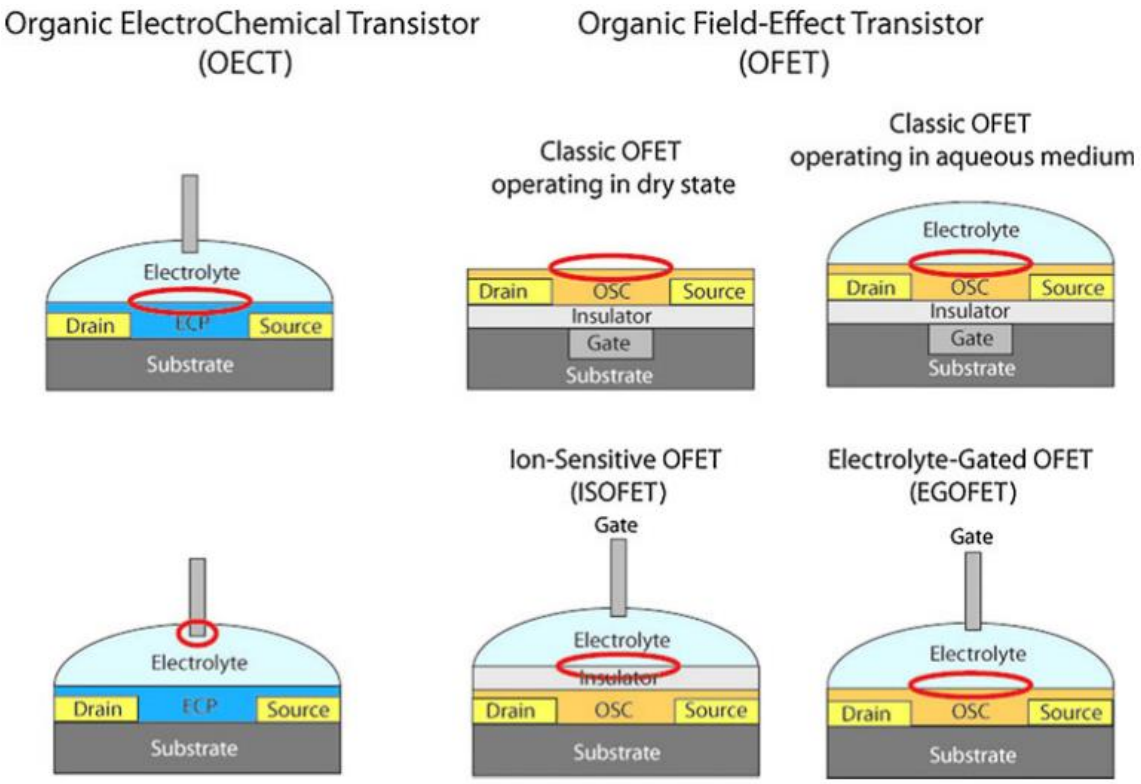

Figure 1.11: OECT and OFET architectures for possible different biosensors. The red circle reported in each schematic stands for the interfaces involved in the biosensing detection of the target analyte/biomolecule.[128]

OFET working principle is the following: when the gate is negatively (positively) biased (V_g) in a p-channel (n-channnel) device, free holes (electrons) in the OSC are attracted toward the semiconductor/insulator interface in order to compensate the negative (positive) charge induced by the bias at the gate/insulator interface. This creates a conductive channel at the semiconductor/insulator interface. Thus, when a negative (positive) potential is applied at the channel edges (V_{ds}), holes (electrons) are introduced from the source, leading to a current flow inside the OSC channel (accumulation mode). The gate voltage is used to modulate the transistor current (capacitive-coupled with the OSC channel), but in particular the voltage required to switch the device from its "off" to its "on" state is called *threshold voltage* and it is a key parameter of the transistor, together with the charge carrier mobility and the charge current modulation ratio between the two states. On the contrary, if gate voltage biases are reversed for the p-channel and n-channel devices the relative mobile charge carriers, holes and electrons respectively, are pushed towards the bulk of the semiconductor, thus depleting the channel of the transistor and decreasing the source-drain current, I_{ds} (depletion mode). Since the OFET characteristic curves are affected by the dielectric/insulator interface or by the grain boundaries, this device is a perfect transducer for sensor application.[128] To further understand this working behaviour one can refers to Figure 1.12, reporting the band-diagram of a metallic gate, an insulator and an OSC p-channel when no bias is imposed (Figure 1.12a) and for accumulation (Figure 1.12b) and depletion(Figure 1.12c) modes. It can be noted that the field generated by the negative gate potential induces a band bending in the semiconductor. In particular, a negative V_{gs} allows the confinement and accumulation of positive charges, creating a conductive channel perpendicular to the pictured plane which leads to a two-dimensional (2D) transport (Figure 1.12b).[135] Differently, a three-dimensional (3D) transport occurs when $V_{gs} = 0$, cause it involve the charges in the whole p-type OSC film, introduced with doping processes and related to impurities or structural defects (that are not easily controllable) that must be an order of magnitude lower compared to their amount in the on state. When a positive potential is applied, it induces the band-bending on

the opposite way, causing an acceleration of the charges towards the bulk of the material, thus closing/destroying the channel (Figure 1.12c). Noteworthy, the 2D transport inside the channel occurs only when the electric field generated by V_{gs} is much higher than the one generated by V_{ds} (gradual channel approximation).[133] All the voltage potentials are usually applied with respect to the grounded source, which is called common source configuration.

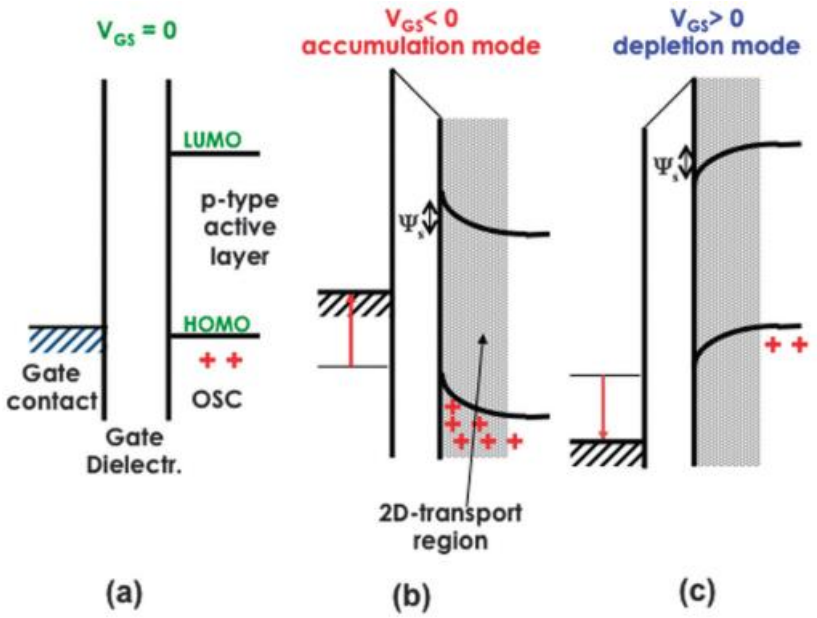

Figure 1.12: Band diagram of a metal-insulator-(*p*-type) semiconductor structure under (a) zero gate potential (V_{gs} = 0), and in (b) accumulation (V_{gs} < 0) and (c) depletion (V_{gs} > 0) modes.[133]

In OFETs the OSC should be highly resistive when no bias is applied (V_{gs} = 0), in order to have low I_{ds} in the off state; on the contrary, the current should be as high as possible once the transistor is turned on for V_{gs} < 0.[133] As introduced before, the switching between the two states is obtained via capacitive accumulation of charges at the dielectric/semiconductor interface induced by the gate voltage. Charge accumulation results proportional both to V_{gs} and the capacitance of the insulating layer (C_i), highlighting why high capacitances, thus high dielectric constants and/or low thickness dielectric layers (ε_r), are required. Moreover, using high capacitances one can reduce power consumption and operating voltage of the device.[136]

The use of OFETs as chemical sensors rely on the exposure of the OSC directly to the gas or solution under analysis, acting as electronic transport material and sensing element. The interaction with the analyte leads to variations in OSC properties, i.e. carrier mobility, on/off ratio and threshold voltage, that can be correlated to the analyte concentration. The same principle works when a recognition element, which is able to electrochemically react with the target analyte, is integrated in the device structure or chemically anchored on the OSC surface to impart selectivity. This functionalization helps to overcome OFET selectivity limitations, allowing for label-free and repeatable sensing in different fields, ranging from ammonia[137] and peroxides[138] to a broad range of biomolecules.

Ion-Selective Organic Field-Effect Transistors (ISOFETs)

One of the most common OFET-based biosensor architecture is the ion-selective OFET (ISOFET)[139]: here, the gate electrode and the dielectric layer are not in direct contact, but they are instead separated by an electrolyte solution, containing the analyte. In ISOFET a reference electrode is used as gate, dipped into the electrolyte, as reported in Figure 1.11. The potential at the electrolyte/ dielectric interface is the drain current regulator (and exploits the presence of ions in the electrolyte solution) and the detection occurs making the insulator sensitive (functionalization) to the target analyte. A typical ISFET example was developed by Bartic et al[140] that fabricated a pH sensor with a silicon

nitride deposited on P3HT layer. Even though pH variation in the range from 2 to 10 were detected, high voltages (10V) were required for the device operation, preventing its use in acqueous environments. Thus, a thin tantalum oxide (Ta_2O_5) layer was introduced as gate, with two purposes: enhance the capacitance, thus lowering the working voltage, and increase the sensistivity.[141] The authors exploited this device as glucose monitor, immobilizing GOx in the dielectric layer: in presence of glucose, gluconic acid was generated, which in turn led to local pH changes, resulting in drain current variations. The glucose sensor proved to have a final detection limit of 10 μmol L^{-1}.
Since the main limit of ISOFET is the need of a reference electrode,[133] a new interesting ISFET-like sensing approach that overcome this limit has been proposed, the so-called Carge Modulated (CM) OFET. In this configuration, the gate sensing area and the channel are physically separated by an insulator layer, with a floating gate, coupled to a control capacitor and in contact with the sensing area, that allows the device polarization. With this architecture, reported in Figure 1.13a, DNA detection was performed in the sub nM range.[142]

Electrolyte-gated Organic Field-Effect Transistos (EGOFETs)

Another interesting approach is obtained in the EGOFET sensors, where the dielectric is replaced by an electrolyte, used to produce the gating for the device, as can be seen in Figure 1.11. The substitution of the dielectric with the electrolyte, reduces the voltage require to operate the OFET.[143] EGOFET working principle is based on the formation, upon gating, of a Debye-Helmoltz double layer at the interface electrolyte/OSC film, as well as at electrolyte/gate interface. The high capacitance of this electric double layer (EDL), ca. 10 $\mu F \cdot cm^{-2}$, allows the device to work with sub-volt V_{gs} and V_{ds}. For example, in a p-channel EGOFET, upon negative gate polarization, the anions migrate towards electrolyte/semiconductor interface, while cations are attracted to the gate electrode, forming the double layer at both interfaces, as shown in Figure 1.13b. As stated by Stern's model, the electrical double layer at the gate/electrode interface is composed by electrons in the metal gate and two layers of cations, the compact (Helmholtz) layer and the diffuse one. The Helmholtz layer is composed in turn by a single layer of solvent molecules and a single layer of solvated ions, while the diffuse layer has free cations (anions), that decrease in number with the distance from the gate (semiconductor). Potential drop occurs at the interfaces only inside the double layer, which acts as a dipole and impedes any electrical current flow across the interfaces. Thus, EDL is compared to a capacitor, whose capacitance results proportional to the charge separation.
Several electrolytes have been used for EGOFETs, including liquids,[144] polymers,[145] ionic liquids,[146] polyelectrolytes[147] and ionic gels.[148] In particular, ionic gels have been exploited to have shorter polarization times (about 1ms),[148] since one of the main drawback of EGOFETs is their low switching speed between on and off states, due to the low ion mobilities in the electrolyte.[149]
However, it must be taken into account that organic semiconductors, and even more semiconducting polymers, are not impermeable to ions, thus it is possible to consider that electrostatic (at the interface) and electrochemical (inside the material bulk) doping occur simultaneously.[149,150] Electrochemical doping can increase the switching time and degradate the polymer. Thus, polyelectrolytes have been used ot overcome this issue, thanks to the fact that anions groups are linked to the polymer backbone and are not allowed to enter in the semiconductor material.[151]

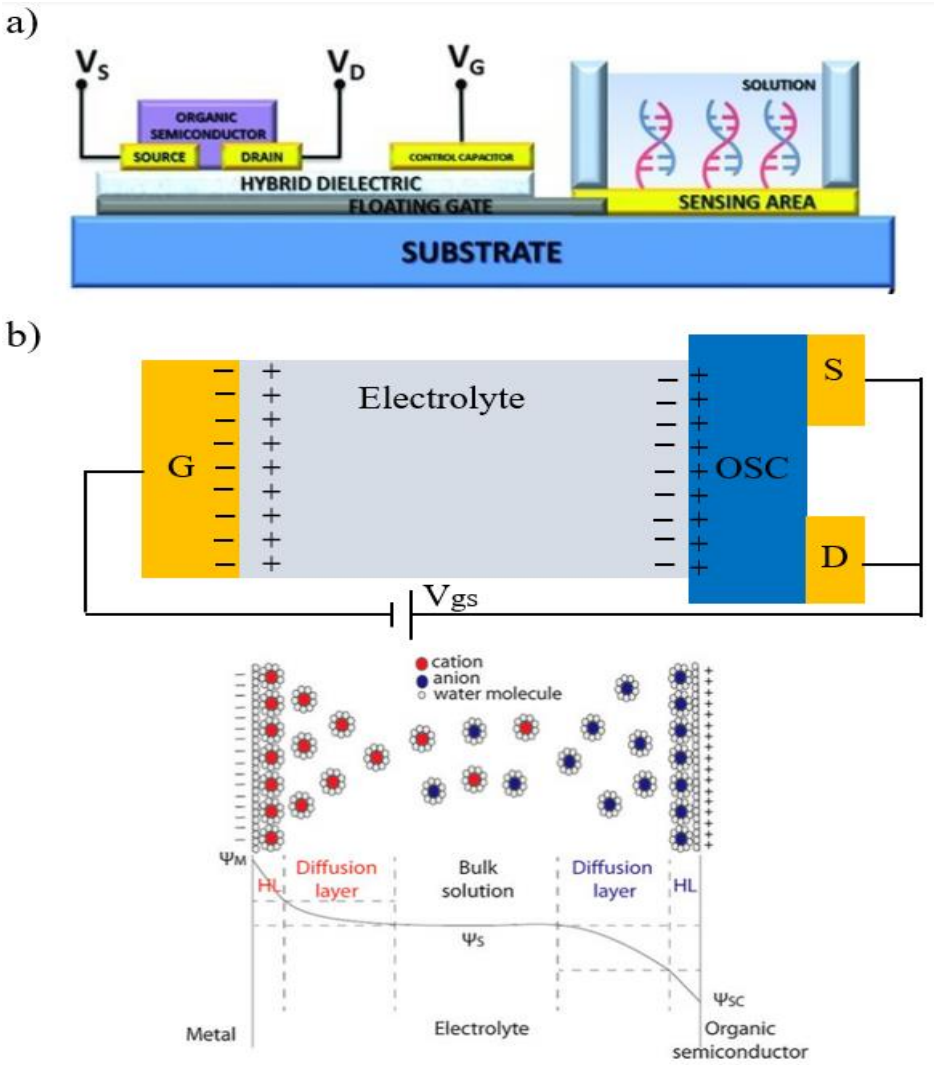

Figure 1.13: a) CMOFET configuration, with gate sensing area and the channel physically separated by an insulator layer. b) EGOFET schematic and illustration of the ion distribution and the potential spatial distribution in the electrolyte, upon the application of a negative bias on the gate. [128,142]

Organic Electrochemical Transistors (OECTs)

The first organic electrochemical transistor was developed by Wrighton *et al* in the early 80s,[152] and nowadays OECTs are gaining much interest due to the new and innovative opportunities related to printed electronics. As presented in Figure 1.11, OECTs are fabricated with the same geometry as EGOFETs, using an electrolyte solution to contact gate and semiconductor channel. However, OECTs employ a permeable conducting polymer as semiconducting channel, such as PANI, PPy, polycarbazole, PEDOT:PSS and other polythiophene derivatives. Due to the permeability of the polymer used, the whole material bulk interact with the electrolyte solution and can be used for the detection (while in EGOFETs only a charge accumulation at the electrolyte/channel interface occurred). Thus, reversible doping and dedoping of the polymer result in bulk changes in the channel conductivity, giving a very high transconductance (i.e. high amplification properties for low voltage application) dictated by the volumetric capacitance.[3,128,153] Transconductance is an important figure of merit of the OECT representing the efficiency of its transduction mechanism and is calculated as the first derivative of the transfer curve $g_m = \frac{\partial I_{ds}}{\partial V_{gs}}$.[154]

OECT working principle can be described referring to Bernards and Malliaras model:[155] according to their work, the device is divided into two circuits, an ionic and an electronic one. The former takes in account ion flow in the gate-electrolyte-channel structure, while the latter describes the electronic

charges (electrons or holes) in the semiconducting channel (Figure 1.14a). This model is based on capacitive processes, where ions pushed in the channel electrostatically compensate the presence of opposite charges,[156] without exchanging charges with the semiconducting film, thus without electrochemical reactions between channel and electrolyte.[154] Further insights on OECT model and features will be described in Section 2.5.1. Here, the description is limited to the introduction of two different OECT regimes of operation, the Faradaic and non-Faradaic (capacitive):[157]

- *Faradaic regime*

  In the Faradaic regime, irreversible reduction/oxidation ractions occur between electrode and electrolyte upon the application of a gate voltage, thus leading to a steady-state gate current, which lowers down the potential drop at the gate/electrolyte interface, increasing the gate effect operating on the channel. Even though this regime owns the highest sensitivity, the irreversible oxidations/reductions taking place in the electrolyte affect device characteristics that will decay with time and will be sensitive to electrolyte nature.

- *Non-Faradaic regime*

  In this regime, gate voltage application leads only to a capacitive current at the gate electrode,[149] cause the gate electrochemical potential remains inside the stability window of the electrolyte, thus only reversible charging of ionic double layer at the gate/electrolyte interface occurs. Therefore, a significant potential drop is present at this interface, which reduces the effective gate voltage operating on the channel.

Since both regimes depend on the quantity of active material and the capacitances at the interfaces, the geometry of the transistor matters, and, in particular, the ratio between gate and active channel areas A_g/A_{ch}, explored and studied in many works.[157–159] More precisely, it has been proved that also channel thickness affects OECT behaviour and sensistivity,[154,160,161] thus highlighting that volumetric capacitance should be taken into account.[153,156] Indeed, the potential drop in the ionic circuit at gate/electrolyte and electrolyte/channel interfaces will depend on gate and channel capacitances, respectively, as shown in Figure 1.14a. In particular, the solid line corresponds to an efficient gating, where the highest drop occurs at the electrolyte/channel interface, thus driving ions inside the semiconducting channel. In contrast, the dashed line stands for poor gating and the drop is mainly present at the gate/electrolyte interface.

As stated above, signal amplification is the main feature of OECTs, quantified by the parameter of transconductance, which values reach the order of millisiemens (mS) in micrometer-scale devices.[153] However, this comes at the cost of quite slow time operation, which is limited by ionic or electronic circuit. Indeed, in most devices the ionic circuit is the limiting element and the time response is proportional to channel capacitance, that is in turn proportional to channel thickness d. Since also the g_m is proportional to channel thickness, this parameter can be used to tune the trade off between gain (amplification) and bandwidth (time response, velocity) of the devices.[161]

Due to low-voltage operation, ease of fabrication (also on flexible substrates[162]) and the possibility of integration in biological environments, OECTs have been used for several applications, including analyte sensing (dopamine,[38] ascorbic acid,[160,163] ions,[158] adrenaline,[164] lactate[165]), tissue engineering biosensors,[166–169] neural activity sensing,[170] neuromorphic devices[171] and even in wearable platforms.[172,173] In Figure 1.14b it is reported a schematic of the neural activity, tissue integrity and analyte sensing mechanism.

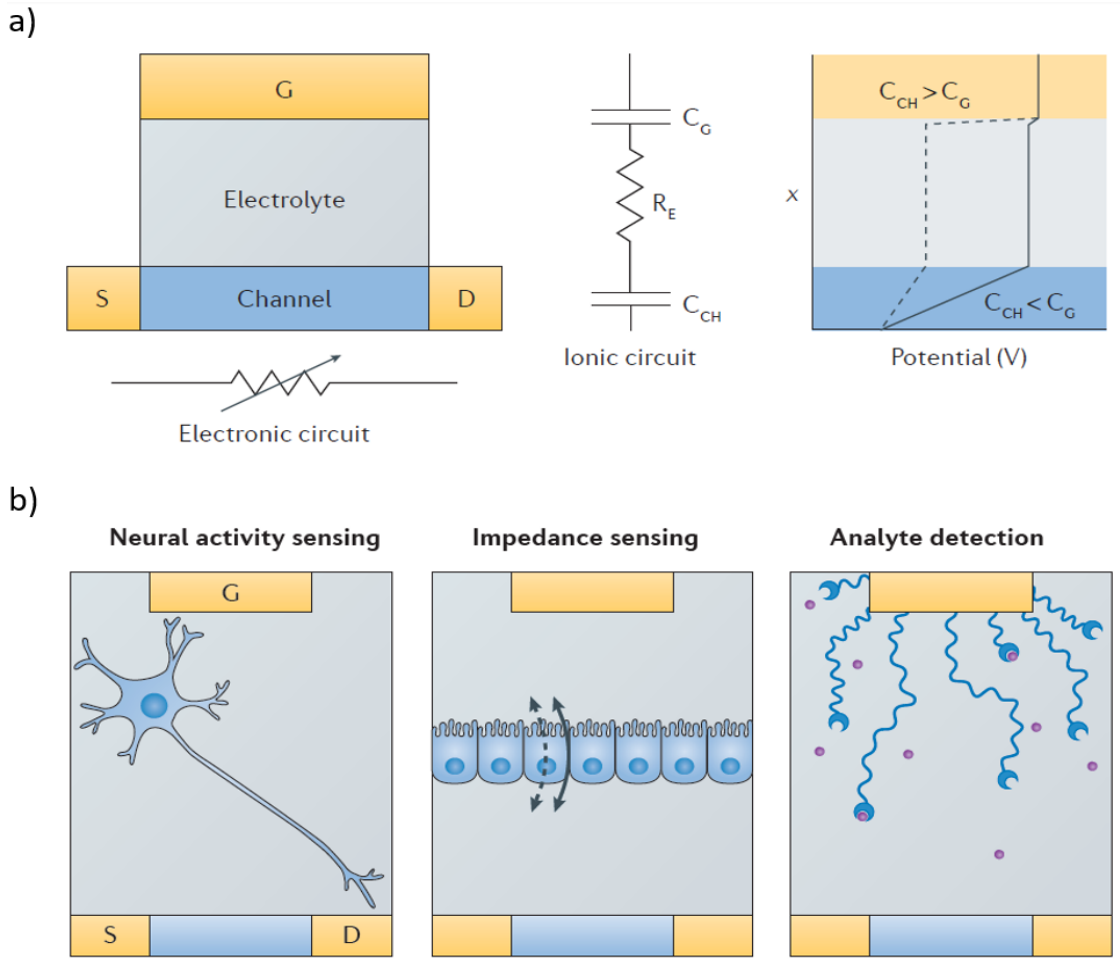

Figure 1.14: a) Ionic and electronic circuits used for OECT model: the electronic circuit (shown below the device layout) is modelled with a variable resistor, taking in account of the channel conductivity modulation, upon gating; the ionic circuit (reported on the right of the schematic) is modelled throughout two capacitors, for the channel (C_{CH}) and the gate (C_G), in series with the electrolyte resistance (R_E). On the right the efficient (solid line) and poor (dashed line) gating is represented, depending on the comparison between the gate and channel capacitances. b) Schematic representation of OECT possible application and working principle. On the left, OECT is used in electrophysiology to record electrically active cell activities (neurons, cardiomiocytes). In the center, OECT is used as impedance sensor to detect ion permeability changes in cell layers. On the right, the transistor is used for analyte (red circles) sensing, using receptors bound to its gate or channel.[154]

1.3.3 Electrodes for sensing and stimulation

Neurons live within high-dimensional networks over the entire brain and have specific individual and collective tasks, in order to generate, process, store and relay information.[174] Even though new molecular tools for neuromodulation and new technologies for neuronal studies have increased scientist abilities to control and investigate neurons activity and characteristics, observing connections between neural pathways and behaviors,[175] the immense complexity of nervous system makes our understanding of brain activity and ability to prevent or treat neurological disorders poor.[174] The ability to monitor and modulate neuronal activity can, indeed, enrich our knowledge of disease progression and lead to multiple clinical applications, such as alleviating motor symptoms related to Parkinson's diseases or slowing down the neurodegeneration of Alzheimer's disease or even treat epilepsy, deadfness and chronic pain.[1,176,177] Thus, motivated by increasing demand, federal, academic and private sector increased neural technologies research, which led, for istance, to project such as the BRAIN Initiative[178] in USA, the China Brain Project[179] and the Human Brain Project in UE.[180]

In last years, much efforts have been directed towards making smaller and more flexible electrodes to interface with the nervous system, aiming to reduce the insertion trauma and the following chronic

inflammation and damage. For this reason, microfabricated conducting polymers have been widely exploited to improve the electrode/tissue interface, thanks to their biocompatibility, electrical activity (to probe and stimulate), softness (low Young modulus) and flexibility, thus being more comformable with brain tissue and neurons (owing to their ability to move and flex with body micromovements, respiration and blood flow)[18], compared to the previous standard Si shanks. To minimize implant damages many researchers have introduced electrode coatings with polymer for the probes that are inserted into the brain, this way improving the impedance of the electrodes, having better signal-to-noise ratio.[28,181,182] Moreover, also the problem of degradation over time of the electrode/electrolyte interface has been partially resolved.[63,183] The electrode coating polymers act as a transducer between the electrons in the electronic circuit and the ions in the biological tissue, either by charging the double layer on the electrode surface or with faradaic electrochemical reactions. The latter are often undesired since can alter the chemical composition of outer electrolytes or induce the formation of toxic byproducts.[184] The easeness of electronic to ionic current conversion is measured throughout the impedance of the electrode, which can be lowered if high amount of charges are stored at the interface and if the interface is easily accessible by the ions.[1] With their porous coating, CPs allow for electrodes with high storage capacity and fast ionic conduction,[185] having also the possibility to tune biocompatibility, impedance and stability with chemical composition modifications.

Among the different polymers, the majority of the works rely on the use of PPy and PEDOT.[186–189] A better investigation on the use of PEDOT:PSS for neural recording and stimulation electrodes will be discussed in paragraph 2.5.3. Instead, PPy was exploited for the preliminary and initial studies on neural probes. For example, P.M. George and co-workers developed a neural probe made with PPy doped with PSS or sodium dodecylbenzenesulfonate (NaDBS).[190] Dopant and temperature of the electrochemical deposition were varied to change the electrode conductivity and surface roughness, respectively. It was shown that neural networks of axons, dendrites, glia and synapses grown *in vitro* on all PPy films (as visible in Figure 1.15a), while, *in vivo*, better implant integration and reduced gliosis were present in rougher implants, compared to the control ones. Furthermore, the addition of biological moieties can offer other advantages to the neural probe. Thus, different peptides have been introduced to dope PPy, such as p31(CDPGYIGSR) [187,191] or p20 (RNIAEIIKDI).[191]

Even though most studies are focused on recording using CPs for neural probes, there have been several works on the use of these electrodes for stimulation. Even in this case, the reduction of electrical impedance is the main benefit of CPs, since it allows low stimulating voltages, thus reducing the amount of electrochemical side reactions that can potentially create toxic products. For example, D.C. Martin and colleagues, at the University of Michigan, electropolymerized thick PSS-doped PPy films on Au and Ir electrodes in order to enhance the capacitance per electrode area.[186]

Recently, besides electrode coating with CPs, all-polymer, metal-free electrodes have been developed. Without metal, it is possible to explore new fabrication methods and develop new device formats and architectures.[18] Indeed, metals can reduce device stretchability, cause they crack if no "wavy" shape is previously provided,[192] and exhibit poor bonding with the deposited CPs, limiting long-term performances in acquoes environment because of cracking or delamination. Finally, CPs elastic modulus can be tuned to match the one of biological tissues while preserving conductivity.

Like CPs, hiydrogel elastic modulus can be tuned to match the mechanical properties of biological soft tissues and their structure is similar to native extracellular matrix one. Moreover, they have high water content, resembling the hydrateted biological environment surrounding cells or tissues. However, this impedes to incorporate such materials in standard photolithography or etching fabrication techniques, requiring the use of hard and stiff silicon or metal connections to control and read from soft CP electrodes. A significant challenge is thus to form stable connections between hydrogel/CPs and metallic pins and maintain it under mechanical stress.

In order to mimick tissues, S. Sekine *et al* electropolymerized PEDOT on Pt electrodes covered by agarose hydrogel,[193] using electrochemical actuation to delaminate PEDOT/agarose hydrogel from Pt, this way creating a free-standing electrode exploited for the stimulation of C2C12 immortalized mouse myotubes *in vitro* (Figure 1.15b). As can be seen from the final cross-section configuration, PEDOT penetrated through the agarose (Figure 1.15c).

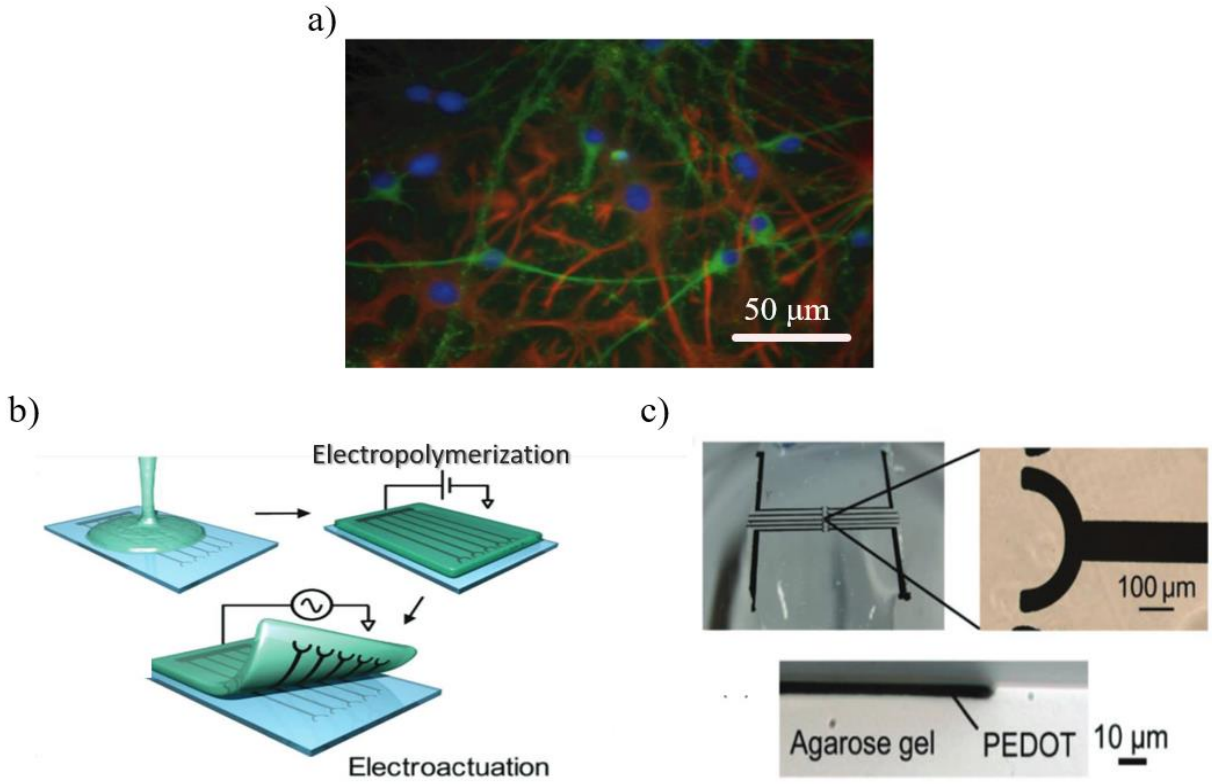

Figure 1.15: a) Fluorescently labelled cortical neurons grown on top of PPyNaDBS surface after 21 days from seeding. Green, red and blue colors stand for neurons, glia and nuclei, respectively.[190] b) Fabrication schematic of PEDOT/agarrose electrode: initially, liquid agarose is poured in Pt electrodes; then, PEDOT is electropolymerized inside the hydrogel to form electrodes; finally, electrochemical actuation enable the hydrogel delamination from the underneath Pt electrode substrate, creating a free-standing CP/hydrogel electrode. c) Images of PEDOT electrodes in the hygrodel and gel cross-section (below) to show PEDOT penetrating in agarose.[193]

Besides, Guo *et al* worked towards the realization of a metal-free electrode array developing PPy/polycaprolactone-block-polytetrahydrofuran-blick-polycaprolactone (PCTC) electrodes sandwiched between Polydimethylsiloxane (PDMS) films (Figure 1.16a).[194] It showed lower impedances at low frequencies (below 80 Hz) compared to a Pt electrode of the same area (Figure 1.16b) and it was used to measure hindlimb muscle electromyography (EMG) in a rat after sciatic nerve squeezing (Figure 1.16c).

To further improve layer adhesion, a research group used PPy nanowires to anchor PPy electrodes into the underneath PDMS substrate (Figure 1.16d).[43] They applied a prestretched PDMS film to PPy nanowires, using a semi-cured PDMS layer as "glue", this way having "wavy" morphology electrodes when releasde from the stretching and semi-cured PDMS improving PPy adhesion to PDMS. The electrode arrays proved to be useful to monitor low frequency signals, normal and epileptic mice electrocorticography (ECoG) and to stimulate the sciatic nerve.

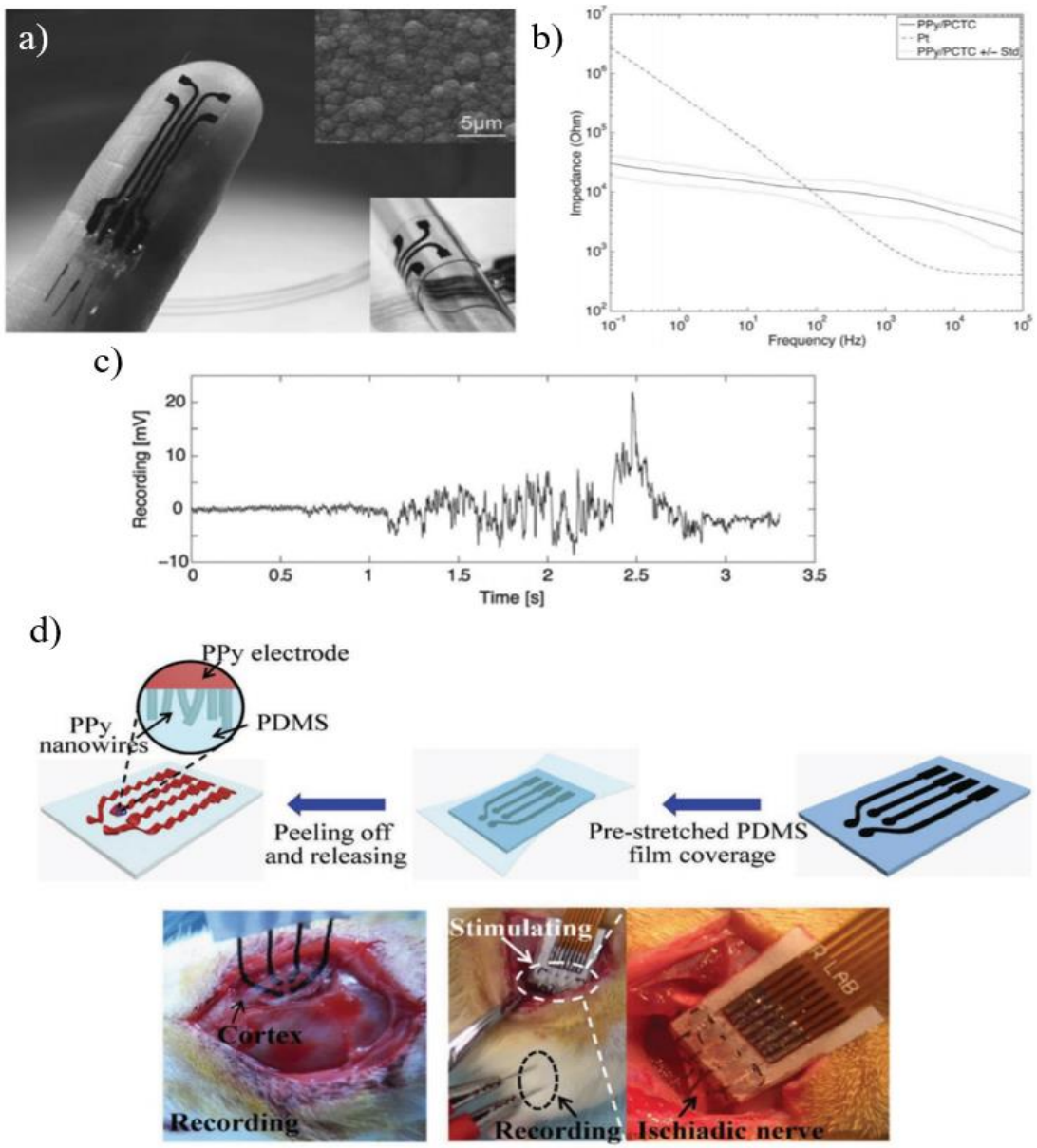

Figure 1.16: a) 1mm diameter PPy/PCTC electrodes in PDMS film. Top inset: electron microscopy image reporting the roughness of the electrode surface morphology. Bottom inset: electrode flexibility is proved rolling it around a glass pipette. b) Comparison between impedance spectra of PPy/PCTC electrodes and Pt ones with the same geometric area. c) EMG trace of the stimulated hind-limb muscle after squeezing of the sciatic nerve.[194] d) PPy nanowires realized on PPy electrodes on indium tin oxide. PDMS was prestretched, then applied to the electrodes, released and peeled off in order to create wavy PPy electrodes, anchored in PDMS with nanowires. The resulting electrode arrays were exploited for healthy and epileptic mice ECoG monitoring, together with sciatic nerve stimulation.[43]

Chapter 2

Conjugated polymers and PEDOT

2.1 Conjugated polymers

A milestone in the history of conjugated polymers was the publication of doped polyacetylene in 1977:[195] the discovery that an organic conjugated hydrocarbon $(CH)_x$, doped with halogens for example, could reach extremely high electrical conductivity spreads the interest over these organic materials and was honoured with the Nobel Prize to Alan J. Heeger, Hideki Shirakawa and Alan G. MacDiarmid.[196,197] Among many interesting and diffused conducting polymers, the ones based on polyanilines, polythiophenes, polyphenylenes, polypyrroles and poly(*p*-phenylene vinylene)s have attracted particular attention.[198–201] The structure of the more common conductive polymer are reported in Figure 2.1.

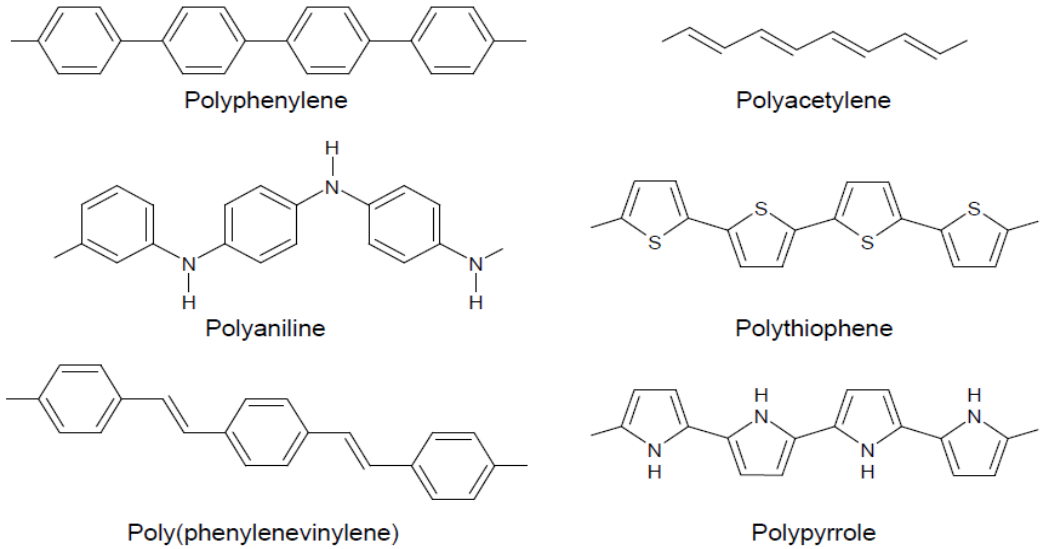

Figure 2.1: Schematic of the chemical structure of the most diffused and studied conjugated polymers.

2.1.1 Electrical conductivity in conjugated polymers

In saturated polymers, such as polyethylene, valence electrons are usually forming σ-bonds, thus the gap between the valence and the conductive band is large enough to have the polymer displaying insulating properties. On the other hand, conjugated polymers form a π-bond along the polymer backbone: three σ-bonds are formed with neightbouring atoms and the remaining *p* orbitals (described as p_z) engage a π system. As a result, one unpaired electron (named π-electron) per carbon (C) atom is present and there is an overlapping of successive atom orbitals along the polymeric backbone.[202] The consequent electronic delocalization provides the "highway" for charge mobility along the polymer backbone and the electronic structure of the CP results determined by the chain symmetry, i.e. the number and kind of atoms within the repeated unit. Thus, such polymers can exhibit semiconducting or even metallic properties,[202] having a broad range of possible conductivities as shown in Figure 2.2.

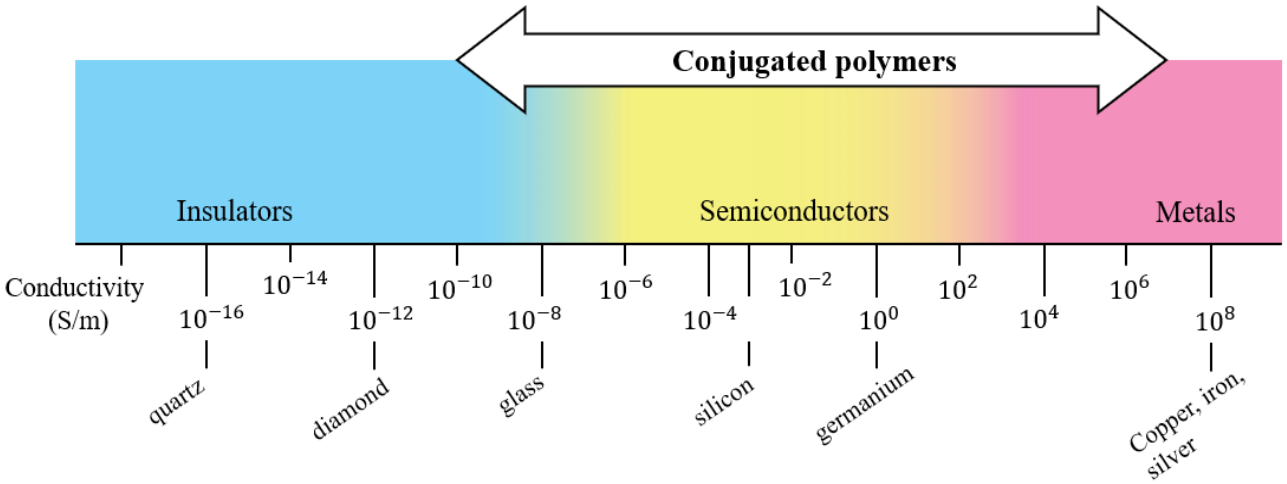

Figure 2.2: Conductivity range of conjugated polymers, compared to other material, from insulators, like quartz(10^{-16} S/m) to metal, such as copper, iron and silver (conductivity around 10^{8} S/m).

The simplest model of electrical conductivity in conducing polymer is polyacetylene (PAc, with molecular fomrnula $[-CH]_n$), reported in Figure 2.1. Each carbon atom, with four valence electrons, has three σ-bonding with other two neightbouring C atoms and a hydrogen one, leaving and unpaired π electron. Thus, using a simple free-electron molecular orbital model, it is possible to give a quantititative description of a conductor, semiconductor or insulator built up of a linear chain of atoms, such as in PAc.[196,203] Assuming a row of N atoms, separated by a distance *d* one another, thus a total chain length of (N-1)*d* or, N*d*, for large enough N, the quantum-mechanical model of a free particle in one-dimensional box (the potential is zero inside the box and infinite outside it) expresses the wave function eiegenvalues (Figure 2.3a and b) as:[204]

$$E_n = \frac{n^2 h^2}{8m(Nd)^2} \text{ , with n= 1,2,3…} \quad (2.1)$$

where h is the Planck's constant, m the electron mass and n a quantum number.
We can then assume that π electrons from the N *p*-orbitals fill this eigeinvalue ladder, with two electrons per molecular orbital (according to Pauli principle), up to the highest occupied molecular orbital (HOMO), which has the energy:

$$E\ (HOMO) = \frac{\left(\frac{N}{2}\right)^2 h^2}{8m(Nd)^2} \quad (2.2)$$

while for the lowest unoccupied molecular orbital:

$$E\ (LUMO) = \frac{\left(\frac{N}{2}+1\right)^2 h^2}{8m(Nd)^2} \quad (2.3)$$

Thus, the energy required to excite one electron from HOMO to LUMO level is:

$$\Delta E = \frac{(N+1)h^2}{8m(Nd)^2} \approx \frac{\left[\frac{h^2}{8md^2}\right]}{N},\ for\ large\ N \quad (2.4)$$

The bandgap is then decreasing for increasing 1/N polymer length, thus vanishing for macroscopic dimensions. Adapting this model for a many-electron system, Figure 2.3c and d report the case for a *ground state* and an *excited state*, respectively: in the former, an even number of electrons are distributed in pair for each orbital in the lower part of the energy ladder; instead, in the latter an electron is excited to a higher empty molecular orbital, increasing the energy of the system. The band gap is the minimum energy difference needed to shift between these two states, thus to create a charge pair with one electron in the upper manifold of orbitals and a hole in the lower one.[196]

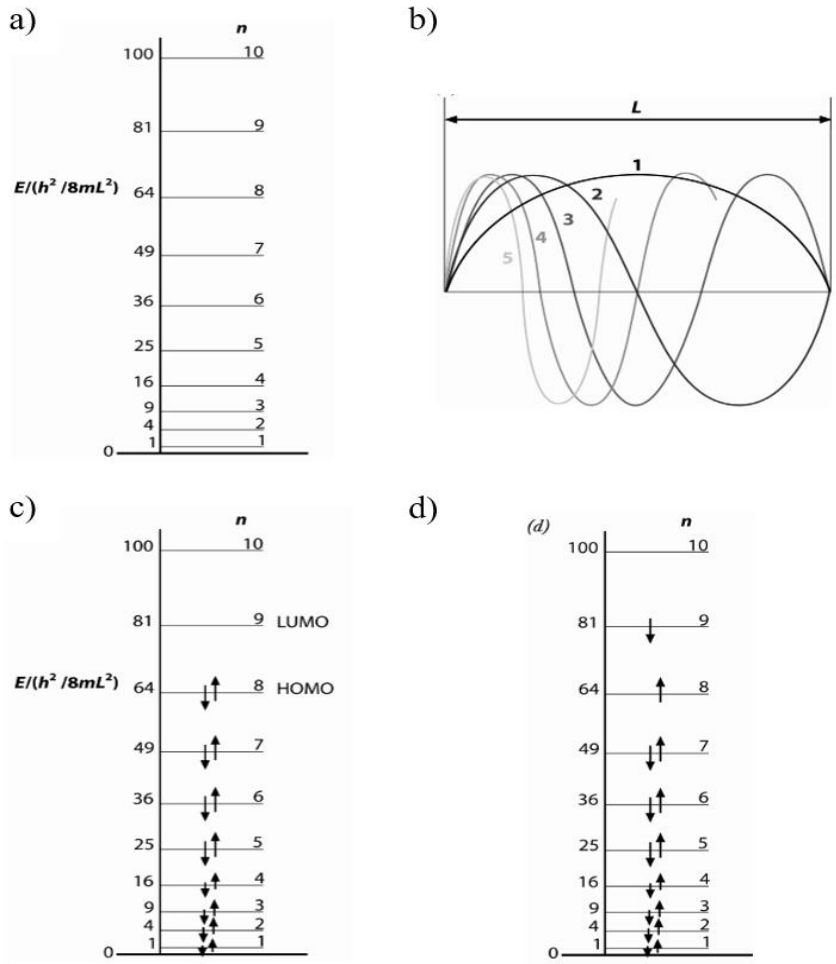

Figure 2.3: Free electron model (one-dimensional box with length L: a) energy level and b) wavefunctions. Adapting this model to multi-electron molecular orbital description, a state with 16 electrons is reported in (c), where they occupy the first eight molecular orbitals, with the highest occupied molecular orbital named HOMO and the next empty one LUMO. The excitation of one electron in the LUMO state is shown in (d).[196]

From this model, the bandgap would vanish for sufficiently long chain, with polyactetylene behaving as a conductor. Unfortunately, this is not the case, since it seems to be a limit to the bandgap decreasing upon increasing length chain. This convergence was confirmed by several theoretical predictions, the first by Lennard-Jones in 1937. It can be explained taking into account the distortion of the chain, called Peierls distortion:[205] Peierls theorem states that a one-dimensional system with an incompletely filled band distorts itself opening a gap at the Fermi level. The degeneracy of π levels is resolved with a geometrical distortion, which reduces the symmetry and induces a rearrangement of the orbital levels. For polyacetylene, the lattice distortion leads to repeated units of two carbon atoms close together and two further apart, that can be written as [−CH=CH−] (instead of [−CH−]). If the carbon atom bonds were equally long, electrons would have been in a half-filled continuous band, delocalised in the entire chain (like in metals). Since the chain has anternatingly short and long bonds, the energy structure results in an energy gap between a completely filled π band and an empty π* one (as for insulators or semiconductors),[197] whose energy difference is the band gap, E_g.
Due to this distortion, common to all conjugated polymers, intrinsically conducting polmers typically shows low conductivities: for example, polyacetylene has intrinsic conductivity from 10^{-5} to 10^{-7} S/m. Moreover, differently from metals, semiconductor conductivity decreases with decreasing temperature due to the loss of thermal excitations to the electrons (required to "jump" in the LUMO state).[196]

2.1.2 Charge transport and role of the dopant

As previously stated, conjugated polymers are not intrinsically conductive, thus a doping process to introduce charge is required: in conjugated polymers this simply means a charge transfer reaction with a partial oxidation (for *p*-type), or reduction (for *n*-type) of the polymer. However, most of the studies have been directed towards the *p*-doping case. Depending on the couple polymer-dopant, the conductivity can be changed in a broad range, raising it up to 10-12 orders of magnitude, thus moving from an uncharged polymer (insulator) to values higher than 1000 S/cm.[206] Changes in the doping state can also occur upon the so called "electrochemical doping", when ions from an electrolyte are pushed/pulled in/from the organic film, using a metal contact to supply charges.

Differently from the standard inorganic semiconductor, where a neutral atom is introduced in the host lattice to change its electronic structure,[205] in CPs the doping process recalls a redox reaction: indeed, for *p*-doping, the neutral polymer is converted into an ionic complex, made of a polymeric cation and a counterion which is the reduced form of the oxidizing agent; on the other hand, for *n*-doping, a polymeric anion and the oxidized form of the reducing agent are formed. The ease of oxidation/reduction evaluate how potentially conducting is the polymer and π-bonded unsaturated polymers are particulary useful due to their small ionization potentials and/or large electron affinities. As a matter of fact, π electrons can be easily added or removed with small effect to the σ-bonds of the polymer and this principle was applied with success to several organic polymers, including polyacetylene.[207] The subsequent increase in conductivity originates from the charge carrier generation and from their ability to travel along the π-system, thus CPs are suitable conductors for two reasons:[202] (1) doping introduces charge carriers in the polymer electronic structure, with relatively high charge density, since every repeated unit is a potential redox site; (2) electrons are attracted from neightbouring nuclei, leading to charge delocalizaiton along the polymer chain and charge carrier mobility, extended to the 3D system throughout interchain electron transfer.

Charges introduced in polymers are stored in novel states, which include charge and lattice distortion, called *polarons*, *bipolarons* or *solitons*.[208] The equilibrium geometry in organic molecules varies between the ground and the ionized state, as for example occurs in the transition from benzenoic-like to quinoid-like structure in polythiophene, reported in Figure 2.4. Indeed, differently from inorganic solids, where the removal of an electron leads to the generation of a hole in the valence band (see Figure 2.5a), in organic polymer it can be energetically favourable to localize the charge in the chain and generate a local distortion (relaxation) of the lattice around it, creating localized electronic states in the energy gap due to local upward shift Δε of the HOMO and downward shift of the LUMO (Figure 2.5b). If the energy variation of the HOMO and LUMO level is higher than the energy for lattice distortion E_{dis}, the charge localization process is favoured relative to the band process and a polaron with energy $\Delta\varepsilon - E_{dis}$ is formed. In conjugated polymers polaron formation with lattice distortion is always favourable compare to ionization.[207]

In case of electron polaron, an electron is added in the new level under the conduction band, while in case of hole polaron, an electron is removed from the new level moved up to the valence band (Figure 2.5b), in both cases creating a spin ½, half-filled level. Since the polaron formation leaves the valence band full and the conduction one empty, no metallic features appear. However, for high doping level, the polaron is able to move in the field of close counterions due to their high concentration, thus having high mobility.

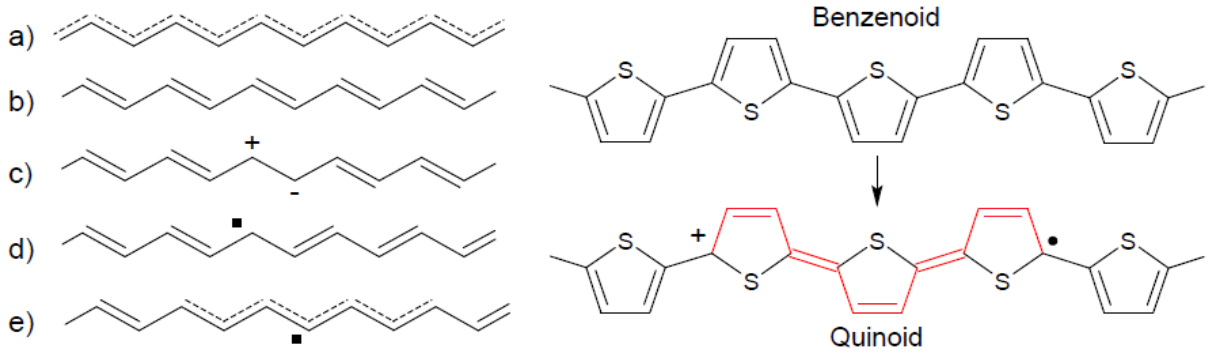

Figure 2.4: On the left, charged states in trans-polyacetylene are reported: (a) undimerized structure; (b) dimerized structure caused by Peierls instability; (c) polaron formed after one electron removal from a C atom in the chain; (d) soliton formation; (e) structural relaxation with corresponding delocalized charge distribution. Adapted from [202]. On the right, benzoid to quinoid transition due to the introduction of a positive charge.

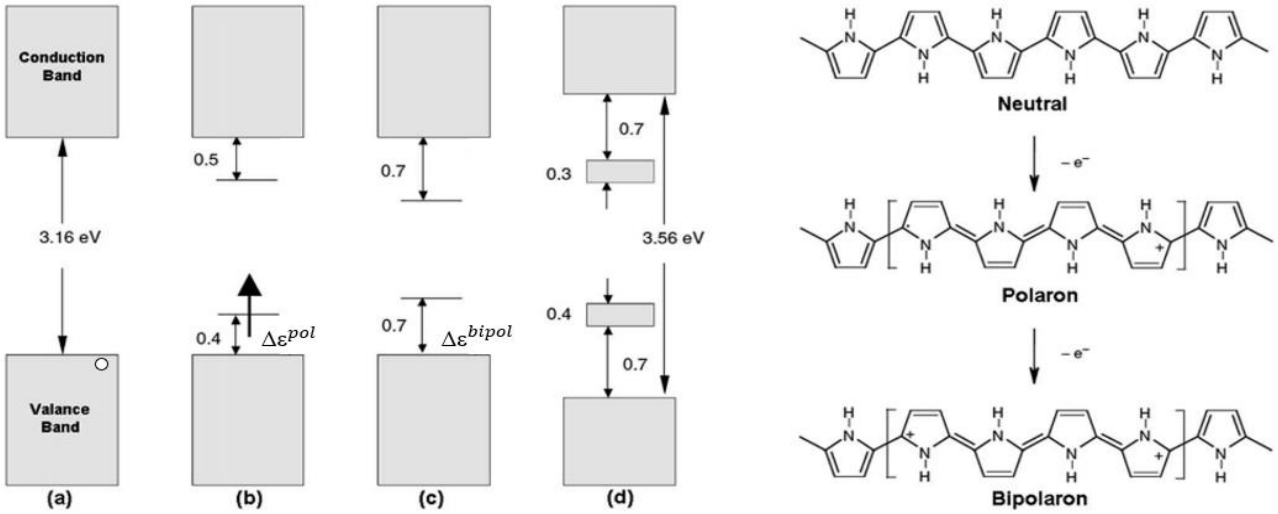

Figure 2.5: Illustration of the band structure of inorganic solids upon the formation of a hole (a) and of polymeric chain, using PPy as model, in case of the formation of: (b) a polaron, where the lower level in the gap is occupied by a single electron, while the upper is free; (c) a positive bipolaron, where the inner levels in the gap are empty; and (d) a bipolaron bands in high doping conditions, where several inner levels merge into bands. Adapted from [209].

The removal of a second electron leads to two possibilities: the electron can be removed from a polaron, thus forming a bipolaron (its electronic structure is reported in Figure 2.5c and on the bottom right), or from another part of the chain, creating another polaron. A bipolaron is a non-indipendent pair of charge which have the same polarity, associated with a strong local lattice deformation and it has two levels in the energy gap: they are fully occupied for a negative polaron, while they are both empty in case of a positive bipolaron, as in Figure 2.5c. The bipolaron spins sum to zero and the energy gained from lattice deformation is higher compared to the energy coming from Coulomb repulsion, since they have the same sign.[210] Moreover, also the lattice distortion increases after this second ionization, thus the reduction of ionization energy must increase in order to still have $\Delta\varepsilon > E_{dis}$. Furthermore, the decrease in the ionization energy is much higher for the bipolaron case than for two polaron formation, making a bipolaron thermodinamically more stable than two polarons.
Several experimental and theoretical studies have been done since the early 80s on the electronic and transport properties as a function of doping level for different conjugated polymers.[207] Optical absorbance spectra[211] and electron spin resonance[212] experiments show that at low doping (~1 mol %) an increasing in polaronic states occurs, while at higher dopant concentrations (~10 mol %) there is the gradual formation of spinless bipolarons. By further enhancing the dopant concentration (~30 mol %), two bipolaron bands are formed due to the overlapping of the level within the energy gap,

which gets wider (cause the new states are extracted from the valence and conduction bands), as reported in Figure 2.5d.
The third type of excited state is the soliton, which only occurs in polymers that posses two different geometrical structure of the ground states having the same energy, called degenerate polymers, whose main example is *trans*-polyacetylene (PAc).[213] Indeed, as can be seen from Figure 2.4, single and double bonds alternate along the PAc chain with the same structure. When an electron is extracted from a polaron along the chain, the two positive charges are not coupled. The geometric structure between the two charges has the same energy of the geometric structure on the other sides of the charges, thus when the charges separate, there is no increase in the distortion energy, letting the charges free to move away from each other. A single charge on a PAc chain constitutes a boundary between two segments with specular geometry and it is called soliton, due to the fact that it recalls a solitary wave able to propagate without deformation or dissipation.[214] The soliton is a localized electronic state in the center of the bandgap, which can be filled with one electron (neutral soliton, spin 1/2), two electrons (negative soliton, spin zero) or empty (positive soliton, spin zero). The spin and charge (in case of charged soliton) densities for solitons are not localized on one carbon atom, but spread over several ones,[213] giving a width to the soliton (Figure 2.4e). Solitons can contribute to charge-transfer and propagate via "intersoliton hopping", consisting in an electron jump between localized states on adjacent polymer chains by means of a phonon-assisted process.[214]

2.1.3 Doping techniques

In this paragraph, a brief overview of the different reversible doping techniques that can be used on conducting polymers will be introduced,[202] which are schematically reported in Figure 2.6a.

Chemical doping

In chemical doping the charge transfer between the dopant and the polymeric chain happens *via* redox reactions: oxidation produces a *p*-type doping while reduction an *n*-type one, [195,215,216] as illustrated in the following examples (*p*-type the first, *n*-type the second) :

$$(\pi\text{–}polymer)_n + \frac{3}{2}ny(I_2) \rightarrow \left[(\pi\text{–}polymer)^{+y}(I_3^-)_y\right]_n \quad (2.5)$$

$$(\pi\text{–}polymer)_n + [Na^+(naphthalide)^\bullet]_y \rightarrow \left[(Na^+)_y(\pi\text{–}polymer)^{-y}\right]_n + (naphth)^0 \quad (2.6)$$

Even though complete doping at high concentration yields high quality materials, this method is quite difficult to control, cause low concentration dopings often result in non-homogeneous materials.

Electrochemical doping

This method was invented to solve chemical doping problem.[217] In electrochemical doping the electrode supplies the redox charges to the CP, while ions flow inside (or outside) the polymer matrix from the electrolyte in order to compensate the electronic charge (thus electrolyte gives the counterions necessary for the polymer charge neutrality). The doping level depends on the voltage difference between the counter electrode and the conducting polymer and it is precisely defined by this difference at the electrochemical equilibrium. Thus, the desired level of doping can be achieved applying a selected voltage and waiting till the electrochemical equilibrium of the system, indicated by the cell current going to zero. Again, a *p*-type and an *n*-type examples are reported, respectively:

$$(\pi\text{–}polymer)_n + [Li^+(BF_4^-)]_{soln} \rightarrow \left[(\pi\text{–}polymer)^{+y}(BF_4^-)_y\right]_n + Li(electrode) \quad (2.7)$$

$$(\pi\text{–}polymer)_n + Li(electrode) \rightarrow \left[(Li^+)_y(\pi\text{–}polymer)^{+y}\right]_n + [Li^+(BF_4^-)]_{soln} \quad (2.8)$$

Doping by acid-base reaction

Protonation using acid-base chemistry leads to an internal redox reaction and the consequent conversion from semiconductor (emeraldine base) to metal (emeraldine salt), whose schematic is reported in Figure 2.6b for polyaniline. Upon protonation of the emeraldine base to the emeraldine salt, the proton-induced spin unpairing mechanism brings a structural change with one unpaired spin per repeat unit, without changing the number of electrons. The result is a half-filled band, thus potentially a metallic state with a positive charge in each repeat unit (from protonation) and an associated counterion (i.e. HSO_4^- , Cl^-, $DBSA^-$ etc), not shown in Figure 2.6b. Even though the conversion from semiconductor to metal has been well-described, it is not well understood from basic theory: indeed, there are no calculations showing that the metallic final state is lower in energy than the semiconductor one, thus no detailed understanding of the rearrangement reactions, that are sketched in Figure 2.6b.[202]

Photodoping

During photodoping, the semiconducting polymer is locally oxidized and (nearby) reduced by photoabsorption and charge separation (free carriers are formed by electron-hole pair creation and separation), as can be seen from the following:

$$(\pi\text{–}polymer)_n + h\nu \rightarrow [\{\pi\text{–}polymer\}^{+y} + \pi\text{–}polymer^{-y}]_n \qquad (2.9)$$

where *y* is the number of electron-hole pairs (it depends on the pump rate and the recombination rate). After the photoexcitation from the ground state to the lowest energy state with proper symmetry, the subsequent recombination can be radiative (luminescence) or nonradiative. Some conjugated polymer families have high luminescence quantum efficiencies (for example polyparaphenylene vinylene (PPV) and polyparaphenylene (PPP) and their soluble derivatives), while others do not (for example, polyacetylene and the polythiophenes). Several mechanisms have been observed to give low quantum efficiencies for photoluminescence: rapid bond relaxation in the excited state and the soliton formation in the midgap prevent radiative recombination in polyacetylene;[218] moreover, interchain interactions in the excited states (called "excimers") lead to nonradiative channels for decay.[219,220]

Charge injection at a Metal-Semiconducting Polymer (MS) Interface

Holes and electrons can be directly injected using a metallic contact into the π*- and π-bands, respectively according to the following:

a) Hole injection into an otherwise filled π-band

$$(\pi\text{–}polymer)_n - y(e^-) \rightarrow [(\pi\text{–}polymer)^{+y}]_n \qquad (2.10)$$

b) Electron injection into an empty π*-band

$$(\pi\text{–}polymer)_n + y(e^-) \rightarrow [(\pi\text{–}polymer)^{-y}]_n \qquad (2.11)$$

With charge injection method the polymer is oxidized or reduced (removing or adding electrons, respectively), but there is no counterions (as it happens for chemical or electrochemical doping).

As reported in Figure 2.6a, each method leads to unique and usefull features. Chemical and/or electrochemical doping induce permanent electrical conductivity, until the carriers are chemically compensated or purposely removed by "undoping". On the other hand, photoconductivity is transient and lasts only until the excitations get trapped or decay back to the ground state. In the case of charge injection at metal-semiconductor interface, electrons stay in the π*-band and holes stay in the π-band only while biasing voltage is applied.

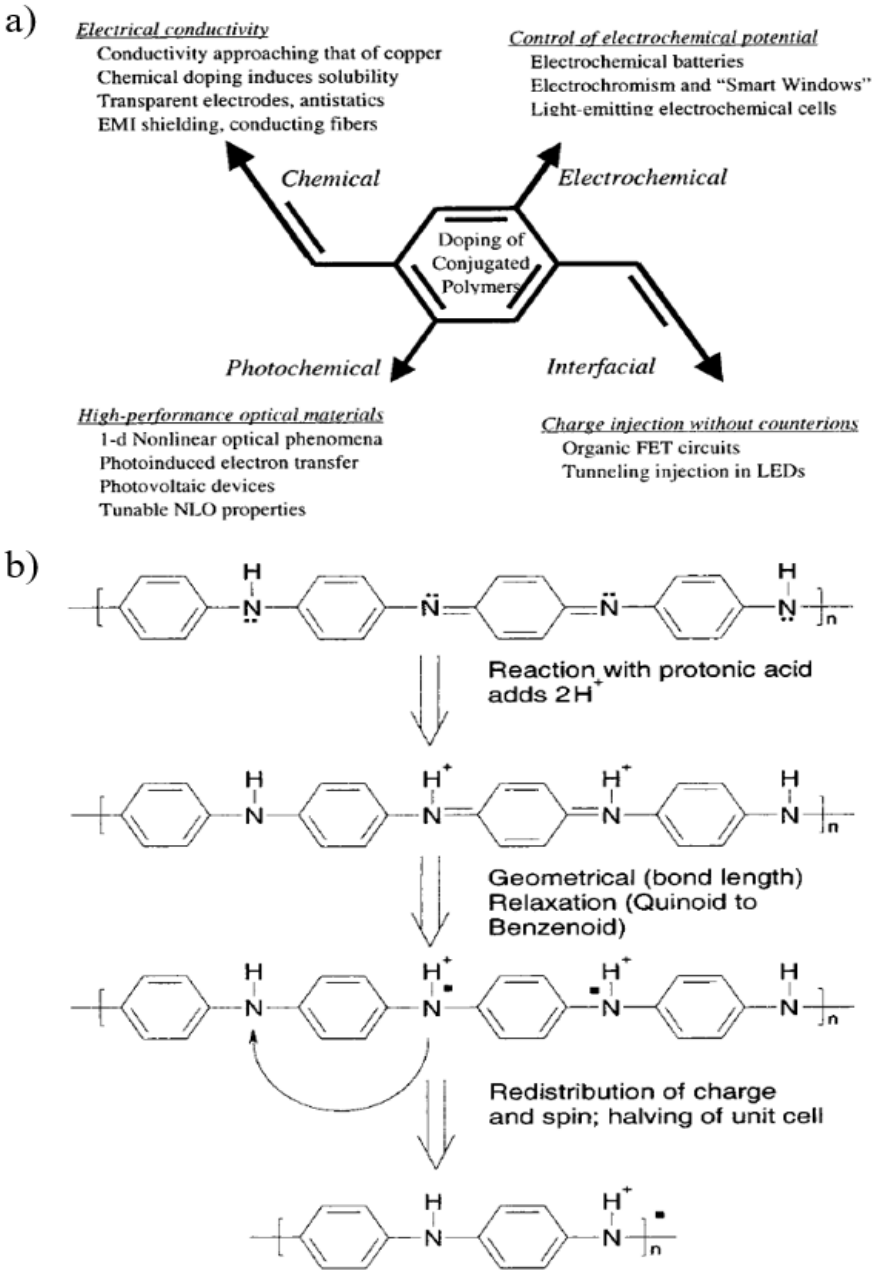

Figure 2.6: a) Various doping mechanism with related applications. b) Protonation-induced spin unpair in polyaniline with the conversion from an insulator to a metal; no change in the number of electrons occurs.[202]

1.2 PEDOT

Since in the early 1980s, the Bayer's Central Research Department attempts to stabilize polyacetylene in its highly doped form and to achieve processability ultimately failed,[221] several projects were started on polyheterocycles, like polypirrole, poly(3-alkyl-thiophenes), etc, but without much success. It was only in the second half of 1980s that the synthesis of 3,4-ethylenedioxythiophene (EDOT) monomer leads to a technical breakthrough, particularly due to its polymerized form poly(3,4-ethylenedioxythiophene) (PEDOT), which exhibited high conductivity and stability in the doped state (the only state available at the time).[197] PEDOT is an intrinsically conductive conjugated polymer, formed by a chain of its EDOT monomers, that are visible in Figure 2.7a, and it can be prepared using standard oxidative chemical or electrochemical polymerization methods.

2.2.1 Syntesis and features of EDOT monomer

EDOT chemistry started in 1930s, after the synthesis of the corresponding 2,5-dicarboxylic acid esters.[222,223] More elaborated studies follow these first investigations and in particular Jonas *et al* developed a usefull synthetic strategy for 3,4-ethylenedioxythiophene-2,5-dicarboxylic acid (EDOT-2,5-dicarboxylic acid), that was detailed descripted by Gogte *et al* in 1967.[224] This synthesis started with a Hunsdiecker condensation reaction of axalic acid diester with thiodiacetic diester to 3,4-dihydroxythiophene-2,5-dicarboxylic acid diester as the first step. 3,4-Dihydroxythiophene-2,5-dicarboxylic acid diester was then alkylated with 1,2-dichloro- or 1,2-dibromoethane and saponified. Decarboxylation of EDOT-2,5-dicarboxylic acid led to EDOT.[225] After its introduction into chemistry, the industrial manufacture uses Gogte pathway with slightly minor changes, such as the introduction of copper-catalyzed decarboxylation in the last step (Figure 2.7b).[225,226] These copper catalyst are basic copper carbonate ($CuCO_3Cu(OH)_2$) or copper quinolone complexes.

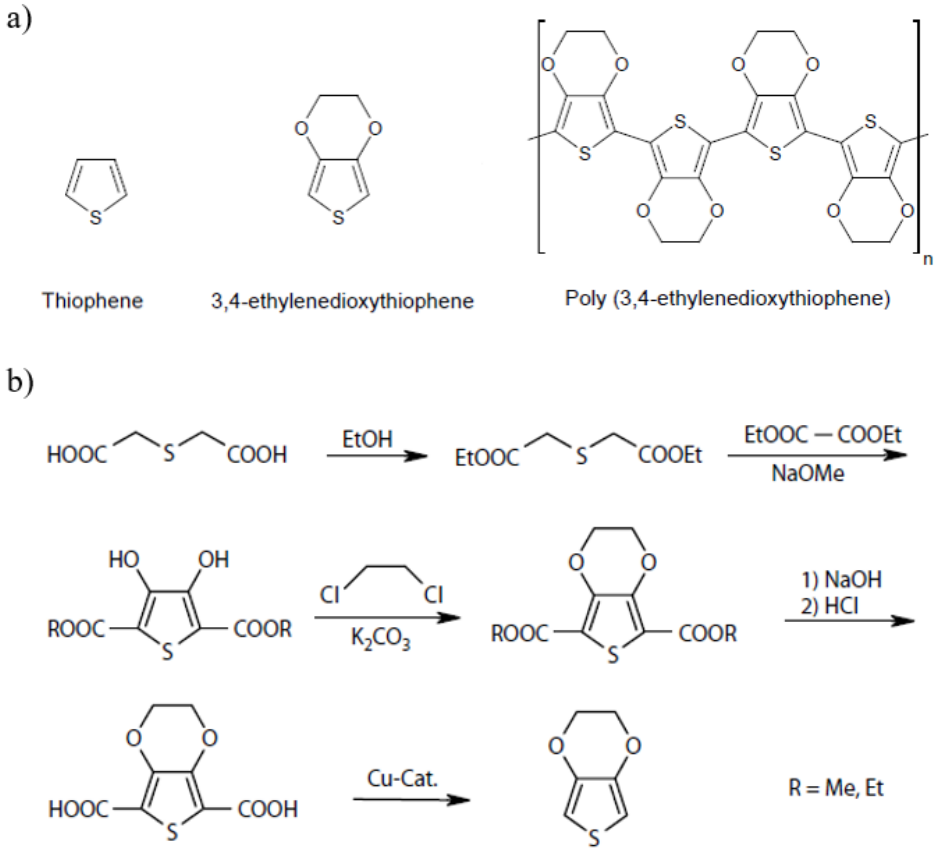

Figure 2.7: a) Chemical structure of thiophene, 3,4-ethilenedioxythiophene (EDOT) and poly(3,4-ethilenedioxythiophene) (PEDOT). b) Synthesis of EDOT monomer from oxalic acid ester and thio-diacetic acid ester.[197]

Freshly and pure distilled EDOT presents as a nearly colorless liquid with unpleasant odor. A small change to pale yellow is possible after long storage time (especially in daylight), without significantly affecting its purity.[197] On the contrary, air and light exposure makes it turn dark due to partial oxidation.[227] The main physical EDOT properties are reported in Table 2.1.

The purification procedure for EDOT is vacuum distillation. Moreover, the melting point at 10.5 °C permits a very efficient low temperature recrystallization from solvents like methanol, ethanol and their mixtures.

Regarding the chemical properties, EDOT main reactions are its oxidation reactions, that typically result in conductive oligomeric to polymeric materials when charge balancing is possible, i.e. when there are doping counterions (anions). These reactions will be discussed in paragraph 2.3 as the ones needed to realize PEDOT:PSS.

Table 2.1: Selected EDOT properties.[197]

Property	*Value*
Viscosity (20 °C)	*11 mPa·s*
Densisty (20 °C)	*1.34 g/cm^3*
Melting point	*10.5 °C*
Boiling point (1013 mbar)	*225 °C*
Vapor pressure (20 °C)	*0.05 mbar*
Vapor pressure (90 °C)	*10 mbar*
Solubility in water (20 °C)	*1.2 g/l*
Flash point	*104 °C*
Ignition temperature	*360 °C*

Bayer AG produces EDOT on a wide scale, offering it commercially with the name of BAYTRON M (where the M stands for monomer).[227]

2.2.2 Synthesis and polymerization of PEDOT

The synthesis of PEDOT derivatives can be divided into three main types of polymerization reactions:[227]

a) Oxidative chemical polymerization of EDOT-based monomers

Chemical polymerization can be obtained using different methods and oxidants. The classical method exploits oxidizing agents such as $FeCl_3$ or $Fe(Ots)_3$, finally obtaining a black, insoluble and infusible compound, diffilcult to characterize. However, it can give substrate-supported films with useful electrical and optical properties.[228–231]

A second polymerization method has been reported bt de Leeuw *et al*:[232] using $Fe^{III}(OTs)_3$ at high temperature with imidazole as a base, it resulted in a black insoluble and infusible PEDOT film, which exhibited conductivities of up to 550 S/cm,[233,234] after rinsing with H_2O and *n*-butanol.

The third and most useful polymerization method is called BAYTRON P synthesis and developed by Bayer AG.[231,235] It is based on the polymerization of EDOT in an aqueous polyelectrolyte (usually PSS) solution using $Na_2S_2O_8$ as oxidizing agent at room temperature. It results in a dark blue, aqueous PEDOT:PSS dispersion, commercially available with the name of BAYTRON P. Interestingly, once dryed the remaining PEDOT:PSS film is transparent, highly conducting, mechanically durable and insoluble in common solvents.

b) Electrochemical polymerization of EDOT derivatives

Another useful polymerization method is based on electrochemical oxidation of the electron-rich EDOT-based monomers and requires low amounts of monomer, short polymerization times and can give electrode-supported or free-standing films, according to the required application/purpose.

For EDOT, this method results in a highly transmissive sky-blue and doped PEDOT film at the anode.[228,236,237] Several electrolyte can be used for EDOT polymerization, including polyelectrolytes, as proved by Wernet and co-workers,[238–240] and even aqueous micellar medium.[241–243]

A slightly different electrochemical polymerization is the electrochemical desilylation, which uses α,ω-disilylated EDOT-based monomers.[244] This techinique, based on the loss of a trimethylsilyl (TMS) group, gives polymer with the same repeat unit as that obtained by the polymerization of the parent monomers. Using bis-TMS-derivatized monomers, the films adhere more strongly to oxide-

based electrode surfaces, such as on indium tin oxide (ITO) or gold (Au), thus having improved switching properties. Moreover, TMS derivatization increases complex and larger multi-ring monomer solubility, enhancing their polymerization characteristics.

c) Transition metal-mediated coupling of dihalo derivatives of EDOT

Several thiophene-based polymers have been developed using transition metal-catalyzed coupling of activated organometallic derivatives.[245] For example, Yamamoto *et al.* used this technique to directly prepare neutral PEDOT.[246,247] Even though this method yields low molecular weight materials, it can be interestingly applied to monomers with solubilizing side groups.

2.2.3 PEDOT properties

Even though PEDOT is an insoluble polymer, it exhibits some very interesting properties that justify its wide-spread use in industry and academic research:[248]

Reversible doping state

PEDOT can be reversibly and repeatedly doped and undoped. A PEDOT thin film is almost transparent and light blue in its oxidized state, while it can be turned into opaque and dark blue upon switching it to the neutral state. The color variation according to its doped state may be used as a suitable property for optical applications, such as electrochromic displays.[249]

Excellent stability

PEDOT has good chemical and thermal stability: thermal studies proved that a continuous degradation only occurs over 150 °C and a complete decomposition above 390 °C.[250] Moreover, electrical conducting properties seem to be unaltered after aging in environmental conditions. Its high stability is due to the favourable ring geometry and electron-donating effect of the oxygen atoms at the 3,4-positions, which stabilizes the positive charge on the polymer backbone.[251]

Regular structure

Thanks to its structure, competing polymerization through 3- and 4- positions as in thiophene are avoided, while only 2,5-couplings of the 3,4-ethylenedioxythiophene are present. For this reason, PEDOT is expected to have less defects than thiophene analogues.

Low band gap (high conductivity)

PEDOT low band gap (1.5-1.6 eV)[228] is though to originate from the influence of the electron-donor ethylene dioxy groups on the energies of the frontier levels of the π system.[252] It was experimentally proved that PEDOT exhibits reduced absorption in the visible after doping, the oscillator strength shifting from around 1.5 eV (lowest π-π* transition) to below 1 eV in the metallic state.[225] Thus, PEDOT presents high electrical conductivity (up to 550 S/cm) in the doped state.

Electrochemical properties

Synthesized PEDOT films have low redox potential and excellent stability in the doped state, when compared to other conducting polymers.[230] Using cyclic voltammetry, it was found that redox peaks are approximately at 0 mV (oxidation) and -400 mV (reduction) and remained almost unaffected during cycling. However, only under an applied negative potential of -700 mV the films were found to be stable. The neutral film are rapidly oxidized, as shown by open circuit potential measurements.[253]

2.3 PEDOT:PSS

2.3.1 PEDOT:PSS dispersion

One of the main reason for PEDOT success as conducting polymer is its availability in aqueous dispersion.[197] Although PEDOT is an insoluble polymer, combined with poly(styrenesulfonic acid) (PSS) as a counterion, it creates a polyelectrolyte complex (PEC), that can be prepared in stable dispersions, produced on industrial scale and used through several deposition techniques. PEDOT:PSS chemical structure is reported in Figure 2.8: it must be noted that PEDOT chains are much shorter compared to PSS ones (Figure 2.8a): the molecular weight of PEDOT molecules is between 1 and 2.5 kDa (for 6 to 18 repeating units), resembling an oligomer nature of these segments,[254] while PSS average molecular weight is usually 70 kDa at least.[255]
Polyelectrolyte complexes are typically formed mixing aqueous solutions of polyanions and polycations, resulting in a compound that can be either water-soluble or insoluble, depending on the parameters.[197] PSS was the first polyelectrolyte to be used with PEDOT in 1990, creating a water-soluble PEC and remaining an industrial standard ever since.[231] PSS is commercially available with different molecular weights and polydispersities. It is soluble in water and forms durable and transparent films.[256] As PEDOT counterion, PSS is always used in excess, thus as host polyelectrolyte (HPE). In standard PEDOT:PSS dispersions the molar ratio between thiophene groups and sulfonic acid groups is in the range of 1:1.9 to 1:15.2 (weight ratio range 1:2.5 up to 1:20). Since there is one charge every three to four thiophene rings,[257–259] the charge excess of PSS is between 6-fold and 46-fold.[197] According to the delocalization of positive charges in PEDOT, the weak polar groups and the different spacing of PEDOT charges compared to PSS ones, there in no molecular or supramolecular order in PEDOT:PSS, but only a random interaction between polymer chains giving the so-called pancake-like structure, as shown in Figure 2.8.[260] PSS is thus used in combination with PEDOT for two main reasons: first, it is used as counterion, balancing the positive PEDOT charges; second, it is used to keep PEDOT segments dispersed in water owing to its high hydrophilicity.[254] Indeed, water is the solvent chosen for PEDOT:PSS synthesis, due to the fact that it is inert to most oxidation or reducing agents, it is highly polar and a good PSS solvent. Even though EDOT presents poor solubility in water (at 20 °C only 0.21 g of EDOT can be dissolved in 100mL of water), it increases with PSS presence and with increasing temperature.

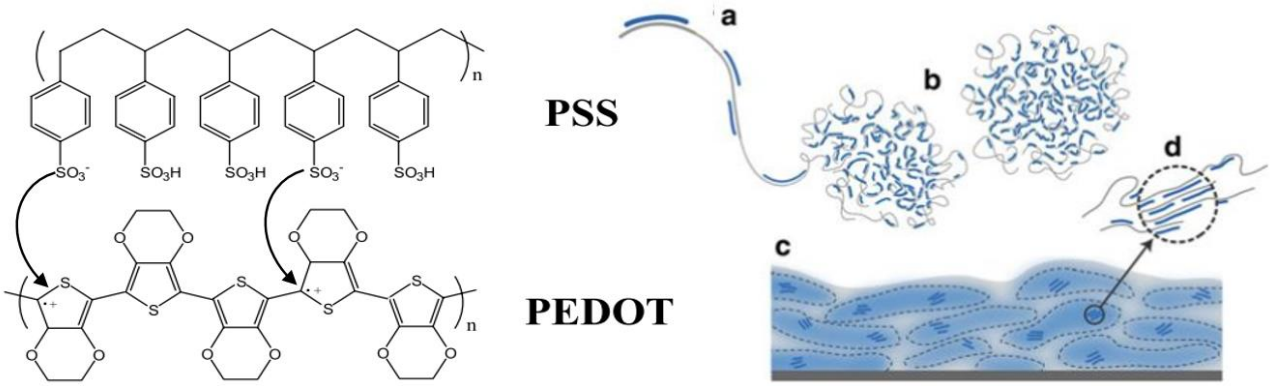

Figure 2.8: On the left, PEDOT and PSS chemical structures: the PSS is used as counterion to balance PEDOT positive free-charges. On the right, the PEDOT:PSS microstructure with PSS in grey and PEDOT in blue: a) synthesis onto PSS template; b) colloidal gel particle formation in dispersion; c) PEDOT:PSS films with PEDOT-PSS-rich (blue) and PSS-rich (grey) phases; d) aggregates/crystallites supporting enhanced electronic transport.[260,261]

As shown in Figure 2.8, PEDOT:PSS final structure is a cross-linked and highly swollen polymer gel, composed by gel particle with 90-95% of water content, with the maximum solid content that grows with decreasing PEDOT to PSS ratio.[254] This ratio also influences other physical parameters of the polymeric film, such as bulk conductivity, sheet resistance and surface roughness. For example, higher relative concentrations of PSS give less conductive and flatter films, because of a size reduction of PEDOT particles in the PEDOT:PSS dispersion.[262,263] This is in accordance with the

observation that films with smaller particles present lower conductivities.[254] The average particle size in a PEDOT:PSS dispersion is typically in the range between 10 and 100 nm.

2.3.2 Deposition of PEDOT:PSS

PEDOT:PSS dispersion in water can be deposited using all the main common techniques employed for depositing waterborne coatings, namely slit coating, drop casting, bar coating, spin coating, electrospinning and spraying. If there is the need of a structured deposition, other techniques, such as screen printing, nozzle printing, inkjet and several forms of contact printing, are employed.[264] Other structured deposition methods for PEDOT:PSS relied on a modification of the surface wetting properties, depositing of water repellants[265] or employing photo-lithographical[266] techniques.
The pristine PEDOT:PSS dispersion in water is adjusted before the deposition in order to meet the requirements for the deposition method used and to obtain an uniform film. Film quality is determined by viscosity, surface tension and the adhesion of the film itself to the substrate. To change such properties and match the required ones, it is possible to use different PEDOT:PSS solutions, varying the solid content, the PEDOT to PSS ratio, the gel particle distribution or adding water soluble or dispersible additives (for example surfactants, stabilizers, cross-linking agents or inert polymers).
Among the different techniques, PEDOT:PSS deposition by spin coating has proven to be a suitable method to obtain uniform films with thickness from 10 to 1000 nm. Two typical spin curves are reported in Figure 2.9 for CLEVIOS P AI 4083 (designed for hole injection in OLEDs) and CLEVIOS PH 500 (used for transparent electrodes).[267] These films, having a root-mean-square roughness of the order of 1 nm,[268] attract great interest as cladding layer for thin film device applications.

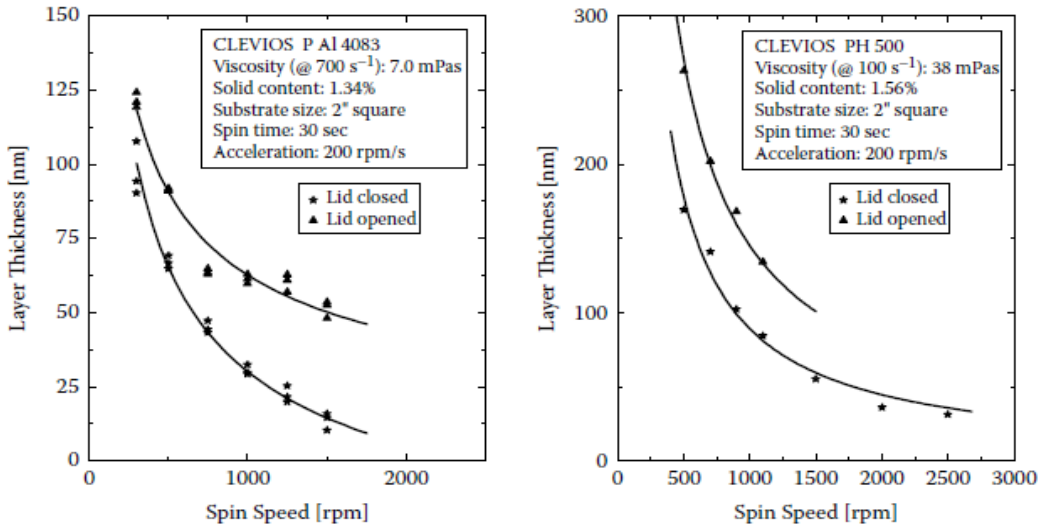

Figure 2.9: Spin curves for CLEVIOS P AI 4083 and CLEVIOS PH 500 taken on a Carl Süss RC8 spin-coater, with a closed or opened rotating lid.[197]

It is finally worth noting another useful technique for PEDOT:PSS thin film preparation, that does not start from a previously prepared PEDOT:PSS dispersion: electrochemical polymerization. Developed at the beginning for polypirrole,[269] and then extended to many other polymers, this method allows for a precise control of the quantity of the material deposited on the substrate, also providing an easy way to functionalized it with inorganic[270] or bio-molecules.[189] PEDOT:PSS electropolymerization has been demonstrated to produce films and micro-structured systems with facile electrochemistry, high-ionic conductivities, good electrochemical stability and capacitances, suitable for electrochemical supercapacitor applications.[271–273]

2.4 PEDOT:PSS thin-film properties

2.4.1 Thermal and UV stability

Before further processing or use, PEDOT:PSS deposited films have to be dried, removing water by baking the layers at high temperature, applying vacuum or using infrared (IR) radiation. Sometimes even a combination of these processes may be employed.

As for the PEDOT, also PEDOT:PSS films have very high thermal stability, that was studied at Bayer Laboratories using thermogravimetrical analysis (TGA) on thick layers. Figure 2.10 shows the weight loss and the ion currents of relevant masses during sample heating at a constant rate in helium: between 100 °C and 200 °C, only the evaporation of the remaining water determines the weight loss, while over 250 °C, there is a significant weight drop. At the same time, also the ratio *m/e*=64 increases, attributed to SO_2 ions, indicating the fragmentation of the PSS sulfonate group. For temperatures higher than 350 °C also fragments caused by carbon oxidation are detected. Thus, after TGA studies the material is considered stable up to a temperature of 200 °C.[197]

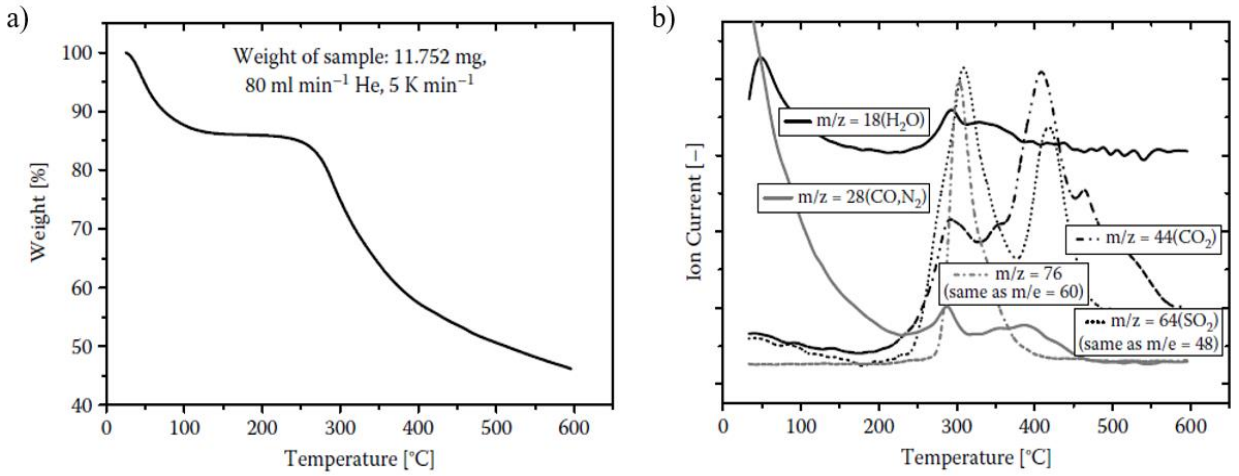

Figure 2.10: Thermogravimetric analysis (TGA) of PEDOT:PSS samples with a PEDOT to PSS ratio of 1:20 by weight a) Weight loss, monitored while heating at a constant rate of 5 K/min. b) Ion currents of different masses recorded simultaneously. Data are from Bayer Technology Services, Leverkusen, Germany.[197]

Despite PEDOT stable conductivity, it can be subject to degradation, once exposed to harsh condition (like happens for all carbon compounds). Thus, PEDOT:PSS light stability have been studied in detail[274] and the decay mechanism was found to be related to oxidation by oxygen enhanced by light.[275,276]

A proper way to keep PEDOT:PSS conductivity over time is to avoid ultraviolet(UV)-light exposure and temperature above 70°C in combination with oxygen, for example hermetically encapsulating the devices. Indeed, like most of the polymers, PEDOT:PSS degradates with UV-light, as it is proved from Figure 2.11a, where a resistivity increase happens for UV adsorbed photon ($\lambda < 320$ nm). This fact limits PEDOT:PSS use in outdoor applications if proper protection are not taken to encapsulate thin films. Figure 2.11b reports the sheet resistance over time for thin films of PEDOT:PSS (PEDOT to PSS as 1:2.5) including 5 wt% dimethyl sulfoxide (DMSO) under continuous illumination of a xenon (Xe) lamp. The films unprotected from air showed a steep increase of resistivity, while films encapsulated by a thin glass plate exhibited only a slow increase, comparable to the one obtained for the film stored in air but in absence of light. This result proved that degradation occurs because of air-induced PEDOT oxidation, accelerated by simultaneous absorption of light.

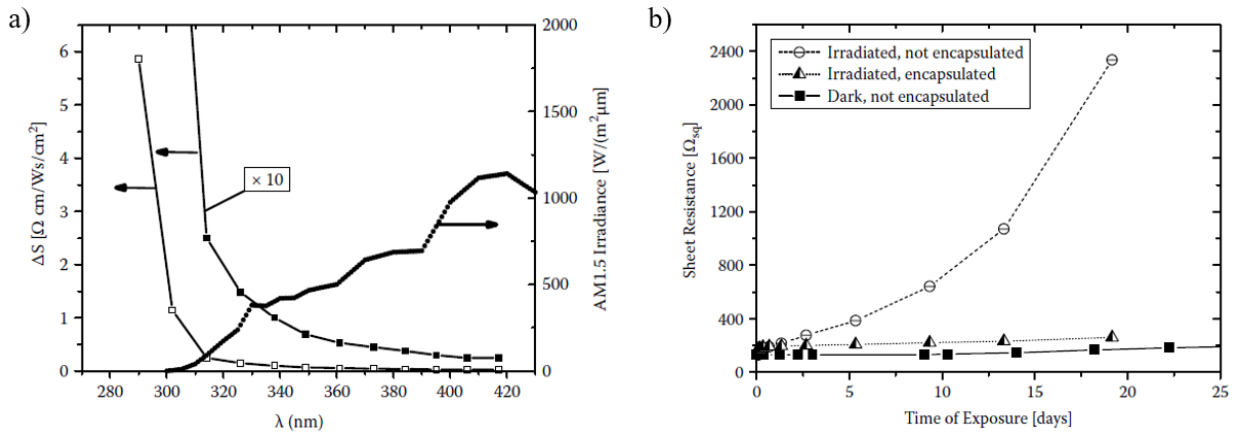

Figure 2.11: a) Activation PEDOT:PSS (Clevios P) spectrum reporting the change in resistivity on irradiation dose and wavelength. Data taken from A. Elschner, H.C. Starck Clevios GmbH, unpublished results. A spectrum of solar AM1.5 irradiance, adapted from Bird7Hustom, is inserted for comparison. b) Sheet resistance of PEDOT:PSS films with 5 wt% of DMSO were monitored over time , during the exposure to a Xe lamp. Data from A. Elschner, H. C. Starck Clevios GmbH, unpublished results.[197]

2.4.2 *Water uptake*

PEDOT:PSS, like other polymers with sulfonic acid groups, is hygroscopic and takes up moisture in ambient conditions. The weight loss in Figure 2.10a after baking can be ascribed to loss of previously absorbed water. As an example, water absorption of a predried PEDOT:PSS sample (flakes peeled off from underlying substrate with 10 μm thicknesses) of 1.5g is reported in Figure 2.12a: in the first 3 minutes the weight increases of 10% when the sample is brought in contact with ambient air. Noteworthy, the sample geometry and the humidity level influence the kinetics of water absorption.
Thin films of PEDOT:PSS with thickness around 100 nm absorb water almost immediately and their thickness increases, in particular depending on relative humidity. High increases in layer thickness are especially present for high PSS content films, raching up to 30% of thickness rise. Again, to avoid water absorption hermetic encapsulation can be exploited.

2.4.3 *Mechanical properties and morphology*

Flexibility is another important PEDOT:PSS film properties which is highly advantageous, since PEDOT:PSS films do not crack upon bending,[277] differently from their inorganic metal oxide counterpart. For this reason, their mechanical features have been investigated using tensile strength tests on free-standing PEDOT:PSS films.[278] Both tensile strength and Young's modulus were found to depend on the relative humidity (rH) level, as reported in Figure 2.12b. The polymer exhibits brittle fracture behaviour for rH = 23% (with Young's modulus of 2.8GPa), while it changes to plastic fracture behaviour at rH =55% (Young's modulus of 0.9 GPa).
Due to PSS film-forming properties, PEDOT:PSS films are amorphous:[279] indeed, no crystalline regimes have been found, except for short-range order, using x-ray diffraction (XRD).[280] Differently, chemically in situ polymerized PEDOT films, which do not contain PSS, exhibit crystalline ordering and fibril-like structures.[258,281]
While no phase segregation occurs between PEDOT and PSS on microscopic scale in thick dried films, phase separation happens on uniform thin films, spin-coated on glass substrate, creating PSS-rich phases of 30-40 Å. This was determined for the first time by Greczynski *et al* while investigating PEDOT:PSS film surfaces with photoelectron spectroscopy.[282]
Many other studies were based on the analysis of the surface roughness of PEDOT:PSS films using scanning atomic force microscopy (AFM). The surface roughness depends on the weight ratio between PEDOT and PSS and on the distribution of the gel particle size: in general, film surface smoothness increases with the reduction of the gel particle size.

Different models were developed to describe PEDOT:PSS morphology. The one proposed by Nardes *et al*[283] suggests that the film morphology resembles stacked pancakes. This model states that sphere-shaped gel particles with PEDOT-rich core and PSS-rich outer shell usually shrink in the vertical direction during the film formation (drying process), having in the end a disc-like shape with PSS-rich region in the contact area. Thus, free-charge carriers will travel easier along the long than along the short axis of the disks. Moreover, the PSS-rich regions act as charge barriers, being poor electrical conductors due to the lack of PEDOT transport sites. The material cohesion is achieved by hydrogen bonds between PSS shells. The morphological and micromechanical model is represented in Figure 2.12c. As it is shown, different relative humidities lead to two behaviours: at low relative humidities, hydrogen bonds between PSS-rich regions are very strong, thus fractures occur through individual grains (transgranular fracture); on the opposite, at high relative humidities, water uptake (due to hydrophilic and hygroscopic PSS nature) makes the material swelling and enhances the distances between grains, reducing the cohesion and mechanical strength, letting the grains slide by each other under tensile loading (intergranular fracture). This results in a rough surface and explains the previous stated macroscopically plastic failures at high relative humidities.

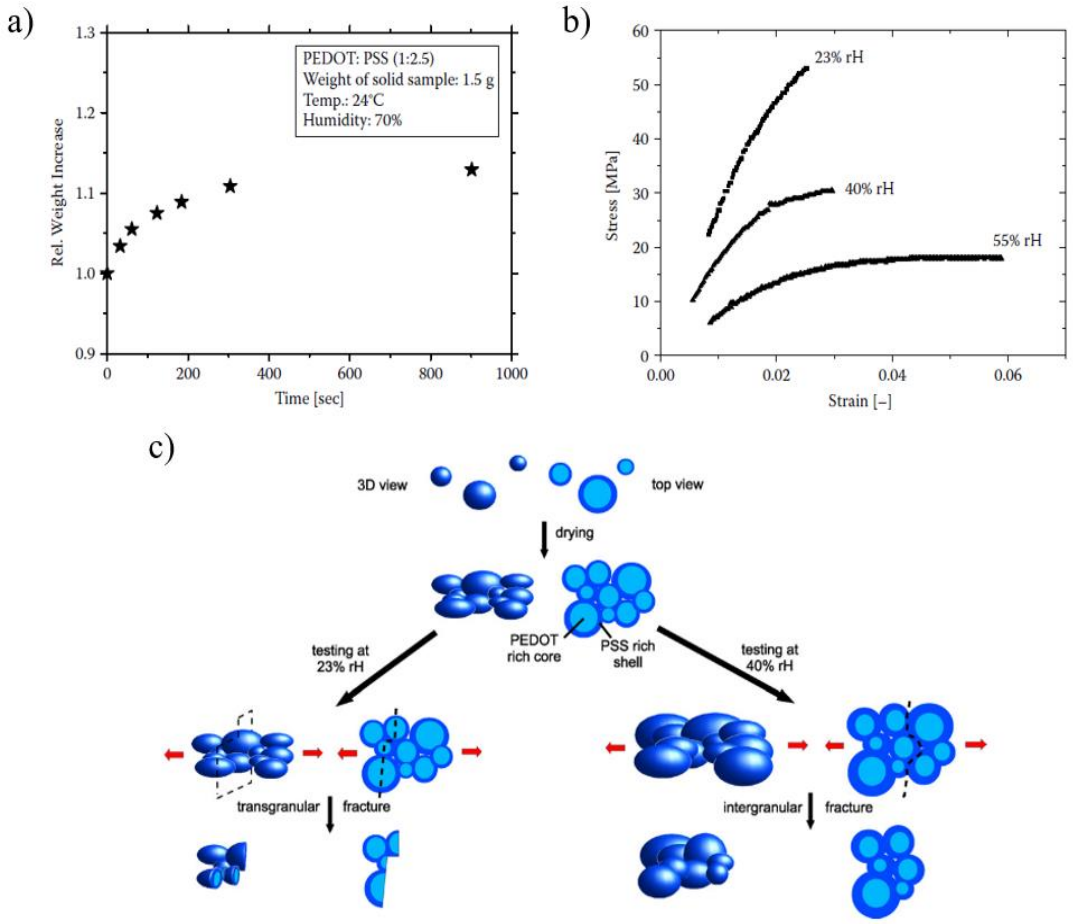

Figure 2.12: a) PEDOT:PSS (weight ratio PEDOT to PSS 1:2.5) pre-dried sample several micrometers thick exposed to air wth a relative humidity of 70%, monitoring the weight increase due to water absoprtion in function of time. Data from Bayer Technology Services, Leverkusen, Germany. b) Stress-strain diagrams fro PEDOT:PSS films at different relative humidity levels.[278] c) Schematic overview of the proposed model with PEDOT:PSS forming spherical gel particles with PEDOT-rich core and PSS-rich shell, that elongate upon drying. Moreover, different humidity levels lead to diverse behavior upon fractures: transgranular fractures occur at relatively low humidity while high humidity brings intergranular fractures.[278]

2.4.4 *Electronic states*

The absorption spectrum of PEDOT:PSS is almost identical to the absorption of in situ chemically polymerized PEDOT without PSS. Figure 2.13a reports the relative transmission, absorption and

reflection spectra of CLEVIOS PH1000 with 5% DMSO.[197] The broad absorption in the visible and infrared regions are the contribution of free charge carriers to absorption or the excitations of midgap states (polarons or bipolarons).[284] In addition, PEDOT:PSS and only PSS report strong absorption at 193 nm and 225 nm (not shown here) that are attributed to π and π* transitions of the benzene rings in the PSS system.[284]

In general, the absorption spectrum of PEDOT:PSS depends on its oxidation state. Figure 2.13b depicts Gustafsson *et al* investigations on PEDOT:PSS (deposited on ITO) optical absorption spectra as a function of photon energy at different applied bias.[285] Increasing the applied bias, the peak at 2.3eV (560nm), which is the bang gap of absorption, is reduced and two new peaks appear at lower energies. The partly neutralized polymer with -1.5V applied is absorbing in the visible range, while in its oxidized form (0.5 V) it is basically transparent. This feature renders it suitable for electrochromic applications, such as displays or smart windows.[286]

The two peaks reported in Figure 2.13b stand for the charge electrochemically introduced in the polymer, stored as polarons and bipolarons at high oxidation level, thus creating new electronic levels inside the energy gap,[287–289] as we previously explained in paragraph 2.1.2. Due to the amorphous nature of the film, the length distribution of PEDOT segments and the interaction of charge carries (forming bands without a clear defined structure), these energy levels are broadened.

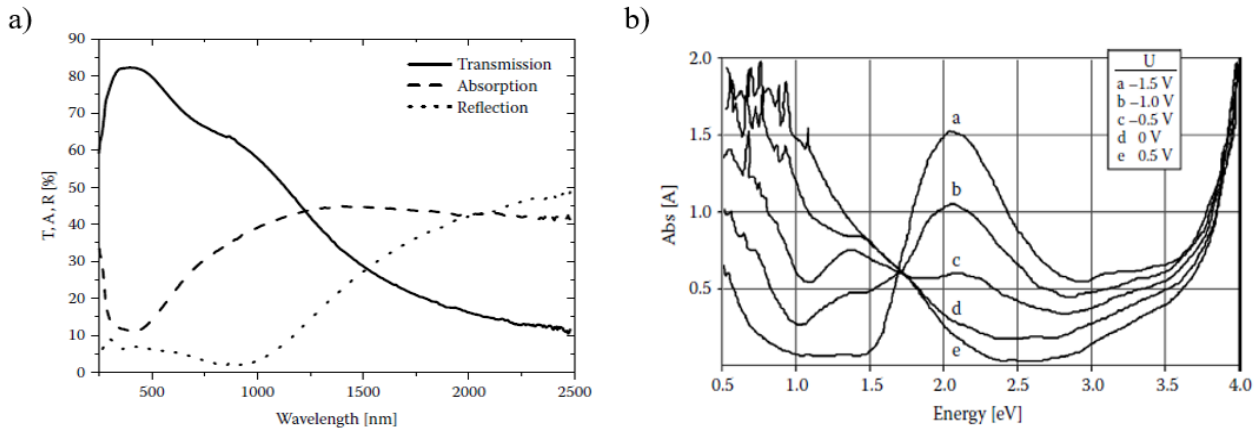

Figure 2.13: a) Relative transmission, absorption and reflection spectra of a 190nm thick CLEVIOS PH1000 film with 5% DMSO added. Data from A. Elschner, H. C. Starck Clevios GmbH, unpublished results.[197] b) Optical absorption of a PEDOT:PSS film electrode under different applied voltages: (a) -1.5V, (b) -1.0V, (c) -0.5V, (d) 0V and (e) 0.5V.[285]

2.4.5 *Vibrational states*

Vibrational states of *in situ* PEDOT and PEDOT:PSS have been studied using IR and Raman spectroscopy.[285] As can be seen from Figure 2.14a and 2.14b, several well-defined bands, due to PEDOT vibrations, are found in the region between 500 and 200 cm^{-1} and Raman bands were assigned (both with experiment and theoretical calculations) to intramolecular vibrations by Garreau *et al*.[290] As confirmed by further works,[253,291] the form of the spectra and the relative intensity of the peaks strongly depend on the PEDOT oxidation level. In particular, the band from 1400 to 1500 cm^{-1}, associated with C=C symmetrical stretching, was used to distinguish PEDOT being in its quinoid or benzoid form,[261] drawing conclusions on secondary doping, as will be later shown in paragraph 2.4.7.

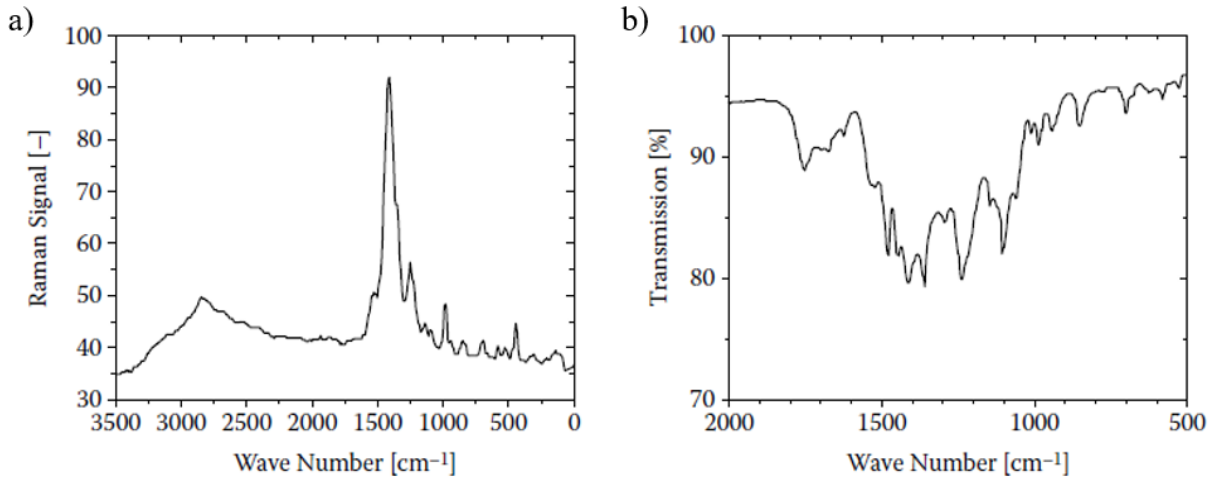

Figure 2.14: a) Raman spectra for oxidized PEDOT, using PSS as counterion. b) IR spectra for PEDOT:PSS.[291]

2.4.6 *Electrical conductivity and microscopic model*

As already stated, PEDOT:PSS is an intrinsically conducting polymer, presenting metal-like properties with free charge carries coming from the p-doped conjugated π system of the thiophene rings: indeed, the oxidative polymerization reaction triggered by radicals creates one free charge every three to four thiophene rings. PSS does not contribute to charge transport directly, but it behaves as a template to keep PEDOT in the dispersed state, provides film-forming properties and balance the cationic PEDOT charges in order to form a stable salt.[197]

PEDOT:PSS conductivity is usually determined through four-point or two-point probe measurements of thin films deposited onto non-conductive substrates. This method allows for the sheet resistance measurement (R_{sq}), which is related to the conductivity through the equation:

$$\sigma = \rho^{-1} = \frac{1}{R_{sq} \cdot d}, \tag{2.12}$$

where d is the film thickness, typically determined with a profilometer or using ellipsometry.

The conductivity (σ) is defined as the product of elemental charge (e), charge carrier mobility (μ) and charge carrier density (n). Thus, for a hole- and electron-conducting material, σ can be written as:

$$\sigma = e \cdot \mu_p \cdot n_p + e \cdot \mu_n \cdot n_n \tag{2.13}$$

In the case of PEDOT:PSS, only holes contribute to charge transport, while injected electrons recombined at the oxidized PEDOT sites. Hole densisty can be then calculated using geometrical considerations. In highly conductive PEDOT:PSS films, the ratio between PEDOT and PSS is 1:2.5 and the density of these solid films is approximately 1 g/cm^3. Since the molecular weight of monomeric PEDOT or PSS units is, respectively, 140 and 182 g/mol, EDOT monomer density can be estimated as $1 \cdot 10^{21}$ cm^{-3}. Furthermore, we already introduced that oxidation level per monomer unit is known to be 1 charge per 3 EDOT units, thus hole density in PEDOT:PSS films is estimated to be $n_p = 3 \cdot 10^{20}$ cm^{-3}. Then, for highly conducting films, according to the estimated hole density and the conductivity value around σ = 1000 S/cm, PEDOT:PSS hole mobility can be calculated to be μ_p = 20 cm^2/Vs. This value is in accordace with Winther-Jensen *et al* work,[292] who investigated vapour-phase –polymerized EDOT, obtaing a PEDOT:PSS hole mobility values of 11 cm^2/Vs, which was considered as a lower limit by Prigodin and Epstein stating that only a part of the free charge carriers in the conducting polymer will contribute to charge transport.[293]

Conductivity of PEDOT:PSS films can be altered by various means: changing the ratio between PEDOT and PSS, because it determines the density of charge transporting PEDOT sites; adding other

electrical inert components (such as polyvinylalchool)[294] reduce conductivity; addition of water miscible high boiling solvents (like ethylene glycol or dimethyl sulfoxide) to PEDOT:PSS solution will boost conductivity, impacting on gel particles distribution and orientation (thus producing thin film morphological changes), as will be explained in the next paragraph; pH variations of the solution will also influence the conductivity, as reported by Aleshin *et al*,[279] who found highest conductivity for pH in the range between 0 and 3.
Following the theories of charge transport on amorphoug inorganic semiconductors, the conduction mechanism of CPs is often explained as charge hopping between adjacent sites. Conjugated polymer segments are preferentially forming electronic active sites thanks to their capability of being easily oxidized or reduced. Charge transport frequency between adjacent sites then depends on their relative energetic position, distance and relative orientation, as studied by Borsenberger and Weiss.[295]
One of the first studies on conductivity mechanisms in PEDOT:PSS films was done by Aleshin *et al*,[279] who examined PEDOT:PSS conductivity and magnetoresistance in function of temperature(T), observing that both parameter increase with increasing T. The variable range hopping (VRH)[296] model was employed to discuss the temperature dependace of conductivity, giving:

$$\sigma(T) = \sigma(0) \cdot exp\left[-\left(\frac{T_0}{T}\right)^{\propto}\right], \tag{2.14}$$

where σ(0) is the conductivity at infinite temperature, k_bT_0 is the energy barrier between localized states and α is equal to 1/(1+D), with D representing the dimension of the system and assuming that the density of states near to Fermi level $N(E_f)$ is constant or varies smoothly with energy. Thus, for 3-D systems α=1/4 and $T_0= 16/[k_bN(E_f)L^3]$, while considering 1-D systems, it comes out α=1/2 and $T_0= 16/[k_bN(E_f)L_{\parallel}L_{\perp}^2]$. L is called localization length and it is the distance from a site for the electron wave function to decay to 1/e of its value,[297] while its parallel and perpendicular components are referred to the directions of the system.[296]

2.4.7 *Secondary dopants*

MacDiarmid and Epstein have used the term *primary dopig* to describe the addition of small nonstoichiometric quantities of a material to conducting polymers, leading to strong conductivity enhancements. For example, redox agents able to oxidize (*p*-doping) or reduce (*n*-doping) the polymer chain or the protonation of polyaniline are referred as primary doping or doping. Thus, the term *secondary doping* was introduced by MacDiarmid and Epstein to refer to additive further enhancing the conductivity of an already doped polymer (even of several orders of magnitude).[298]
The main difference between primary and secondary doping is that the first has a reversible effect, while the second a permanent one, remaining even after the additive removal.[197] Noteworthy, secondary dopants do not actually change the PEDOT doping level,[280] thus they are often referred a *conductivity enhancing agents* (CEA).[299]
Typically, CEA are added to PEDOT:PSS water dispersion (but they can also be added after the film formation) and the effects on conductivity are clearly visible once the film is formed. A heating treatment in not always mandatory, since drying the film at room temperature under reduced pressure can lead at the same results. However, the heat treatment can further increase the final conductivity[262] and has the ability to remove many of the CEA from the final film.
An exhaustive list of chemicals used as secondary dopants for PEDOT:PSS is reported in the book "PEDOT: principles and applications of an intrinsically conductive polymer"[197], but the most effective, thus most used, substances are dimethyl sulfoxide (DMSO), copper(II) chloride, ethylene glycol (EG) and dodecylbenzenesulfonate (DBSA), which give an increase of several orders of magnitude to pristine PEDOT:PSS conductivity. Moreover, Kim *et al* demonstrated that PEDOT:PSS conductivity can be increased with a sulforic acid treatment up to ~4000 S/cm,[300] similar to the one

of indium-tin-oxide. However, the use of this acid strongly limits applications in bioelectronics. Indeed, not only just one parameter, but a combination of factors is needed in order to have a suitable secondary dopant, i.e. high solubility in water, high boiling point and high dielectric constant.[301]
One of the main observations that needs to be done is that the conductivity increase is not proportional to the additive concentration, as proved by Crispin *et al*[301] and by Zhang *et al*[302] works. As can be seen in Figure 2.15a and b, after a certain concentration (dependent on the secondary dopant taken into account) the further addition of secondary dopant does not enhance the conductivity of the film but either ir remains constant (Figure 2.15a) or it gets even reduced (Figure 2.16b). Moreover, as shown in Figure 2.15a, under a certain concentration there is no effect of the CEA on the conductivity. Thus, it can be noted that there are small concentration ranges, depending on the conductivity enhancing agent itself, where their effect on conductivity is almost linear with the concentration.
Other two important aspects have to be underlined: i) the presence of the secondary dopant is not necessary to maintain the conductivity once the film is formed;[197] ii) even thought the initial concentration of CEA in the solution is low, their concetration increase during film drying due to their lower vapour pressure compared to water,[301] and a small quantity can thus strongly influence the whole film. For these reasons, the effect of the CEA is considered to take place during the film formation, i.e. during solvent evaporation.

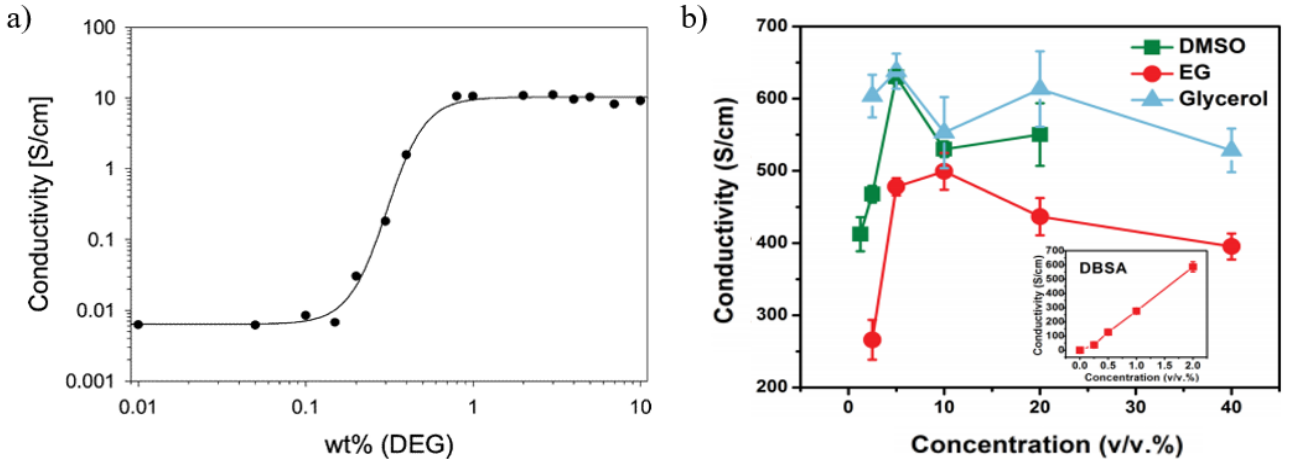

Figure 2.15: a) Plot of PEDOT:PSS film conductivity as a function of dyethylene glycol introduced in the water emulsion.[301] b) Conductivity of Clevios PH1000 PEDOT:PSS films with the addition in the mixture of 0.5 v/v% DBSA and different v/v% concentration of CEA (DMSO, EG, glycerol). The inset shows the conductivity variation upon different DBSA concentrations without any other CEA.[302]

Upon the introduction of conductivity enhancing agents, both the surface and bulk of the material are subjected to changes. For pristine PEDOT:PSS films, PSS is found in excess on the surface, while, after the addition of CEA the surface composition has an increase in PEDOT to PSS ratio, as confirmed by STM[303] and AFM[301] measurements. These images show an increase in more conductive and harder areas (PEDOT-rich regions) on the surface of PEDOT:PSS films for enhancing CEA concentrations. However, since the conductivity is a bulk property, these changes must be extended also to the whole bulk composition.
During the PEDOT:PSS film deposition from aqueous dispersion, polymer chains are “frozen” in a non-equilibrium state,[304] but in presence of a high-boiling solvent the blend rearrange and the PEDOT olygomers find a new thermodynamically favorable position, similarly to the effect of a platicizer.[305] The same mechanism can be used to explain the conductivity increase upon thermal heating. Due to the fact tha the polymer chains are charged, it can be assumed that the high polarity of the secondary dopant makes it interact with the polyanion and polycation charges, described also as screening effect between the $PEDOT^+$ and PSS^- chains, allowing them to orientate. After the rearrangement, the film remains in its new thermodynamically favourable state, even upon the CEA thermal removal.[304] Such

a rearrangement is, however, not enough crystalline to be observed with x-ray diffraction spectra,[306] possibly due to the polymeric nature of the counterion.
Since the charge transport in PEDOT:PSS films is based on charge hopping between PEDOT-rich region, separated by non-conductive PSS-rich ones, an increase in PEDOT segment order leads to the formation of highly conducting pathways, created only if the CEA is present long enough to allow the order rearrangement to occur.
Ouyang *et al* interpreted the variations observed in Raman spectra as a change from benzoid to a quinoid structure of the PEDOT molecules, moving from a coil structure to an extended coil or linear structure of the chains.[307]
In summary, an increase of the nanoscale organization, facilitating the charge hopping mechanism between conductive PEDOT-rich regions, introduces a macroscopic conductivity enhancement.
A different class of additives are the cross-linkers, which increase the formation of covalent bonds between the polymer chains, thus changing their physical features.
Since PSS is highly hydrophobic, PEDOT:PSS films exposed to water usually delaminates. The addition to the mixture solution of the cross-linking agent 3-glycidoxypropyltrimethoxysilane (GOPS) has proved to enhance the PEDOT:PSS film stability in aqueous solutions,[302,308] as reported in Figure 2.16. Even though GOPS addition induces good mechanical and electrical stability, it gives thicker films with lower conductivities: thicker films have larger amount of PSS units, not removed by the water, due to GOPS cross-linking effect. The PSS excess absorbs larger water amounts and causes irreversible morphological changes in the film, resulting in decreased conductivity.[302,309]

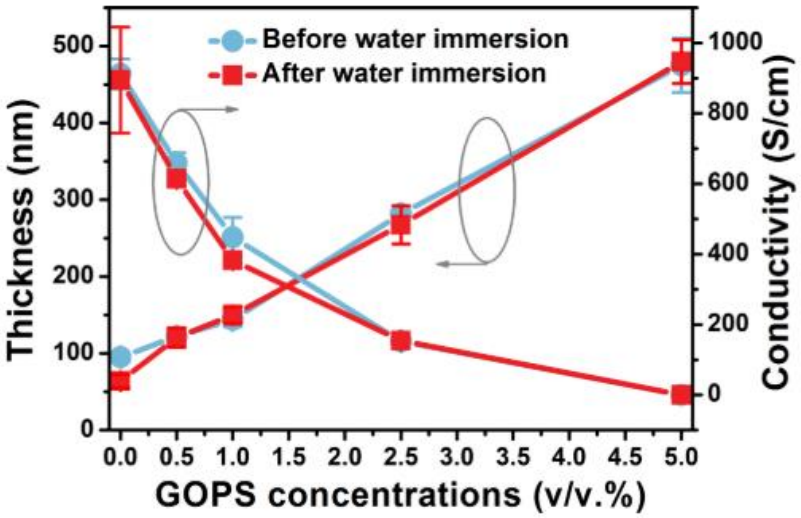

Figure 2.16: Thickness (left y scale) and conductivity (right y scale) changes for films made with mixtures containing 94.5 v/v% of CleviosTM PH1000, 5 v/v% glycerol and 0.5 v/v% DBSA with increasing GOPS concentration.[302]

2.5 PEDOT:PSS technological applications

Due to its ease of processability and suitable electrical and mechanical properties once deposited into thin films, PEDOT:PSS have been widely used for a broad range of applications in organic bioelectronics, some of which have already been seen in Chapter 1. In this Section, a focus on use of PEDOT:PSS for organic electrochemical transistors, biosensors and electrodes will be given.

2.5.1 Organic Electrochemical Transistors (OECTs)

OECTs have been already qualitatively introduced in the paragraph 1.3.2 of this thesis. Here, their quantitative working principle will be described, introducing PEDOT:PSS-based OECTs.

OECTs can work either in accumulation or in depletion mode, the latter being the most found and employed in recent works: in this case the polymer is in its pristine doped state and it is switched to the undoped one, via gate bias. OECTs working in depletion mode will be explained in this Section and, since most commonly used conducting polymers are hole transporter, the nomenclature and the models will be referred to *p*-doping. Thus, being the semiconductor *p*-doped, the application of a positive bias on the gate would push cations from the electrolyte into the semiconducting channel, dedoping it and decreasing the source-drain current, I_{ds}.

2.5.1.1 Working principle: electronic and ionic circuit

As previously seen (paragraph 1.3.2), OECTs can be described as the sum of two electrical circuits, one accounting for the electronic transport in the organic semiconducting channel, and the second representing the ionic circuit for the electrolyte and the electrolyte/semiconducting film interface (reported in Figure 2.17a).[155]

Electronic Circuit

The electronic circuit is employed to describe hole movements in the semiconducting channel, using the approximation of Ohm's law (a resistance behaviour):

$$J(x) = q\mu p(x)\frac{dV(x)}{dx} \tag{2.15}$$

where J is the current flux, q the elementary charge, μ the hole mobility (considered constant in this analysis, thus independent from the field and concentration as it should be for organic semiconductors[310,311]), p the hole density and dV/dx the electric field.

Since an hole semiconductor working in depletion mode is studied, it was considered that each cation, injected from the electrolyte (upon the application of a potive V_g) into the semiconductor, compensate one acceptor. This process thus occurs in two steps in order to maintain electrical neutrality in the semiconductor at the steady-state, i.e. for each cation compensating an acceptor, a hole is extracted from the source contact and not replaced at the drain (if we assume $V_d > 0$). Then, we can write the expression for the effective dopant density inside the volume ν:

$$p = p_0\left(1 - \frac{Q}{qp_0\nu}\right) \tag{2.16}$$

with p_o as the initial hole density in the organic semiconductor before de-doping process and Q is the total charge of injected cations. In order to simplify the equations and calculations, negative ions are assumed to have no effect on the organic semiconductor, and charge densities are assumed to be uniform across the organic semiconductor film thickness, limiting the use of this model to thin films.

Ionic Circuit

The ionic circuit can be described by a resistor (R_s) and a capacitor (C_d) in series,[312] the former taking into account the conductivity of the electrolyte (i.e. its ionic strength), while the latter representing the polarization at the gate electrode/electrolyte and electrolye/semiconducting channel interfaces. It will be seen later in this Chapter that, for a complete description of the system, also a resistance in parallel with the capacitance should be inserted in the mdoel (to consider the electron transfer between the polymer and the electrolyte), but this is above the current explanation. Since the high capacitance of semiconducting polymers (in primis PEDOT:PSS),[313] channel capacitance is expected to be higher than gate one (per unit area), thus properties such as the response time and the gating effect (see Figure 1.14a) will depend on gate capacitance, which is affected by the dimensions and material composition of the electrode.

As introduced in paragraph 1.3.2, current flowing at the gate electrode is a sum of the capacitive charging of an electrical double layer at electrolyte/gate interface (non-Faradaic process) and

electrochemical reactions occurring at the gate electrode (Faradaic process). The model here reported assumes no reaction at the gate, thus considering the OECT operating in non-Faradaic regime.[157] The Faradaic contribution for OECT devices are better discussed in the subparagraph 2.5.2.4.
The RC ionic circuit has a transient behaviour of a charging capacitor, upon the gate bias application, that can be described with the following:

$$Q(t) = Q_{ss}\left[1 - exp\left(-\frac{t}{\tau_i}\right)\right] \tag{2.17}$$

where $Q_{ss} = C_d\,\Delta V$ represents the total charge passing through the circuit, ΔV is the voltage applied across the electrolyte and the ionic transient time is $\tau_i = C_d\,R_s$ (RC constant). In OFET devices the capacitance per unit area is considered the suitable parameter for this model, since the gating effect occurs only at the semiconductor/electrolyte interface, as seen in paragraph 1.3.2. However, a recent work of Rivany *et al*[161] on OECT showed that for organic semiconductors permeable to ions, as PEDOT:PSS and others, capacitance per unit volume (volumetric capacitance, C*) should be used for these calculations. Indeed, they demonstrated a correlation between channel capacitance and film volume, as reported in Figure 2.17b, obtaining a PEDOT:PSS volumetric capacitance value of C* = 39.3 ± 1.3 F/cm^3. The dependance of the capacitance with the volume of the semiconducting channel proves the ion penetration and interaction with the whole bulk of the material in OECT devices. Moreover, the zero offset obtained from the correlation fit proves that no ion accumulation at the surface occurs, indicating a negligible ion injection barrier from the electrolyte into the organic film.

For ease of calculations, the dependences of the ionic double layer from concentration and potential are neglected, assuming a constant value for C_d.

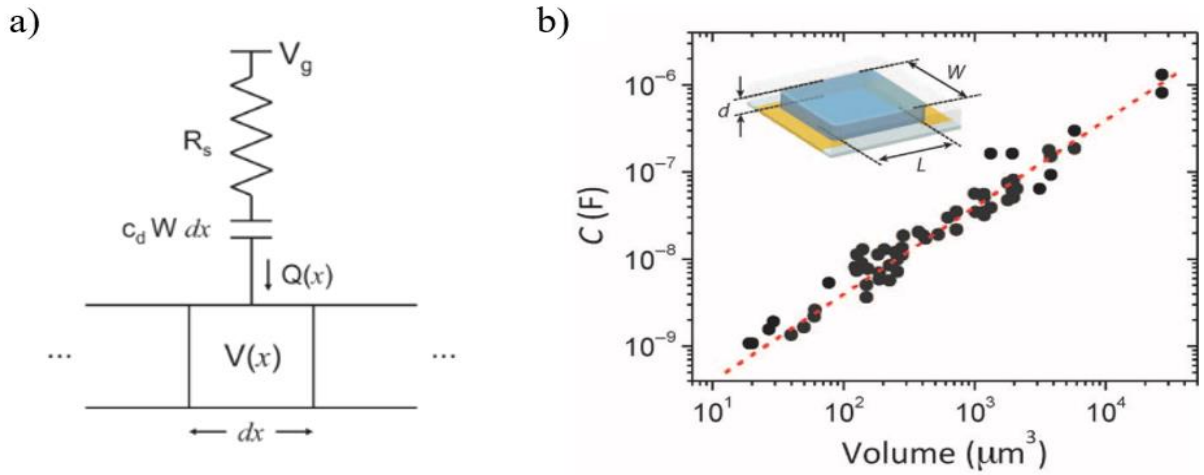

Figure 2.17: a) Schematic of the electronic and ionic circuit composition: the charge from the ionic circuit is coupled with the voltage drop along the semiconducting channel.[155] b) PEDOT:PSS capacitance determined using impedance spectroscopy for devices with different volumes. Inset: OECT configuration and channel dimensions (W, width; L, length; d, thickness).[161]

2.5.1.2 Steady-state behaviour

In order to solve OECT device behaviour, the effective dopant density (Eq 2.16) must be spatially known inside the semiconducting channel. Considering the Figure 2.18a, the charge in the volume fraction WTdx at the steady-state for the differential slice, dx, in the position x, can be expressed as:

$$Q(x) = C^*\big(V_g - V(x)\big)WTdx \tag{2.18}$$

where V_g is the voltage applied on the gate, T and W are the thickness and the width of the slice, respectively, and V(x) is the spatial voltage profile in the semiconductor film. De-doping can occur everywhere in the polymer, due to the high density of electronic charge in the organic material, acting

as source or sink for electronic charges resulting from dedoping. By the combination of Eq. 2.15, 2.16 and 2.18, it is thus obtained the OECT equation at steady-state:

$$J(x) = q\mu p_0 \left(1 - \frac{Q(x)}{qp_0 v}\right)\frac{dV(x)}{dx} = q\mu p_0 \left(1 - \frac{V_g - V(x)}{V_p}\right)\frac{dV(x)}{dx} \quad (2.19)$$

with $V_p = qp_0/C^*$, pinch-off voltage (also called threshold voltage), i.e. the voltage needed to accumulate a charge density equal to the intrinsic dopant density in the semiconductor.
At the steady-state, J(x) must be spatially constant along the channel, thus for the ideal geometry, shown in Figure 2.18, it can be expressed as J(x)=J=I/WT. Thus, I_d can be obtained from Eq 2.19 for different regimes, keeping in mind that $0 \leq |V(x)| \leq |Vd|$ and de-doping occurs only when V(x)< Vg. From the source-drain current it is the possible to calculate the transconductance gm = $\frac{\partial I_d}{\partial V_g}$ of the device, which is the figure of merit that quantifies the efficiency of the transduction (OECT amplification).

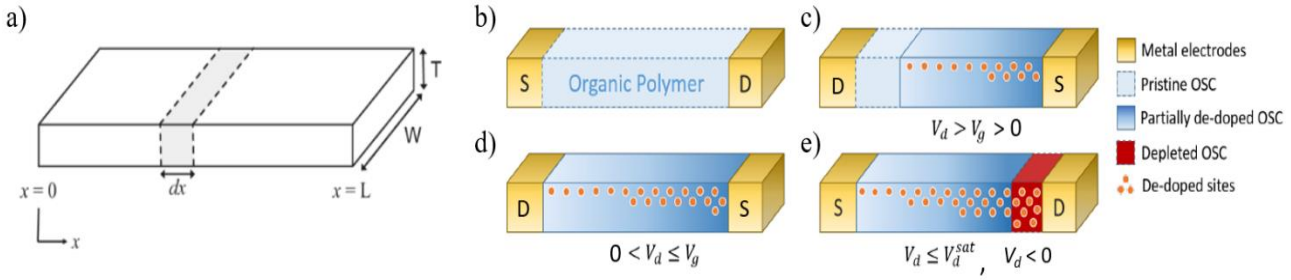

Figure 2.18: a) Organic semiconductor slice geometry used in the model, with source located at x = 0 and drain at x = L.[155] Doping levels for a *p*-type OECT channel with $V_g > 0$ (depletion mode), for different regimes: b) channel scheme in its pristine (fully doped) state; c) with $V_d > V_g$, the doping effect only occurs where $V(x) < V_g$; d) for $V_d^{sat} < V_d < V_g$, cations are injected all along the channel; e) when $V_d \leq V_d^{sat}$, the density of the injected cation fully counterbalance the hole density of the semiconducting film where $V(x) \leq V_d^{sat}$, thus generating a depletion region.

According to the choice of V_d and V_g, different situations may occur, thus different operational regimes. For $V_g > 0$ (Figure 2.18b, 2.18c, 2.18d and 2.18e), we can have:
$V_d > V_g$: for drain voltages higher than gate ones, de-doping can occur only in the regions where $V(x) > V_g$, while in the region where $V(x) < V_g$, it is found $p(x) = p_0$ (Figure 2.18c); the current is thus linear with the drain voltage, according to the Equation:

$$I_d = G\left(V_d - \frac{V_g^2}{2V_p}\right) \quad (2.20)$$

where $G = q\mu p_0 WT/L$ is the organic film conductance and the corresponding transconductance becomes $g_m = -\mu C^*(WT/L)V_g$, independent from V_d and linear with V_g. The onset on the linear behaviour occurs when $V_d = V_g$.

$0 < V_d < V_g$: in this situation, partial de-doping occurs all along the channel length (Figure 2.18d), thus the current can be written as:

$$I_d = G\left(1 - \frac{V_g - \frac{1}{2}V_d}{V_p}\right)V_d \quad (2.21)$$

In this case, the transconductance is independent from V_g and linear with V_d.

$V_d < 0$: in this case, it is possible to completely de-dope portions of the organic semiconductor, in which the local densisty of injected cations becomes equal to intrinsic dopant density (Figure 2.18e). This happens when $(V_g - V_d) > V_p$, with the critical saturation voltage $V_d^{sat} = V_g - V_p$. The

semiconductor will be locally depleted near the drain contact (where the difference with the gate voltage is higher), but holes injected in this region will still be transported to the drain.
If the drain voltage magnitude increases beyond V_d^{sat} (thus $V_d < V_d^{sat} < 0$), the region where $V(x) < V_d^{sat}$ will be depleted, slightly moving towards the source electrode. In the limit of long channels, the depleted region near the drain contact will not extend significantly, thus the source-drain current saturates to the value:

$$I_d^{sat} = -G\frac{(V_p - V_g)^2}{2V_p} = -G\frac{(V_d^{sat})^2}{2V_p} \quad (2.22)$$

Thus, the channel current will only depend on the saturation drain voltage for a particular gate voltage and the correspondent transconductance is given by $g_m = -\mu C^*(WT/L)(V_p - V_g)$.
A complete de-doping may also occur for $V_d > 0$ when $V_g = V_p$, though this behaviour is not interesting due to the high gate voltage required.[155]
Experimental steady-state transistor characteristics (source-drain current plotted in function of drain voltage for various potential applied on the gate) for PEDOT:PSS OECTs are reported in Figure 2.19a, showing an excellent fit between the model (solid lines) and the experimental data (dots).
On the other hand, when $V_g < 0$, two regimes may occur: if $V_g < V_d$, then cations are not pushed inside the semiconductor, thus no de-doping happens and the current is linear with V_d (and independent from V_g); if, instead, $V_g > V_d$, de-doping occurs where $V(x) < V_g$, with a final current expression similar to that in Eq. 2.20.

2.5.1.3 Transient behaviour

Since the OECT can be modelled as a combination of an electronic and an ionic circuits, these two elements will determine also the transient behaviour: in particular, it will be dominated by the injection of cations from the electrolyte into the semiconducting channel and by the removal of holes at the source electrode (for $V_d > 0$). For the ease of calculations, the spatial variation of the voltage and the hole densisty are neglected, taking average ionic current and hole density. Studying the current caused by hole removal (de-doping) together with the Ohm's law, it can be written:

$$J(t) = q\mu p(t)\frac{V_d}{L} + qfL\frac{dp(t)}{dt} \quad (2.23)$$

where f is a constant that accounts for the non-uniformity of the de-doping process and depends upon gate and drain voltages, ranging from 0 (when $V_d >> V_g$ for positive V_d) to 0.5 (when $V_g >> V_d$).[314]
For ideal geometrical conditions it is know that $J(t) = I(t)WT$, thus using Eq. 2.16, the transient source-drain current is expressed as:

$$I(t) = G\left(1 - \frac{Q(t)}{qp_0\nu}\right)V_d - f\frac{dQ(t)}{dt} \quad (2.24)$$

with Q(t) representing the transient charge response of the ionic circuit.
Solving the expression for the ionic circuit transient response two experimental conditions can be taken into account: constant gate current or constant gate voltage. The former is not a typical employed regime, but it can be used to understand this device model: indeed, fixing the gate current, ion kinetics will be fixed, thus shifting the focus on the electronic behaviour. For constant gate current, the transient behaviour simplifies to:

$$I(t, I_g) = I_0 - I_g\left(f + \frac{t}{\tau_e}\right) \quad (2.25)$$

where I_0 is the source-drain current before the application of the gate current and τ_e is the electronic transit time, expressed by $\tau_e = L^2/\mu V_d$. This equation provides a simple way to extract the hole mobility

in the organic film. Typical constant gate current OECT transient response characteristics are reported in Figure 2.19b and agrees with the model expressed by Eq. 2.25. Noteworthy, once the gate current is removed, there is a slow recovery of transistor initial source-drain current.

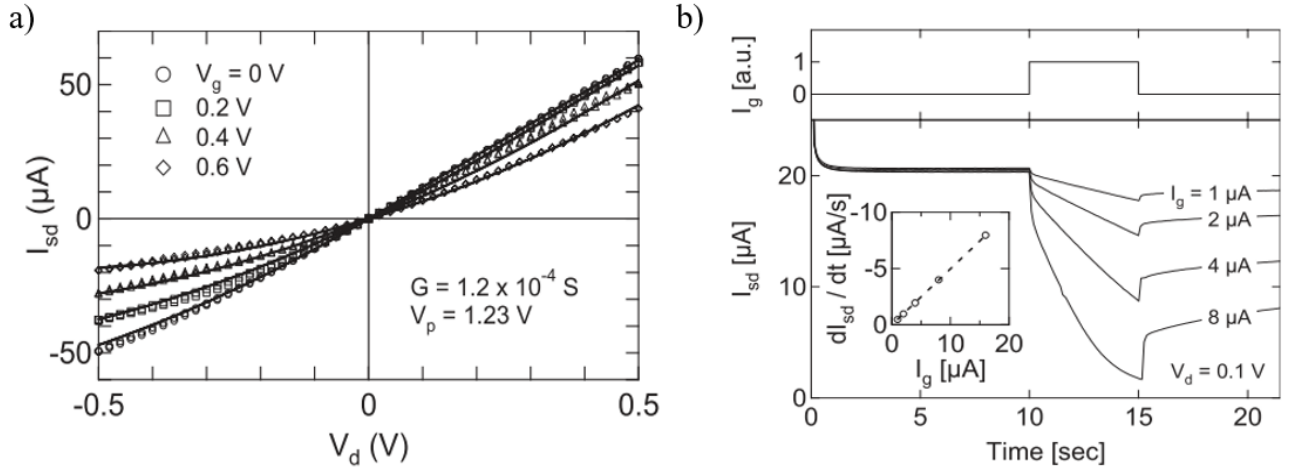

Figure 2.19: a) Experimental (dots) steady-state transistor characteristics (source-drain current plotted versus the drain voltage) for an OECT fitted with modelled data (solid lines). 10 mM NaCl was used as electrolyte and the thin film dimensions were L=5 mm and W=6 mm. b) Experimental OECT transient response upon the application of a constant gate current, reported above. In the inset, the slope of the transient response is plotted versus gate current, predicting τ_e = 0.5s and a hole mobility of 10^{-2}-10^{-3}cm^{2}V^{-1}s^{-1}. 1M of NaCl is used as electrolyte and the organic film dimensions are L=0.5mm and W=6mm.[155]

For simplicity, the study of transient behaviour under constant gate voltage is reported only for de-doping occurring everywhere inside the semiconducting channel, without saturation effects. Moreover, an average voltage drop is taken between the organic film and the gate electrode, $\Delta V = V_g - 1/2V_d$. Using these assumptions and the Eq. 2.17, the following is obtained:

$$I(t, V_g) = I_{ss}(V_g) + \Delta I_{ss}\left(1 - f\frac{\tau_e}{\tau_i}\right) exp\left(-\frac{t}{\tau_i}\right) \qquad (2.26)$$

where I_{ss} (V_g) is the steady-state channel current for an applied gate voltage V_g and ΔI_{ss} is the difference between the base current ($V_g = 0$) and I_{ss} for an applied V_g. The Eq. 2.26 depends primarly on two parameters, namely τ_i and τ_e, that describe the time scales of the transport. τ_i is the characteristic time constant for ionic transport, determined by the solution resistance and the solution/electrode interface capacitance ($\tau_i = R_sC_d$). Using Gouy-Cahpman theory for the double-layer capacitance, it can be estimated as $\tau_i \sim l/C^{1/2}$, with l being the distance between organic channel and gate electrode and C the ionic concentration.[313] On the other hand, also the electronic response time is used to describe the behaviour of the OECT in this regime, having the value $\tau_e = L^2/\mu V_d$. Thus, since the dependace in Eq. 2.26a is on electronic and ionic time constant ratio, $\tau_e/\tau_i \sim L^2C^{1/2}/(l\mu V_d)$, it can be noted that varying the electrode location, the organic film length, the source-drain voltage or the electrolyte concentration, the Equation can behave differently. In particular, as shown in Figure 2.20, the decrease of the current upon a positive voltage application can follow a monotonic decay or a spike-and-recovery curve, according to the ratio $f\cdot\tau_e/\tau_i$. A monotonic decay ($f\cdot\tau_e < \tau_i$) means that the hole transport and extraction is sufficiently fast and the transient behaviour is dominated by the ionic transport. On the contrary, a spike-and-recovery ($f\cdot\tau_e > \tau_i$) indicates that hole transport in the film occurs at a relatively slow rate, with the transient current controlled by hole extraction. Figure 2.26b reports experimental transient current for constant gate voltage, where the variation of V_d changes the transient behaviour.

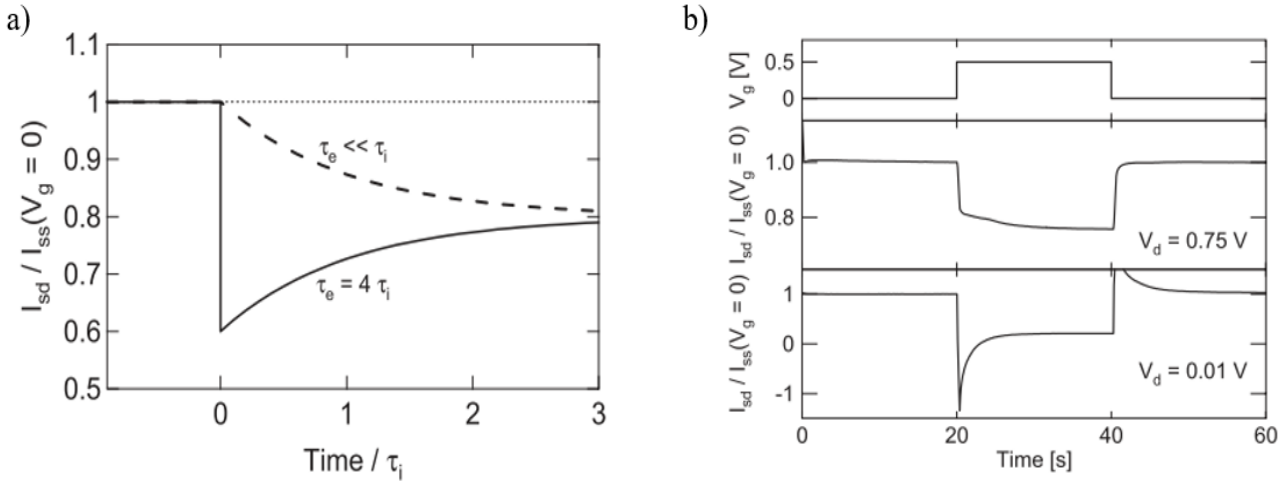

Figure 2.20: a) Modelled source-drain transient current for constant drain voltage, an arbitrary ΔI and $f = 1/2$, demonstrating the two different possible behaviours. b) Experimental source-drain transient current with constant applied gate voltage, normalized to the I_{ds} $(V_g = 0)$. Two behaviour are present upon the variation of V_d. 10mM NaCl was used as electrolyte and the film dimensions were L = 5mm and W = 6mm.[155]

This model can be modified to describe OECT as biosensor, for example introducing new elements to the ionic circuit for cell layers seeded and grown on the semiconducting channel, as will be described in the sub-paragraph 2.5.2.1.

2.5.1.4 PEDOT:PSS-based OECTs

Several semiconducting polymers have been used to fabricate OECTs: among them, some of the most important are polyaniline,[315,316] polypyrrole,[123] polycarbazole,[317] polythiophene and derivatives.[318,319] However, these materials often present limitations concerning their applications: for example, polypirrole conductivity gets irreversibily lost upon its exposure to H_2O_2, impeding its use with enzymes that produce it (such as the glucose oxidase, GOx); polyaniline loses its electrochemical activity and its analyte detection capability at pH higher than 5.[320] Part of these problems can be solved using an electrochemically active and highly stable conducting polymer, PEDOT:PSS, which has widely diffused for OECT applications.[321]

In a PEDOT:PSS-based OECT, PEDOT:PSS in its pristine state, i.e in its highly conductive (doped) state, can be used as source, drain and gate electrode material. In the film, PEDOT positive charge are compensated by the negative polyanion, PSS, thus de-doping occurs when the film is reduced: upon no applied voltage ($V_g = 0$), the transistor is in its "on" state, while the application of a positive bias on the gate, makes it switch off, as positive cations penetrate in the polymer bulk, compensating the free holes (de-doping) and reducing the total source-drain current passing through the channel.[155] The de-doping is not uniform in the semiconducting channel, as already seen in the previous sub-paragraph, with the source (grounded) being higher doped than drain, for $V_d > 0$.[321]

The reduction of the highly conductive $PEDOT^+$ (oxidized state) to the less conductive $PEDOT^0$ (neutral state) occurs throught the following reversible reaction:

$$PEDOT^+ : PSS^- + M^+ + e^- \leftrightarrow PEDOT^0 + M^+ : PSS^- \qquad (2.27)$$

where M^+ is a cation in the electrolyte solution and e^- is an electron provided by the source electrode. Cations migration inside the channel thus causes the reduction of the PEDOT state, while PSS^- ions are too large to migrate out of the polymer matrix. Once the gate bias is stopped, M^+ cations diffuse back in the electrolyte, thu restoring the original channel conductivity. The switching of PEDOT:PSS bulk conductivity (between its oxidized and neutral forms), which varies over several orders of magnitude, can be achieved with the applications of only a few volts: this is know as one of the most

important properties of the OECT, i.e. the transistor amplification (gain), that allows for high current changes in the channel upon small voltage variations at the gate electrode.[321]
Typical characteristic curves for PEDOT:PSS-based OECTs are shown in Figure 2.21a. In general, the relation between the channel current (I_{ds}) and the source-drain voltage (V_{ds}) is almost linear for low (positive or negative) source-drain voltage and all the applied V_g. The application of higher positive V_{ds} (first quadrant in Figure 2.21a) makes the current increase at higher rate, until the overoxidation of PEDOT:PSS: this is a non-reversible state of the semiconducting polymer, thus the transistor is no longer working properly. Instead, applying "higher" negative V_{ds} (third quadrant of Figure 2.21a), the current saturates, remaining constant for "increasing" (in modulus) V_{ds}. Considering the V_g, it can be noted that for no applied gate bias, the transistor is correctly in the "on" state, while upon the application of positive higher potential on the gate, the source-drain current decreases, due to two following mechanisms:[321] i) the cations migrating in the channel bulk disrupts the hole tunnelling (ion-leverage mechanism), thus increasing the mobility;[322] ii) at the same time, cations pushed inside PEDOT:PSS film cause its reduction, decreasing the hole density.[323] The combination of these two mechanisms lead to a current decrease.
PEDOT:PSS-based OECTs can have two main architectures, namely planar or vertical configuration (Figure 2.21b). The former allows for a simpler fabrication with all the device electrodes present in the same plane and electrolyte medium placed above them. Moreover, it has the advantage to have a greater exposure of the channel and more open and accessible structure. On the other hand, the vertical configuration has the gate electrode facing the channel, with the medium in between. Since the distance of gate and channel can be made very small and uniform (keeping them parallel), this configuration can be exploited to have faster response compared to the planar one. Part of the work of this thesis was the investigations of these two configurations for tissue integrity biosensing OECTs.

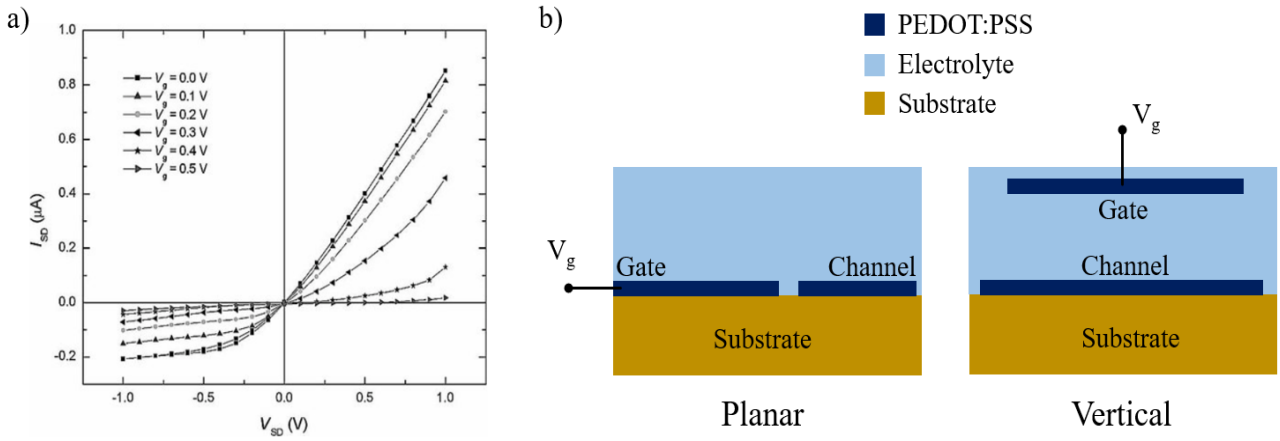

Figure 2.21: a) Source-drain current versus applied drain voltage (characteristic curves) for different potentials applied on the gate electrode. b) Schematic cross-sections of planar (on the left) and vertical (on the right) configurations.

2.5.2 *Biosensors*

PEDOT:PSS-based OECTs can be used as biosensors due to the biocompatibility of the semiconducting polymer, the capability of working in aqueous environment, the possibility to incorporate a biorecognition element into the material (such as enzimes, biomolecules, antibodies) and thanks to the inherent transistor amplification. Among the different possibilitities, in this paragraph the use of OECT to sense tissue integrity (cell health status) and as an electrochemical biosensor for reducing or oxidizing agents will be investigated.

2.5.2.1 Cell tissue monitoring

Electrochemical Impedance Spectroscopy (EIS) has been a gold-standard and wide-spread method to study cell layer adhesion and status,[324] with cells directly grown on top of the lelectrode area. EIS allows high sensitivity but often requires bulky and expensive equipment, together with the use of a reference electrode to set the potential of the solution and a counter electrode to provide the current.
Interestingly, PEDOT:PSS-based OECTs have been developed as alternative smart devices for monitoring cell layer formation[166,167,169] and disruption[325] with cells seeded directly on top of the active area of the OECT[168,326] or using transwell filters.[327–329] In particular, it was theoretically and experimentally demonstrated that the presence of a cell monolayer between the gate and the channel of the OECT slowed down the ion exchange at the electrolyte/semiconductor interface, with the works of Prof. A. Salleo's group and R. Owens' group. Noteworthy, this ion velocity reduction alters the device response, providing this way an electronic readout of the cell layer integrity and health.
Here, it will be reported the currently accepted and used model for monitoring cell tissues with OECT, that was also exploited for the measurements of this thesis, but also electrostatic interactions between cells and the active layer of the device have proved to be useful to detect cellular layer presence.[330] Faria *et al* worked on the theoretical model of the OECT,[31] using a three element circuit for a plain OECT, as shown in the Figure 2.22a: a resistor (R_d) and a capacitor (C_d), in parallel with each other, were used to represent the channel double layer capacitance and charge transfer resistance, respectively, in series with a resistance for the electrolyte solution. In order to build a tissue integrity biosensor, a cellular layer should be inserted between the channel and the gate electrode, investigating its impact, as "ion-barrier", in the OECT behaviour. In Faria's work PEDOT:PSS-based OECTs and supported lipid bilayers (SLBs) were employed, though the model results general for all organic semiconductor and biological barrier layers. To study the influence of the barrier layer on the ion flux between the electrodes, the barrier layer was modelled with a resistor and a capacitor in parallel with each other (R_{bl} and C_{bl}), in series with the circuit elements of the OECT, as seen in Figure 2.22b. For more flexibility and a wider description of the model, the barrier was set on a support substrate with hole diameter of L_{bl} and area A_{bl}, while the device active area was defined by its length L_d and area A_d. Applying a positive voltage on the gate electrode (V_{in}), cations will migrate toward the channel, but the properties of the barrier layer will influence this migration, changing the voltage at the electrolyte/channel interface, V_{ch}, considered as the effective voltage acting on the channel. Thus, the different impedance for the principal components influencing the ionic transport were determined:

$$Z_{bl} = \frac{R_{bl}}{1+s(R_{bl}C_{bl})}, \tag{2.28}$$

$$Z_s = R_s, \tag{2.29}$$

$$Z_d = \frac{R_d}{1+s(R_dC_d)}. \tag{2.30}$$

Then, V_{ch} is calculated accordingly:

$$V_{ch} = \frac{Z_d}{Z_{bl}+Z_s+Z_d} V_{in}. \tag{2.31}$$

Using an inverse Laplace transform, V_{ch} was calculated as a function of time.

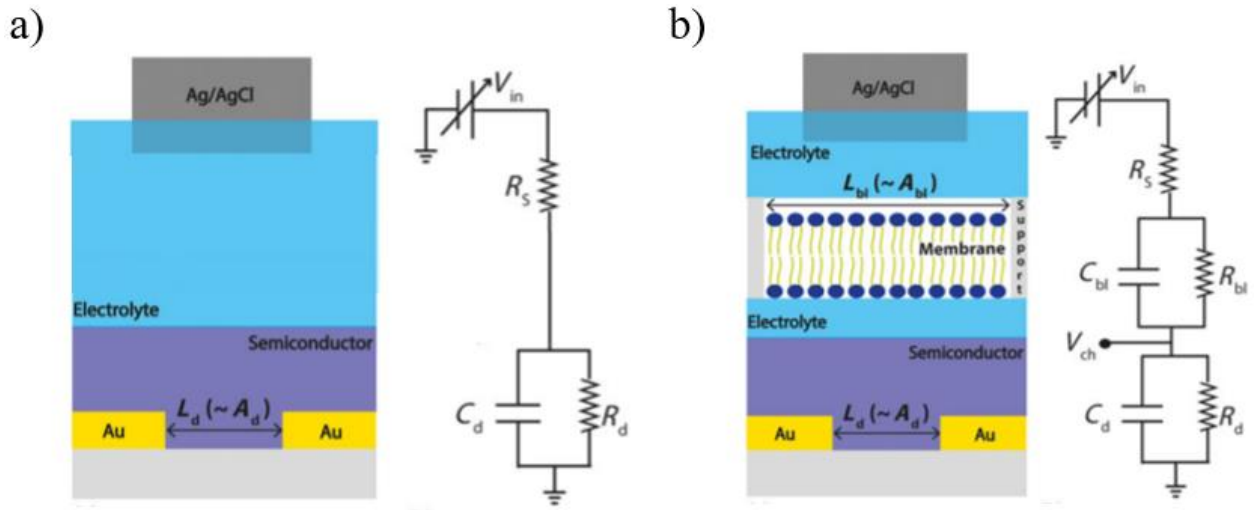

Figura 2.22: a) Schematic model of the ionic circuit for a plain OECT, with the corresponding equivalent circuit modelling the electrical response. b) Schematic model of the ionic circuit for an OECT with a cellular layer between the gate and the channel, with the corresponding equivalent circuit, modelling the electrical response.[31]

Here, we report only the study for a step voltage input for V_{in}, since it was the mechanism exploited for the sensing in this work. If we consider the application of a positive voltage pulse (V_0) of 1 V from time 0 to time t_0, cations migration towards the channel will increase V_{ch}. In Figure 2.23a, V_{ch} is plotted in function of time for several barrier-to-device area ratios and for no lipid membrane present, $V_{control}$. When no lipid membrane is present, a single exponential increase in V_{ch} is present (only one RC circuit in the equivalent circuit model), while after the addition of the membrane two different time constants are obtained. In detail, τ_{fast} and τ_{slow} represent the fast charging kinetics of the lipid membrane (dependent on C_{bl} and R_s mainly) and the slower charging of the channel (dependent on all the circuit elements), respectively. τ_{slow} characterizes the device operation affected by the presence of the lipid bilayer. As seen from Figure 2.23b, decreasing the membrane area (using a smaller support area), C_{bl} decreases, resulting in shorter charging time of the membrane. On the other hand, the reduction of the membrane area leads to higher R_{bl} and slower charging time for the OECT device, reaching a plateau for barrier-to-device area ratio below ~100:1. In this regime, the device resistance becomes the dominating factor and the lipid bilayer impedance is difficult to sense. Instead, when the area of the lipid membrane is too big, for example when the ratio is higher than 10^6:1, the time constant is close to the plain OECT one, the impedance of the membrane being too small to be detected.

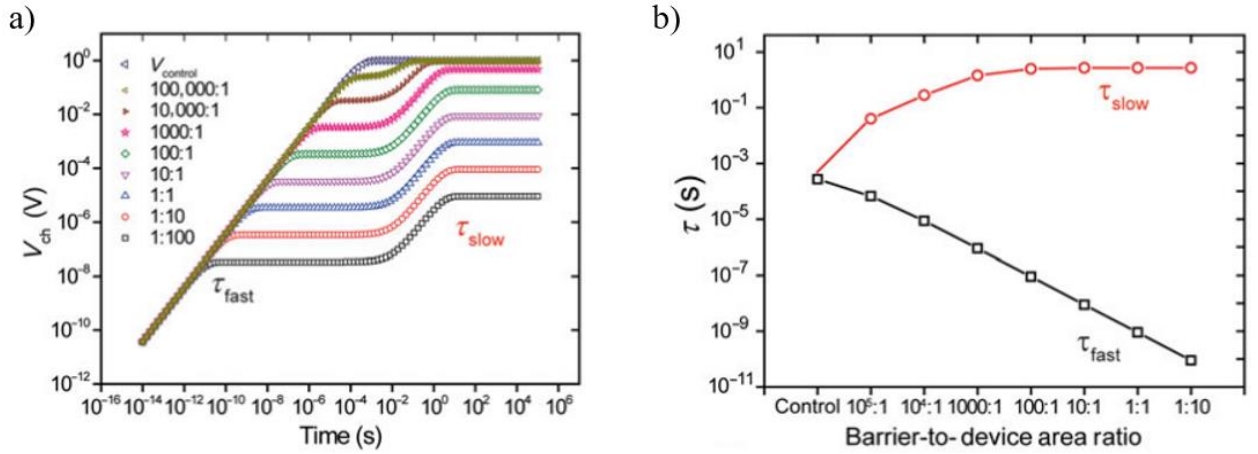

Figura 2.23: Plots of simulated (a) V_{ch} as a function of time and (b) τ_{slow} and τ_{fast} as a function of barrier-to-device area ratio, seeing the two different chargin kinetics.[31]

These final contraints can be understood focusing on Figure 2.24. In particular, Figure 2.24a shows the plots of τ_{slow} and the steady-state V_{ch} in a step voltage experiment (V_{in} = 1 V) as a function of membrane resistance for different device area, in the case of the membrane directly grown on top of the OECT channel, thus with a 1:1 membrane-to-device area ratio. A can be seen there are three distinct regimes, clearly demonstrated by the inset in the top graph of Figure 2.24a. First, below a certain threshold both τ_{slow} and V_{ch} remain constant as a function of membrane resistance, thus the device is not able to sense the membrane impedance since it is too low compared to the resistance solution. This is the *electrolyte-dominated* regime, where the membrane layer does not significantly hinder the ion flux from the electrolyte to the device. Second, above the threshold, τ_{slow} starts to increase exponentially as a function of membrane resistance, while V_{ch} remains constant. This is called *optimal operation* regime: the membrane slows down the ion flux similar to a bottleneck effect, but the total amount of ions reaching the channel does not change, thus keeping steady-state (i.e. for long times) V_{ch} constant. Third, when the membrane resistance is too high compared to R_d, it results in the *device-dominated* regime, where a plateau for τ_{slow} and an exponential decrease for V_{ch} are present, marked by the dotted line in the inset in the bottom graph of Figure 2.24a. These trends can be explained considering that ion current (directed towards the channel by the voltage on the gate) depends on R_s and R_{bl}, and the ions charge the device with a capacitance that corresponds to the bulk of the film. However, there is also a leakage current to the metal contact that depends on R_d. For too big R_s and R_{bl}, the current reaching the channel do not compensate the leakage one and the steady-state capacitance (dependent on V_{ch}) decreases while the τ_{slow} no longer increases, impeding the detection of cell layer impedance.

Is it worth noting that the two threshold points are related to the device area and, in particular, thresholds can be shifted to lower membrane resistance values, upon reducing the OECT active area dimensions. Thus, this model demonstrates that, by properly adjusting OECT area dimensions, it is possible to monitor a broad range of cell layer resistances (see Figure 2.24b), sensing from strong-barrier to leaky-barrier or non-barrier (barely forming a layer without junctions) cell lines. For istance, a device with channel area of 1 cm^2 cannot detect cells with membrane resistances lower than 10 $\Omega \cdot cm^2$, but has a good linear response between 10 $\Omega \cdot cm^2$ and 10^5 $\Omega \cdot cm^2$. For a properly patterned device, different impendaces in the optimal operation range will present different I_d curve response to the gate pulse, thus giving different time response, as reported in Figure 2.24c.

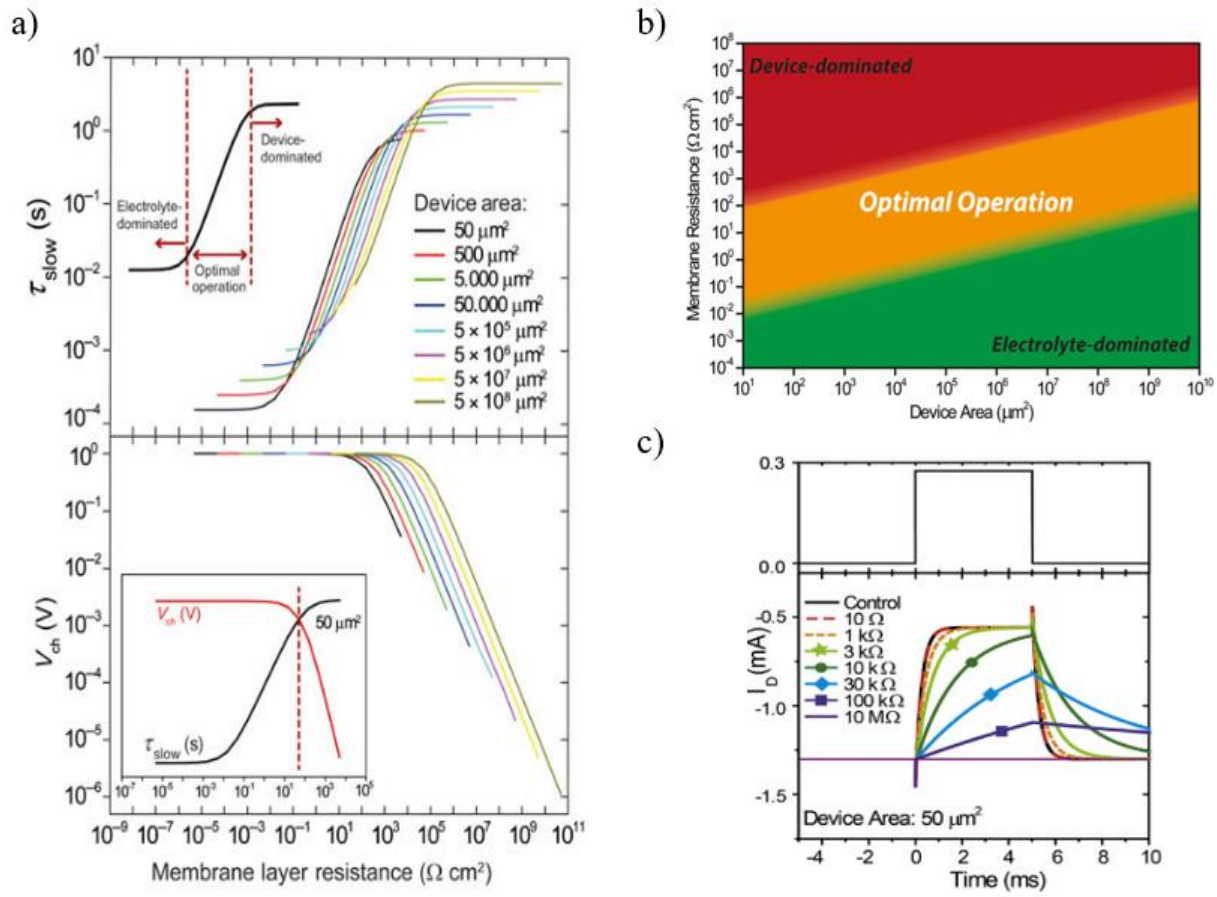

Figura 2.24: a) Plots of simulated τ_{slow} (top) and V_{ch} (bottom) responses as a function of membrane layer resistance for different device areas, considering a 1:1 membrane-to-device area ratio. The three different regime are underlined in the inset in the top graph, while the inset in the bottom one highlights the transition from the optimal to the device-dominated regime.[31] b) Simulated schematic plot of the membrane resistance as a function of device area, highlighting the three different OECT regime.[31] c) Simulated drain currents upon the application of a positive step gate voltage for OECTs containing membranes of different impedances.[331]

In order to extract τ_{slow} and use it as quantitative parameter to assess layer formation, Salleo's group modelled[331] the following bi-exponential expression:

$$I_{ds}(t) = A + B \cdot exp\left(-\frac{t}{\tau_1}\right) + C \cdot exp\left(-\frac{t}{\tau_2}\right) \quad (2.32)$$

Owens's group employed a similar bi-exponential formula for cell layer formation and disruption monitoring, using PEDOT:PSS-based planar OECTs.[167,325] In particular, they showed that their OECT was able to assess the growth of only barrier-forming cell layer, such as Caco-2 cell (human colorectal epithelial cell line, that are a typical model for barrier cellular tissue). Moreover, they demonstrated that the devices allowed for a real-time screening of the layer disruption upon the introduction of Trypsin-EDTA, a protease that is exploited to detach cells from substrates.[167]

2.5.2.2 Electrochemical sensing

OECTs have also been successfully employed for sensing several analytes, such as glucose,[332,333] ascorbic acid,[160,334] adrenaline,[164] dopamine[335], metabolites[123,336] and other molecules.[337] Indeed, the presence of reactive species inside the electrolyte solution shift its electrochemical potential and this can be detected through the shift of the gate voltage, $V_g^{eff}=V_g+V_{offset}$, where V_g^{eff} is the effective gate voltage that acts on the channel and V_{offset} is the offset voltage that depends on the analyte concentration (see Figure 2.25a).[338]

A clear example can be found in the linear dependence of the offset voltage from the logarithm of glucose concentration (in the range between 1μM to 1mM) in a PEDOT:PSS-based OECT with Pt as

gate electrode, employed as glucose sensor, shown in Figure 2.25b. The trend points out that the electrochemical potential variations follow Nerst equation, which describes the dependence of the chemnical potential on the concentration of redox species in the solution:[312]

$$E_N = E_0 + \frac{kT}{ne} \cdot ln\left(\frac{[Ox]}{[Red]}\right) \tag{2.33}$$

where *[Ox]* and *[Red]* are the concentration of oxidation and reduction species, respectively, E_0 is the formal potential, *k* the Boltzmann's constant, *T* the temperature, *e* the fundamental charge and *n* the number of electrons transferred during the reaction.[338] Notewothy, for OECT based on different semiconducting material, the Nerstian relationship may not occur due to the different properties that the solid/electrolyte interface may have.[158] In order to understand the physical meaning of the offset voltage, OECTs can be compared with standard electrochemical sensors, where the change in the potential electrode is measured relative to the reference electrode. In OECTs the gate potential is fixed, thus the potential shift described in the Nerst equation is an electrolyte potential shift, relative to that of the gate, as shown in Figure 2.25a.

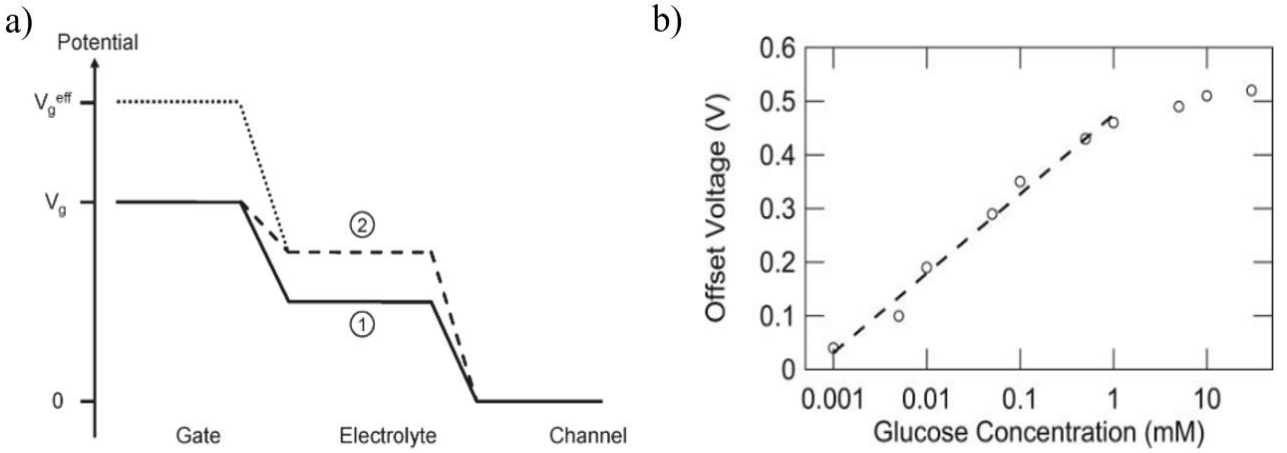

Figure 2.25: a) Potential diagram of an OECT, under the application of a potential on the gate and considering $V_d << V_g$, thus assuming the channel everywhere at the same potential. In the absence of glucose (solid line) the electrolyte potential (1) is only determined by the capacitance of the gate and the channel. After an analyte addition (dashed line), the electrolyte potential (2) is increased according to Nerst equation. The effective gate voltage (dotted line) is the gate voltage required to produce the same electrolyte potential shift but without any analyte in solution (thus in the absence of Faradaic effect). b) Dependence of the offset voltage on glucose concentration, with the dashed line fitting the data in the linear range betwen 1μM and 1mM.[338]

Starting from the absence of analyte in the solution, the electrolyte potential V_{sol} depends on the capacitances associated with the gate and the channel.[338,339] The total charge introduce in the semiconducting channel can be written as a sum of charges injected in differential volumes $dV=WTdx$ along the channel:

$$Q = \sum C_{ch}^{*} WTdx\ (V_{sol} - V(x)) \tag{2.34}$$

with C^*_{ch} being the capacitance per unit volume of the channel, $C^*_{ch}=C_{ch}/v$, *W* and *T* the width and thickness of the channel, respectively. For *dx* small enough, the equation can be approximated by:

$$Q = C_{ch}V_{sol} - C_{ch}^{*} WT \int_{x=0}^{L} V(x)dx \tag{2.35}$$

where *L* is the total length of the channel. Two capacitors in series accumulate the same charge *Q*, that can be written referring to the gate electrode interface as $Q=C_g\cdot(V_g - V_{sol})$. Thus, the potential of the solution in relation to the capacitance can be explicated as:

$$V_{sol} = V_g \frac{C_g}{C_g + C_{ch}} + \frac{C_{ch}^{*} WT}{C_g + C_{ch}} \int_{x=0}^{L} V(x)dx \tag{2.36}$$

For gate voltages small enough to avoid water hydrolysis, thus no charge transfer at the electrolyte/Pt interface (non-Faradaic regime), and assuming the channel at a zero potential ($V_d << V_g$), only the double layer formation determines the electrolyte potential:

$$V_{sol} = \frac{V_g}{1+\gamma} \tag{2.37}$$

with $\gamma = C_{ch}/C_g$.
Once a redox-active analyte is added in the solution, it starts to exchange charges with the gate electrode (Faradaic regime), shifting the electrolyte potential to a new value, related to the Nernst equation:[338]

$$V_{sol} = \frac{V_g}{1+\gamma} + \frac{kT}{ne} \cdot ln(A) + constant \tag{2.38}$$

where A is the redox-active analyte concentration and the constant contains the details of proton (taken as constant) and oxygen (at the equilibrium concentration in solution) involved in the redox reaction and the formal potential. This change is illustrated in Figure 2.25a with the dashed line. The increase in the electrolye potential is followed by a decrease in the channel current. It is thus convenient to introduce an effective gate voltage:

$$V_g^{eff} = V_g + (1+\gamma)\frac{kT}{ne} \cdot ln(A) + constant \tag{2.39}$$

So that the electrolyte potential can be expressed, in presence of a redox-active analyte, as:

$$V_{sol} = \frac{V_g^{eff}}{1+\gamma} \tag{2.40}$$

V_g^{eff} is the equivalent voltage that needs to be applied in the absence of Faradaic effects (no analyte in the solution) to have the same electrolyte shift, thus the same channel current change (dotted line in Figure 2.25a).
Comparing $V_g^{eff} = V_g + V_{offset}$ with Eq. 2.39, it is clear that:

$$V_{offset} = (1+\gamma)\frac{kT}{ne} \cdot ln(A) + constant \tag{2.41}$$

V_{offset} then describes the Faradaic contribution to the effective voltage, depending on the analyte concentration and the capacitance ratio.
In conclusion, this analysis demonstrates the variation of the OECT response once a redox-active analyte is introduced in the electrolyte solution and can be used to quantify the analyte concentration, extracting the source-drain current variation and substituting V_g with V_g^{eff}. For example, from Bernards and Malliaras model,[155] for uniform de-doping:

$$I_d = G\left(1 - \frac{V_g^{eff} - \frac{1}{2}V_d}{V_p}\right)V_d \tag{2.42}$$

while in saturation regime:

$$I_d^{sat} = -G\frac{\left(V_p - V_g^{eff}\right)^2}{2V_p} \tag{2.43}$$

where G is the conductance of the organic semiconductor film and V_p the pinch-off voltage.
Redox-active species can be divided into reducing and oxidizing agents, that are able to give or take electrons from their interaction with the electrode (in some cases the PEDOT:PSS itself). As seen from Nernst equation, their presence changes the effective voltage, thus changing the current flowing in the semiconducting channel: in particular, reducing agents impact on the device behavior reducing

the current flowing in the device channel upon increasing concetration, while oxidizing agents increase I_{ds} for increasing concentrations.

Reducing agents

In order to explain the reducing agent action on PEDOT:PSS-based organic electrochemical transistors, their application as an ascorbic acid (AA) biosensor will be explained. AA is a reducing analyte very important in many applicative context and considered a benchmark to test and compare electrochemical transduction systems.[340] In general, several reducing agents can be detected using OECTs, such as dopamine, adrenaline, uric acid and gallic acid.

Considering a transistor entirely made in PEDOT:PSS, then ascorbic acid reaction can occur at the gate or at the channel of the device, accordingly to the potential applied on the gate. For PEDOT sufficiently oxidized (thus for PEDOT in its pristine form), the following reactions occur:[160]

$$Reaction\ 1: \quad 2PEDOT^+ + AA \rightarrow 2PEDOT^0 + oxidized(AA) \qquad (2.44)$$

$$Reaction\ 2: \quad PEDOT^0 \rightarrow PEDOT^+ + e^- \qquad (2.45)$$

Thus, for positive V_g, the potential on the gate E_g is higher than that on the source electrode E_s (also with $E_d < E_g$, for $V_d < 0$), so AA oxidation occurs mainly at the gate electrode, while PEDOT:PSS de-doping takes place at the channel. On the contrary, for negative V_g, E_g is lower than that E_d and the AA mainly reacts at the channel, extracting holes with a consequent variation of its redox state and charge carrier concentration. Both cases lead to a reduction of the source-drain current, that, once stabilized, can be used as analytical signal to calibrate the sensor. For $V_g > 0$, I_d reaches a stationary state when the rate of hole extraction is equal to the rate of hole injected in the channel (by the reaction of PEDOT:PSS with some species in the solution): I_g measures these rates that must be equal to the rate of PEDOT:PSS reduction in the channel and AA oxidation at the gate at the stationary state. The same dynamic equilibrium must be reached when $V_g < 0$, wherein the number of holes extracted by AA is equal to the number of holes injected by the electronic read-out and the speed of this charge-transfer process is again measured by the gate current.[39]

Figure 2.26a reports the source-drain current over time upon incremental addition of AA in solution, for an all-PEDOT:PSS OECT with V_d = -0.3 V and V_g = -0.9 V. Since the potential of the gate can not vary, the current in the channel changes, as previously described and its variations can be correlated to the analyte concentration by means of the following equation:

$$\Delta I_d = gV_g^{eff} = g\left(1 + \frac{C_C}{C_g}\right)\frac{kT}{ne} \cdot ln\frac{[a_{AA2}]}{[a_{AA1}]} \qquad (2.46)$$

where g is the transconductance of the device, C_c and C_g the volumetric capacitance of the channel and the gate, respectively, and the AA concentration passes from a_{AA1} to a_{AA2}.

The Figure 2.26b shows I_d *vs log(*C_{AA}) plot, which can be linearly fitted to extract sensitivity, calculated as the linear slope of the fit, and limit of detection (LOD), usually calculated as three times the error of the blank measurement (LOD = 3·(intercept error)/slope) of the sensor.

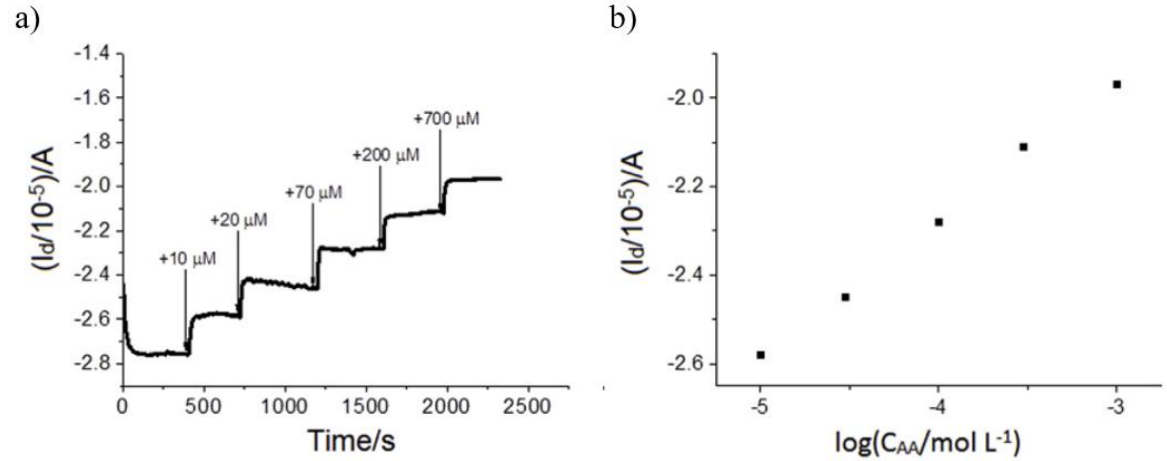

Figure 2.26: a) $I_d(t)$ curve for an all-PEDOT:PSS OECT for incremental addition of AA in the electrolyte solution (V_d = -0.3V and V_g = -0.9V). Addition are labelled with an arrow and the corresponding total molar concentration in the solution. B) I_d vs log(C_{AA}) plot.[39]

Oxidizing agents

OECTs are mainly used to detect reducing agents dedoping PEDOT:PSS channel in the transistor, leading to a source-drain current reduction. However, PEDOT:PSS-based OECT can be used also for monitoring some oxidizing species. As a matter of fact, applying a positive bias on the gate electrode to turn off the OECT and, afterwards, introducing an oxidizing agent in the solution, the reduced $PEDOT^0$ in the channel, reacting with the analyte, turns back to its conductive form, thus increasing I_d.

Oxygen is an example of oxidizing agent. Applying the Density Functional Theory (DFT), S. Singh demonstrated that PEDOT chains possess catalytic properties (thus they do not require any external dopants to facilitate oxidizing reaction, in contrast to metallic electrodes), related to the formation of polaron states that reduced HOMO-LUMO gap and thus enhanced the reactivity of the system.[341] According to this model, among the different possibilities, the energetically favourable redox reaction between oxygen and PEDOT is the following:

$$4PEDOT^0 + O_2 + 4H^+ \rightarrow 4PEDOT^+ + 4H_2O \qquad (2.47)$$

Thus, OECTs can be used as sensors of oxygen dissolved in solution, as will be shown in Section 6.1. However, at the same time, since oxygen is present at relatively high concentration in ambient condition, its contribution to OECT performances must be taken into account when other analyte are studied: indeed, oxygen can interphere with OECT performances and, in particular, it can increase the time required to reach a steady-state equilibrium, causing a drift in the source-drain current. Thus, OECT measurement to detect oxidizing agents should be carried in a nitrogen-saturated (oxygen-depleted) atmosphere.

Other oxidizing agents that can be detected, exploiting PEDOT:PSS-based OECT as sensors, are Fe^{3+} and 2,2.diphenyl-1-picrylhydrazyl (DPPH).

2.5.2.3 Influence of the geometry

In OECT, the geometrical configuration of the gate electrode relative to the channel can be tuned with small limitations, thanks to the electrochemical gating. Thus, planar device architectures can be varied easily, choosing area, shape and channel and gate relative positions.[159]

As it was seen from Eq. 2.40, the influence of an analyte on the potential offset, thus on the final source-drain current, depends on the ratio between the channel and gate capacitance, γ. The gate electrode can be either metallic or directly in PEDOT:PSS (polymeric), having a capacitance depending on the area or the volume of the material (the effective area of the double-layer scales with the volume of the PEDOT:PSS film)[342], respectively. For these reasons, the sensitivity of the device

will depend on the material chosen, the ratio of the channel to gate area,[159,339] and the thickness of the semiconductor.[160,161] For a metallic gate, the ratio γ can be controlled through channel thickness and gate area. For an all-PEDOT:PSS OECT, channel and gate volumes should be taken into account, but the issue can be simplified considering fixed channel and gate thicknesses (for example due to a spin-coating process for the device fabrication), then γ will be controlled by the ratio A_{ch}/A_g.

The sensing capability of an OECT can be assessed using the normalized current modulation, $\Delta I/I_0 = |I-I_0|/I_0$, with I being the "off" current ($V_g > 0$) and I_0 the "on" current ($V_g = 0$). Two plots of $\Delta I/I_0$ for different H_2O_2 concentrations and γ value are reported in Figure 2.27 for an OECT with the channel in PEDOT:PSS and a platinum gate, having different channel dimensions.[159] It can be seen that for low concentration a constant current modulation was measured, indipendent of the concentration variations, but different for different γ values. A second regime follows, where the current modulation is linearly proportional to the logarithm of the concentration and the sensistivity varies according to γ. Finally, a third zone is present, in which the normalized current modulation saturates, not increasing with concentration. This behaviour was demonstrated not to depend on the absolute area of the electrodes but only on their ratio (as can be seen with a comparison of Figure 2.27a and 2.27b).[159]

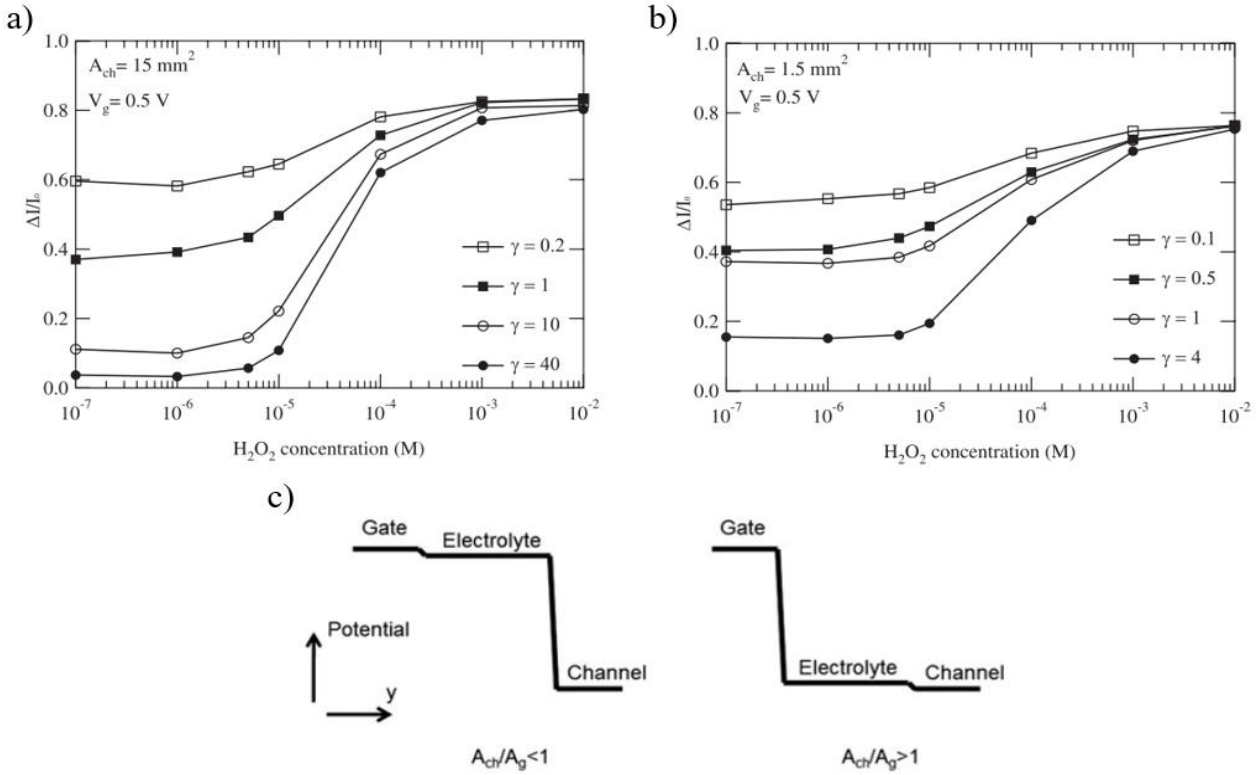

Figure 2.27: Current modulation response of organic electrochemical transistors having PEDOT:PSS channel and a Pt gate with different γ values in function of H_2O_2 concentration for V_d = 0.2V and V_g = 0.5V, with a constant channel area of A_{ch} = 15 mm$_2$ (a) and A_{ch} = 1.5 mm$_2$ (b).[159] c) Potential drop between the gate/electrolyte interface and electrolyte/channel interface for different channel/gate area ratio.[339]

Observing Figures 2.27a and 2.27b, it can be noted that: i) for low concentrations the value of $\Delta I/I_0$ decreases for increasing γ, thus small gate areas lead to small current modulations when no analytes are present; ii) the sensitivity increases with γ in the second zone, meaning that devices with small gates are more sensitive; iii) for high concentrations a saturation is reached at the same current and concentrations, independently from γ; iv) the detection range is independent from γ.

In order to explain these results, the two working regimes, Faradaic and non-Faradaic, expressed in Eq. 2.37, must be considered: in Eq. 2.37 the first term stands for the non-Faradaic capacitive gating effect, while the second is related to Nernstian charge transfer reaction. The former states that large

gate areas (small γ) lead to small potential drop at the gate/electrolyte interface, while high differences in the potential on the gate and the one in the solution occur from small gate areas (large γ), as reported in Figure 2.27c. Consequently, the current modulation, that depends on the potential drop between the channel and the electrolyte, increases for increasing gate area.
At the same time, for large gate areas the potential drop at the gate/electrode interface is small, thus analyte additions, causing V_{sol} increase, will have small effects compared to a OECT with small gate area, that favors a small V_{sol} when no analyte is present, with an higher modulation after its addition. Devices with smaller gates thus have the highest sensitivity.[159,339] At the same time, for large gate areas, analyte additions lead to an increase in V_{sol}, but with small effects compared to an OECT with small gate area, that favors a small V_{sol} when no analyte is present, with an higher modulation after its addition. Devices with smaller gates thus have the highest sensitivity.[159,339]
Finally, the last regime of saturation is almost independent from γ because the electrolyte potential is comparable to the gate one, $V_{sol} \sim V_g$, due to Faradaic contributions. The potential drop is then almost entirely at the electrolyte/channel interface and for further analyte additions, V_{sol} can not increase significantly and no changing occurs in the gating effect on the channel. This is also confirmed by the dependence of the saturation value of $\Delta I/I_0$ from the gate applied potential.[159]
In conclusion, OECTs with large γ have electrolyte potentials close to the channel one (small gate area compared to the channel one) at low analyte concentration (thus having a low background signal, i.e. a low current modulation), but adding analyte, the electrolyte potential increases as well, until it reaches the gate bias and saturation occurs. On the other hand, devices with small γ have electrolyte potential close to the gate one (large gate area compared to the channel one), so it does not increase significantly upon analyte addition.

2.5.3 *Electrodes*

2.5.3.1 PEDOT:PSS as electrodes

PEDOT:PSS has been widely employed as material coating for electrodes to reduce electrical impedance and improve charge injection capability, enhancing the surface area by introducing roughness, porosity and a volumetric dependence of the capacitance. As a matter of fact, Figures 2.28a and 2.28b report the Bode and Nyquist plot (impedance spectra) of a bare gold electrode compared to a PEDOT:PSS coated one, having the same geometric area. As can be noted from the Bode plot (Figure 2.28a), upon PEDOT:PSS coating, there is an impedance drop of one-two orders of magnitude in the impedance value, especially at lower frequencies. This is further described by the Nyquist plot (Figure 2.28b), where the imaginary and real part of PEDOT:PSS impedance are much lower compared to the Au ones: for a bare gold electrode, a stronger ion barrier at the liquid/electrolyte interface, thus a limited ion diffusion (visible from the long straight gold line in the graph), is present, while the capacitance increase after the polymer deposition improve ion diffusion in the PEDOT electrode, further demonstrated by the slope reduction of the line representing diffusion processes (visible in the inset).
To further analyze PEDOT:PSS behaviour as electrode, a PEDOT:PSS/Au electrode cyclic voltammogram (CV), recorded in nitrogen-saturated atmosphere in the potential range from -1.0V to +0.5V at different scan rate (10, 20, 100 and 200 mV/s) in 0.1M of KCl, can be studied (Figure 2.28c).[343] The CV has the typical rectangular shape in the range from -0.5V to 0.5V, which indicates the electrode capacitive nature.[344] This nature is further confirmed by dependence of the current from the scan rate. The C* reported here is 34 $F \cdot cm^{-3}$, clearly in accordance with a previous study that obtained values in the range between 39 $F \cdot cm^{-3}$ [161] to several hundreds of $F \cdot cm^{-3}$.[345] Observing the total shape of the CV curves, it can also be noted that a single anodic peak is present (at V ~ -0.7V), which is attributed to hole injection into the undoped polymer and cation expulsion. At the same

voltage, the voltammogram shows one cathodic peak on the reverse scan, that corresponds to electron injection and cations incorporation, while the negative current contribution at V ~ -0.9V is caused by the reduction of residual dioxygen.

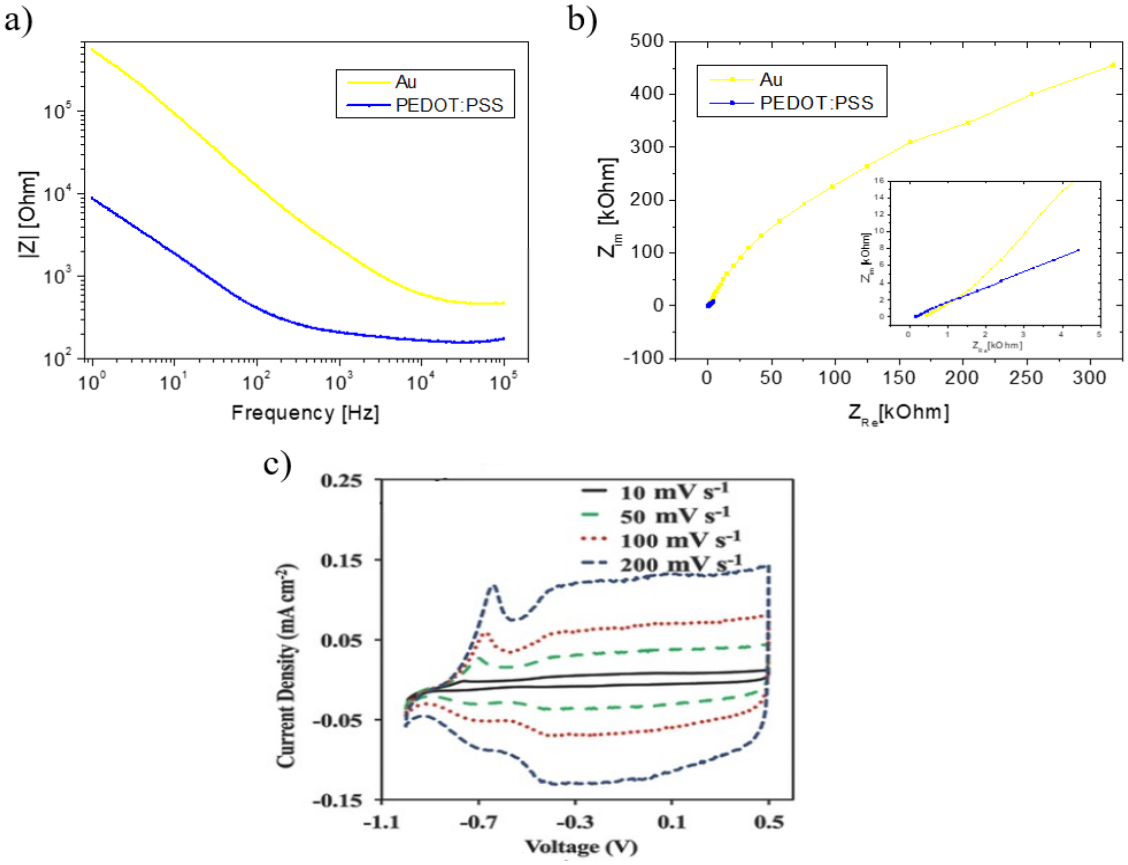

Figure 228: Electrical impedance measurements in Phosphate Buffere Saline 10X of a bare (yellow dotted line) and PEDOT:PSS coated (blue dotted line) electrode, reported in a Bode (a) and a Nyquist (b) plot. An Ag/AgCl electrode and a Pt wire were employed as reference and counter electrodes, respectively. The inset shows a zoom of the PEDOT:PSS/Au electrode Nyquist plot. c) Cyclic voltammogram of a PEDOT:PSS electrode in a 0.1 KCl solution at different scan rate, using an Ag/AgCl reference electrode.[343]

PEDOT:PSS as electrodes have been recently used for sensing and stimulation applications, including biosensors, tissue engineering, neural probes and implants, overcoming the PPy, mostly employed in early works. The main reason for that is the PEDOT superior stability,[185] that is important for biological purposes. Moreover, electropolymerization allows for a precise control of the film thickness, deciding the total amount of deposited material with a proper control of the charge/current flowing in the electrode.[187] Besides, other experimental conditions, such as the electrodeposition method used, the solvent and the use of dissolvable templates, can be tuned to modify the morphology and porosity of the films.[1] Here, a special focus on PEDOT:PSS neural interfaces/probes for sensing or stimulation of the neural system will be present.

2.5.3.2 Applications for sensing

In order to minimize brain damage in neural recordings, researchers introduced organic-based neural probes, having better compliances, smaller device footprints and reduced chronic inflammations and damagess of the surrounding tissues, compared to the standard Si shanks.[18] For example, PEDOT:PSS was electrochemically deposited onto the tips of insulated carbon fibers with diameter of 7 μm (Figure 2.29a). Their final stiffness was one order of magnitude lower than Si neural probes.[346] Immediately after the implant, these polymer-coated carbon fibers resulted in less bleeding and, after two weeks, in less astrocytes and microglia with increased healthy vasculature, around the implantation site, compared to standard Si shanks. Moreover, PEDOT:PSS coating was proved to be necessary to detect

single unity activity (i.e. the action potential of a single neuron) in rat motor cortex, as shown in Figure 2.29b, demonstrating high signal-to-noise ratio and a good stability over 5 weeks.
Improvements were developed thanks to the introduction of microfabricated, thin film neural probes in order to have conformable devices with better biocompatibility.[347,348] Conformability is very important for brain meaurements, due to the fact that the probe should be able to follow brain folds, moving and flexing with micromotions associated with body movements, blood flow and respiration. With standard lithography techniques and PEDOT:PSS spin coating, 4 μm thick flexible probes with PEDOT:PSS-coated electrodes were fabricated, together with OECT encapsulated in Parylene C (Figure 2.29c).[347]
As stated in paragraph 1.3.3, recently research developments are directed towards all-polymer, metal-free electrodes. An example exploiting PEDOT:PSS as semiconducting material is reported in the work of A. Blau *et al*.[349] They fabricated a microelectrode array using replica PDMS moldings, having the microchannels filled with PEDOT:PSS to create electrode paths. These devices were evaluated both in vitro and in vivo with several recordings of cardiac activity in embryonic mice hearts, individual action potentials of stimulated retinal explants, spontaneous activity from cortico-hippocampal cells for a period of 63 days and local field potentials on the primary visual cortex in rats with epidural and epicortical consigurations.

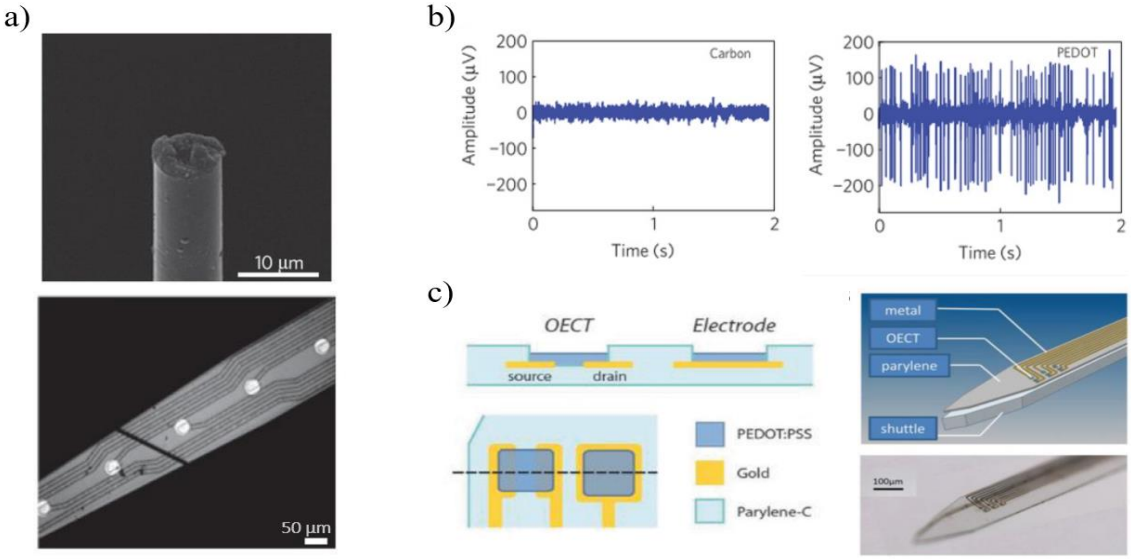

Figure 2.29: a) Scanning electron microscopy images of (top) PEDOT:PSS-coated carbon fibers for neural probe implants and (bottom) carbon fiber neural probe on top of a 10 μm silicon electrode array. PEDOT:PSS was electrochemically deposited on the exposed tip of an insulated carbon fiber.[346] b) Simultaneous neural recordings with (right) and without (left) PEDOT:PSS, with the detection of single unit activity being possible only with PEDOT:PSS coatings.[346] c) Flexible, Parylene C neural probes made of PEDOT:PSS/Au electrodes. On the left, neural probe schematic (lithographically fabricated), with recording sites that can be in electrode or OECT configuration. On the right, schematic (top) and image (bottom) of a neural probe with delaminating shuttle for brain insertion.[347]

2.5.3.3 Applications for stimulating

Even though several studies are focusing on PEDOT:PSS electrodes for recording applications, there are also works investigating their employment for stimulation, thanks to their low impedances, especially concentrating on auditory brainstem implants.[350] Indeed, patients that can not benefit of cochlear implants may try auditory brainsteem stimulation to have auditory sensations, even though this rarely leads to speech comprehension.[351] Since this is supposed to be due to the lack of specificity during stimulation, higher density arrays of smaller electrodes may overcome this limitations. Moreover, also flexibility and conformability can be improved to have brainstem implants that perfectly comfort to the implant sites.
In order to achieve these required features, Guex *et al*[350] used PEDOT:PSS coating to improve charge injection properties of bare metal electrodes and to enhance the device biocompatibility with the

flexible tissues. Pt electrodes, encapsulated in polyimide, were coated with electropolymerized PEDOT:PSS, this way increasing their charge storage capacity. The final 8 μm thick electrode showed efficient operation even under bending conditions, that were imposed by the implant site (bending of radius of 1.65mm, as seen in Figure 2.30a). Indeed, there was no difference in the impedance at 1 kHz up to a bending ratio of 2 mm (Figure 2.30b), nor any crack or delamination were seen under optical inspection before and after bending (Figure 2.30c). *In vivo*, they delivered enough current to stimulate auditory brainstem responses in rats, clearly visible in Figure 2.30d.

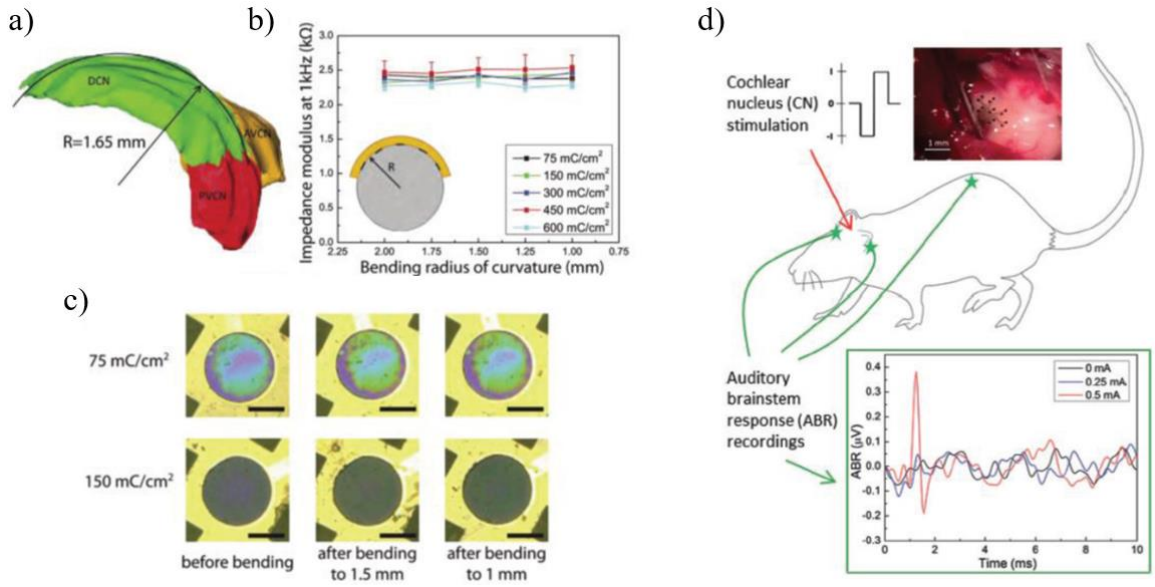

Figure 2.30: PEDOT:PSS-coated Pt electrodes on flexible polyimide used for auditory brainstem stimulation. a) a three-dimensional model of the implantation site. b) Electrode impedance measurements, showing that its value at 1kHz does not change up to a bending radius of 2 mm. c) Electrode optical images before and after bending, that show no cracks or delamination of the polymer. Scale bars: 50mm. d) Cochlear nucleus successfully stimulated by the electrode, as seen from the auditory brainstem response recorded.[350]

Chapter 3

Materials and Methods

In this Chapter, the details of the materials used, together with the experimental techniques employed for device fabrication and characterization, are presented and explained. In the first section are reported the PEDOT:PSS deposition and characterization techniques, while Section 2 and 3 discuss their use for the fabrication of OECTs as sensors and electrodes for neural implants, respectively. Section 4 and 5 regard the biological *in vitro* and *in vivo* measurements, respectively. Finally, the last Section explains the technique employed for the layer functionalization characterization.

3.1 PEDOT:PSS : deposition and characterization

PEDOT:PSS has been used as the semiconducting polymer in this thesis work, through two principal deposition techniques (namely, spin coating and electrochemical deposition) that are properly described in the next paragraph. Noteworthy, polyethylene glycol (PEG) has been added to PEDOT:PSS only for the latter deposition method, in order to achieve a softer and more stretchable material, as will be shown in Section 5.1. Here, the main techniques used to deposit and characterize the two materials are reported.

3.1.1 Deposition techniques

According to the final purpose/application, different PEDOT:PSS formulations have been deposited through spin coating to realize thin polymeric films, representing channels or gates of OECT devices. The PEDOT:PSS dispersion Clevios (Heraeus, PH1000) was mixed with ethylene glycol (EG) (Sigma Aldrich) and 4-dodecylbenzenesulfonic acid (DBSA) to improve the final semiconducting film conductivity and its adhesion on the glass substrates (or gold contacts), respectively. Moreover, 3-glycidoxypropyltriimethoxysilane (GOPS) was added in the solution as cross-linking agent aiming to improve film resistance to delamination in aqueous environment.[352] The concentration percentages for the final mixture is reported in Section 3.2 and, as already stated, differ from the selected OECT application. The realized suspensions were sonicated for 10 minutes and then filtered using 1.2 μm cellulose acetate filters (Sartorius) before the spin coating on oxygen plasma (100 Watt for 5 min) cleaned glass substrates (having the gold patterned on top for the contacts), with time and velocity selected, accordingly to the required thicknesses. A schematic of the spin coating process is reported in Figure 3.1a. Samples were then annealed at 120°C for 1h hour to remove water and solvents and to enhance the conductivity due a reorganization process that occurs upon thermal treatment.
The second deposition technique employed in PEDOT:PSS film formation is the electrochemical deposition, which allows a precise control over the quantity of the deposited material and provides an easy way to functionalize the samples.[270] The limitation of this procedure is the need of an electrically conductive substrate on which the film is formed: for this reason, gold wires or thermally evaporated gold stripes on glass/PDMS substrates were used.
A 25 ml, deaerated, nitrogen saturated solution of 10 mM EDOT monomer and 0.1 mM PSS (and 5mM PEG for PEDOT:PSS:PEG deposition) in water was used for the electrodeposition (schematic in Figure 3.1b) in a three electrode electrochemical cell, equipped with a saturated calomel electrode (SCE) as reference electrode (RE), a Pt wire as counter electrode (CE) and the chosen conductive substrate acting as working electrode (WE). The inert atmosphere enables the reduction of oxygen related termination of the polymer chains that otherwise lead to shorted PEDOT chains, easier to be

subjected to delamination. The depositions were realized with two different procedures: the first employed a cyclic voltammetry (CV), with E_{low} = −0.01 V, E_{high} = +1.2 V, scan rate = 0.1 V/s, for 8 deposition cycles and was used with the gold wire as substrates, aiming at the realization of the gate for the OECT vertical configuration (see paragraph 3.2.1 and 4.3.1); on the other hand, the second method uses a potentiometric control, applying a constant potential of E = 1.2 V while counting the total amount of the polymer deposited, thus the polymer thickness. This fabrication process was employed for the realization of the stretchable microelectrodes, thus paragraph 3.3.1 and Section 5.2 will present further details. Even though electrochemical deposition is already a viable technique to control polymeric layer thickness and amount deposition (tuning the deposition cycles), this improvement leads to a better control on the nanometric scale. Both methods were realized under a constant magnetic stirrer to avoid mass diffusion limit in the region, close to the WE, depleted of EDOT monomer due to the film formation.

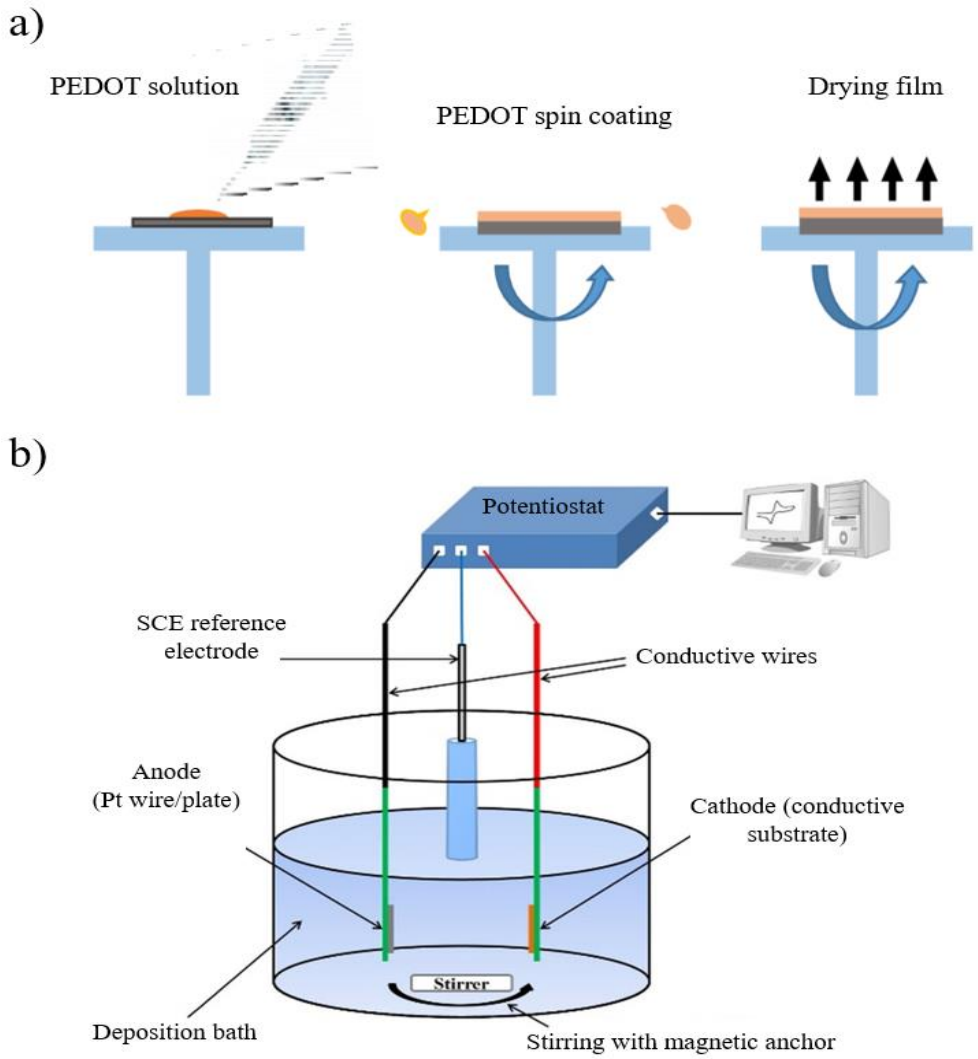

Figure 3.123: a) Schematic representation of spin coating steps: the PEDOT solution is drop casted on the glass substrate; then, spin coating rotation spreads the solution onto the whole substrate, getting rid of the excess solution, while the evaporation of the solvents leads to the final film formation. b) Electrochemical deposition method using an electrochemical cell with three electrodes, namely a saturated calomel electrode (SCE) as reference electrode (RE), a Pt wire as counter electrode (CE) and a conductive substrate as working electrode (WE). The stirrer is constantly used to have a uniform solution and avoid depleted region during deposition.

3.1.2 Electrochemical characterization

Electrochemical characterizations of PEDOT:PSS enable to achieve information on the kinetics and charge transport involved in electrochemical reactions and doping mechanism, together with the electrode/electrolyte interfacial properties. Our measurements were carried out using CV (mainly

exploited for polymeric electrochemical deposition, rather than a characterization technique) and electrical impedance spectroscopy (EIS). Both employed an electrochemical cell with three electrodes, namely a WE, a RE and a CE, dipped in an electrolyte solution to electrically connect them. Our samples were placed as working electrode and their potential was measured with respect to the RE, represented either by a saturated calomel electrode (SCE) or by a silver/silver chloride (Ag/AgCl) one. The counter electrode is used to generate a current, flowing between WE and CE, that keeps the working electrode at the selected potential.

Cyclic Voltammetry (CV)

In a cyclic voltammetry, the electrochemical potential of the samples is swept linearly (as shown in Figure 3.2a) over time at a fixed scan rate $v=dE/dt$ up to the switching potential, E_λ, reached a time $t = \lambda$, then the scan rate is switched and the electrochemical potential is brought back to its initial value, E_i. The potential during each cycle can be mathematically represented by the following:

$$E = E_i - vt \qquad (o < y \leq \lambda) \tag{3.48}$$

$$E = E_i - 2\lambda t + vt \quad (t > \lambda) \tag{3.49}$$

This sweep reversal method is very powerful and useful, and it is widely practiced as an electrochemical method.[312]

In CV experiments the shape of the resulting curve (I-t, but more commonly I-E, as reported in Figure 3.2b) represents the superposition of a capacitive current and a Faradaic one. The former is related to the charging of the electrical double layer at the electrode/electrolyte interface, while the latter comes from the mass transfer due to the eventual electrochemical reaction $O + ne \leftrightarrow R$ at the electrode. The charging current during a potential sweep can thus be written as:[312]

$$I_c = vC_d \left[1 - exp\left(-\frac{t}{R_s C_d}\right)\right] \tag{3.50}$$

with R_s being the electrical resistance of the solution and C_d the double layer capacitance. This time-dependent current saturates when $t >> R_sC_d$, having a steady-state current of $I_{c,ss} = vC_d$. If the sweep has a triangular shape (not just a linear one), then the steady-state current changes from vC_d during the forward scan (the potential E is increasing) to $-vC_d$, during the reverse scan (decreasing E), due to the change of sign of the scan rate dE/dt.

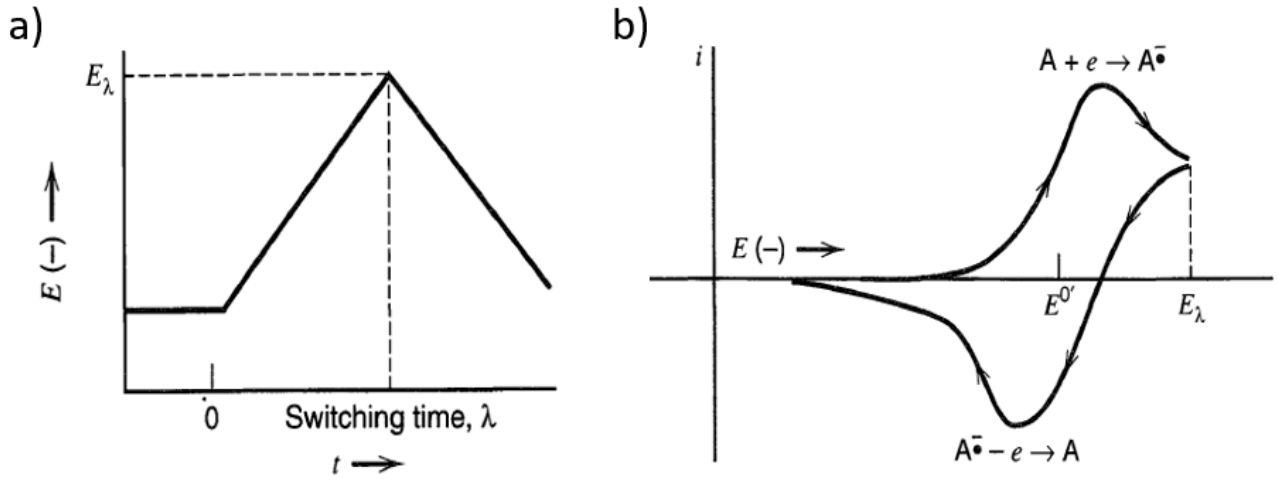

Figure 3.2: a) Cyclic potential sweep (triangular shape); b) Resulting cyclic voltammogram, I-E.[312]

The Faradaic depends on two laws, namely the Fick's law of diffusion for the planar electrode (Eq. 3.4) and the Nernst equation (Eq. 3.5):

$$\frac{d[O]}{dt} = D\frac{d^2[O]}{dx^2} \tag{3.51}$$

$$\frac{[O]_{x=0}}{[R]_{x=0}} = exp\left[\frac{nF}{RT}(E(t) - E_0)\right] \tag{3.52}$$

Fick's law governs the mass transport process towards the electrode, where *D* is the diffusion coefficient and *x* is the parameter denoting the distance from the electrode surface. On the other hand, Nernst equation is related to the surface concentration of oxidized and reduced forms of the redox agents as a function of *E(t)* and E_o, that are the applied and formal potentials, respectively.[353] In Eq 3.5, *t* is the time, *n* the number or electrons transferred per molecule of *O* reacting at the surface of the electrode, *F* the Faraday constant, *R* the constant for ideal gas and *T* the absolute temperature.
For a reversible, diffusion-controlled process, where the reaction rate is limited by the transport rate of the reactants to the electrode surface,[312] the current response at each potential may be calculated for a reversible cyclic voltammogram, with $E(t)=E_i - \nu t$,[353] using a mathematical procedure called semi-integration ($d^{1/2}y/d^{1/2}x$) or convolution[354]:

$$I(t) = -nFA[O]_{bulk}\sqrt{D}\frac{d^{1/2}}{dt^{1/2}}\left(\frac{1}{1+e^{\frac{nF}{RT}(E_i-\nu t-E_0)}}\right) \tag{3. 53}$$

where *A* is the area of the electrode.
To verify the hypothesis of the diffusion-controlled process the Randles-Ševčik equation can be used, expressed as:

$$I_p = 0.446nFA[O]_{bulk}\sqrt{\frac{nF\nu D}{RT}}. \tag{3.54}$$

Electrochemical Impedance Spectroscopy (EIS)
Impedance spectroscopy is a very powerful technique to analyse the complex electrical resistance of a system and results sensitive to the surface phenomena and changes in the bulk properties of the electrode under study.
The impedance of a system is generally investigated applying a voltage perturbation with small amplitude and measuring the consequent current response. From this analysis, the impedance *Z* can be expressed as the ratio between the time-dependent voltage *V(t)* and the time-dependent current *I(t)*:[324]

$$Z = \frac{V(t)}{I(t)} = \frac{V_0\,sin(2\pi ft)}{I_0\,sin(2\pi ft+\varphi)} = \frac{1}{Y} \tag{3. 55}$$

where V_0 and I_0 are the maximum voltage and current signals, *f* is the frequency, *t* the time, φ the phase shift between the voltage and the current functions and *Y* is the admittance (complex conductance). Since the current can differ in terms of amplitude and phase shift, the impedance is a complex value, that can be described either by modulus $|Z|$ and phase shift φ, or by the real Z_R and imaginary Z_I part of the impedance, as illustrated in Figure 3.3a. Thus, impedance measurements can be reported using two different graphs, namely a Bode plot which shows $log|Z|$ and φ as a function of *log(f)*, or a Nyquist plot reporting Z_I as a function of Z_R. The name "spectroscopy" underline that the impedance is often determined at different frequencies and the resulting spectrum is then analysed through an equivalent circuit (commonly made of resistances, capacitances), representing the physicochemical properties of the investigated system.[355,356] An example of the two plots is reported in Figure 3.3b for a simple gold electrode.

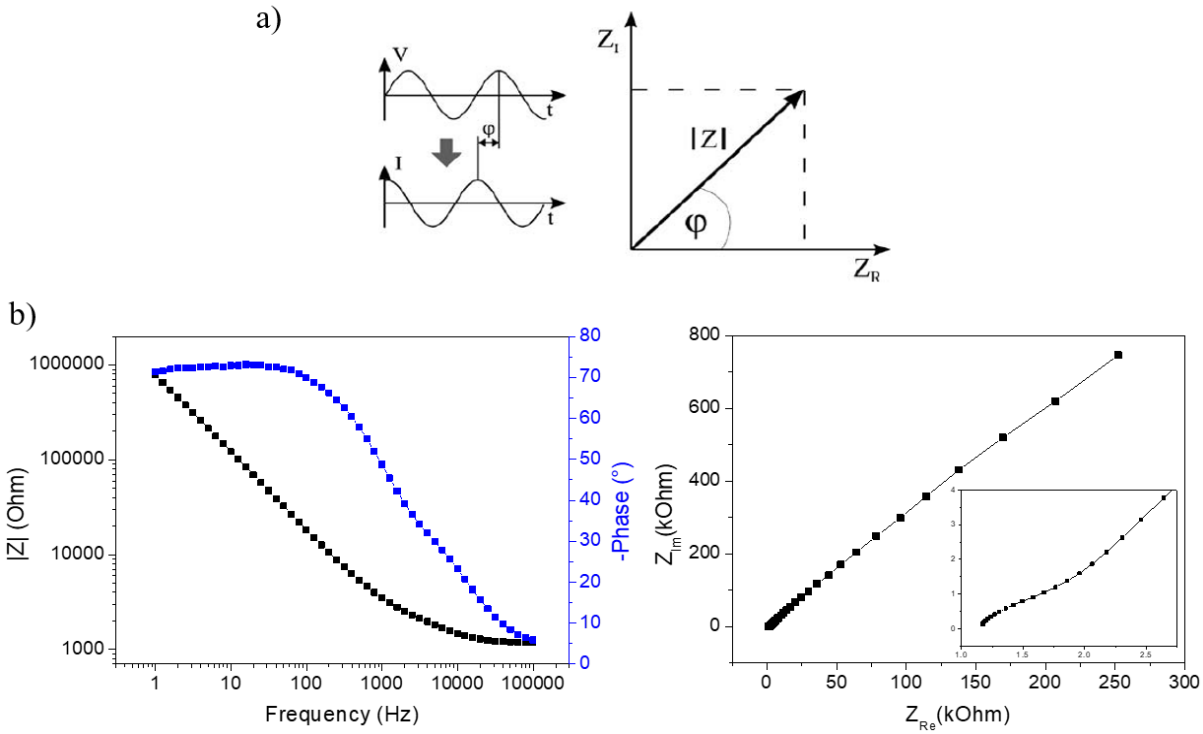

Figure 3.324: a) Impedance as a complex value, that is defined by the ratio between the time-dependent voltage and the time-dependent current. It can be expressed with the modulus |Z| and phase shift φ, or by the real Z_R and imaginary Z_I part of the impedance.[324] b) Bode plot (on the left) and Nyquist plot (on the right), representing two alternative graphs to plot impedance versus frequency analysis. The inset in the Nyquist plot reports a zoom of the graph to show the high frequency impedance points.

In electrochemical impedance spectroscopy, where the electrolyte solution is part of the system under study, four elements are usually employed to describe the impedance equivalent circuit: ohmic resistance (*R*), capacitance (*C*), constant-phase element (*CPE*) and Warburg impedance (*W*). These elements are summarised in Table 3.1 and are used to develop equivalent circuits able to correctly approximate the experimental results.

Table 3.1: Most diffused elements to describe the impedance equivalent circuit.

Impedance Elements	Definition/Formula	Phase angle	Frequency dependence
R	$= R$	0°	No
C	$Z_C = \frac{1}{j\omega C}$	90°	Yes
CPE	$Z_{CPE} = \frac{1}{A(j\omega)^{\propto}}$	0-90°	Yes
W	$Z_W = \frac{\sigma}{\sqrt{w}}(1-j)$ $\sigma = \frac{RT}{n^2F^2\sqrt{2}}\left(\frac{1}{c_O\sqrt{D_O}} + \frac{1}{c_R\sqrt{D_R}}\right)$	45°	Yes

Many systems have been described using these four elements, but here the standard one employed for a typical electrode in contact with an electrolyte will be reported: the Randles circuit (Figure 3.4a), comprising the solution resistance R_s, the charge transfer resistance R_{ct}, the double layer capacitance C_{dl} and the Warburg impedance *W*. The Nyquist plot, reported in Figure 3.4b, explains how the

parameters can be extracted from the graph of the Randles circuit: R_s and R_{ct}, can be easily determined (the real impedance values at the edges of the ideal semicircle); the double layer capacitance can be calculated, according to the following formula $\omega=2\pi f=1/R_{ct}C_{dl}$, using the frequency at the maximum of the semicircle; Warburg impedance can be calculated from the extracted intercept of the straight, 45° line, whose value is $R_s+R_{ct}-2\sigma C_{dl}$. In particular, this line indicates the Warburg-limited behaviour and is representative of a mass transfer controlled process, limited by diffusion. On the other hand, the high frequency regime (left part of the graph) is a region of kinetic control, regulated by R_{ct} and C_{dl}, whose product is the time constant τ of the electrochemical process.[312,324] For analytical applications, however, the equivalent circuit is often used in a simplified way, avoiding the introduction of the Warburg impedance.
Electrical Impedance Spectroscopy was mainly used to characterize the electrode interface with saline solution, checking its features before and after the polymer coatings and their electrochemical properties in time and under strain.

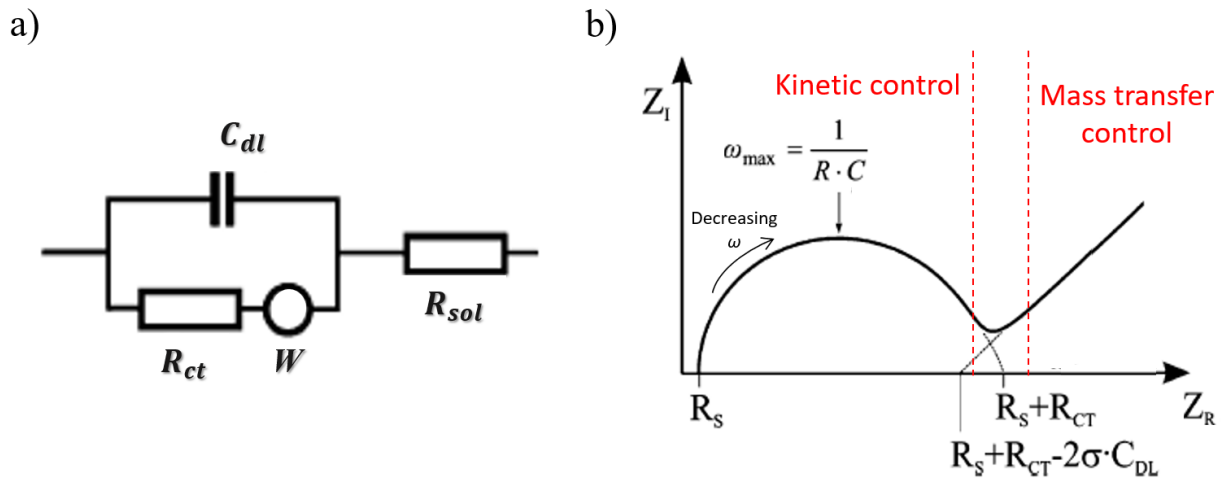

Figure 3.25: a) Randles equivalent circuit model for an electrode in contact with an electrolyte. b) Impedances spectra schematic for a typical Randles circuit: the double-layer capacitance C_{dl} derives from charge stored in the double layer formed at the interface; charge transfer resistance R_{ct} results from the current flow produced by redox reactions at the electrode interface; Warburg impedance W is due to the impedance of the current resulting from the diffusion from the bulk solution to the interface; finally, R_s is the solution resistance. The red dashed line separate two different region where the process (thus the impedance) is controlled by the kinetic of the reaction (high frequencies, on the left) or by the mass transfer diffusion (low frequencies, on the right).[324]

3.1.3 Atomic Force Microscopy (AFM) characterization

One of the most suitable methods to investigate morphology, electric, magnetic or other surface characteristics at the micro- and nano-scale is the Scanning Probe Microscopy (SPM). The instrument uses specially prepared tips in the form of needles as probes, with the working part (apex) usually of the size of ten nanometer or lower, mounted on a flexible supporting cantilever. One side of the cantilever is fixed to a support, while the other edge, where the tip is located, is free to move and is approached to the sample down to tip-surface distances of 0.1-10 nm, according to the technique used for the measurement. When the tip approaches the sample, several interactions between the tip and the substrate can be studied in order to get information on the sample surface features. Let the interaction be van der Waals forces between the two elements, as in the case of our morphology analysis, and the technique is thus referred as Atomic Force Microscopy (AFM); then, the tip will induce a deflection of the cantilever. A schematic of the experimental technique, its working principle and data trace obtained are represented in Figure 3.5. Since the dimension of the edge of the tip is close to atomic dimension (nanometric size or even lower, as shown in Figure 3.6a), the van der Waals energy of two atoms can be used to approximate the potential energy of the tip, as plotted in Figure 3.6b and approximated by the following:

$$U_{LD}(r) = U_0\left\{-2\left(\frac{r_0}{r}\right)^6 + \left(\frac{r_0}{r}\right)^{12}\right\} \quad (3.56)$$

where r_0 is the equilibrium distance between the atoms.

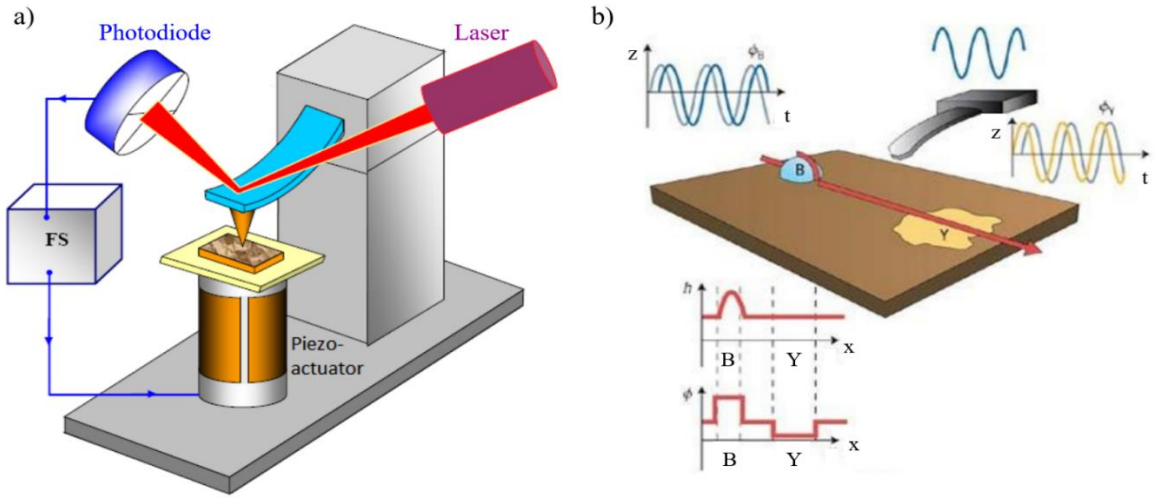

Figure 3.26: a) Schematic of an AFM. A laser shine on the cantilever head and the reflected beam is collected by a photodiode, thus obtaining the bending of the cantilever due to atomic forces. The feedback mechanism (FS) is used to control the tip-surface distance, through the piezoelectric actuator under the sample holder, according to the deflection of the cantilever.[357] b) Scheme of the AFM operation, with the cantilever oscillation depending on the topography and its surface composition. The height and the phase images are registered, with phase-shift signal changing with dissipated energy variations on the sample surface.[358]

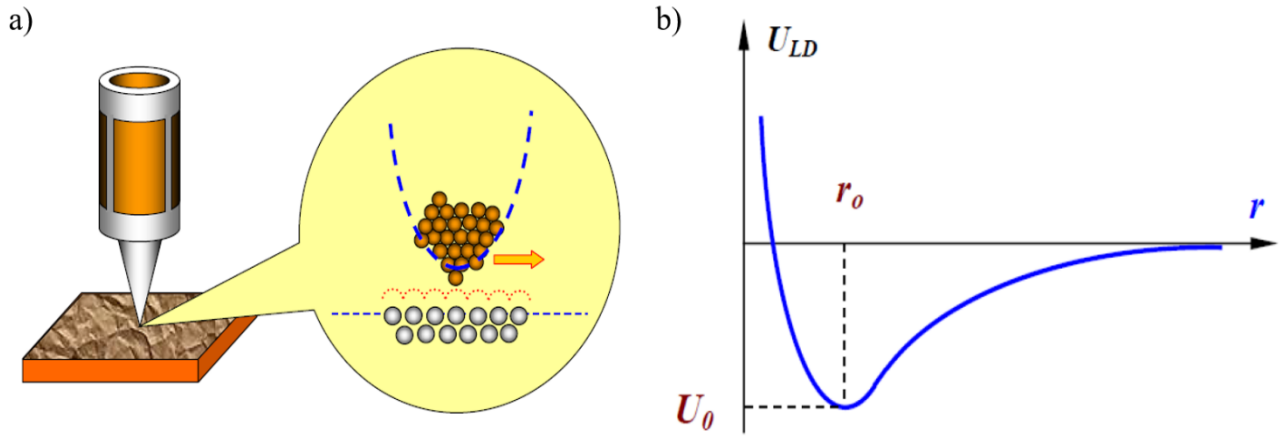

Figure 3.27: a) Atomic resolution with the AFM: the tip edge dimensions allow for an atom-atom interaction with the sample surface.[357] b) Qualitative form of the Lennard-Jones potential.[357]

To detect the cantilever slight deflections, a laser beam, focused on its back and reflected, is acquired by a photodiode divided in four sectors: from the measurements of the relative intensity variations on the different sections, the amount of vertical and lateral deflection of the cantilever are extracted.

3.1.3.1 Surface morphology

Imaging of morphological surfaces were carried out with Park NX10 AFM system, operating in non-contact mode in air or PBS 1X (measurements performed in liquid allowed us to mimic biological environment), with the tip oscillating close to its resonance frequency, ω_0. The height of the samples surface is then described by the equation:[357]

$$z(t) = z_0 + A_0 cos(\omega t - \varphi) \quad (3.57)$$

where z_0 is the mean height of the cantilever, A_0 is the amplitude of the free oscillation, ω is the oscillation frequency and φ is the phase constant that is set to 90° for the free oscillating tip. The non-

contact mode is obtained when the tip is far enough from the surface of the sample and stay in the attractive regime of the Lennard-Jones potential, thus where $F = dU/dz > 0$) for the whole amplitude of the oscillation. When the tip is closer to the sample, the oscillation amplitude decreases to $A(z)$, with $A(z) < A_0$. This value is employed as set-point to control the height of the tip, using a feedback system that gave the height of the sample surface.
For data analysis the height-height correlation function (HHCF) was used in order to extract surface roughness and correlation length. For a randomly rough surface with a Gaussian correlation function (used in this work), the height-height correlation function can be written as:[359]

$$HHCF = 2S^2\left[1 - exp\left(-\frac{d^2}{T^2}\right)\right] \quad (3.\ 58\ )$$

where S is the surface roughness (root mean square deviation of the height), d the distance between height points and T denote the autocorrelation length. These parameters were used to compare PEDOT:PSS and PEDOT:PSS:PEG film electrodeposited on gold.

3.1.3.2 Surface conductivity

Conductive Atomic Force Microscopy (C-AFM) was invented in 1993 by M. P. Murrell and co-authors at the University of Cambridge and it is an AFM technique able to record also the current flowing between the tip/sample nanojunction, simultaneously to the topography.

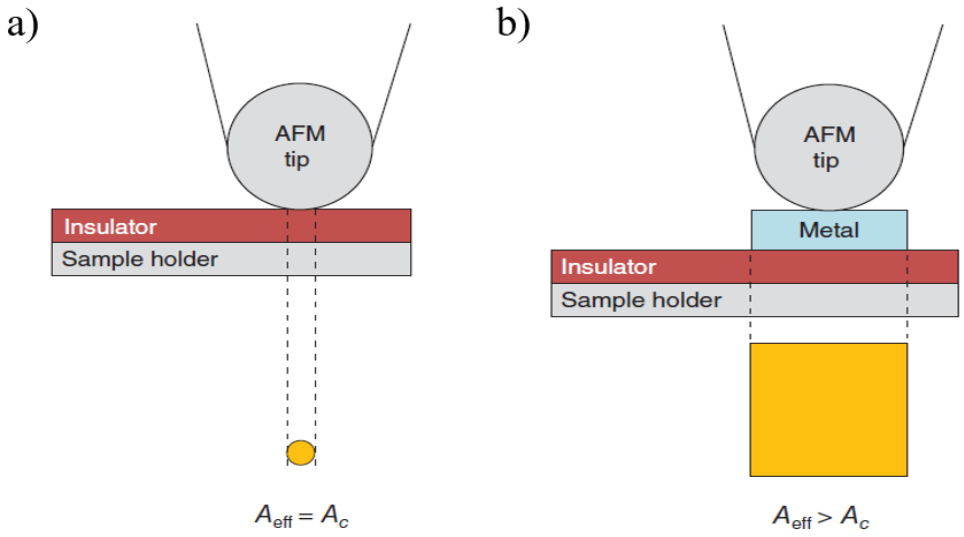

Figure 3.28: Schematic of the emission area (A_{eff}) in C-AFM when the tip is on an (a) insulating sample and a (b) metallic electrode deposited on an insulating substrate, that is not always equal to the contact area between the tip and the sample.[360]

C-AFM structure is similar to standard AFM, save three main differences: i) the tip probe must be conductive; ii) since a potential needs to be applied between the tip and the sample, a voltage source is present; iii) a preamplifier is introduced with the aim to convert the analogical current signal into a digital voltages, read by the computer.[360] Moreover, in C-AFM experiments the sample is often fixed to the holder with conductive tape or paste, in order to have a net current flowing from tip to sample once the potential difference is imposed. Therefore, the local electrical properties of the sample surface can be studied with nanometric resolution.[360] The current that is collected by C-AFM is the product of the current density J and the effective emission area through which electrons flow A_{eff} (effective area), i.e. $I = J \cdot A_{eff}$. J value depends on conductivities of the tip and sample and on the voltage applied between them, being affected by inhomogeneities in the sample, like local defects, thickness fluctuations and doping. The lateral resolution is defined by A_{eff}, that can range from tenths of square nanometers to thousands of square micrometers depending on the conductivity of the

sample, the tip/sample contact force, the relative humidity of the atmosphere, the geometry of the tip and other experimental factors.
An important feature that has to be taken into account for C-AFM is that effective emission area, A_{eff}, not always equals physical contact area, A_c, because in many tip/sample system the electrical field can propagate even laterally in the sample, as can be seen in Figure 3.7. This event happens for example when the tip goes on a conductive metallic electrode (that is part of the sample), where A_{eff} is the entire area covered by the electrode due to the high lateral conductivity.[361,362] The effective area can indeed be defined as the sum of all infinitesimal spatial locations on the sample surface that are electrically connected to the C-AFM tip, thus having negligible potential differences.
This technique was applied to study pristine and (3-Aminopropyl)triethoxysilane (APTES)-functionalized PEDOT:PSS films to investigate their surface conductivity differences, using a conductive MLCT tip.

3.1.3.3 Indentation

AFM has also been used to obtain information on the mechanical properties of thin film for neural interface application, such as Young's modulus.
For a system with only one degree of freedom, the stiffness can be defined as $k = F/\delta$, with F being the force applied and δ the displacement caused by the force along the same degree of freedom. Instead, Young's modulus (or elastic modulus) is the ratio of the tensile stress $\sigma(\varepsilon)$ under an applied strain ε in the elastic regime of the stress-strain curve:

$$E(\varepsilon) = \frac{\sigma(\varepsilon)}{\varepsilon} = \frac{{}^{F}/_{A_0}}{{}^{\Delta L}/_{L_0}} = \frac{FL_0}{A_0 \Delta L} \tag{3. 59}$$

where A_0 is the cross-section area through which the force is applied, ΔL is the change in the length of the object and L_0 its original length. While the stiffness is a property depending on the material and geometrical structure of the sample, the Young's modulus is an intensive property of the material. However, these two properties are related and for an element in tension or compression, the axial stiffness results $k = AE/L$.
Acquiring the force-distance curve during an indentation experiment using AFM, the stiffness and Young's modulus of a selected sample can be extracted, employing a tip with a defined force constant k. Measuring the deflection δ of the tip, the Force is calculated using Hooke's law $F = k\,\delta$. Moreover, the displacement z of the z-scanner of the AFM, that is the variation of the tip height caused by the AFM indentation, is related to the indentation length d through $d = z - \delta$. Thus, the stiffness results as $k = F/d$, as previously defined. Hertzian model is then one of the most employed theory to extract the Young's modulus values and, for a paraboloid shape tip, force relation to Young's modulus can be written as:[359]

$$F = \frac{4}{3} E \sqrt{R\delta^3} \tag{3. 60}$$

where R is the radius of the paraboloid tip.
The Young's modulus of PDMS layers, uncoated or coated with Au, Au/PEDOT:PSS, Au/PEDOT:PSS:PEG was measured in PBS 1X in order to test the micromechanical properties of electrodes as experienced by the neural tissue. Indeed, the micromechanical investigation, together with the liquid environment, allowed the mimicking of the micro-scale of the implant and the biological environment, respectively. Force distance curves were measured with the PARK NX10 AFM using a NSC36_B (k = 2 nN/nm).
3.1.4 Vibrational states with Fourier Transform Infrared (FTIR) Spectroscopy

Fourier Transform Infrared (FTIR) Spectroscopy is a technique employed to obtain an infrared spectrum of absorption or emission of a solid, liquid or gas substance and is based on the idea of the interference of radiation between two beams (interferogram).[363] The interferogram is a signal produced by the change of pathlength of the two beams with the domains of distance and frequency being interconvertible using the following Fourier transformation analysis.

The basic setup of the FTIR spectrometer is shown in Figure 3.8a: the radiation is emitted from a source and passes through an interferometer to the sample and then reaches the detector. After the amplification of the signal and the elimination of high frequency contributions (filtered), the data are collected for a subsequent Fourier transformation:[363]

$$I(\delta) = \int_0^{+\infty} B(\bar{\nu})\, cos(2\pi\bar{\nu}\delta) d\bar{\nu} \tag{3.61}$$

$$B(\bar{\nu}) = \int_0^{+\infty} I(\delta)\, cos(2\pi\bar{\nu}\delta) d\delta \tag{3.62}$$

These equations relate the intensity falling on the detector as a function of difference in pathlength, $I(\delta)$, to the spectral power density at a certain wavenumber, $\bar{\upsilon}$, given by $B(\bar{\upsilon})$ and vice versa.

The basic experiment to obtain FTIR spectrum consists in an interferogram production with and without a sample on the beam, then transforming the interferogram into the spectra for the source with the sample absorption and another one for the source without sample absorptions. Then, the ratio of the former and the latter results in a double-beam dispersive spectrum.

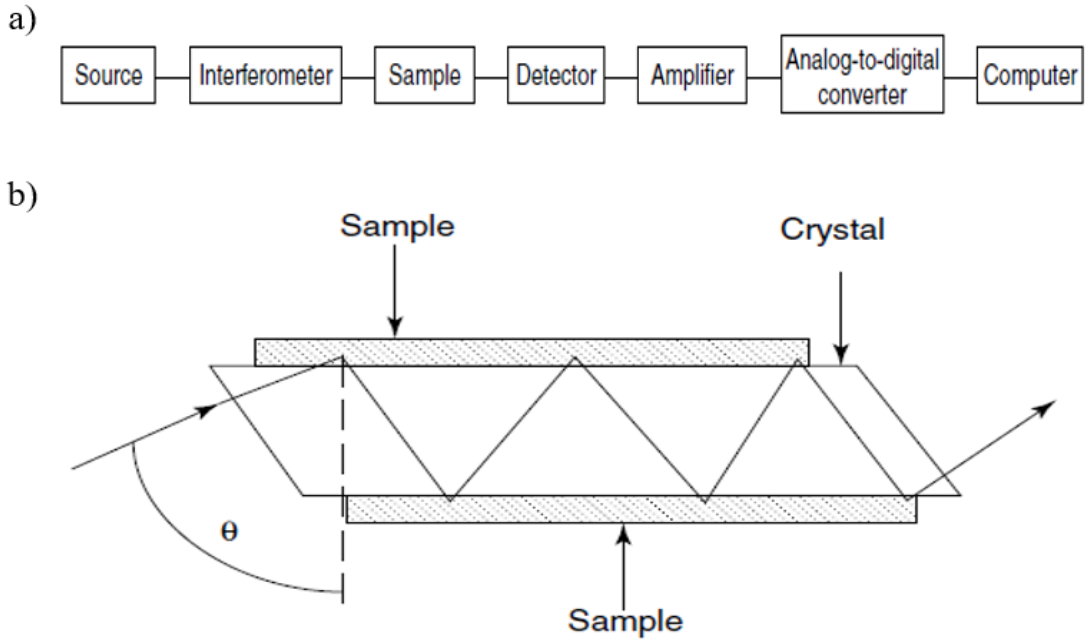

Figure 3.29: a) Block-schematic of the basic components in a FTIR spectrometer.[363] b) Schematic of a typical ATR cell, with θ being the incident angle of the beam.[363]

Reflectance methods can be used for samples difficult to analyse using the conventional transmittance study. In particular, Attenuated Total Reflectance (ATR) spectroscopy was employed which exploits the phenomenon of total internal reflection, as shown in Figure 3.8b. A beam of radiation that enters in a crystal is totally reflected when the incident angle at the interface between sample and crystal is higher than the critical angle. A fraction of the beam wavelength penetrated the reflecting surface and the sample selectively absorbs radiation, thus making the beam lose energy. The depth of penetration in ATR spectroscopy for a non-absorbing medium can be calculated using the following:

$$d_p = \frac{\left(\frac{\lambda}{n_1}\right)}{\left[2\pi\sqrt{sin\theta - \left(\frac{n_1}{n_2}\right)^2}\right]} \quad (3.63)$$

where λ is the wavelength, n_2 the refractive index of the crystal, θ the incident angle and n_1 the refractive index of the sample.
The resulting attenuated radiation is collected and plotted over the wavelength using a spectrometer, giving the typical spectral characteristics of the investigated sample. Indeed, the interaction of infrared radiation with the matter is translated in variations of molecular dipoles due to vibrations (stretching and bending) and rotations. Since each compound and substance has its own bondings and is composed by determined molecules with their typical infrared absorption (vibrations and rotations), ATR-FTIR spectroscopy was used to study the changes in vibrational spectra after the PEG addition in electrochemically deposited PEDOT:PSS thin film.[363]

3.2 Organic Electrochemical Transistor

3.2.1 Fabrication process

OECTs were fabricated with different geometries and configurations, depending on the application they were foreseen. Thus, here, the fabrication procedures separated for the specific purposes are reported: cell tissue monitoring biosensors, oxygen sensors and biosensors for analytes released by stem cell.

OECT for cell tissue monitoring
The devices were fabricated using two different configurations, a planar and a vertical one, that differ for the position of the gate electrode, in order to investigate the influence of these geometries on their performances as cell tissue integrity biosensors. After glass substrate cleaning, a 10 nm of chromium and 50 nm of gold were thermally evaporated with selected geometry to create the metallic contact for the devices. Then, the substrates were treated with oxygen plasma and a PEDOT:PSS solution, made of 94% PEDOT:PSS (Heraues, Clevios PH1000), 5% ethylene glycol (EG) (Sigma Aldrich), 1% of 3-glycidoxypropyltrimethoxysilane (GOPS) and 0.25% of 4-dodecylbenzenesulfonicacid (DBSA), was spin coated at 3000 round per minute (RPM) for 10 s (t_{acc} = 1s, t_{dwell} = 9s), using Teflon mask to shelter areas from the PEDOT:PSS solution. The planar configuration, reported in Figure 3.9a, consists in an all-planar OECT, where both channel and gate are deposited with spin coating: the two channels has length and width of 2 mm and 1.5 mm, respectively, while the inner gate is 2 mm long and 5 mm wide. All the polymeric films have thicknesses of (140 ± 10) nm.
On the other hand, only the four channels of the OECTs in the vertical configuration (Figure 3.9b) were spin coated (having the same dimensions of the channels of the planar configuration), while the gate is realized through PEDOT:PSS electropolymerization on gold wires (diameter of 0.5 mm and 15 mm length), carried out by cyclic voltammetry with 8 cycles, as described in paragraph 3.1.1. A comparison before and after the PEDOT:PSS coating of the wires is reported in Figure 3.9c. The gate is then inserted from the top in the setup measurement called TECH-OECT (described in Section 4.1), placed 3 mm above the patterned channels, as clear from the image 3.9b.
After the preparation, the devices were put in water for 1 h, allowing to the residual substances, that are unbound to the polymer chain, to be expelled from the polymer matrix and finally dried with nitrogen flux.

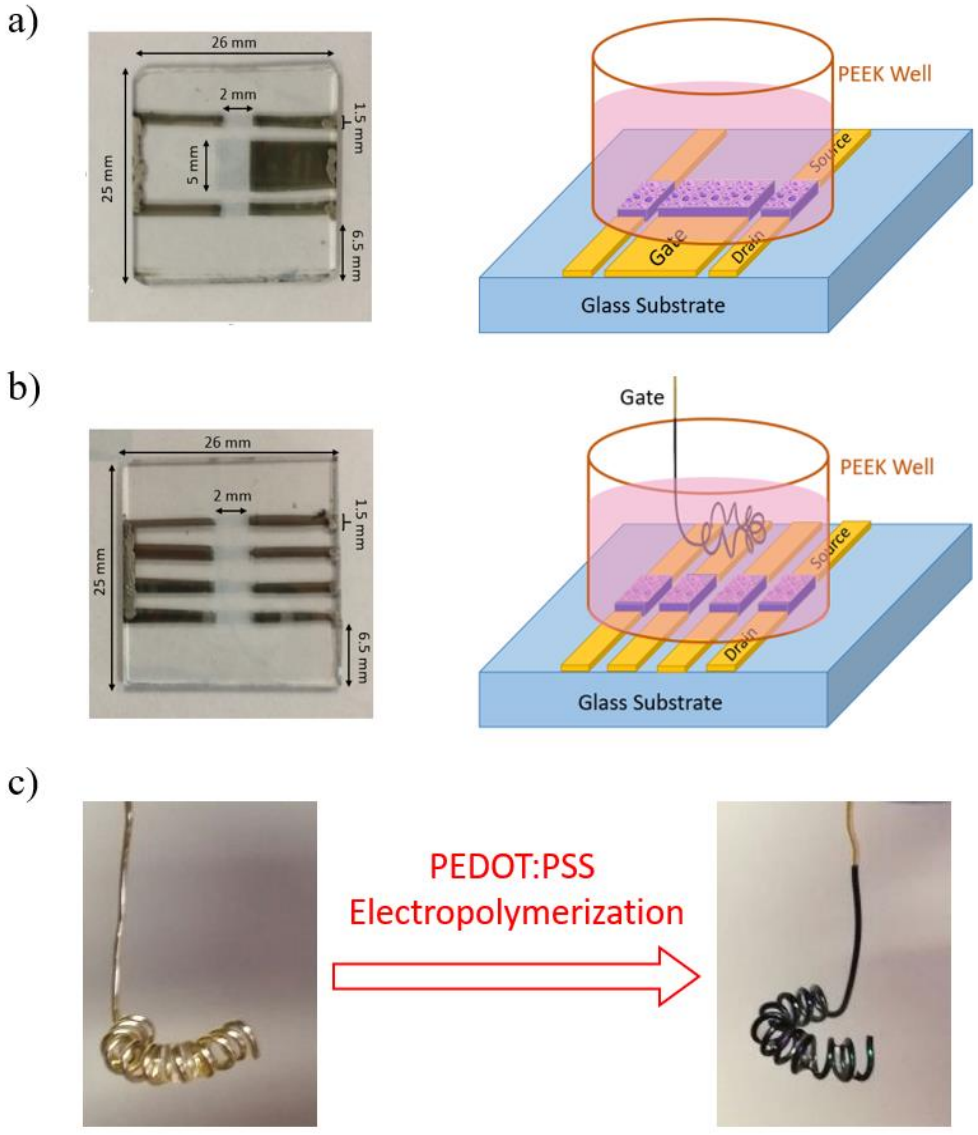

Figure 3.30: OECT planar (a) and vertical (b) configurations. On the left a picture of glass substrates with device patterned on top reports their dimensions, while on the right their implementation in the well for cell culture growth is shown. C) Gold wire before (left) and after the electrochemical polymerization of PEDOT:PSS, using CV technique.

OECT as oxygen sensors

The monitoring of oxygen percentage dissolved in solution was performed using OECTs in planar configuration. Also for this devices, a 10 nm of chromium and 50 nm of gold were thermally evaporated with selected geometry to create the metallic contact for the devices and also to have a gold layer underneath the PEDOT:PSS gate, in order to have an uniform potential on the whole electrode. Indeed, for the oxygen sensor the gate was bigger than the previous reported configuration, as seen from the dimensions reported in Figure 3.10 (gate area 156 mm^2 while the channel area is 36 mm^2). The PEDOT:PSS solution composition for these measurements was 94% PEDOT:PSS (Heraeus, Clevios PH1000), 5% EG, 1% GOPS and 0.25% DBSA, spin coated on glass substrates to form a layer of 500 nm (700 RPM, t_{acc} = 1s, t_{dwell} = 9s) and then annealed for 30 min. Again, the devices were put in water for 1 h to get rid of unbounded molecules and then fluxed with nitrogen.

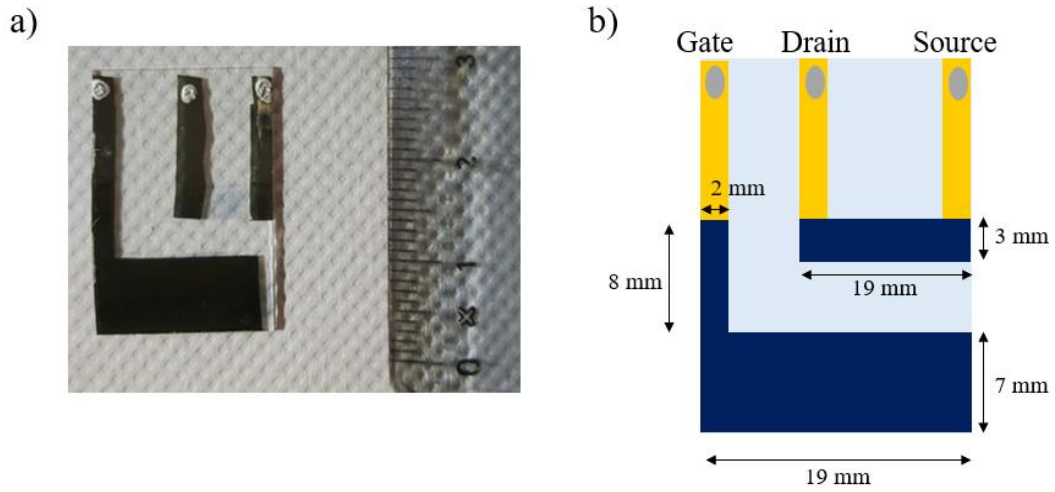

Figure 3.31: a) Picture of OECT employed as oxygen sensor. b) Schematic view of OECT as oxygen sensor, with reported channel, gate and gold contact dimensions. PEDOT:PSS, gold and silver paste are reported in dark blue, gold and silver, respectively.

OECT for detecting analyte released from stem cells

OECTs employed as biosensors for analyte released from stem cells undergoing osteogenic differentiation were fabricated via photolithography, using a parylene-C lift-off process, as described in Ref[364]. The patterned gold layer served as source, drain and gate electrodes with PEDOT:PSS used for the channel active layer and the gate coating, resulting in a device geometrical configuration with channels of width-to-length (W/L) of 100/10 (μm/μm) and a planar gate of 600 x 600 μm^2. The PEDOT:PSS formulation was composed by 89% of PEDOT:PSS (Heraeus, Clevios PH1000), 10% EG, 1% GOPS and 0.5% DBSA with ultrasonication used after each addition to improve the additive dispersion. The solution was deposited through spin coating at 1500 RPM for 30s with 3s of acceleration, followed by a thermal baking of 120°C for 1h. The resulting films of (210 ± 20) nm were put in water overnight to clean the polymeric film from unbound molecules and have stable sensor performances in liquid. The functionalization strategy to impart specificity for the detection is described and characterized in paragraph 6.2.1.

3.2.2 Electrical characterization

OECT electrical measurements were used both to investigate their characteristic behaviour and to evaluate their performances as sensors. According to the purpose and the detected element of the sensor, the most suitable measurement was employed. The electrical measurements performed on OECT can be summarized in four main categories: characteristic curves (output), transcharacteristic curves, current evaluation with fixed voltages over time and device response to pulsed voltages on the gate. The first three measurements are steady-state response on the device, where it was waited for a stable value of the current to get the parameter for the data analysis and employing either Keysight B2912A or Keithley 2612 Source Meter Units (SMU); on the other hand, the latter explore OECT dynamic response and was exploited for the monitoring of cell tissue layer formation and disruption (see Sections 4.3 and 4.4), using Keithley 2612. These instruments were used in order to simultaneously control source-drain (V_{ds}) and gate (V_g) voltages, measuring the respective currents (I_{ds}, I_g). Data acquisition was obtained with a customized PC program and the subsequent analysis required a customized Matlab routine or OriginPro 8.5.

Since different parameters and analysis are used according to the sensor application, in the course of this thesis the corresponding procedure will be directly described in the target paragraph or Section. Here, the main electrical measurements were briefly introduced and are reported in Figure 3.11.

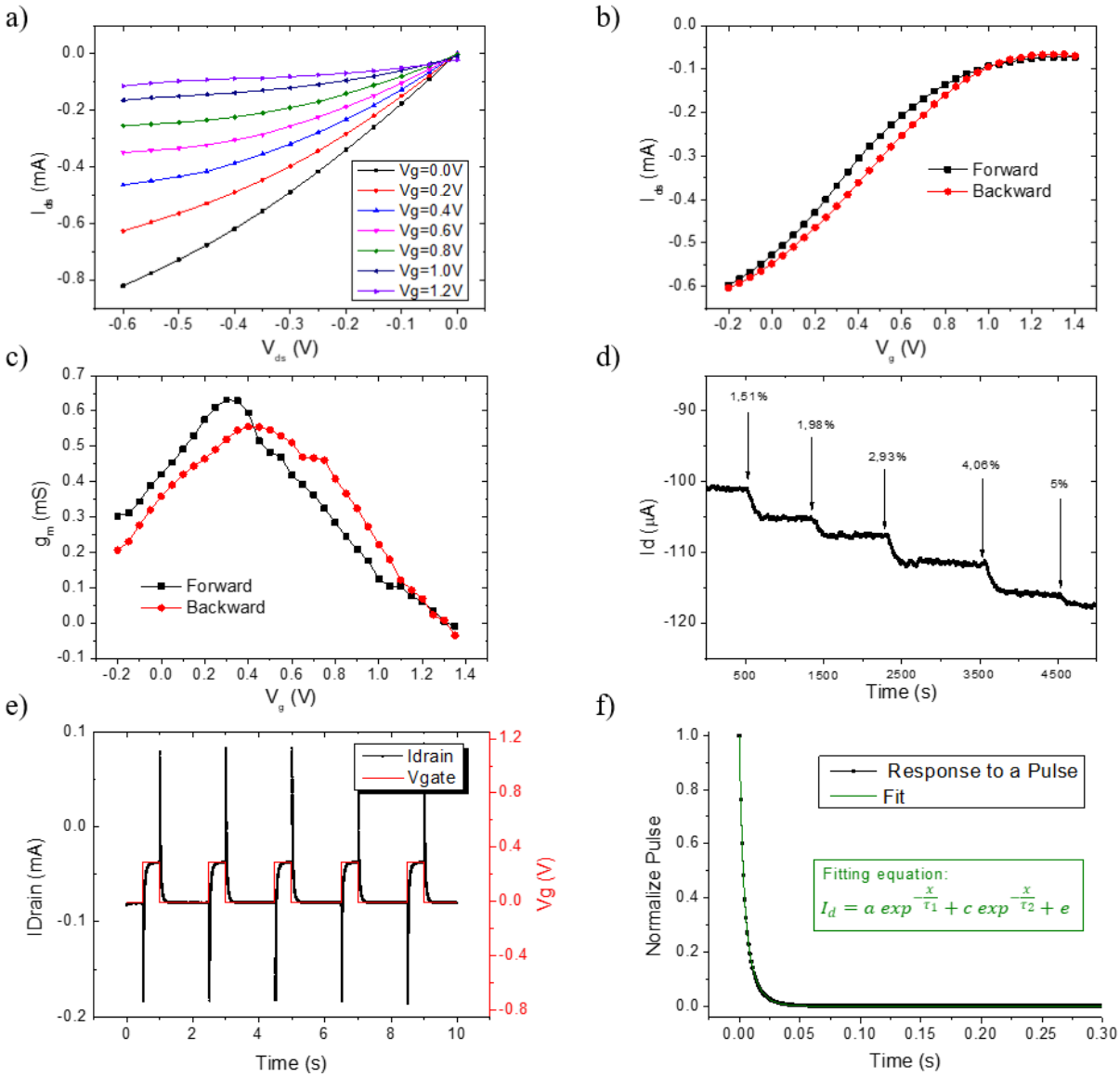

Figure 3.32: a) Output curves of an all-PEDOT:PSS OECT for different potential on the gate. b) Transcharacteristic forward (black) and backward (red) scan for all-PEDOT:PSS OECT with V_d = -0.3V. c) Transconductance forward (black) and backward (red) over V_g, representing the derivative of graph (b). d) Partial I(t) measurement of an all-PEDOT:PSS OECT for different oxygen addition. e) Pulsed measurement on all-PEDOT:PSS OECT, showing the gate potential applied and the corresponding channel current response. f) Zoom on a normalized drain current response, fitted in order to extract the time constants, necessary for data analysis.

Output, transfer curves and I(t)

Output and transfer curves were used in particular to characterize OECT steady-state response, but were also employed as a means to extract current values to calibrate the oxygen sensor response.

Output measurements (Figure 3.11a) involve the sweep of the source-drain voltage over a defined range, while the gate potential is maintained at a fixed valued, recording the current in the channel as a function of V_{ds}. Then, the potential on the gate is changed and another curve is recorded, picturing this way the transistor standard curves (and modulation) for different gate potentials.

Transcharacteristic curves (transfers) require a fixed drain voltage, while sweeping the potential on the gate and recording the channel current (Figure 3.11b) to monitor how the transistor doping and dedoping process (for an accordingly wide V_g range) influence the current, thus the amplification of the signal. Indeed, an important figure of merit of the devices, reflecting the gain of the transistors, can be extracted from these curves: the transconductance, defined as $g_m = \partial I_d/\partial V_g$ (Figure 3.11c).

Finally, *I(t)* measures the current of the channel once the source-drain and gate potentials were fixed (Figure 3.11d) in order to have current variations only depending on the analyte concentration present in the solution.
To quantify the sensor performances sensitivity and limit of detection (LOD) were evaluated from these measurements, plotting selected, normalized I_{ds} values over the analyte concentration, obtaining a calibration curve. In detail, from the linear part of the normalized I_{ds} vs log(*C*), sensitivity was extracted as the slope of the straight linear line and the LOD was calculated as the lowest addition able to produce a change in the current on the channel.

Dynamic response to a pulsed potential on the gate
The dynamic response of the OECT was investigated monitoring the source-drain current over time, while a constant tension of V_{ds} = -0.1 V on the channel and five pulses on the gate were applied, from $V_{g\text{-}OFF}$ = 0.0 V to $V_{g\text{-}ON}$ = 0.3 V with t_{ON} = 0.5 s and t_{OFF} = 1.5 s (duty cycle of 25%), as shown in Figure 3.11e. Then, each single response from the pulse was isolated, normalized (between 1, for the current value after the peak of the spike deriving from the pulse, to 0, for the current value at the end of the pulse) and fitted with a bi-exponential curve $I_d = a \cdot exp(-x/\tau_1) + c \cdot exp(-x/\tau_2) + e$ (as reported in Figure 3.11f), according to the model presented in the subparagraph 2.5.2.1. Finally, the longest time constant was extracted and used to assess the viability and coverage of the cell tissue layer in time (named τ in the course of this work). For growth experiments, time response values of five pulses of the same channel were averaged (using the standard deviation as error). For detachment experiments, where pulses were collected sequentially to improve the device temporal, τ were directly taken with the error from the fit. With these latter measurements, the system was able to provide a real-time monitoring with high temporal resolution, using a scan rate of 0.5 Hz, thus increasing the information obtainable from fast processes.

Transconductance over frequency measurements
Alternating current (AC) measurements of the device transconductance versus frequency were also run to assess device performances, using an NI PXI-4071 digital multimeter to simultaneously acquire drain and gate currents. This technique relies on the application of a potential bias on the OECT channel, then a 0 V offset and 10 mV amplitude sinusoidal wave is generated from the gate terminal, scanning the device behaviour over a defined frequency range. Using the formula $g_m = \partial I_{ds}/\partial V_g$, the monitored current was converted in transconductance values in function of frequency.
These measurements were used to evaluate the device response upon several functionalization layers deposited on top of PEDOT:PSS gate electrodes of OECT devices, as will be shown in Section 6.2.

3.3 Electrodes for neural implants

3.3.1 Fabrication process

The main steps of the fabrication process are reported in Figure 3.12. Glass substrates were cleaned and treated with oxygen plasma (100 Watt for 5 minutes), then a sacrificial layer of Polyacrylic acid (PAA) dissolved in DI water (10% in volume) was spin coated on top of them (500 RPM for 20s) and annealed for 3 minutes at 80°C. Afterwards, PDMS and its curing agent (Sylgard 184, Silicone Elastomer, Dow Corning) were mixed in 10:1 weight ratio and spin coated on the PAA layer (300 RPM for 3 min) with a subsequent annealing of 1h at 90°C, obtaining a 100 μm thick silicone layer. The same method was employed on cleaned and oxygen plasma treated (100 Watt, 3 min) Polyethylene terephthalate (PET), used for the upper PDMS layer to encapsulate the gold evaporated stripes. Indeed, 3 nm of titanium (Ti) and 30 nm of gold (Au) were deposited by laser electron beam evaporation on the glass/PAA/PDMS substrates with the pattern reported in the step 2.) of Figure

3.12. The kinked shape is introduced in order to facilitate the implant procedure. Then, the sealing of the interconnects was achieved sticking together glass/PAA/PDMS and PET/PAA/PDMS substrates, previously plasma activated in air (100 Watt, 30 s) and patterned in order to have a 400 μm wide trench that exposes the electrode and will serve also as a guide for the nerve strand during the implant Electrical contacts were then realized between extremely thin and flexible metallic wires and the gold pad on the PDMS layer, using silver paste for the connection and Silicone Dow Corning 734 Clear for the sealing and fixing. Once the contacts were dried, PEDOT:PSS or PEDOT:PSS:PEG were electrochemically deposited on uncovered Au microelectrodes, using a chronoamperometric method with potentiometric control, that was introduced in the paragraph 3.1.1 and will be better described and compared to the standard method in Section 5.2. Finally, the electrode was trimmed and released from its carrier substrate and a Ti/Au thin layer was deposited on the back of the free-standing electrode, then connected with a wire and silver paste (as described above) in order to realize a ground contact able to shield the signal acquired by the electrode from external noises. In the end, the three wires were connected to a battery-operated differential amplifier and a transmitter (provided by Data Science International), placed subcutaneously for wireless *in-vivo* recordings.

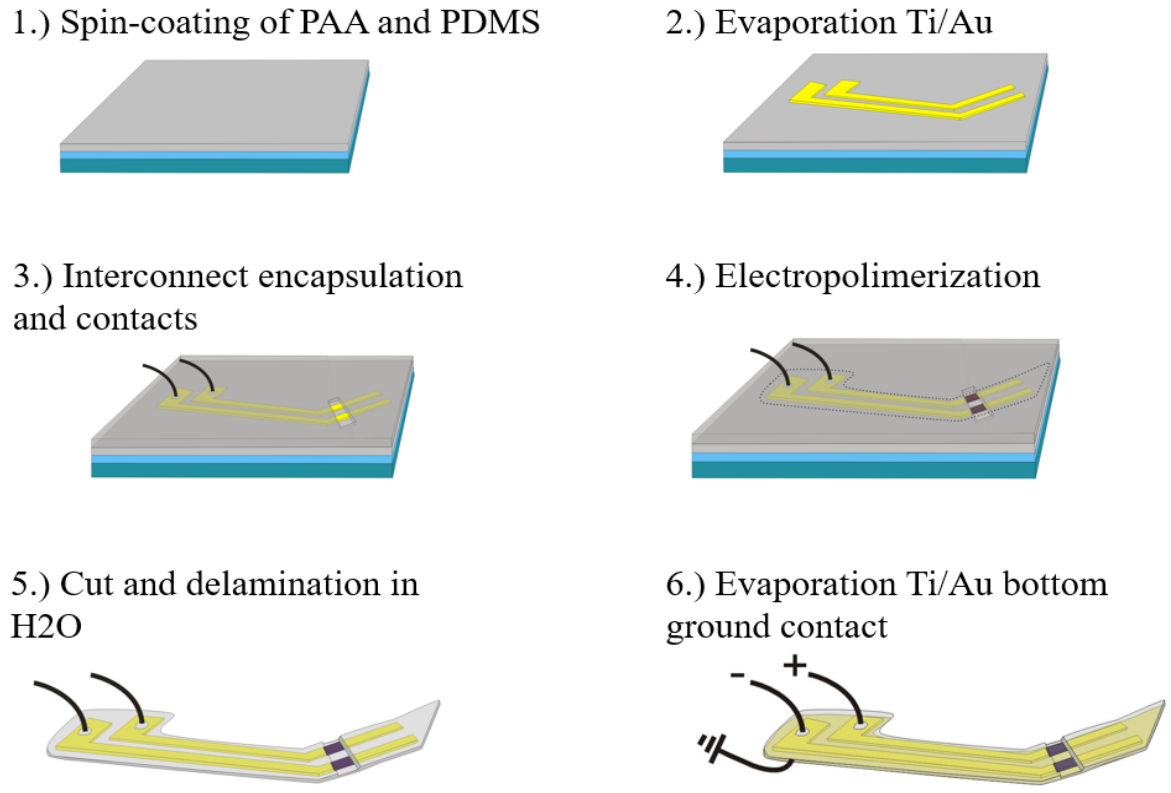

Figure 3.33: Fabrication procedure underlining the main required steps: 1.) layers spin coating to fabricate the supporting substrates, that have to be easily delaminating at the end of the fabrication; 2.) interconnects evaporation in the kinked shape; 3.) encapsulation with the patterned trench and contact realization; 4.) Electrochemical PEDOT:PSS or PEDOT:PSS:PEG deposition of the uncovered microelectrodes; 5.) Trimmering and detachment of the device from the carrier substrate; 6.) Evaporation of the ground contact on the back of the device, needed to shield the signal from external noises.

3.3.2 Electrical, electrochemical and mechanical characterization

Several measurements were employed to investigate the performance of the electrodes for neural implants, in order to assess its electrical conductivity, stretchability, aging and so on.
In detail, electrical measurements of the resistance of the interconnects under strain were performed to study gold behaviour upon stretching, checking the limit of the device (see paragraph 5.3.1). Moreover, the singular microelectrodes for each device were characterized, before and after the polymeric film deposition, using electrochemical impedance spectroscopy to control the correct

deposition and then to compare the different depositions (with thickness or composition variation). Electrochemical techniques were also employed for evaluating the aging of the electrode in PBS (paragraph 5.4.1), the difference arising from the chemical composition of the polymeric material under strain (paragraph 5.1.3) and the effect of repeated stress on electrode response (paragraph 5.4.2). For strain measurements the elongation of the electrode was monitored using an optical calibrated microscope, taking images for each stretched configuration and calculating the resulting strain variation from the starting situation. Three measurement of the electrode length (at the top edge, in the middle and at the bottom) at each step were taken and the middle value was used for the strain percentage calculation, as shown in Figure 3.13a. Finally, micro-mechanical analyses were employed to investigate the property of the electrode in liquid as experienced by the nerve tissue. Indeed, the use of AFM in liquid for nanoindentation experiments was a powerful tool to mimic the situation of the real implant and extract the Young's modulus and mechanical properties at the micro/nanoscale, which can be different from macroscale mechanical features. Moreover, polymer changes its behaviour in liquid due to water uptake and subsequent swelling, being softer and thicker once immersed, as shown in Figure 3.13b and 3.13c.

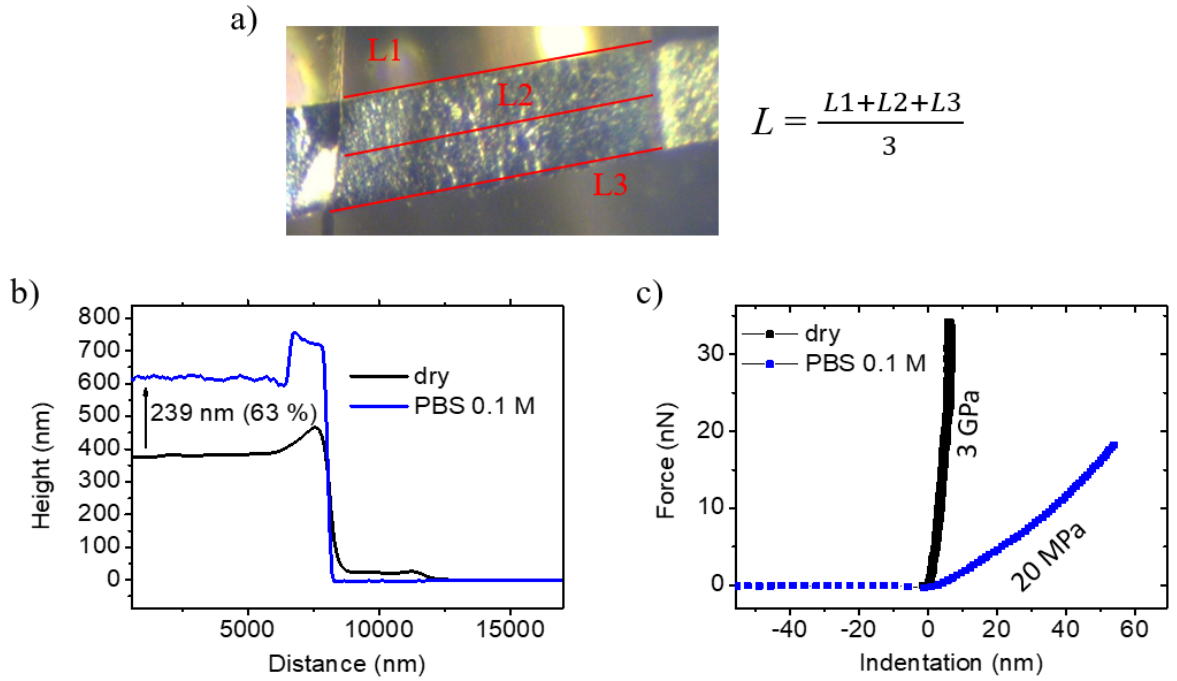

Figure 3.34: a) Optical image of a stretched electrode and average length calculation to obtain a strain value. b) Polymer thickness profile in air (black) and in PBS 0.1M (blue) with non-contact mode AFM. c) Polymer force-vs-indentation curve with AFM in air (black) and in PBS 0.1M (blue). Once in liquid, the polymer results thicker and softer due to water uptake and subsequent swelling.

3.4 Biological materials and measurements

3.4.1 Cell cultures

In this paragraph are reported the cell cultures grown on OECTs in order to monitor the cell coverage and health with these alternative and powerful tools. Two different cell line were investigated to characterize and understand the device performance with barrier and non-barrier cell lines, namely human colorectal epithelial cells (Caco-2) and mouse embryonic fibroblast (NIH-3T3). Their brief description is treated in the next subparagraphs.

Cells were cultured in Dulbecco's modified Eagle medium (DMEM) (4.5 g/L glucose) supplemented by 10% (v/v) fetal bovine serum (FBS), 2 x 10^{-3} M L-glutamine, 100 U/mL penicillin and 100 mg/mL streptomycin with 0.1 x 10^{-3} M MEM nonessential amino acids (NEAA). For cell experiments,

OECTs were cleaned and sterilized with ultraviolet (UV) light for 20 minutes before the use. All cells were grown in simulated physiological conditions inside an incubator (37 °C, 5% of CO_2 and 95% of humidity).
Cells were culture on both the devices, encapsulated in the TECH-OECT (a customized support for cell growth whose fabrication and feature is reported in Section 4.1), and on standard petri dishe to have the control experiments and thus assess that OECTs do not alter cell growth mechanism and vitality.
Cell experiments were done at the National Centre of Research- Institute of the Study of Materials Nanostructured (CNR-ISMN) in a collaboration with the group of Massimiliano Cavallini. In detail, cell cultures were carried on and followed by the biologist Dr. Marianna Barbalinardo.

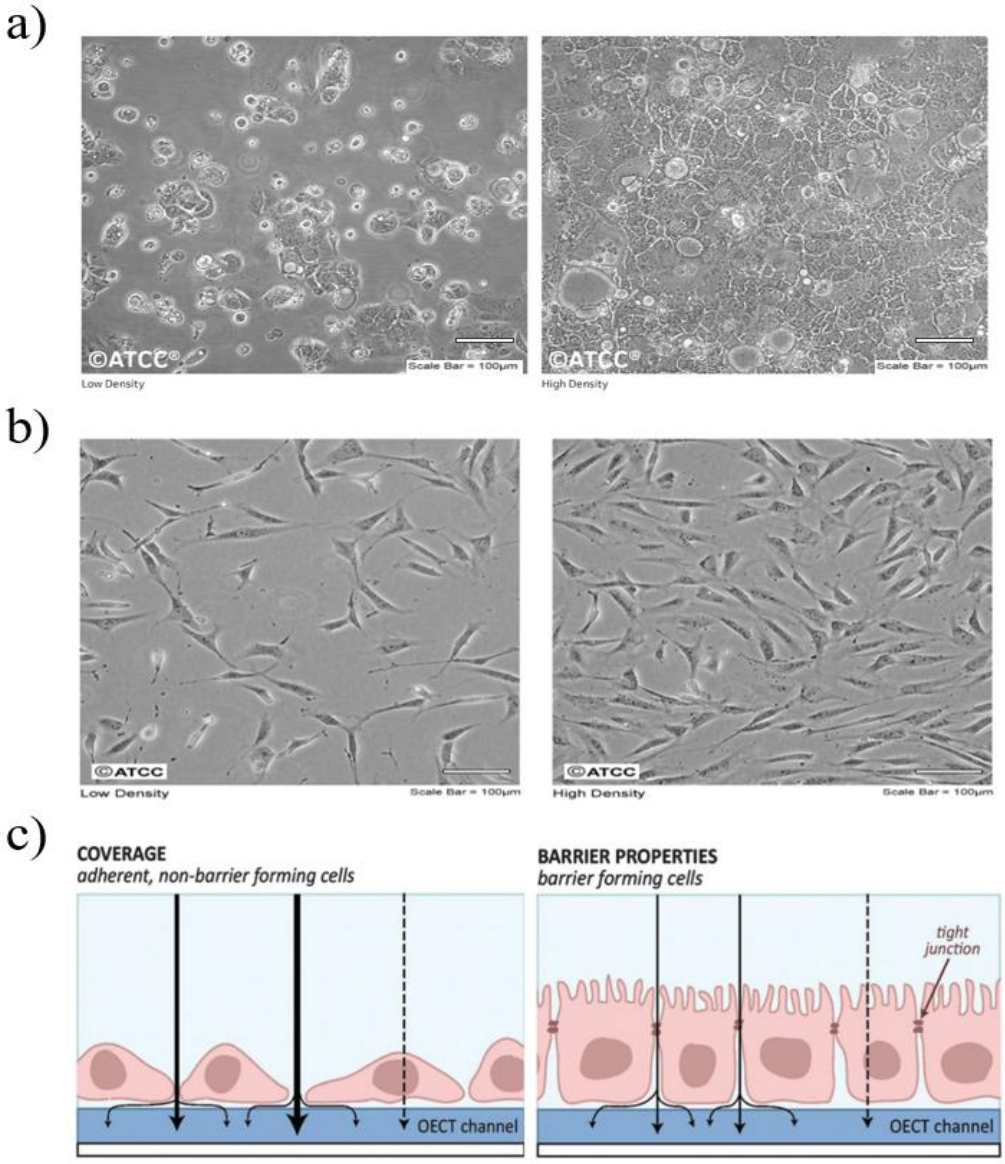

Figure 3.35: Caco-2 (a) and NIH-3T3 optical images for a low (left) and high (right) density growth.[365,366] C) Comparison of coverage vs barrier forming cells, the latter being able also to shield the paracellular flux between adjacent cells (full black arrow). The transcellular flux (dashed arrow) is present for all kind of cells and is the flow of ions and molecules through the cell itself.[169]

3.4.1.1 Human colorectal epithelial cells

Human colorectal epithelial cells (Caco-2), purchased by Sigma Aldrich, are heterogeneous epithelial colorectal adenocarcinoma cells, developed by J. Fogh in the 1975,[365] having an intermediate barrier tightness.[169] Optical images of Caco-2 grown with low and high density are shown in Figure 3.14a.

The reason for the use of Caco-2 cells in this work is two-fold: from one hand, they represent a standard widely used model for barrier-forming cell line, thus presenting Tight Junctions (TJ) between them, able to screen the paracellular flux (flux of ions and molecules between adjacent cells); on the other hand, they represent the gastrointestinal barrier in our body, being one of the main shield against the absorption of nanoparticles (NPs), that can be ingested due to their widespread presence in food packaging.[367]
TJs are apical junctions, linked to other cells by the transmembrane proteins, occludin[368] and claudin[369], while bound to the cytoskeleton with intracellular proteins.[370] Since the presence of TJs seals intercellular space between cells, the passage of ions, as well as macromolecules, is regulated by this physical barrier. As previously explained in paragraph 2.5.2.1 OECTs can be used as cell tissue monitoring devices, exploiting this ion limited flow to extract a quantitative signal of the layer formation or disruption.

3.4.1.2 Mouse embryonic fibroblast

Mouse embryonic fibroblasts (NIH-3T3), purchased from Cell Biolabs, is a cell line of contact-inhibited cells able to grow in flat monolayers, that were isolated in 1962 from a NIH Swiss mouse embryo (shown in the images in Figure 3.14b).[366] These cells do not present TJ formation (non-barrier properties) and thus form only a coverage l: their influence on the ion flux will then be lower (but noteworthy detectable with OECTs) compared to barrier cells, as can be seen from Figure 3.14c, reporting the comparison between coverage and barrier properties.
Accordingly, NIH-3T3 cell line was chosen due to their non-barrier properties, being a valuable way to test device performances for cell forming only a coverage layer on top of them, and moreover because they represent the skin "barrier" against the absorption on nanomaterials present in cosmetics and makeups.[371]

3.4.2 Vitality tests

Studies of cell viability, grown on our devices or on standard substrates, were performed using 3-(4,5-di-methyl-2-thiazolyl)-2,5-diphenylttetrazolium) bromide (MTT) assays and taking optical and fluorescent images, in order to simultaneously investigate the cell health and layer progress. MTT assay reflects, indeed, cell metabolism level while fluorescence images report cell morphology and cytoskeleton structure, manifesting cell affected or unaffected growth. On the other hand, optical images were used to monitor the cell layer formation or disruption on the device, counting the covered and uncovered areas to correlate optical view with electrical results from OECT devices.

MTT assay

MTT assay is a colorimetric assay to assess cell viability, proliferation and drug cytotoxicity and relies on the intracellular reduction of Tetrazolium salt (3-4,5-dimethylthiazol-2yl)-2,5 diphenyltetrazoliumbromide) c. After the test, the medium was discarded and cells were incubated with MTT solution (0.1 mg/mL MTT in Dulbecco's phosphate buffered saline (DPBS)) for 2 hours at 37 °C with 5% CO_2 (inside the incubator). Afterwards, MTT solution was discarded and DMSO was added in each well. Optical density (OD) was then read on a microplate reader by a spectrophotometer at 550 nm (Thermo Scientific Varioskan Flash Multimode Reader). Cell viability was calculated as the ratio of the average optical density of replicated wells relative to that of the control.

Optical images

Thanks to PEDOT:PSS optical transparency once deposited in thin film, transmission optical measurements have been done on cells grown on top of the devices, using a Nikon TS100 Eclipse microscope. In particular, the instrument was an inverted microscope with the light source over the

sample and the objectives (4x, 10x, 20x, 40x) below it. A camera, connected to the setup, allowed to acquire and save digital images of the sample.

Fluorescent images

The second optical technique employed was the fluorescence microscopy, which relies on the absorption and subsequent re-emission of light by a sample. This method is often used in biology or biomedical sciences due to the possibility to inspect cellular components, otherwise difficult or impossible to study with standard optical microscopy. Samples may exhibit autofluorescence or they can be treated with fluorochromes, attached to target structures and excited by specific wavelength, in order to make these elements detectable. Figure 3.15 reports a cross-section of an epi-fluorescence microscope, where a multispectral light is produced in the vertical illuminator at the centre of the image by an arch-discharge lamp, then the light is filtered passing through a wavelength selective excitation filter. Afterwards, light is deflected by a dichroic or a beamsplitter, reaching the sample via the microscope objective. If the sample has fluorescence responses, the consequent emission light is gathered by the objective and it follows the backward pathway crossing the dichroic and then a barrier or emission filter (Figure 3.15b) to select the excitation wavelengths.

In this thesis, actin filaments (cytoskeleton) and cell nuclei were stained: to study morphological evidence, cells were fixed with 4% paraformaldehyde in Dulbecco's phosphate-buffered saline 1X (DPBS) and washed with DPBS 1X. Then, cells were permeabilized using 0.01% Triton-X 100 and, afterwards, incubated with 1% bovine serum albumin in DPBS 1X in order to block nonspecific binding sites. TRITC-phalloidin was used to label cells for 1 h, followed by DPBS 1X rinses, aiming at mapping the local orientation of actin filaments of cell cytoskeleton. A 4,6-diamidin-2-phenylindole (DAPI) incubation for 3 min was employed for nucleus counterstaining, followed by rinses with DPBS 1X. Fluorescence images were final taken with a Nikon Eclipse 80i microscope (Figure 3.15) equipped for fluorescence analysis. In details, images reported in this work will show actin cytoskeleton and filament in red and cell nuclei in blue.

3.4.3 Trypsin-EDTA treatment

One of the main topics of this thesis was monitoring cell tissues subjected to stressing agents. There are several ways to compromise and affect cell layer integrity, according to the entity of damage one wants to introduce: indeed, it is possible to simply cut the junctions that link adjacent cells, detach the cell layer without affecting the cell health or induce cytotoxicity. An example of the first kind of damage is the use of Ethylene Glycol Tetraacetic Acid, EGTA, employed in scientific works to study the variation of the paracellular flow using bioelectronic devices, before and after its addition in a barrier-forming cell layer.[167,329] On the contrary, cytotoxic effect can be obtained with high concentration of ethanol (>40%, otherwise lower concentrations only disrupt TJs in a reversible way)[327] or with nanoparticles (described and employed in Section 3.5 and 4.4, respectively). In the end, a simple detachment of the cell layer from the underneath substrate is achieved using Trypsin-Ethylenediaminetetraacetic Acid (EDTA), with the first being a protease capable of detaching cell from substrate and EDTA being able to chelate metal ions like Ca^{2+} and Mg^{2+}. Trypsin is used routinely to detach cell from substrates[167] and is a non-specific protein cutter. Since integrine, one of the major cell-substrate binding proteins, depends on Mg^{2+}, they can be used as a mean to separate cells from substrates without affecting their health.

In this work, cells were incubated and growth until a full confluence on top of the semiconducting polymer films (reached usually in 3-4 days), then the medium was discarded and a solution of trypsin-EDTA 1X (0.05% of trypsin and 0.02% of EDTA) was added to each sample for 20 min at 37 °C with 5% of CO_2 (thus inside the incubator). Meanwhile, measurements were performed to assess in real-time the cell layer detachment with electrical monitoring (see Section 4.3).

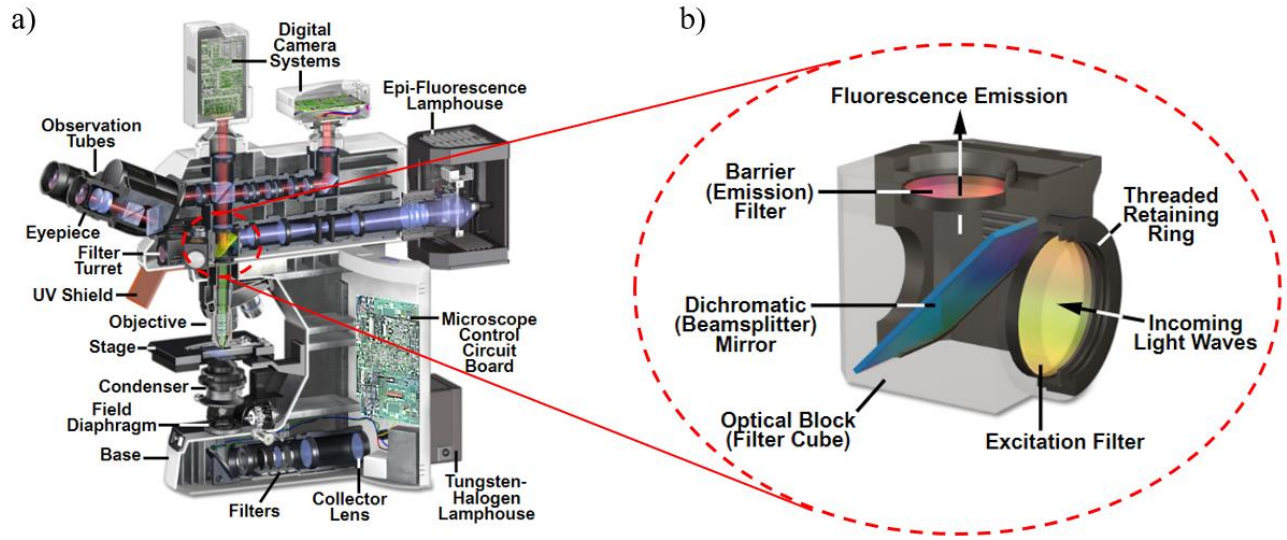

Figure 3.36: a) Schematic cross-section of a fluorescent microscope. b) Zoom on the filter turret, where the filters and beamsplitters are allocated.[372]

3.5 Nanoparticles

According to the definition provided in 2000 by the National Nanotechnology Iniziative, "Nanotechnology is the understanding and control of matter at the nanoscale, at dimensions between approximately 1 and 100 nanometers, where unique phenomena enable novel applications". Indeed, standard materials (gases, liquids, solids) can exhibit unusual properties, extremely different from the bulk features of the same materials.[373,374] Moreover, nanotechnologies involve different scientific disciplines such as physics, chemistry, engineering, material science, molecular biology and much more.

Among the different nanotechnologies, nanoparticles (NPs) are extremely used is consumer goods. The word "nanoparticle" is used to identify a class of particles of different shapes (spherical, cubic, and so on), made of atomic or molecular aggregates with a dimension ranging from 1 to 100 nm. Several materials, including biopolymer and metals (nichel, chromium, gold, silver) can be exploited to realize NPs and, in particular, silver nanoparticles (AgNPs) are widespread in commercially available products, being incorporated into bandages,[375] food containers,[367] disinfectants and makeups/cosmetics.[371] Despite their diffusion, their cytotoxic activity on cells (which depends on several factors, like size, shape and surface coating)[376] has not been fully understood and studied. For this reason, we employed OECTs for monitoring cell layer health during AgNPs exposure, whose fabrication and characterization is reported in the following paragraphs.

3.5.1 Nanoparticles synthesis

Two different NPs types were made with the aim to obtain NPs with cytotoxic effect and others not affecting the cellular growth. In particular, citrate-coated AgNPs were supposed to produce toxic effect on cell forming layers, while their surface functionalization with (11-mercaptoundecyl)hexa(ethylene glycol) (EG_6OH), replacing citrate molecules with OEG-alkanethiol, was employed to neutralize the toxic effect of NPs on cells.

Citrate-coated AgNPs were synthesized by the chemist Denis Gentili (at the CNR-ISMN), following a method reported elsewhere,[377] that is reported here briefly. 100 ml of sodium citrate (5 mM) and tannic acid (0.025 mM) in acqueous solution were refluxed, adding quickly an acqueous solution of silver nitrate (1ml, 25 mM). The reaction mixture was then refluxed for 30 min, giving a bright yellow colloidal silver solution that was left cooling down at room temperature. Afterwards, this suspension

of AgNPs was purified by two centrifugation rounds (30000 g for 2 h) and resuspended in 10 ml of acqueous solution of sodium citrate (2 mM). This procedure allowed for the synthesis of the citrate-coated AgNPs, employed for their toxic effect on our cell lines.
On the other hand, the replacement of citrate molecules on the NPs surface with the thiol was obtained with further steps: the dispersed AgNPs solution was mixed at room temperature overnight with a concentrated 2 mM of EG_6OH in aqueous solution, adjusting the added volume to achieve a stoichiometry of 15 EG_6OH/nm^2 (this ensures the maximum grafting density). Afterwards, three rounds of centrifugation (13000 g for 30 min) were used to remove the excess of ligand, finally resuspending the mixture in acqueous solution of sodium citrate 2 mM.

3.5.2 Nanoparticles characterization

The nanoparticles were characterized using an ultraviolet-visible (UV-vis) spectrophotometer, whose schematic is briefly reported in Figure 3.16a: it is an instrument that measures the absorbed wavelength-selected light through the sample and a "blank" reference, in order to give information on the solution composition (wavelength dependent, because different substances absorbs different wavelength) and the concentration of the solution (dependent on the amount of absorption).
Citrate-coated AgNPs resulted having an average diameter of 15 nm and the band of the characteristic surface plasmon resonance centred at 400 nm, as shown in Figure 3.16b, confirming that the NPs are stable and not aggregated. After the passivation with the EG_6OH, the plasmon resonance band is slightly redshifted (around 10 nm towards higher wavelength) but does not report broadening or shape variation. The redshift occurs due to the change in the chemical surface coverage, while the keeping of the shape states that the aggregation state was not affected by functionalization.

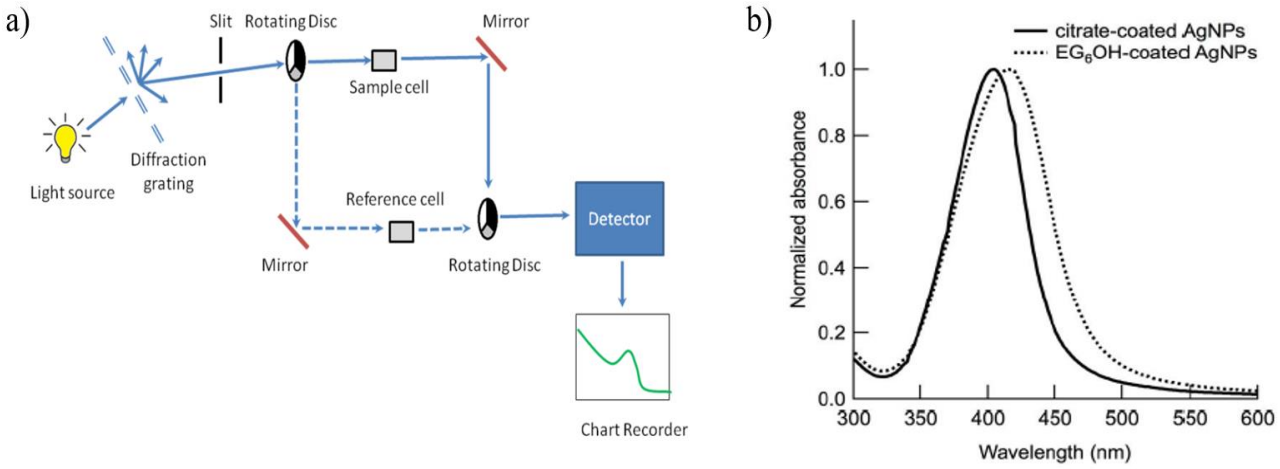

Figure 3.37: a) Spectrophotometer schematic view.[378] b) UV-Vis absorption spectra for the citrate- (full black line) and EG_6OH-coated (dashed black line) AgNPs in sodium citrate (2 mM).

3.6 Neural implants

Stretchable and low-impedance electrodes, fabricated as described in paragraph 3.3.1, were implanted on the renal nerve of Sprague-Dawley rats in order to test their recording performances under acute and chronic conditions. The surgery implantation and the *in-vivo* recording procedures were performed in collaboration with the Department of Biomedical and Neuromotor Sciences in Bologna, by the group of Dr. Davide Martelli and Dr. Roberto Amici, and with the Florey Institute of Neuroscience and Mental Health of the University of Melbourne in Australia, by the group of William S. Korim and Song Yao.

3.6.1 Surgery implantation

The protocol for the surgery was approved by the Florey Institute of Neuroscience and Mental Health Animal Ethics Committee, under the guidelines set out by the National Health and Medical Research Council of Australia "Code of Practice for the Care and Use of Animals for Experimental Purposes in Australia". The complete description of the surgery implantation is reported in paragraph 5.5.

3.6.2 In-vivo chronic recording

To start in chronic recording experiments the wireless recording board was activated moving a magnet close to the animal and signal trace were recorded with the animal awake but in resting position. The signal was then filtered, digitized and transmitted to the external data acquisition computer. Arterial blood pressure (AP) and renal sympathetic nerve activity (RSNA) were monitored using the telemetry system. In particular, RSNA was recorded with the 50-1000 Hz band and sampled at 10000 Hz. Then, AP and RSNA signals were digitalized using Power1401 (Cambridge Electronic Design, Cambridge, UK) with Spike2 v7.02 software. The counting of the spikes was done quantifying the spikes that overcame a defined threshold, considered as the noise level.

3.7 Functionalization layer characterization

3.7.1 Quartz Crystal Microbalance

A quartz crystal microbalance (QCM) measures a variation per unit area evaluating the frequency change of a quartz crystal resonator. The resonance is, indeed, changed by addition or removal of small mass due to oxide growth or decay or film deposition on the surface of the acustic resonator. QCM can be employed under vacuum, in gas phase or even liquid environment.
In detail, in this work quartz crystal microbalance with dissipation monitoring (QCM-D) was used, which is based on a ring-down technique, described by Hirao *et al.*[379] and Rodahl *et al.*[380] in the QCM context. The QCM active component is a thin quartz crystal disk in the middle of two electrodes, that oscillates upon the application of an AC voltage over the electrodes. Once the voltage is turned off, the resulting exponentially decaying oscillations are recorded and the resonance frequency (*f*) and the energy dissipation factor (*D*) extracted. The latter can be defined as the loss of energy per oscillation period divided by the total energy stored in the system and is then equal to the ratio between the resonance bandwidth and the resonance frequency. Commonly, changes in the resonance frequency are primarly connected to mass uptake or release over the sensor surface (as seen in Figure 3.17a), while variations of the dissipation factor can be ascribed to viscoelasticity (softness), in turn related to structural changes of the film adhering to the sensor surface.[381]
In this thesis work, QCM-D analysis were performed in collaboration with Dr. Achilleas Savva and Prof. Sahika Inal at the Engineering Division of the King Abdullah University of Science and Technology in Thuwal (Saudi Arabia). In detail, QCM was employed for swelling and mass adsorption over bare and APTES-functionalized PEDOT:PSS thin films, using the Q-sense analyser (QE401, Biolin Scientific). Swelling was studied recording firstly the QCM-D response for bare Au sensor in air and, subsequently, in 1X PBS solution (injected into the chamber). The introduction of PBS resulted in a shift of both *f* and *D*, caused by the different densities of the two media. The measurements were stopped and the sensors removed, depositing directly onto the same Au substrate the PEDOT:PSS films with and without APTES functionalization layers above. Then, the absolute *f* for each polymer-coated sensor was extracted in air and 1X PBS, once the *f* signal was perfectly flat, thus assuming the system in equilibrium. Using the "stitched data" function of Q-soft software, the absolute difference in *f* for multiple overtones was compared between bare and polymer-coated sensors. The difference of *f* values are directly correlated to the polymer thickness in both media, calculated through the Sauerbrey equation:

$$\Delta m = \frac{-17.7}{n}\Delta f_n \quad (3.64)$$

Once the QCM-D signal was stable in PBS, water was pumped in the chamber with a flow rate of 70 $\mu l \cdot min^{-1}$ in order to set a baseline. Afterwards, water-based biotin solution was pumped in the chamber, stopping the flow and leaving the protein incubating for 60 min at a constant temperature of 24 °C. Water was used after the incubation to rinse and remove non-bound proteins from the sensors. The same procedure was repeated for 1X PBS and PBS-based streptavidin to test the streptavidin molecule bindings. Finally, in order to quantify the mass added on each sensor (Δm), Sauerbrey and Young-Voigt viscoelastic models were employed, together with Q-tools, D-find and Q-soft software for the data analysis.

3.7.2 Chronoamperometry

Chronoamperometry is an electrochemical technique in which the potential of the working electrode is stepped (square wave) at a certain value and the resulting output current from faradaic processes (occurring at the electrode surface) is monitored as a function of time. An example of the described method is reported in Figure 3.17b.

Chronoamperometry was performed in collaboration with Ellasia Tan and the Prof. Ji-Seong Kim at the Department of Physics and centre for Plastic Electronics of the Imperial College in London (UK). The system was based on an electrochemical cell, comprising an Ag wire reference electrode, Pt-coated fluorine doped tin oxide (FTO) as counter electrode and the working FTO electrode on which the samples were deposited as thin films. Bare and APTES-functionalized PEDOT:PSS samples were studied, using a diluted 0.01X PBS solution as electrolyte. The measurements were conducted with Autolab Potentiostat (PGSTAT), applying a square wave potential on the working electrode at 0 V for 10 s, then reducing it for 90 s and again applying a neutral bias of 0 V for 20 s. the reducing potentials ranged between 0 to 0.6 V.

3.7.3 Electrochemical Raman Spectroscopy

Raman Spectroscopy is a spectroscopic technique employed to study vibrational, rotational and other low-frequency modes in a system. It is particularly sensitive to π-electrons, that are highly polarizable under photoexcitation, giving information on the polymer conformation, chemical structure and the variation in the π-electron distribution.[382,383]

Briefly, the technique relies on Raman scattering, that is an inelastic light scattering process where the energy difference of the incident and scattered photon corresponds to the energy level separation between different states of the scatterer. In simple cases, an optical excitation, with energy lower than the optical energy gap, is used to probe vibrational energy levels. The molecule is then excited from the ground electronic states (S_0) to a virtual excited state (lower than the first excited electronic state, S_1) and relaxes back to the ground state. As reported in Figure 3.17c, according to the final reached ground electronic state, three types of scattering can occur: i) most scatterers relax back to their original vibrational state, thus the scattered photon has the same energy of the incident one (Rayleigh scattering); ii) when the final state has higher energy than the initial one, the scattered photon is less energetic compared to the incident one (Raman Stoke scattering); iii) finally, when the relaxation is to lower-energy final states, the scattered photon has higher energy than the incident one (Raman anti-Stokes scattering).[383] These two latter cases are Raman scattering, when the relaxation is to a different vibrational state than the initial one.

The differences in the energy between the incident and scattered photons (known as Raman shift) are related to the energy level spaces of vibrational modes. Thus, a Raman spectrum is composed by

several scattering intensity peaks as a function of Raman shift, indicating the energies of different vibrational modes.

In this thesis work, Raman Spectroscopy was combined with electrochemical measurements on the sample, in order to study the vibrational states under different biasing (thus oxidation-reduction) conditions of the bare and APTES-functionalized PEDOT:PSS thin films. *In-situ* Electrochemical Resonance Raman Spectroscopy was performed in collaboration with Ellasia Tan and the Prof. Ji-Seong Kim at the Department of Physics and centre for Plastic Electronics of the Imperial College in London (UK), using a Renishaw inVia microscope in a back scattering configuration and the same electrochemical setup described in the previous paragraph. The excitation source used was a HeNe laser at 633 nm with 50% of 12 mW laser power under 50x magnification onto the PEDOT:PSS film, employed as working electrode. The measurements were taken when the output currents of the chronoamperometry reached a steady-state value.

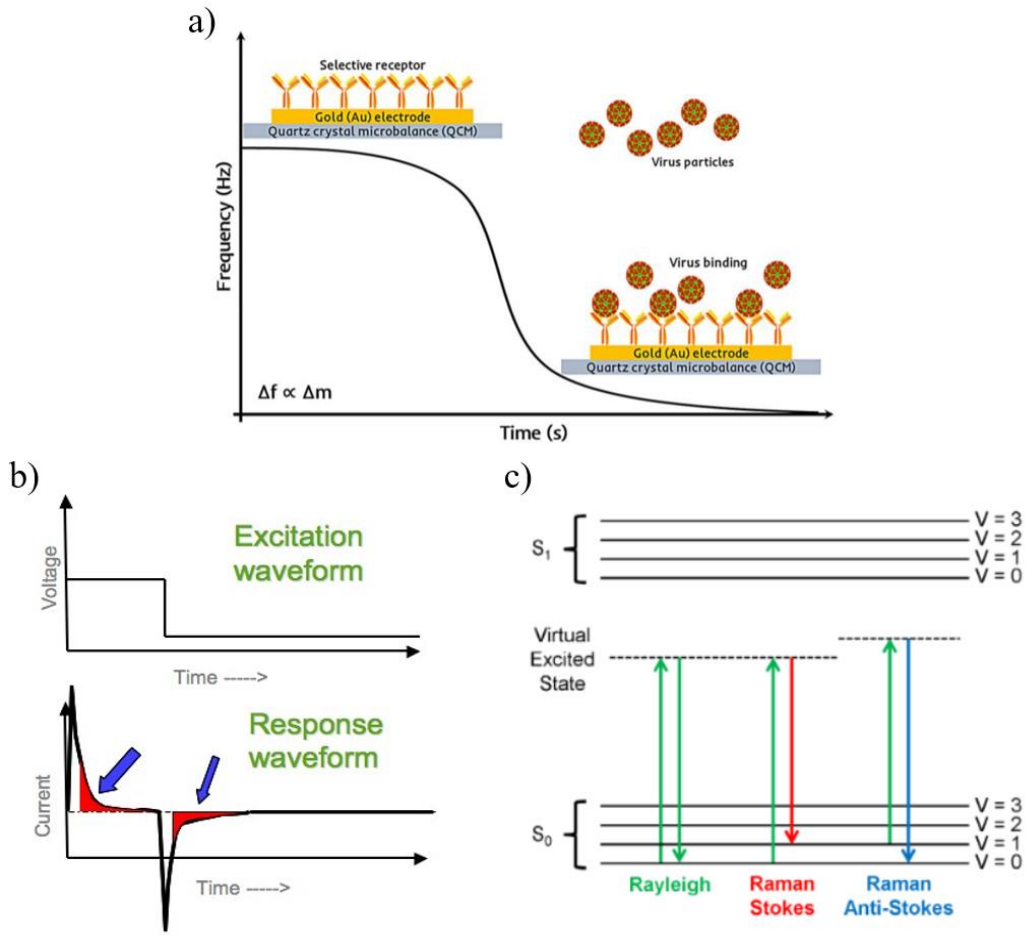

Figure 3.387: a) Quartz crystal microbalance working principle used as virus sensor: the mass change in response to virus binding with the selective receptors is detected as a frequency shift in the QCM.[384] b) Pulsed chronoamperometry waveform, in which the integrated region can be used for charge determination. c) Diagram comparing different transition levels for Rayleigh and Raman scattering, with respect to the ground (S_0) and first excited electronic states (S_1), together with vibrational energy level (V).[383]

Chapter 4

OECT for cell tissue monitoring

4.1 Tissue Engineering Cell Holder for Organic Electrochemical Transistors (TECH-OECT)

Electrical measurements on cells needed to be performed keeping constant parameters for the cell cultures, such as 37 °C with 5% of CO_2 and 95% of humidity, thus requiring the use of an incubator. In order to be able to have a continuous electrical monitoring of cell layers grown on our devices, the Tissue Engineering Cell Holder for Organic Electrochemical Transistor (TECH-OECT) was built. It is a customized sample-holder, whose picture is reported in Figure 4.1, made of three main components, namely a fiberglass printed circuit board (PCB) base, a customized six multiwell polyether ether ketone (PEEK) block and a plexiglass cover. These elements are better described in the following paragraphs.

The TECH-OECT design allow for real-time and fast electrical monitoring of up to 24 devices for the vertical configuration or 12 devices for the planar one without taking the cell cultures out of the incubator, thus keeping the "simulated" physiological condition. Moreover, it is not mandatory to select only one of the two configurations during a running experiment: changing electrical connections, different monitoring combinations can be created in the six wells. Even though this possibility was not exploited in this work, it is also possible to switch from a vertical to a planar gating on the same channels and viceversa.

This is a clear advantage provided by the system, because the monitored cell layers are investigated in ideal living conditions where the only stresses/differences are provided by the holder, the electrical measurements, or the external agents introduced by the scientist. Viability test regarding the first two elements will be reported in the next Section.

Noteworthy, changing the device patterning even more measurements and configurations can be introduced, paving the way to several real-time electrical monitoring of cell viability.

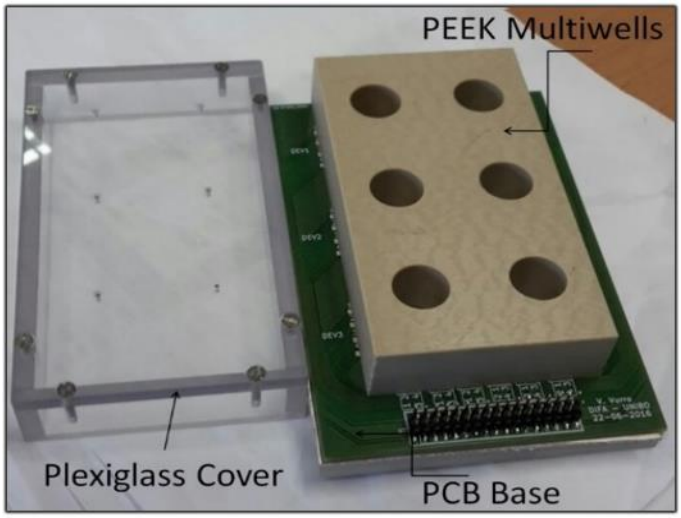

Figure 4.1: Picture of the custom-made TECH-OECT with highlighted its three main components, namely the PCB base, the PEEK block with 6 wells and the plexiglass cover. TECH-OECT allows to perform electrical measurements on the cell cultures inside the incubator, thus under simulated physiological conditions.[385]

4.1.1 Printed Circuit Board

PCB base with electrical circuits and connections was designed using a free software suite for electronic design automation, called *KiCad*.[386] Two steps are needed for the realization of the electrical circuit base: the design of an electronic circuit schematic, using *Eschema*, and its conversion into a PCB design with *Pcbnew*. The former is a schematic capture software that is distributed as part of *KiCad* and where the connection and the circuit components can be drawn, creating a block function diagram with the information on the components and their pins (input and output). On the other hand, *Pcbnew* is a printed circuit board software, able to read the schematic by *Eschema* and realize the footprints associated with the components of the circuit. Indeed, footprints are the physical appearance of the components, containing information on the dimensions and positions of the pins.
The starting point of the work was the design of OECT component, that has to reproduce the glass substrate dimensions and present the electrical connections, according to the device configurations. A small pit for the OECT insertion in the PCB was also foreseen, together with a hole in the middle of the square device for taking optical images. The schematics are reported in Figure 4.2a. Then, other 8 simple holes are made for the screw that will close the sample holder and the circuitry schematic is drawn on the top of the PCB, with the pin header placed at the bottom, as shown in Figure 4.2b. The prototype was fabricated by the fast prototyping company MD Srl[387] and it can be seen in Figure 4.2c. When the samples are inserted, the connections between PCB and OECTs are made using copper wires, welded to the PCB in the corresponding pads and then connected to the drain, source or gate electrodes using the silver paste and then sealed with silicon to prevent their breakage or detachment during the experiment.

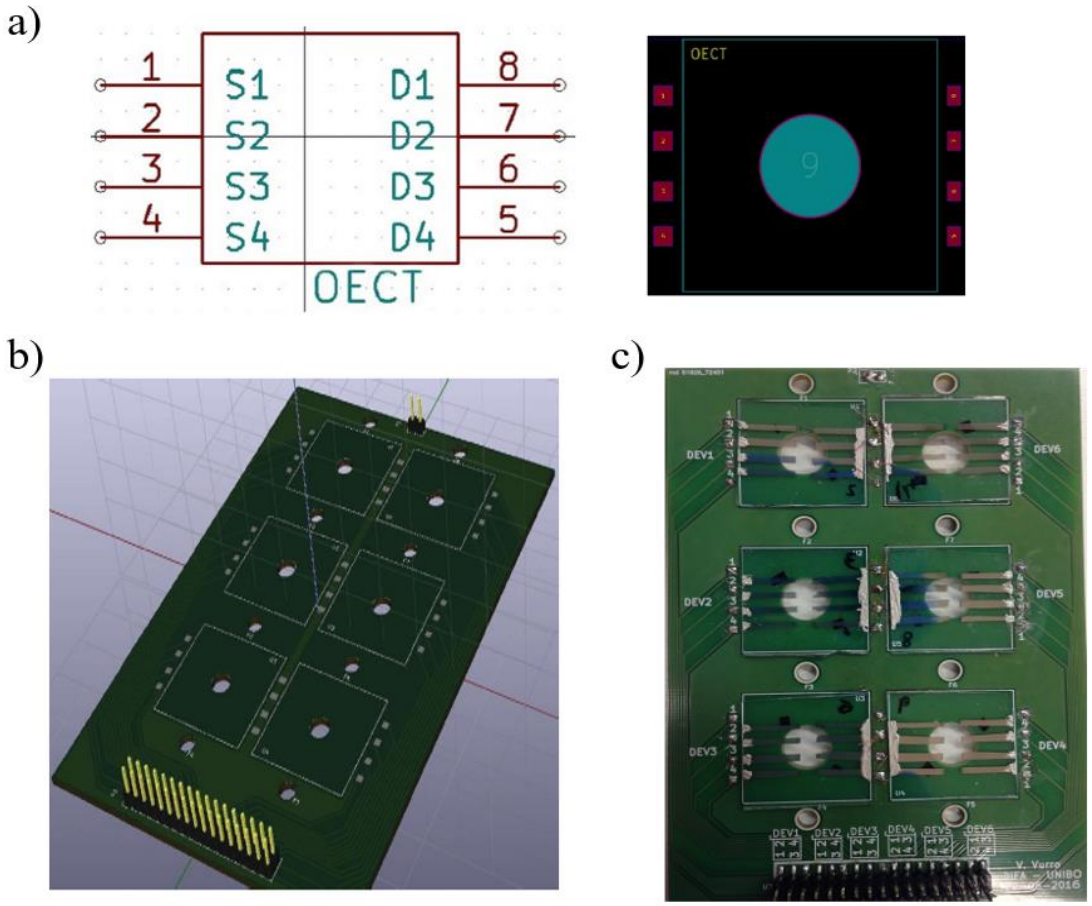

Figure 4.2: Printed Circuit Board schematics (a,b) and prototype (c). a) OECT component custom block diagram (left) and footprint (right). b) 3D view of the complete layout of the PCB board. c) Front view of the realized PCB board, with 6 devices already inserted.

4.1.2 Polyether ether ketone block

Polyether ether ketone (PEEK) is an easy-to-work, biocompatible and thermoplastic organic polymer, that was used for its properties to realize the wells were the cells were grown. A PEEK block of 110 x 60 x 20 mm^3 was perforated to create 6 cylindric wells, having a diameter of 14.5 mm, and other 8 holes, threaded to provide an anchor for the screws. The well diameter was chosen wide enough to take pictures of the cell tissue but small enough to have the vertical electrode (3 mm above the channel) completely immersed in 2 ml of complete medium (used as electrolyte).
For the closure of the TECH-OECT, 6 O-rings were employed to assure the isolation of the biological environment from the electrical connections and avoid the breakage of the glass substrate during the closing compression.
The picture of the final PEEK block with O-rings in position is reported in Figure 4.3a.

4.1.3 Plexiglass cover

The final component of the TECH-OECT is the plexiglass cover, which was realized in order to avoid contaminations in the wells during optical microscope measurements, taken outside the incubator. Moreover, the cover was perforated in order to realize 6 holes with diameter of 1 mm, that ensured the possibility to fix and support vertical gate at a defined height (3 mm above the channel but still completely immersed in the medium). A picture of the described situation is reported in Figure 4.3b.

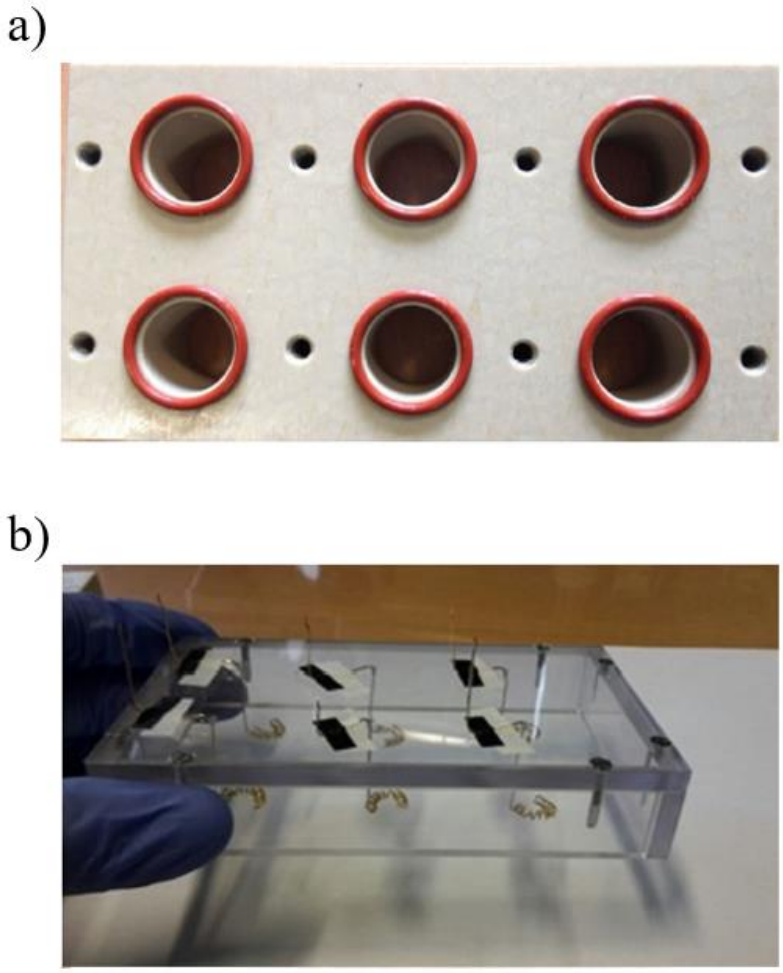

Figure 4.3: a) Picture of the complete PEEK block, with the O-rings positioned for the closing procedure of the TECH-OECT. b) Plexiglass cover with the vertical gate electrodes fixed to have the same height from the channel, once inserted in the wells for the measurements.

4.2 Cell vitality tests

In order to test the biocompatibility of the TECH-OECT and prove that cell growths were not influenced by this setup for the electrical measurement acquisition, viability tests were performed on cell cultures and took optical images of cell layer formation.

4.2.1 MTT assay and optical images

Cell viability on OECT was assessed using the MTT assay, that reflects cell metabolism as explained in paragraph 3.4.2. MTT assays were made for both cell cultures with and without electrical measurements on them, in order to monitor the possible unwanted effect of electrical stimulation while acquiring the OECT response. Data are reported in Figure 4.4 for Caco-2 (red) and NIH-3T3 cells (blue), where the control (CTR) is taken on growths on standard petri dish substrates (set as 100%).
As can be clearly seen, the results of viability tests on NIH-3T3 grown on our OECT devices show, after 96h, a mitochondrial activity from 80% to 85% for measured and unmeasured fibroblast, respectively. The viability, thus, only decreases slightly compared to the standard cell culture substrates, with the electrical measurements that do not change their status significantly. From a biological point of view, viability assays commonly set the 80% as a threshold for healthy cell cultures, therefore it can be concluded that NIH-3T3 growth are altered neither from the OECT substrates, nor from the electrical pulsed measurements.

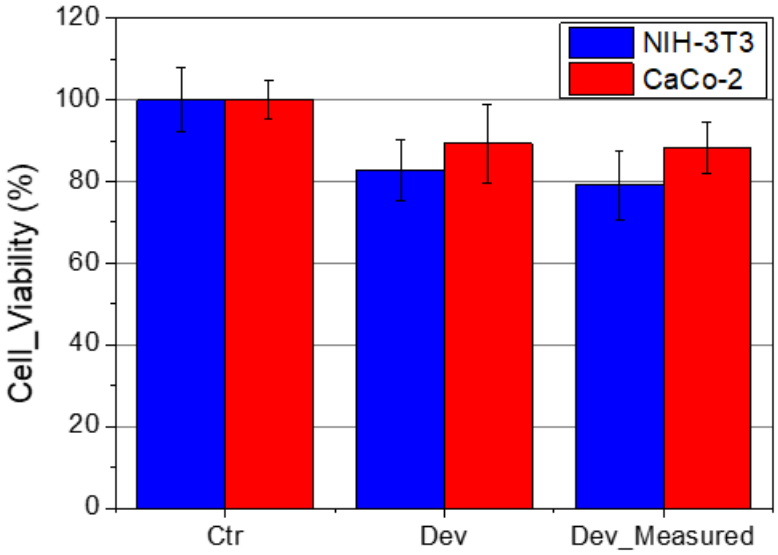

Figure 4.4: Vitality tests on NIH-3T3 (blue columns) and Caco-2 (red columns) cell lines. All data are represented as the average ± standard deviation of several samples.

Similar results can be observed for Caco-2 cell line: in this case, even higher viability percentages are present both close to 90% for epithelial cells grown on measured and unmeasured devices.
Furthermore, optical images have been taken to observe the cell layer formation on these unconventional substrates. Figure 4.5 and 4.6 report the comparison of NIH-3T3 and Caco-2 growth on a standard petri dish and on measured devices. Since it was confirmed with MTT assays that electrical measurements do not affect cell growths and electrical data were needed to study the cell layer formation, optical images of the growth on unmeasured devices are note reported (considering that they show no differences from the pictures on the measured ones). Figure 4.5 clearly shows the formation of fibroblast layers on both petri dishes and OECTs, with the final coverage of the underneath substrate after 72 h. A similar trend is reported also for the Caco-2 in Figure 4.6, even

though after 72 hours there seems not to be the complete confluence on the OECT. Since human epithelial cells growth is slightly lower on the OECTs, the experiments were performed over 96 hours in order to have a final complete layer of cells over the devices.
In conclusion, the optical images further confirm the ability of these two cell lines to grow in flat layers on our devices (leaving only small and rare empty spaces after 72 h), whose response will be dependent on the coverage percentage and the cell nature (barrier-like or not, thus on the resistance against the ion flow introduced by the cells). Moreover, these images also helped us in calibrating the duration of the experiments in order to have complete confluence when needed.

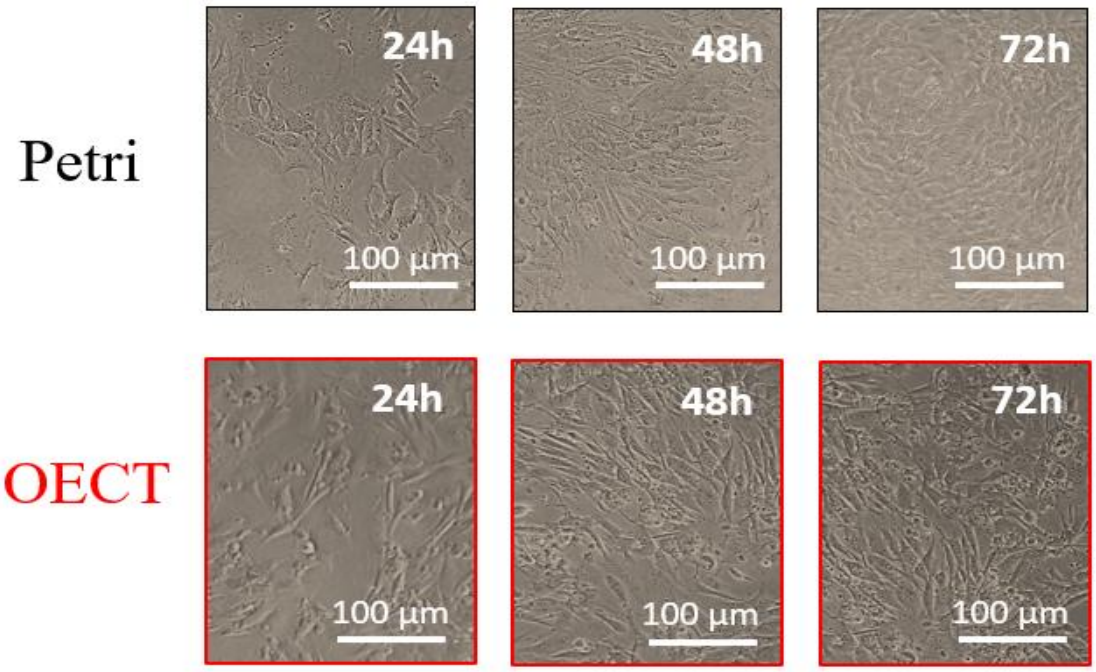

Figure 4.5: NIH-3T3 optical images taken at 24, 48 and 72 hours after seeding on standard petri dishes (black rectangular border) and measured OECTs (red rectangular border).

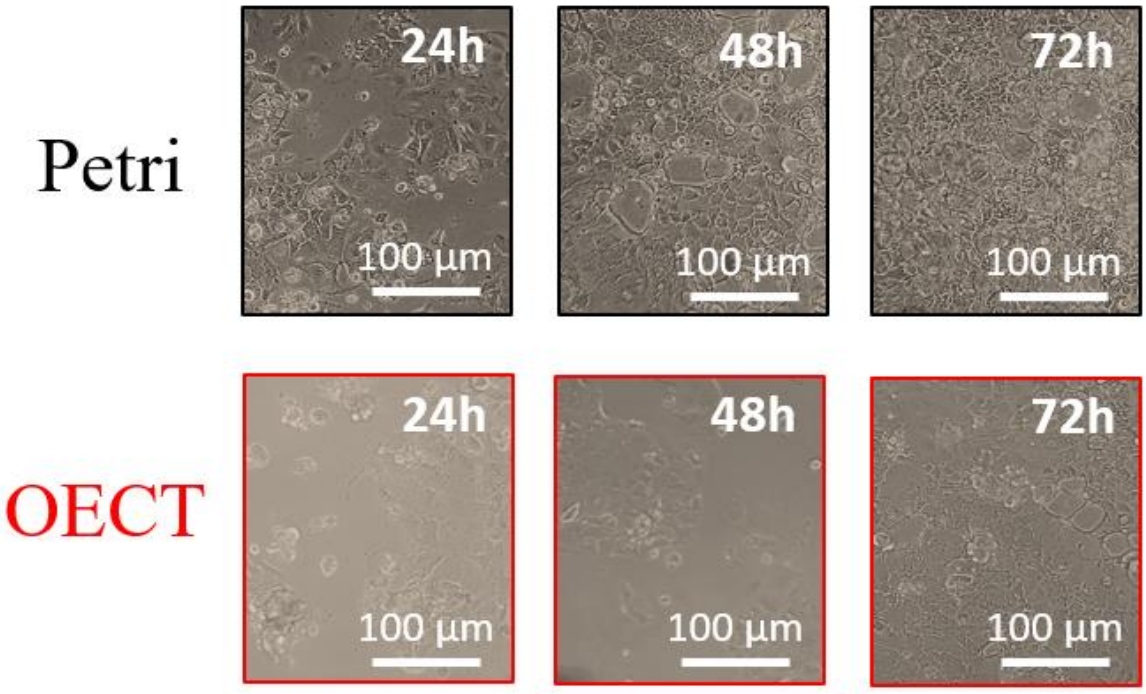

Figure 4.6: Caco-2 optical images taken at 24, 48 and 72 hours after seeding on standard petri dishes (black rectangular border) and measured OECTs (red rectangular border).

4.2.2 Actin and nucleus staining

Further investigations on health status of cells grown on OECTs were done on cell internal structure using fluorescence images, as explained in paragraph 3.4.2. Actin filaments, known to regulate cell functions, like adhesion, proliferation, differentiation and internal architecture,[388] and cell nuclei were fluorescently labelled in red and blue, respectively. Figure 4.7a and 4.7b represent cell morphology of NIH-3T3 and Caco-2 cells on OECT, respectively, after 72 hours for NIH-3T3 and 96 hours for Caco-2 from seeding. Clearly, cell adhesion, growth and morphology are not affected by the OECT substrates underneath and the electrical measurements carried out, since both cell lines keep their standard density and organization, together with the integrity of actin cytoskeleton and a well-spread adhesion to the substrate.

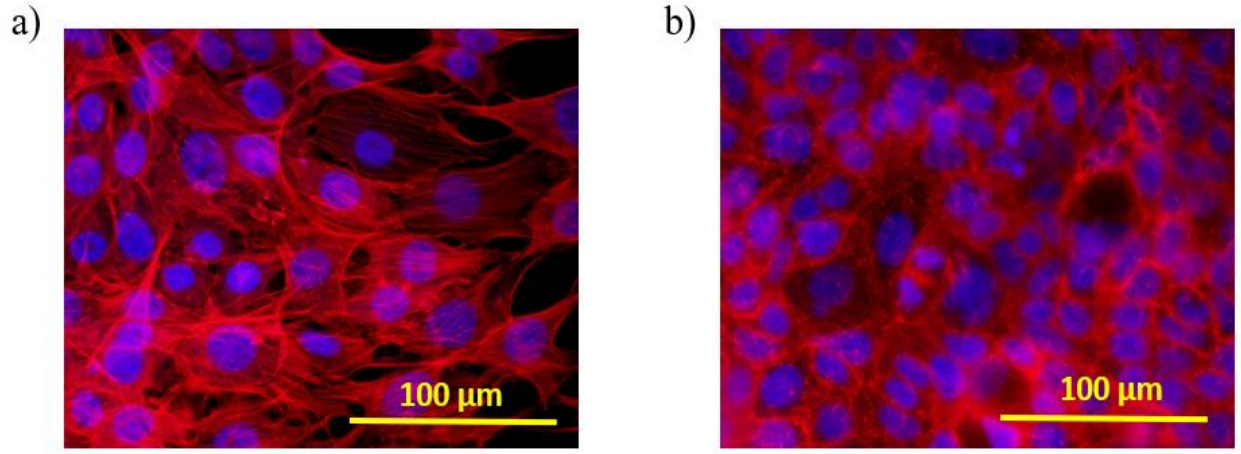

Figure 4.7: Fluorescence images of NIH-3T3 (a) and Caco-2 (b) cell lines, grown on OECT substrates, once a confluent layer was reached.

4.3 OECT Configuration effect on cell tissue monitoring

As introduced in the sub-paragraph 2.5.2.1, OECTs can be employed as biosensors to monitor cell layer formation or disruption with cells seeded directly on top of them.
The starting point of the work was the theoretical model presented by Salleo's group, which correlates cell layer resistances with appropriate OECT active area dimension in order to have reliable monitoring of the cell layer itself. OECTs with bigger active areas can then be used to monitor high resistance cells with barrier-like properties, such as MDCK I (Madin-Darby canine kidney, which are canine familiaris renal epithelial cells) and Caco-2, while devices with smaller areas should be employed for low resistance cell lines, that have no barrier properties, such as Hela (immortalized human epithelial tumor cells) and HEC-1-B (human endometrium epithelial cells).[31] According to this model, the channel area of the devices was chosen as 3 mm^2 in order to have cell layer monitoring devices, covering a broad range of cell tissue resistances, from 5 $\Omega \cdot cm^2$ (leaky/non- barrier cells) up to 10000 $\Omega \cdot cm^2$ (strong barrier cells). Then, two different standard cell lines were used, namely Caco-2 and NIH-3T3 (described in sub-paragraphs 3.4.1.1 and 3.4.1.2, respectively), with the aim of being able to detect only the former cell culture. Indeed, cell confluent layer resistances (widely known as *Transepithelial Electrical Resistance*, TEER) of Caco-2 are between 400 $\Omega \cdot cm^2$ and 1500 $\Omega \cdot cm^2$, while no information regarding NIH-3T3 TEER values have been found in literature, probably due to the TEER detection limit, which is around 20-30 $\Omega \cdot cm^2$,[389,390] or slightly lower with currently available techniques. Noteworthy, the OECT device lower limit is close to TEER limit (5 $\Omega \cdot cm^2$).
On the other hand, two different OECTs were introduced, having a vertical and a planar configuration, as described in paragraph 3.2.1. While the vertical configuration follows the theoretical model

depicted by Salleo's group,[31] allowing the cells to grow only on the device channel, in the planar one cells can spread on both channel and gate, basically doubling the electrical impedance/resistance of the cell layer, because the ion flux are affected by both the cell layer on the gate and the one on the channel.[167] The vertical and planar OECT cross-section schematics, with the ion movements upon the application of a positive bias on the gate, are reported in Figure 4.8a and 4.8b, respectively, together with their equivalent ionic circuit, showing the double ion crossing of the cell layer for the planar configuration.

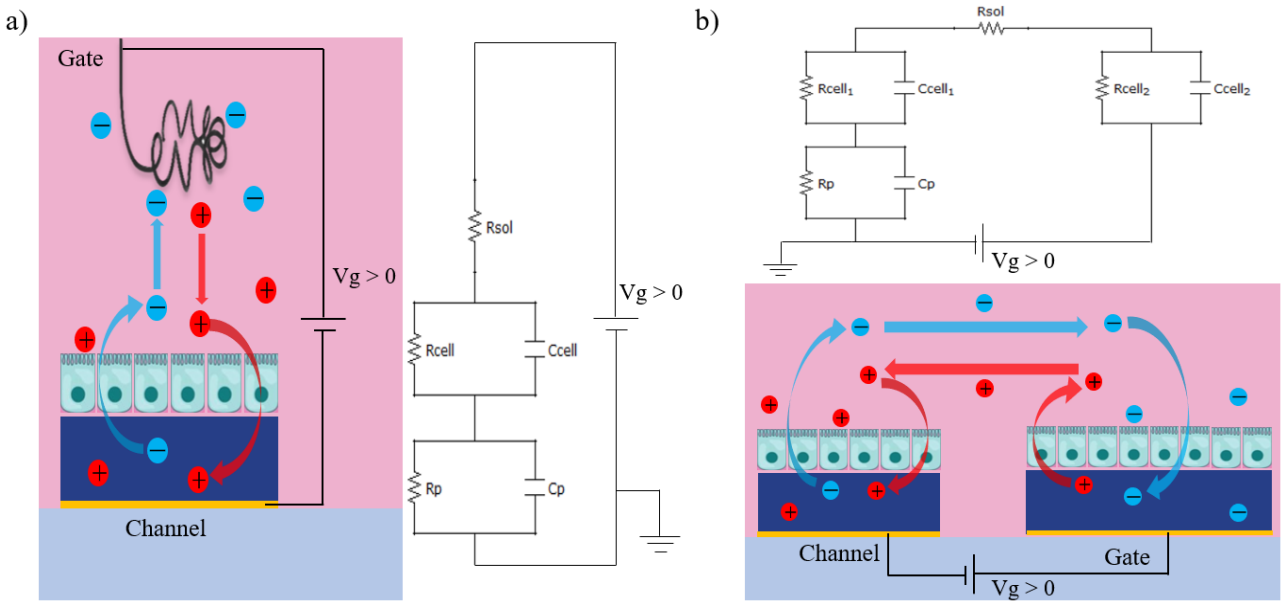

Figure 4.8: OECT **s**chematic cross-sections and relative ionic equivalent circuit for the vertical (a) and planar (b) configuration. Ion movements are represented accordingly to the positive bias applied on the gate.

Vertical and planar devices were characterized by means of transcharacteristic curves in complete DMEM (the cell culture medium was used as electrolyte, since all the following measurements will be with cells), that were also used before starting the cell tissue screening experiments, in order to stabilize the device response (ion uptaking and releasing allow for a stable sensor response after 3 to 4 cycles). Figure 4.9a reports the comparison between vertical and planar OECT transfer curves (acquired with V_d = -0.1V, channel polarization potential also applied in the cell experiments), showing no great differences in the two sensor responses: the two curves have similar trend, except for a slight change in the slope of the transfer that can be ascribed to fabrication variability among different OECTs of the same batch. Indeed, Figure 4.9b clearly confirms this possible variability comparing several transfer curves of vertical and planar devices.

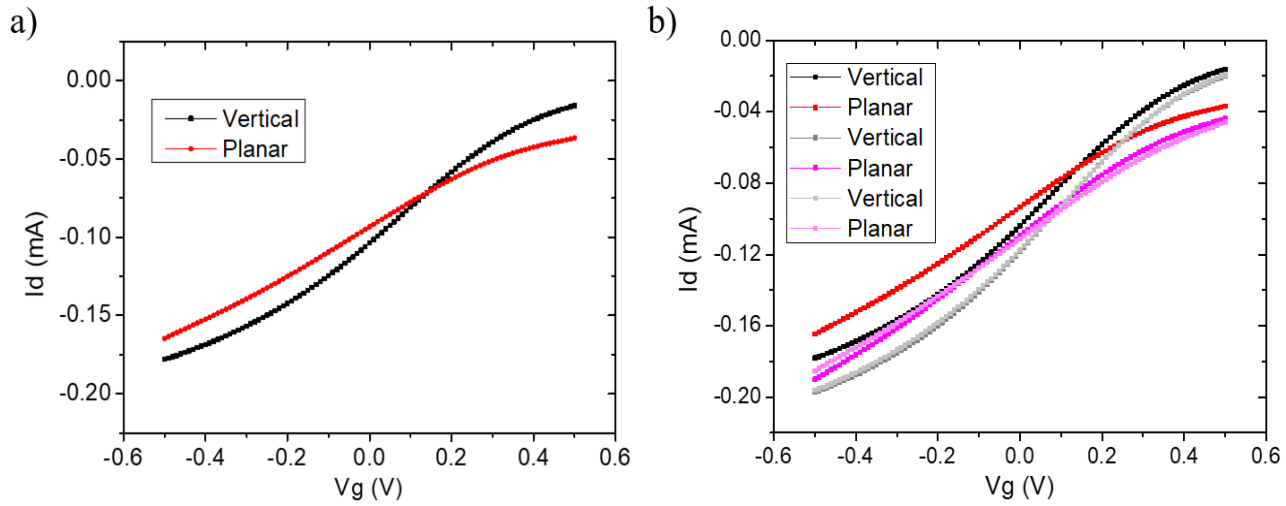

Figure 4.9: a) Transcharacteristic curves for a vertical (black) and planar (red) OECTs. b) Different transcharacteristic curves of vertical (black, dark grey, light grey) and planar (red, magenta, light magenta) OECTs, proving that the OECT responses are very similar for the two configurations in the range of V_g = -0.5–0.5, being included in slight variability among samples.

4.3.1 Vertical configuration

Vertical OECTs were fabricated with a channel active area of 3 mm^2 and a PEDOT:PSS-coated gold wire immersed from the top of the well into the cell medium as a gate electrode. The conducting polymer was electropolymerized on the metallic wire in order to achieve a larger gate capacitance, thus having the greater potential drop at the channel/electrolyte interface (efficient gating to detect on the channel).[154]

Cells were seeded onto the whole device area and measurements were started 4 hours later, in order to have the cells already fallen (or even adhered) on the device and not suspended in the medium. Cell layer monitoring was done studying the dynamic behaviour (time response) of the OECT once a positive square pulse, with V_g = 0.3 V, was applied on the gate electrode, as described in paragraph 3.2.2. The channels were instead polarized with V_{ds} = -0.1 V. The standard device response, without cells seeded on top of it and using complete DMEM as electrolyte is (12.2 ± 0.8) ms, obtained averaging four different devices. Figure 4.10 reports a comparison between the drain current modulation (cut and normalized) of vertical OECT with (Figure 4.10a) and without (Figure 4.10b) Caco-2 cells for 4 days (96 h) of incubation. This Figure demonstrates that cells over OECT channel slow down the OECT response while growing and proliferating on it, hindering ion flux from the medium to the PEDOT:PSS active layer and the other way around: as the cell layer forms on the PEDOT:PSS channel, the effect on the ion is stronger and the transistor response is slower, having the slowest response after 96 h, thus when the layer reaches its confluence. On the other hand, the device behaviour in the medium without any cell growing on it is stable even after 96 h. A final consideration regards the dashed green line in Figure 4.10a, that represents the current modulation after 20 minutes from the addition of Trypsin-EDTA to the cell culture. The curve almost perfectly overlaps to the response after 24 h from seeding, when there was a limited number of cells on the device, unable to form a layer, thus the device response was almost totally independent from the cell. For this reason, it was hypothesized that detaching the cells from the substrate leads to the recovery of the device starting time response before cell seeding, as will be proved later in this paragraph.

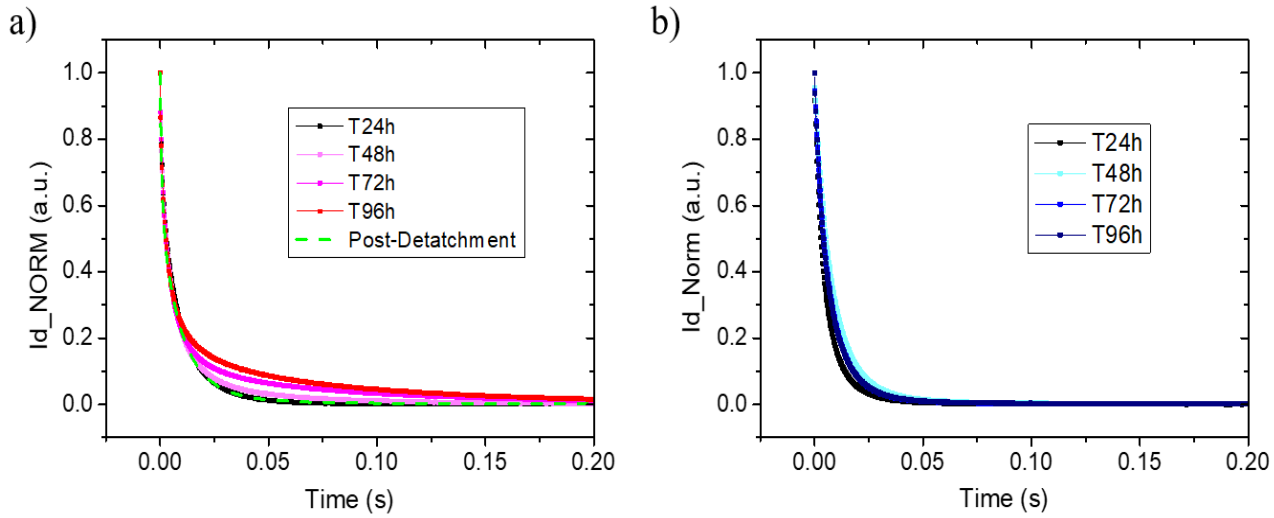

Figure 4.10: Cut and normalized drain current modulation response for seeded (a) and bare (b) vertical OECTs at different time of incubation, using complete DMEM as electrolyte. The green dashed line in (a) is the response after 20 minutes from the addition of Trypsin-EDTA, that detached the cells from the underneath substrate, thus enabling the recovery of OECT standard time response.

Moreover, taking the raw data of current modulations at different times for a vertical device without cells, the choice of the time response as meaningful parameter was confirmed, rejecting $\Delta I_{ds}/I_{ds}(0)$, where $I_{ds}(0)$ is the current value before the pulse and ΔI_{ds} the difference between the current before and during the pulse (once it has reached a steady-state value). Indeed, Figure 4.11 presents the raw current modulation data for a vertical OECT without cells: this data show that the transistor current intensity slightly changes over time, while it is immersed in the culture medium (electrolyte). Thus, this parameter can not be used to monitor cell layer formation due to its instability in time even without cells seeded on the device. Differently, the time response has proved to be stable for devices immersed in medium over 4 days (Figure 4.10b) and dependent on cell tissue coverage (Figure 4.10a).

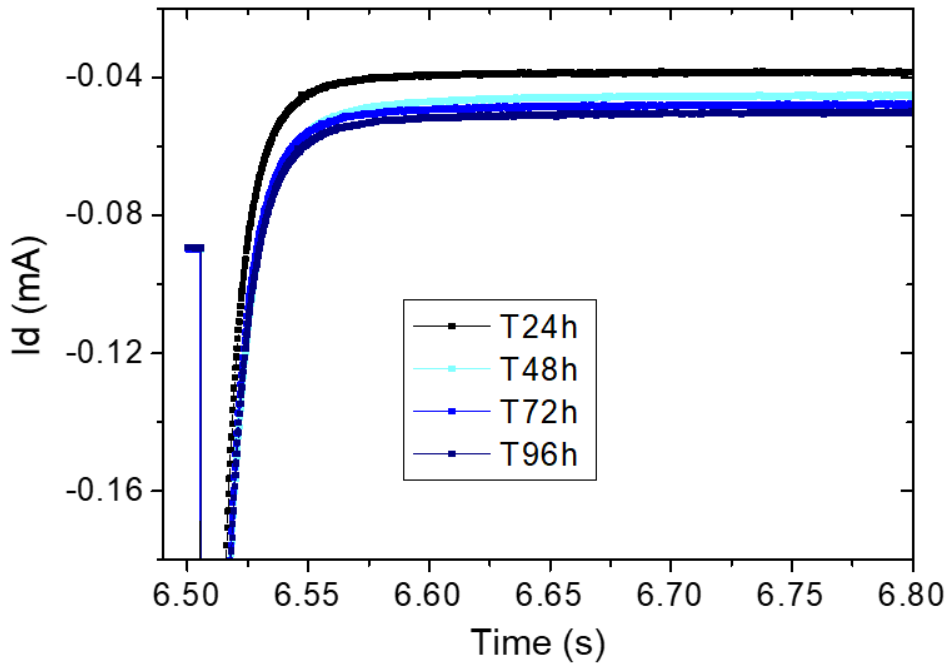

Figure 4.11: Raw data of current modulation upon the application of a positive pulse on the gate electrode (V_g = 0.3V) for a vertical OECT over different times incubated in complete medium without cells.

Human epithelial colorectal cells grown on a vertical OECT were monitored with continuous electrical measurements and the OECT time response, extracted as explained in paragraph 3.2.2, over

time (red dotted line) is reported in Figure 4.12, together with the time response of an OECT in medium inside the incubator without any cell seeded on it (black dotted line). Data are normalized to the value before the seeding at the beginning of the experiment with complete medium as electrolyte. The bare OECT measurements have been inserted in the graph in order to further prove the time response stability of a bare device in time and to compare this behaviour with the cell-conditioned one. As can be seen, the growth of Caco-2 cells over OECT channel slows down the device modulation of the drain current upon the gate pulse, increasing the τ (defined in paragraph 3.2.2) value extracted. Cell layer formation thus is confirmed to hinder the ions in the medium entering into the PEDOT:PSS conducting channel, giving a correlation between cell layer coverage and the OECT output. Indeed, the optical images below, taken at different time during growth, validate the electrical results, proving that the device time response follow the tissue coverage on top of PEDOT:PSS. Quantitatively, τ undergoes an increase of nine times once achieved a confluent cell layer (96 h from seeding), compared to the starting situation with no cells.

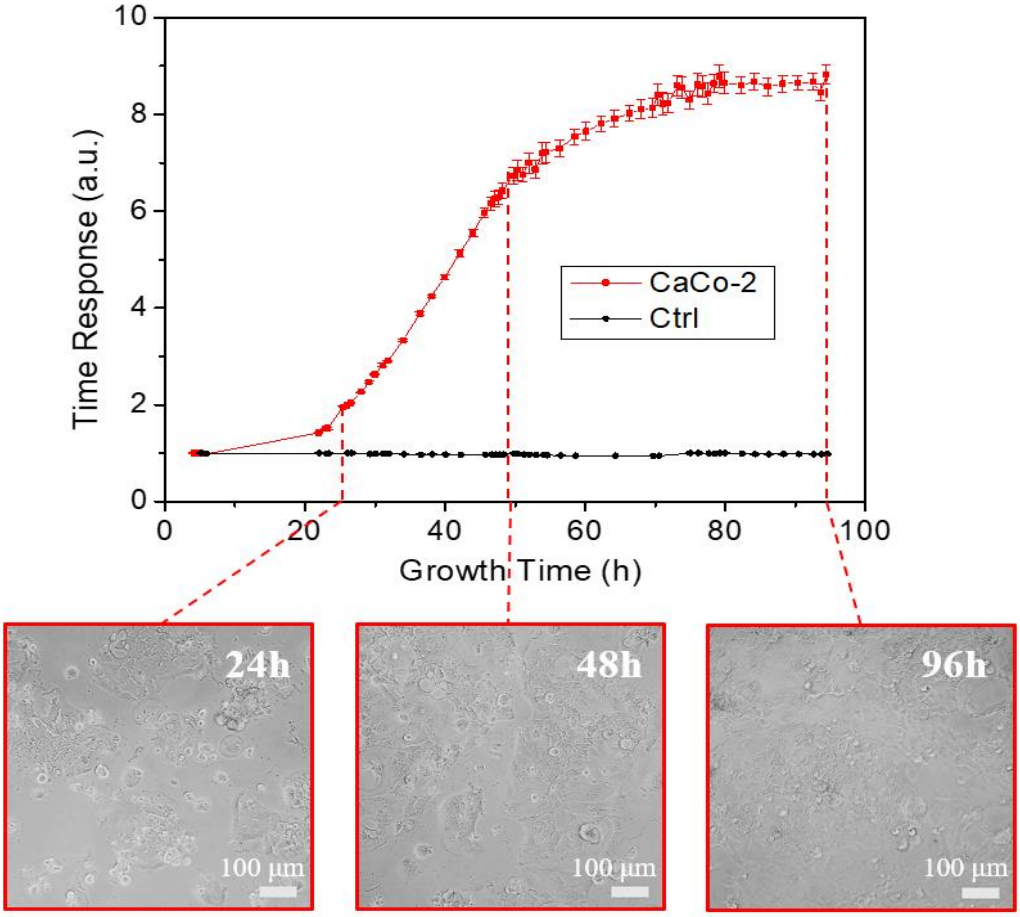

Figure 4.12: Electrical and optical measurements of OECT in vertical configuration seeded with Caco-2 (red dotted line) and only immersed in complete medium (black dotted line). The time response data are normalized as τ/τ_0, where τ_0 is the time response taken before seeding.

In order to prove Caco-2 influence on the OECT response, detachment experiments were performed by adding trypsin-EDTA after the achievement of a confluent layer on the devices. As explained in paragraph 3.4.3, trypsin and EDTA inactivate the adhesion molecules and integrins of cells to the layer underneath, making the device active area free from cells, which start floating in the medium. With continuous monitoring of the OECT time response, a real-time analysis of the cell layer TJ disruption and subsequent detachment from the PEDOT:PSS surface was achieved, as reported in Figure 4.13 (red dotted line). In the curve trend it is possible to highlight two different regions: the former is the region in the first 150 s, where there is an abrupt drop of the time response (device gets

faster, as ions pass easily through the cell coverage), caused by the breaking of the tight junctions that previously connected Caco-2 cells (and hindered paracellular ion flow); the latter region regards the following 17/18 minutes, where a slight decrease in the τ value is observed due to the layer slowly detaching from the substrate. The possibility to discriminate between these two regimes is achieved due to the high time resolution (1 point each 2 s) provided by the electrical monitoring obtained using the TECH-OECT setup and the custom-made Keysight program. In the detachment experiment, the modification of the cell area coverage results much faster compared to the cell tissue growth. Indeed, trypsin action require 20 minutes to detach more than half of the cell layer from the substrate, without mechanical or shaking action (that is usually performed for cell splitting). Again, possible effect of trypsin-EDTA on PEDOT:PSS are investigated performing control experiment on vertical OECTs without cells (black dotted line, Ctrl). As can be seen from the stable time response value in the graph, these agents do not affect the polymer nor the device operation. Optical images are taken before and after the treatment to validate electrical results: the uniform layer (96 % of coverage) and the cleaned PEDOT:PSS area (with only a 33 % of coverage) are shown below in pink and cyan border, respectively, and are highlighted in the graph with the same colours.

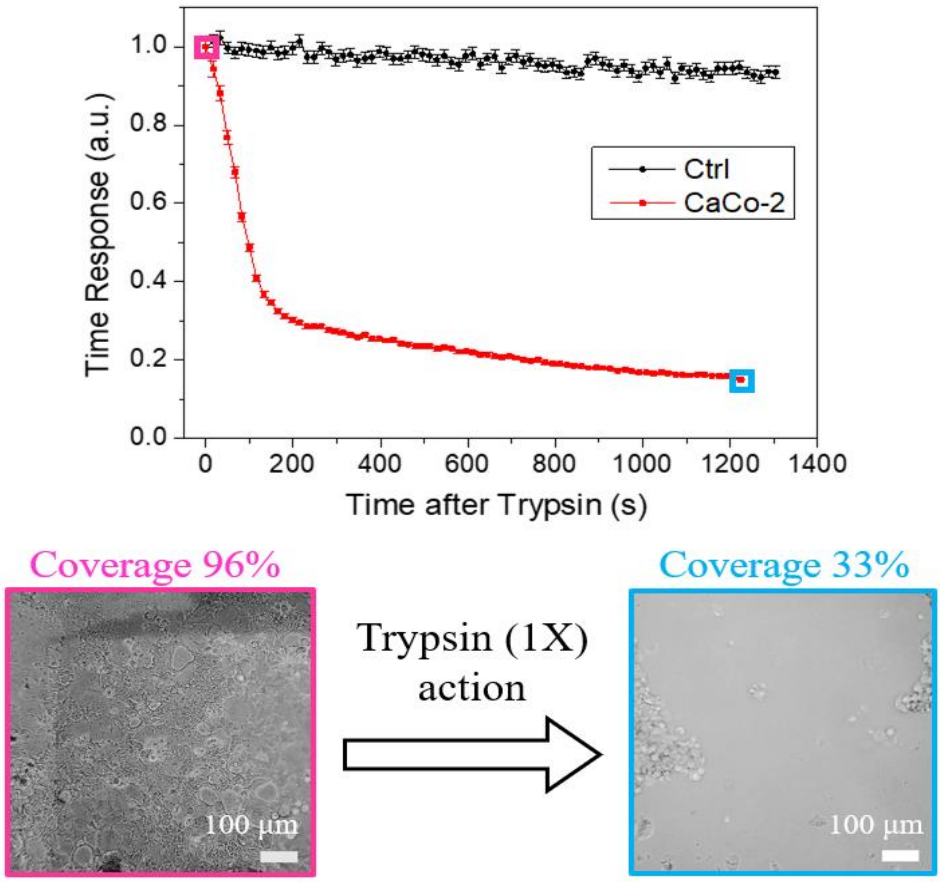

Figure 4.13: Cell detachment electrical and optical measurements with trypsin-EDTA (1X) for vertical OECT after the formation of a confluent layer of Caco-2 (red dotted line) and for a bare device (black dotted line), used as a control. Data are normalized as τ/τ_0, where τ_0 is the time response of the device before the trypsin addition (confluent layer for the red line and bare device in complete medium for the black line). Optical images are taken before and after 20 minutes of trypsin addition, with coverage counting of the cell still present on the PEDOT:PSS active areas

A better understanding of the potential of OECT devices as cell tissue integrity sensors has been developed studying the behaviour of two different devices, where the addition of trypsin to the medium led to a normal and a weak detachment. Figure 4.14 reports the τ response after the addition of trypsin over 10 minutes. The curve trend is the same for both the devices, showing again a first TJ breakage and a slower detachment of the layer. Noteworthy, the final normalized τ value is however

different between them, but clearly correlated to the optical counting of the cell coverage left on the device. Dev2 (green), where the trypsin probably failed in a complete cell layer detachment (coverage of 63 %), has a reduction of the time response of the OECT of ~ 40 % of its initial value (confluence). On the other hand, Dev1 (blue) shows a time response reduction of 80 % compared to the situation with cell confluence and its final coverage is indeed lower (33 %). It can be noted that for a double value of the optical coverage, the final time response is halved, thus giving the opportunity to use this system in future as a coverage counting device, after a proper calibration of these correlated parameters.

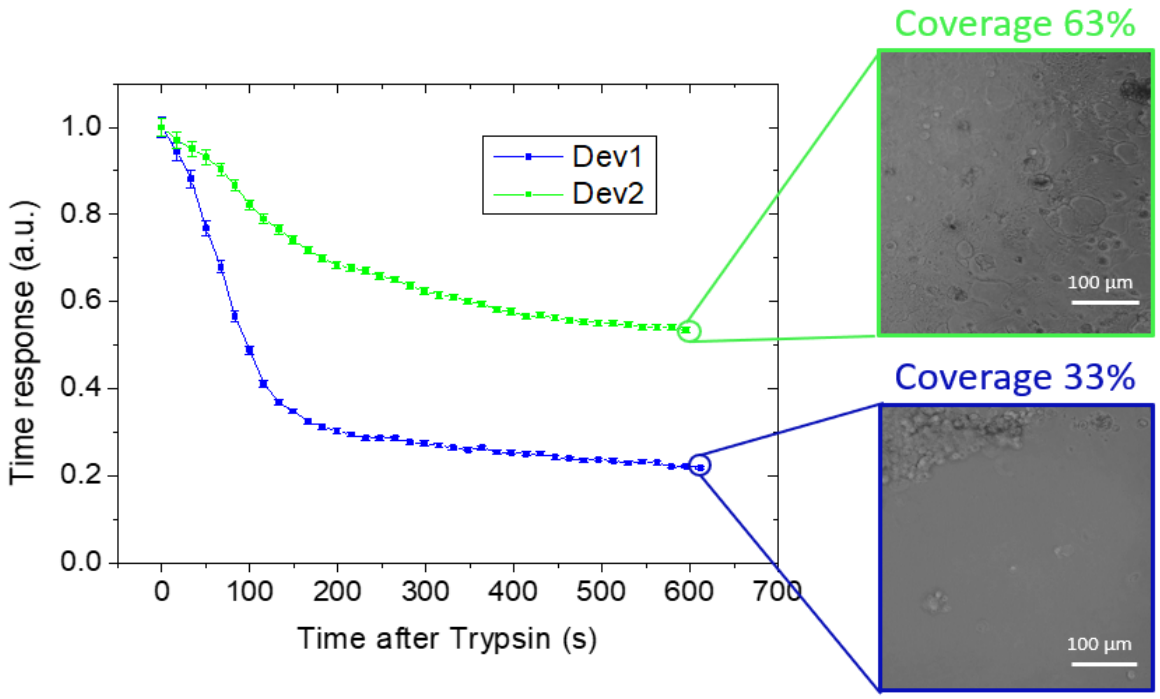

Figure 4.14: Caco-2 detachment experiments on vertical OECTs, where trypsin had a milder (green dotted line) and normal (blue dotted line) effect. Data are normalized as τ/τ_0, where τ_0 is the time response of the device covered with a confluent Caco-2 layer. Optical images are taken after 10 minutes of trypsin addition, with coverage counting of the cell still present on the PEDOT:PSS active areas.

Finally, even though these devices were meant as disposable sensors, especially for the preliminary studies, the device time response recovery was tested after the detachment of the cell layer. Figure 4.15a and 4.15b report electrical measurements of Caco-2 growth and detachment, respectively, on a vertical OECT. The Caco-2 growth is reported with few points because the interest relied only on the starting and final τ value. Time response without any cells is (12.4 ± 0.1) ms, in agreement with the previously obtained value. Once the confluence layer is reached the final time response is about 80 ms: indeed, it is (77 ± 1) ms in the last measurement at the end of the growth and (80 ± 2) ms before the addition of trypsin. After the addition of trypsin-EDTA the known trend with two different slopes is reproduced by the OECT, finally reaching the value of (11.1 ± 0.1) ms after 20 minutes. This value is very close to the pre-cell OECT time response and the device can thus be considered having an optimal recovery after the tissue layer detachment, taking into account small variations that can be ascribed to the slight medium concentration changes (due to trypsin addition or the reduction of cell nutrients) and the cell still suspended in the medium or fallen on the semiconducting channel.

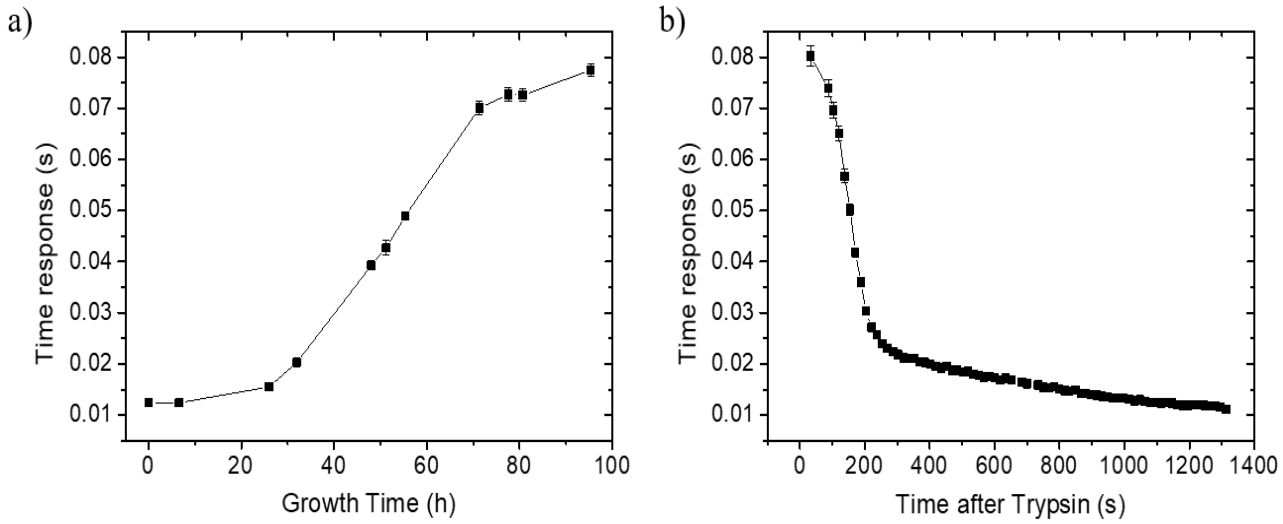

Figure 4.15: Electrical measurements for Caco-2 growth (a) and detachment (b) on a vertical OECT. Data are not normalized, showing the recovery of the device starting τ, after the cells are detached from the PEDOT:PSS active area.

In order to test the devices using a more challenging cell line, NIH-3T3 were seeded on top of the OECTs to study their growth with combined electrical and optical measurements (Figure 4.16). Differently from Caco-2, NIH-3T3 does not form TJs and have a very low transepithelial electrical resistance, whose value was not present in literature to our knowledge. For this reason, fibroblast growth was not detect by vertical OECTs: indeed, Figure 4.16 shows that device response was not affected significantly (blue dotted line) from NIH-3T3 growth and the curve trend is comparable to the bare (no cells) OECT behaviour (black dotted line), taken as a control in every experiments. Optical images were taken to assess the growth of the cell line on the OECTs, proving that the cell reached a confluent layer after 72 hours from seeding, faster than Caco-2, according to their growth rate and body size.

To further confirm vertical OECT inability to monitor NIH-3T3 (no barrier cell), also the fibroblast detachment from substrate was electrically studied (Figure 4.17): as for the growth experiment, vertical OECTs responded to fibroblast detachment (blue dotted line) with variations similar to bare device response (black dotted line). Thus, even though optical images confirmed the complete detachment of cell layer from PEDOT:PSS active area, OECTs in vertical configuration are not suitable to detect this event. Noteworthy, compared to Caco-2 detachment, fibroblasts seems more affected by trypsin-EDTA addition and a final coverage of 3.5 % is reached in 20 minutes (while 33 % was obtained for the Caco-2), probably due to the non-barrier nature of this cell line, which renders them easier to detach.

In conclusion, vertical OECTs proved to be suitable smart devices to electrically measure growth and detachment of Caco-2 cell layer on top of the active areas of the devices (being able to follow both processes and discriminating from a normal and a milder trypsin interaction with the cell layer), while NIH-3T3 do not alter significantly OECT transient response. This, as introduced in the previous paragraph, is probably due to the choice of the active area of these transistor (3 mm^2): according to Salleo's model,[31] these OECTs were able to monitor cell tissue integrity of cell lines whose electrical resistance at the confluence was over 5 $\Omega \cdot cm^2$, close to currently available TEER measuring device limit. Since NIH-3T3 TEER is not found in literature, the value is probably lower than 5 $\Omega \cdot cm^2$, thus correctly not detectable from vertical OECTs.

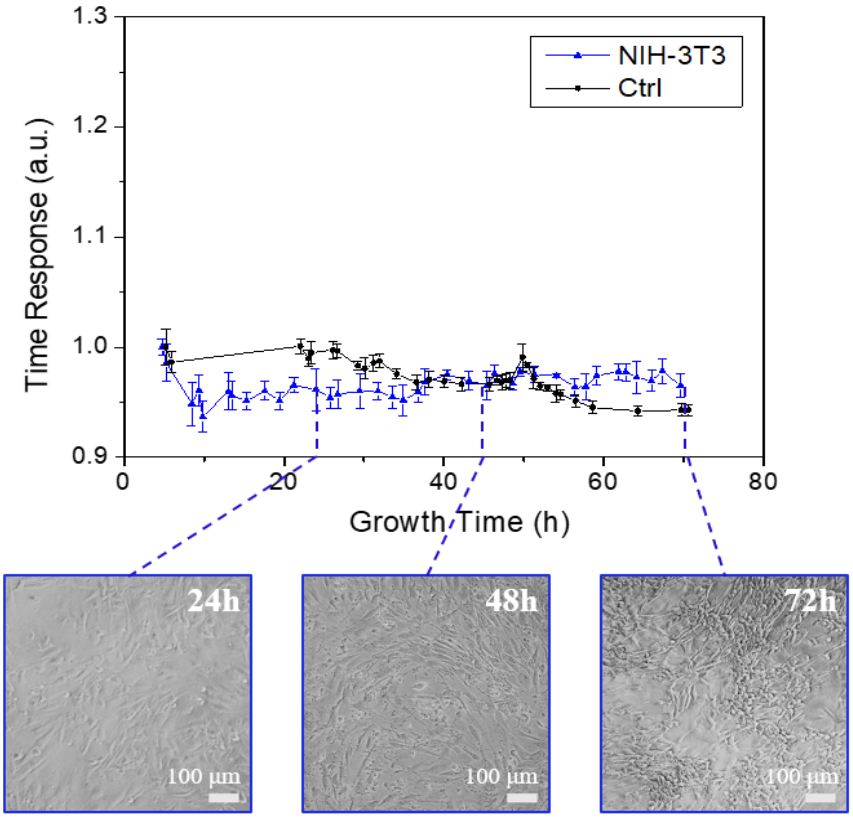

Figure 4.16: Electrical and optical measurement of OECT in vertical configuration seeded with NIH-3T3 (blue dotted line) and only immersed in complete medium without cells (black dotted line). The time response data are normalized as τ/τ_0, where τ_0 is the time response taken before seeding.

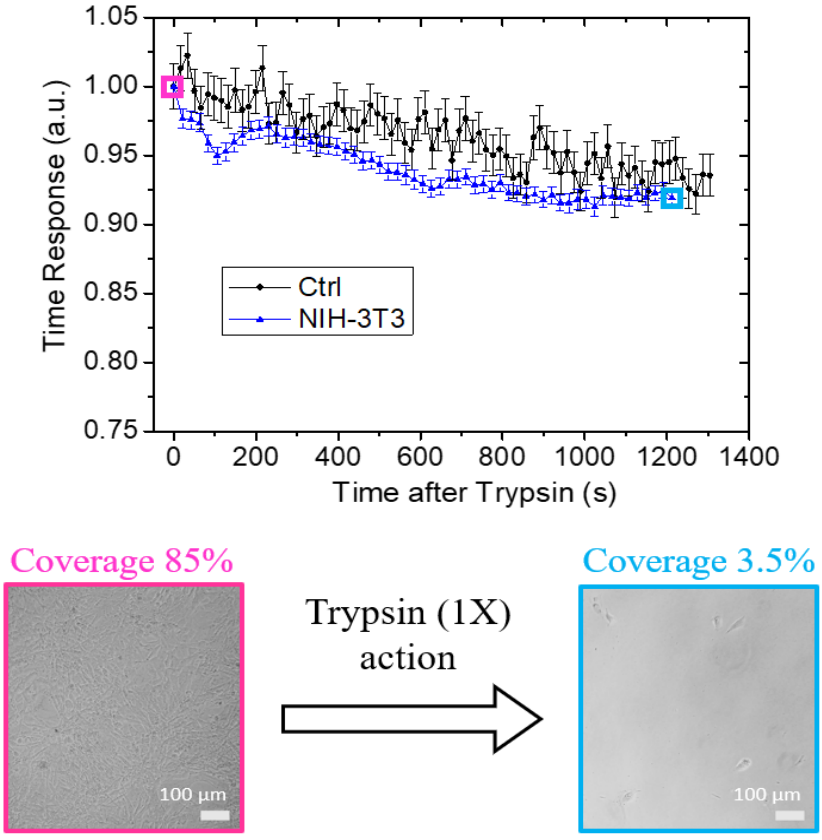

Figure 4.17: Cell detachment measurements with trypsin-EDTA (1X) for vertical OECT after the formation of a confluent layer of NIH-3T3 (blue dotted line) and for a bare device (black dotted line), used as a control. Data are normalized as τ/τ_0, where τ_0 is the time response of the device before the trypsin addition (confluent layer).

4.3.2 Planar configuration

The OECT configuration was also implemented in a planar device, easier to fabricate due to the simple spin coating of both channel and gate areas. Channel active areas are again 3 mm^2. Averaging four bare planar OECT time responses in cell culture medium (DMEM), the extracted τ was (10.1 ± 0.9) ms, similar but slightly faster compared to the vertical configuration.
Figure 4.18 reports a comparison between the normalized current modulation after the positive pulse on the gate for a Caco-2 seeded (Figure 4.18a) and a bare (Figure 4.18b) planar OECTs over time. As for the vertical configuration, Caco-2 seeded on the device (in this configuration over both gate and channel) change the time response of the OECT, as can be seen moving from black line to the red one in Figure 4.18a, while this parameter results unaffected in the culture medium over time (Figure 4.18b). Moreover, also the recovery of the device after the trypsin treatment (green dashed line) is maintained. Noteworthy, the human colorectal epithelial influence on OECT time response variations are much higher for the planar configuration compared to the vertical one, as can be already confirmed comparing the normalized I_d cuts in Figure 4.18a and Figure 4.10a.

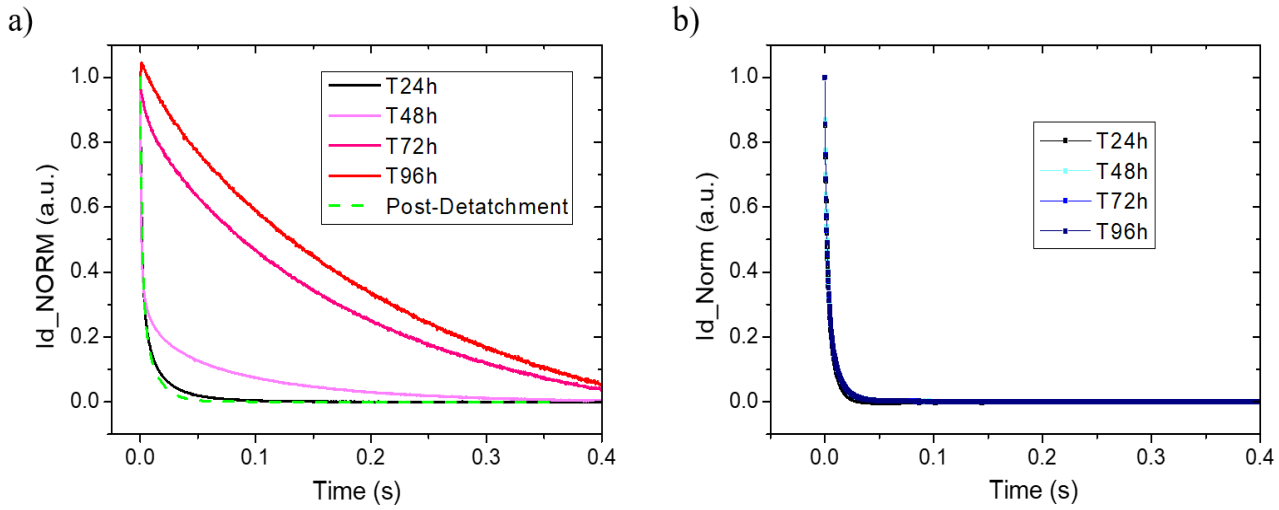

Figure 4.18: Cut and normalized drain current modulation responses for seeded (a) and bare (b) planar OECTs at different time of incubation, using complete DMEM as electrolyte. The green dashed line in (a) is the response after 20 minutes from the addition of Trypsin-EDTA.

The time response was then extracted and plotted for the growth (Figure 4.19) and detachment (Figure 4.20) of Caco-2, as previously done for the vertical configuration, normalizing with the same criteria. The planar configuration proves to be able to monitor Caco-2 layer formation and detachment (in red in the graphs), displaying τ increase and decrease well distinct from the bare OECT control (in black in the graphs). As before, data are validated with optical images. Moreover, two important aspects can be noted: 1) human epithelial cells growth maintains the same trend as for the vertical configuration, but reaches a higher final time response increase (being almost 20 times higher compared to the value extracted before seeding); 2) the trypsin action seems to be less effective on cell layer detachment for planar device, giving a final coverage of 68 % of the substrate. In particular, regarding the former observation, the τ parameter is almost two times greater than its vertical counterpart, confirming the double passage of ions across the adhered and tight cell layer present on OECT channels and gates, enhancing (possibly doubling) device sensitivity. As for the latter aspect, further investigations are needed to understand if the trypsin action results milder for surfaces with larger area covered in PEDOT:PSS. However, the device time response stops decreasing at 0.55 (decreasing only 45% of the initial value) for the 68% of coverage, thus indicating that the PEDOT:PSS areas are still more than half covered.

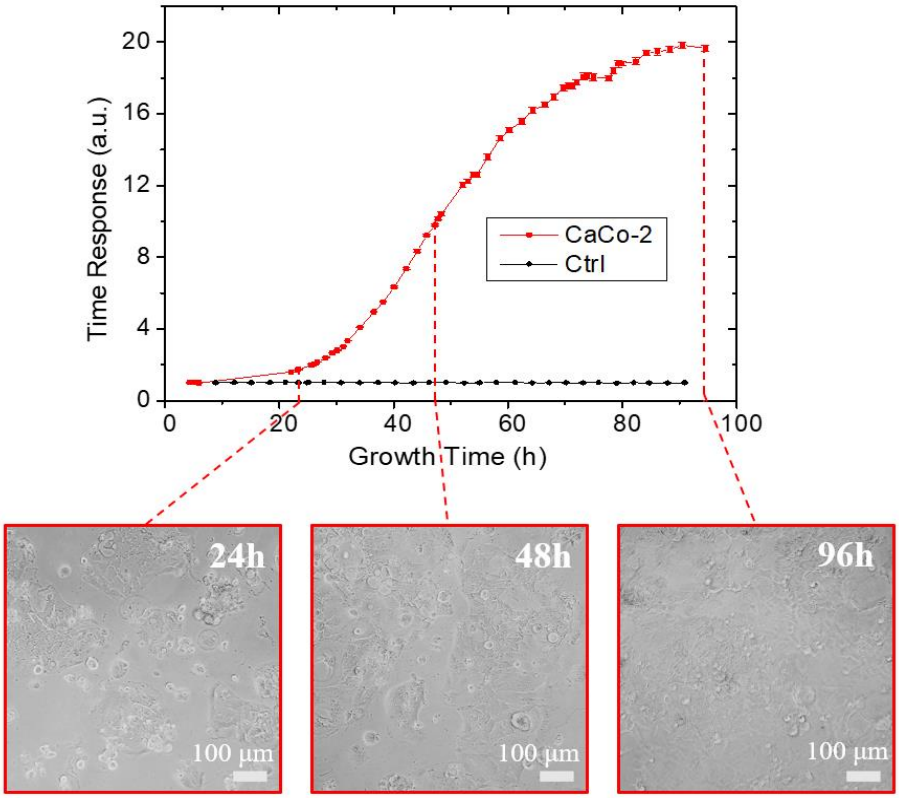

Figure 4.1939: Electrical and optical measurement of OECT in planar configuration seeded with Caco-2 (red dotted line) and bare (black dotted line) in complete medium.

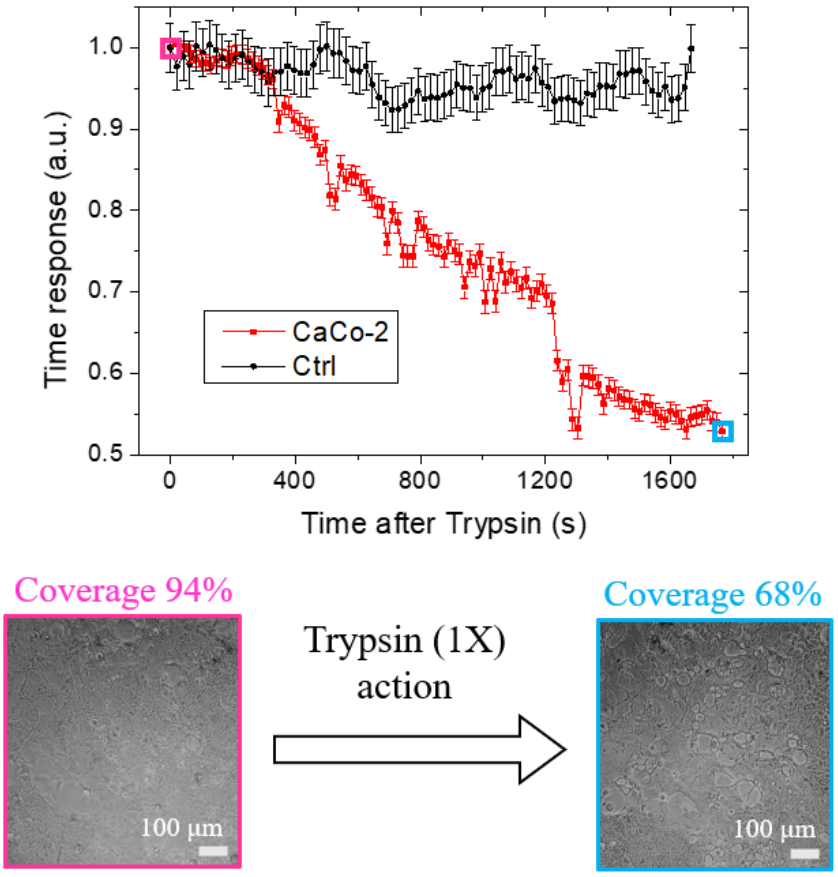

Figure 4.400: Cell detachment measurements with trypsin-EDTA (1X) for planar OECT after the formation of a confluent layer of Caco-2 (red dotted line) and for a bare device (black dotted line), used as a control.

Finally, planar devices were employed for studying fibroblast growth and detachment, reported in Figure 4.21 and 4.22, together with the optical micrographs to validate the results. Noteworthy, planar configuration proves to be capable of monitoring both NIH-3T3 growth and detachment, even though they provide lower increment and decrement, respectively, of the parameter τ. Growth experiment for example shows, after a mild slow down of the device, a final dynamic response that results 1.20 times higher than the bare OECT before the seeding, caused by the formation of the fibroblast layer on both the active channel and gate areas. This smaller variation compared to Caco-2 growth can be explained reminding the non-barrier nature of NIH-3T3, which do not form tight junctions and have bigger intercellular spaces, as shown by the fluorescence images in paragraph 4.4.2. Nevertheless, planar devices can be used to monitor this cell line, obtaining small increment in the time response of the OECT, unseen in the vertical configuration: as previously explained, the planar OECT allows for a dual passage of ions through the cell layer, i.e. from the gate to the medium and from the medium to the channel. The double crossing (see Figure 4.8) let the device detect and study cells with lower TEER compared to the vertical counterpart, because of the doubling of the impedance value of the cell layer. According to this theory, NIH-3T3 can be ascribed in the range between 3-5 $\Omega \cdot cm^2$ which, according to Salleo's model,[31] is lower than the optimal regime for the vertical configuration but, doubled, would be detectable using these devices, as indeed happens with very small time response variations. On the other hand, focusing on the detachment experiment, the time response presents a fast drop in less than 5 minutes, after which there is the stabilization of the curve. Indeed, since fibroblast does not form tight junctions, having leak connection one to another, the action of trypsin-EDTA is stronger than for Caco-2, leading to a complete detachment of the cell layer. As a matter of fact, the final coverage calculated from optical images is 2.3 %.

The role of the OECT geometry and its active area is further confirmed considering the previous transcharacteristic curves of the devices in culture medium without cells (Figure 4.9): vertical and planar OECTs showed similar trends, since the difference reported here rely on how the geometry interfaces with cell tissue and in the single or double ion crossing of cellular layer.

In conclusion, OECTs demonstrated to be smart devices for real-time monitoring of even leaky-barrier or non-barrier cell lines, revealing small ion current changings (with time response enhancements or reductions), paving the way for studies and analysis on cells with unknown or not measurable TEER that represent more challenging but interesting systems.

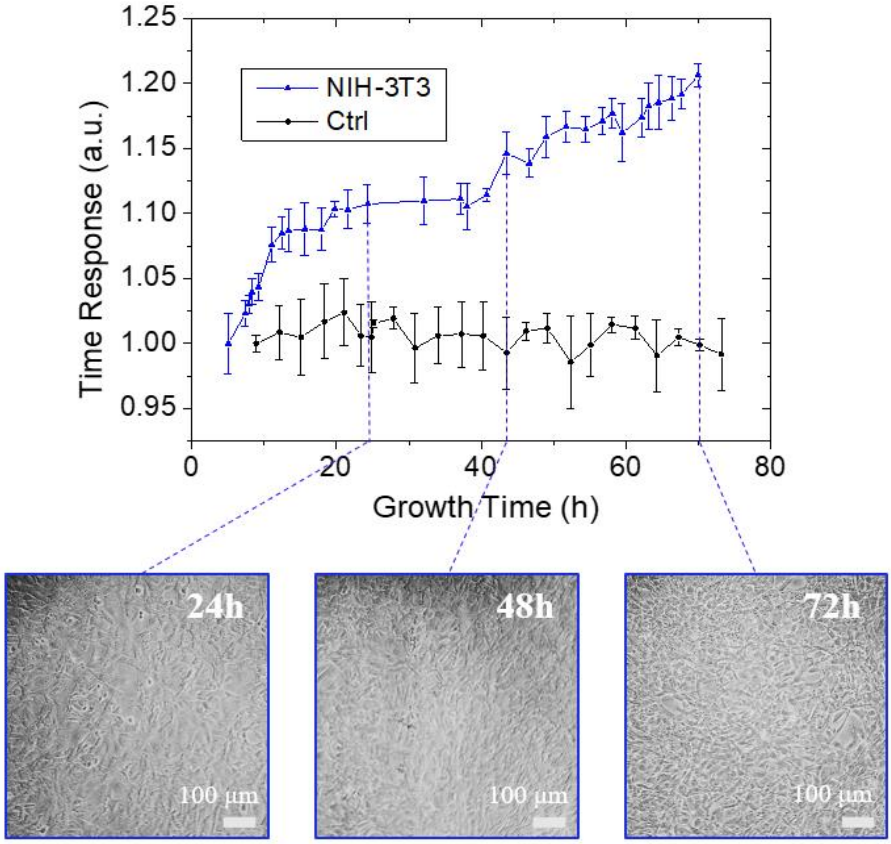

Figure 2.41: Electrical and optical measurement of OECT in planar configuration seeded with NIH-3T3 (blue dotted line) and bare (black dotted line) in complete medium.

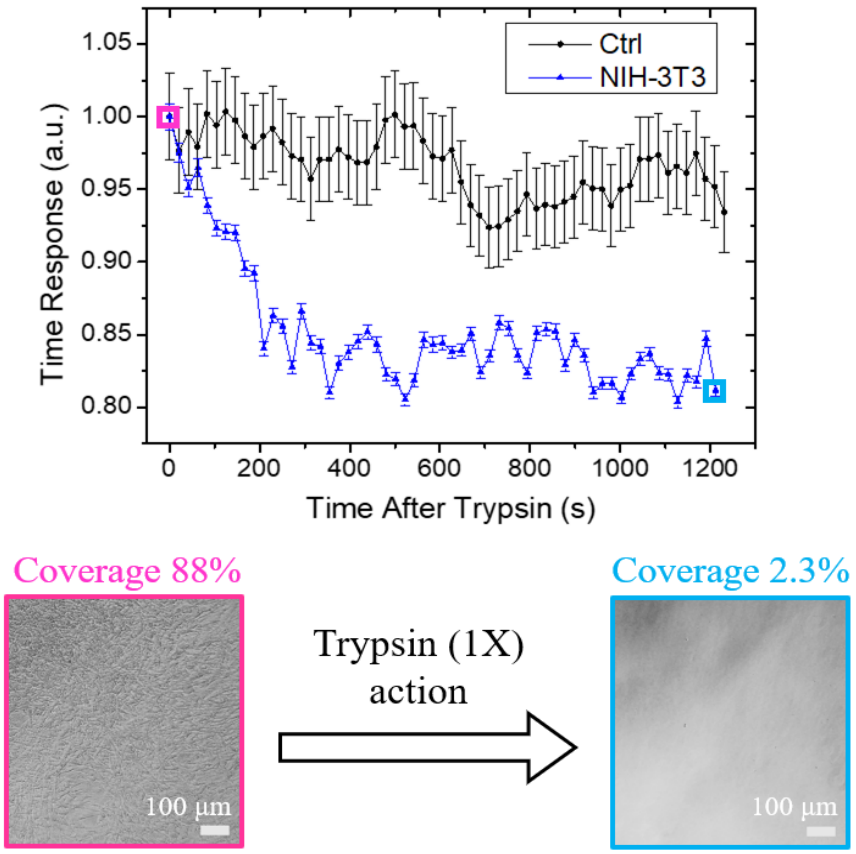

Figure 4.42: Cell detachment measurements with trypsin-EDTA (1X) for planar OECT after the formation of a confluent layer of NIH-3T3 (blue dotted line) and for a bare device (black dotted line), used as a control.

4.4 Toxicity assessment of silver nanoparticles

As stated in Section 3.5, nanomaterials have been applied in many different fields, although their impact on human health is yet to be understood. In particular, silver nanoparticles (AgNPs) are widely diffused in commercial products, due to their antibacterial and antifungal properties.[391]
The safety assessment of novel nanoparticles or novel nanomaterials must be validated with properly calibrated *in vivo* tests, however, *in vitro* models are still playing an important role for preliminary evaluation, due to their relative low cost and high statistical number of experiments. Beside several methods that can be used to assess cytotoxicity or cell *in vitro* viability, planar OECTs have been previously demonstrated (Section 4.3) to be reliable devices to monitor cell tissue integrity in real-time and with relatively high resolution (1 point each 2 s, thus assessing also fast biological processes).
Caco-2 and NIH-3T3 cell lines were chosen as cell models due to fact that they represent intestinal and skin "barrier" to external agents, respectively, thus tissues exposed to AgNPs from consumer products (food containers, cosmetics, bandages).
Finally, since the cytotoxic effect on NPs is strongly dependent from their properties, including size, shape and surface coating,[376] because they affect their biological identity[392] and their interactions with cells, citrate-coated and EG_6OH-coated AgNPs toxicity has been investigated. Indeed, according to the previous work of Barbalinardo *et al*,[393] cellular uptake and, subsequent, cytotoxicity of AgNPs in mouse embryonic fibroblast are affected by the NP surface coating and, in particular, citrate-coated AgNPs results toxic, while the passivation of the NP surface with oligo(ethylene glycol) (OEG)-alkanethiol leads to a non-toxic nanomaterial.
Experiments were performed inside the incubator using the TECH-OECT, as previously reported, employing only planar devices (thus having the capability of monitoring both cell lines). Cells were seeded at the beginning of the growth experiment and NPs or citrate solution were added after 24 hours, screening optically and electrically their influence on cells over the next 3 days. Measurements were performed with the same electrical parameters used in the previous Section and data are presented in the next paragraphs, starting from the control of NP influence on the measured OECT devices.

4.4.1 NPs interference with OECTs

Before starting the experiments with AgNPs on cells, their possible effects on planar OECTs were investigated, in order to being able to discriminate whether the device response was related to NPs toxicity on the cell line or the direct influence of NPs or citrate solution on OECT standard behaviour. OECT transcharacteristic curves were measured under the exposure of citrate- and EG_6OH-coated AgNPs, and after the addition of citrate solution, studying the channel (Figure 4.23) or gate (Figure 4.24) currents over the gate potential sweep (ranging from -0.5 V to 0.5 V to cover the parameters used for cell tissue integrity measurements). Data were collected before and after 24 h, 48 h and 72 h the agent addition, taking a bare control of a planar OECT in complete medium over time, without any additions (Figure 4.23d and Figure 4.24d). As can be clearly seen, neither the citrate solution (200 µl added, as control), nor 40 µg/ml of EG_6OH- and citrate-coated AgNPs influence the transcharacteristic curves of the device. Indeed, all the OECTs displayed the same trend as the one obtained for the device in standard complete culture medium without any additions, that shows a mild shift of the transfer towards lower current value due to the small conductivity decrease in the OECT channels within the first 24 h (Figure 4.23d). Similar variations are observed in the I_g versus V_g curves, where the hysteresis of the cycle increases with increasing immersion time for all the four

samples, independent from the addition (since it is present, in shorter times, also for the OECT immersed in complete DMEM, in Figure 4.24d).

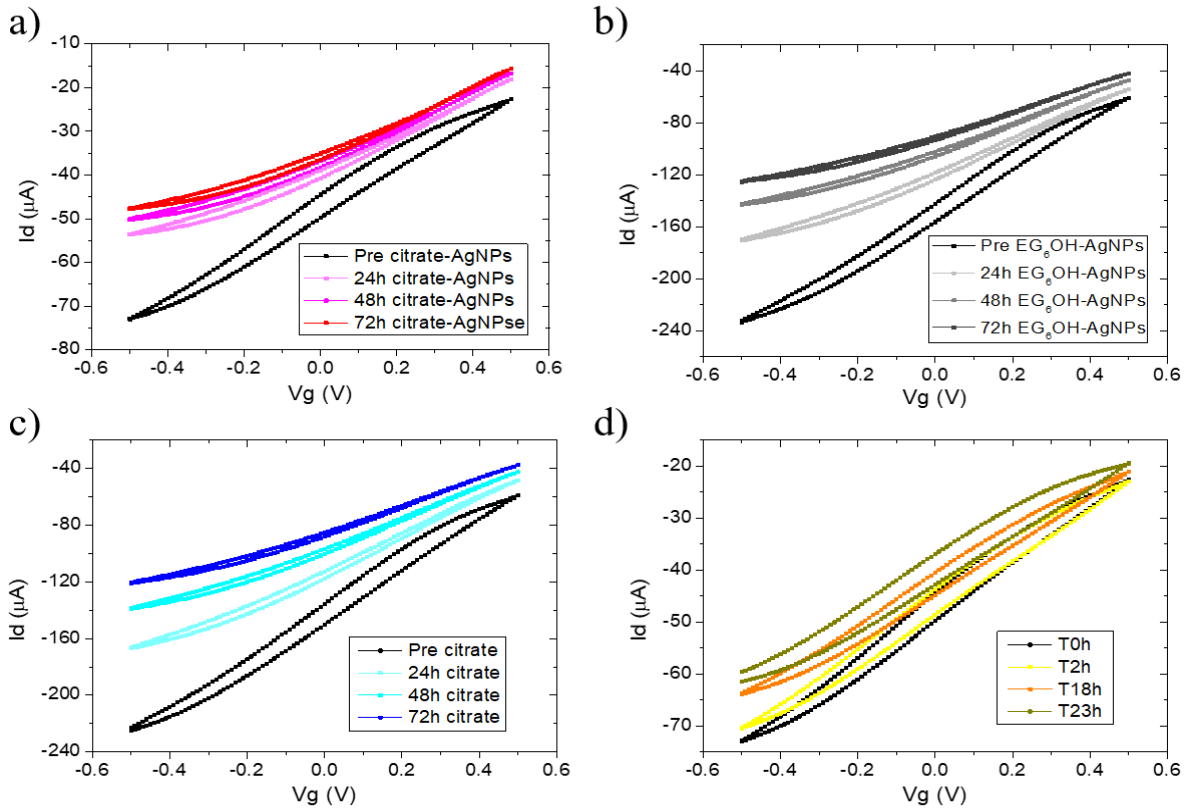

Figure 4.43: Trancharacteristic curve of planar OECTs before and 24h, 48h and 72h after the addition of citrate-(a) and EG_6OH-coated (b) AgNPs, citrate solution (taken as control) (c) and without any additions (d), using the complete medium as electrolyte.

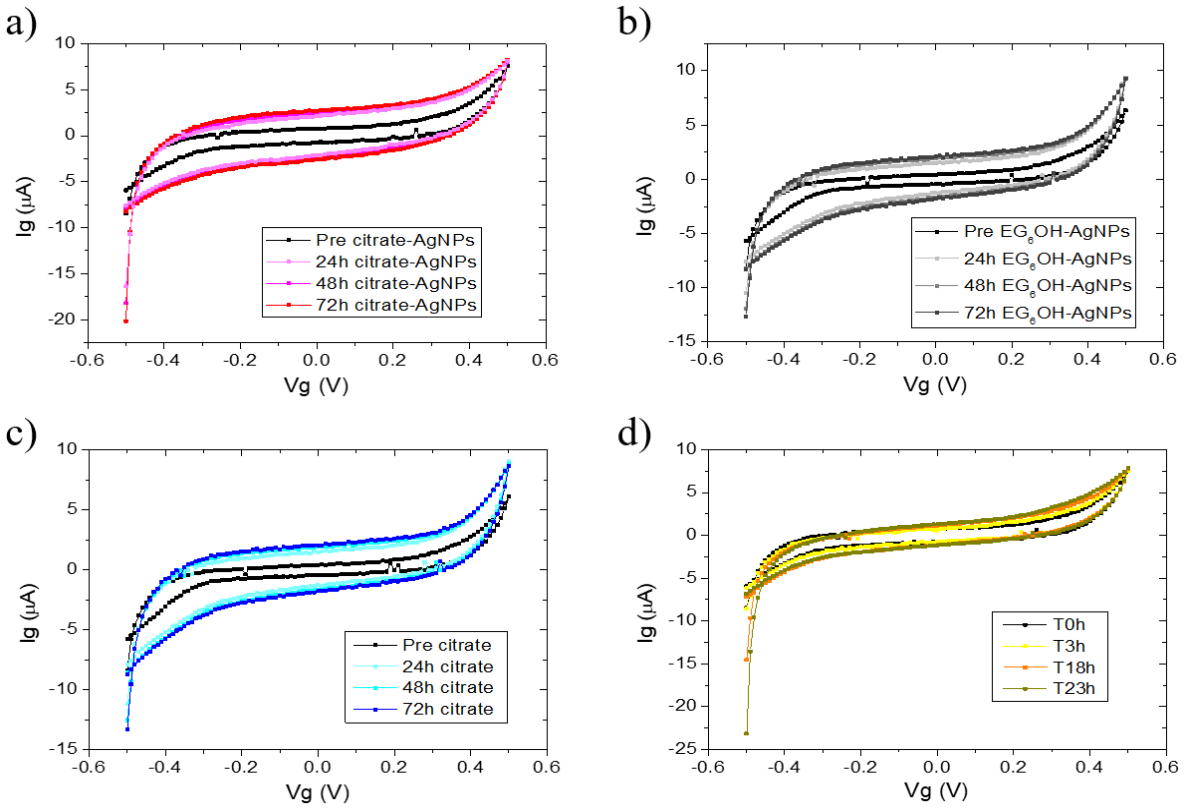

Figure 4.44: Gate currents versus gate potential obtained from transcharacteristic curves of planar OECTs, before and 24h, 48h and 72h after the addition of citrate-(a) and EG_6OH-coated (b) AgNPs, citrate solution (taken as control) (c) and without any additions (d), using the complete medium as electrolyte.

Furthermore, the NPs interference/interaction studies with OECTs were extended monitoring the device time response in simulated growth experiments without cells, but with the addition of 40 μg/ml of citrate- (Figure 4.25a) or EG_6OH- coated (Figure 4.25b) AgNPs or citrate solution (Figure 4.25c) after 24h from the beginning of the experiment. The reported results demonstrated that the normalized time response was not altered after the different additions (marked by a green arrow), except for small fluctuations that have already been seen in previous control measurements. Thus, τ again represents a stable parameter, unaffected by AgNPs or citrate solution, that can thus be reliably used to investigate cell exposed to AgNPs.

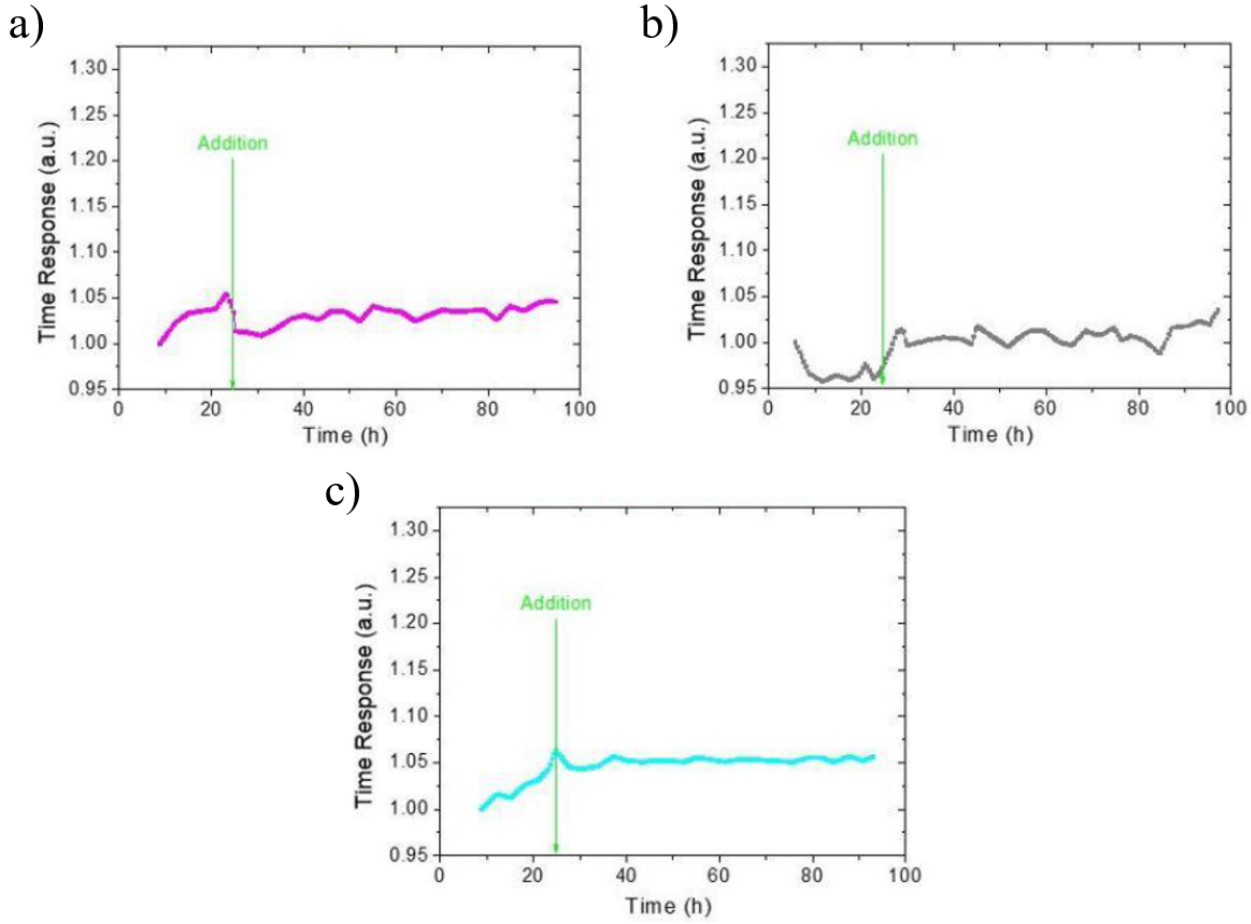

Figure 4.45: Electrical measurements of bare (no cells on top) OECT time response, adding after 24h citrate- (a) or EG_6OH- (b) coated AgNPs or citrate solution (c). The addition time is marked by a green arrow for all the graphs.

A final investigation of the OECT and nanoparticles possible interaction has been made with electrochemistry techniques, namely cyclic voltammetry (CV) and impedance spectroscopy (EIS). In these measurements, a saturated calomel electrode was employed as reference electrode and the gate of the devices as counter electrode, using the channel as working electrode under study. Figure 4.26 reports CV cycles for PEDOT:PSS channels upon the addition of citrate- (Figure 4.26a) or EG_6OH- (Figure 4.26b) coated AgNPs, or citrate solution (Figure 4.26c) and in complete medium over time. As can be clearly observed, citrate-coated silver nanoparticles addition in the cell culture media provoke oxidation and reduction peaks, that enhance with increasing exposure time. On the contrary, both the addition of the EG_6OH-coated AgNPs and the citrate solution do not alter the cyclic voltammetry curve of the system, being comparable with its electrochemical characterization in complete DMEM over time (Figure 4.26d). These results can be explained assuming that the silver present in the nanoparticles electrochemically reacts with PEDOT:PSS: indeed, the oxidation and reduction peaks are shown only for the AgNPs whose surface is not passivated with an oligo(ethylene

glycol) and can not be ascribed to citrate solution or PEDOT:PSS polymer thanks to the negative control.
Noteworthy, the oxidation peaks start at a voltage higher than 0.4 V, moving toward 0.35 V, while the reduction ones are kept at a stable value of 1.5 V. Moreover, all the three CV cycles are plotted, but only the first one clearly displays the electrochemical peaks, while the following have milder response. It is possible that the electrochemical reaction occurring between PEDOT:PSS channels and NPs, deplete the volume close to the channel of NPs, thus rendering the next cycle peaks less intense. This can also explain the increase of peaks over time: once added, AgNPs are homogeneously dispersed in the medium but gravity drives them to the bottom of the well, towards the sensitive part (channel) of OECT devices, thus enhancing its output response. This would mean that PEDOT:PSS electrochemical peak intensities are correlated to AgNPs concentration, thus introducing the possibility to exploit this system as an AgNP sensor. Indeed, the same trend is monitored using the electrochemical impedance spectroscopy with the described sample (Figure 4.27): again, citrate-coated AgNPs alter the PEDOT:PSS EIS spectra in the Nyquist plots (Figure 4.27a), shifting it towards higher real impedance values over incubation time, while only slight variations are present for the introduction of EG_6OH-coated AgNPs (Figure 4.27b), citrate solution (Figure 4.27c) or for the sample where no additions were done (Figure 4.27d).
However, further investigations need to be carried out to properly understand this mechanism and, eventually, connect the NP concentration to the electrode response but this goes beyond the purposes of this thesis and will be the subject of future works. A step towards the sensor development was done studying the difference in the spectroscopic results upon the application of a positive bias of 0.3 V to the working electrode: unfortunately, the Nyquist plots, reported in Figure 4.28, display a shrunk variation of the impedance with citrate-coated AgNPs over time (thus, hypothetically, over concentration), confirming the use of the standard impedance with 0 V as possible future detection technique.
Noteworthy, only electrochemistry measurements report variations due to the AgNPs presence and should be avoided if the cell health and tissue integrity wants to be investigated upon NPs exposure. Thus, the standard OECT time response was used for the electrical studies, since it was previously demonstrated in Figure 4.25 that it is not affected by any of the substances introduced in the system for this work.

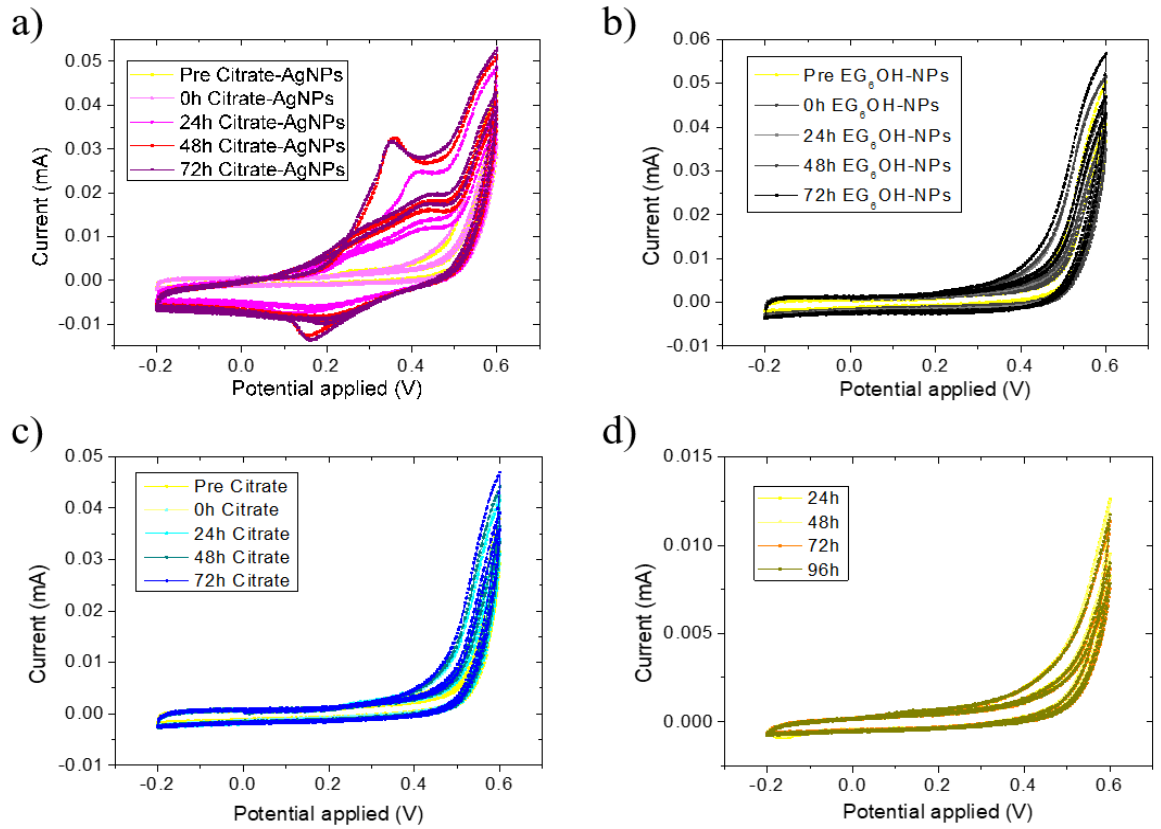

Figure 4.46: Cyclic voltammetry curves (three cycles) on PEDOT:PSS electrodes (used as working electrode), upon the exposure to citrate- (a) or EG_6OH- (b) coated AgNPs, citrate solution (c) or without any additions (d). PEDOT:PSS gates were employed as counter electrode and the complete DMEM medium as electrolyte.

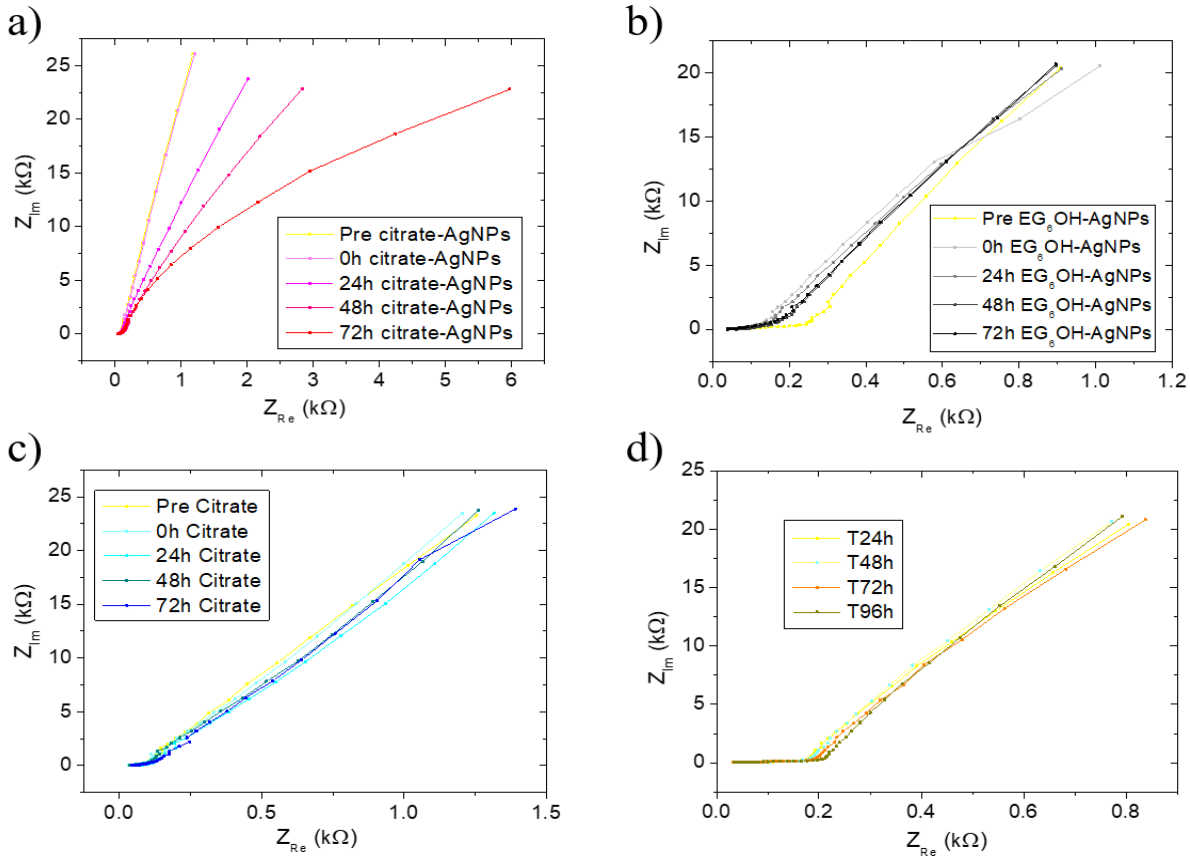

Figure 4.47: Nyquist plots of electrochemical impedance measurements on PEDOT:PSS electrodes (used as working electrode), upon the exposure to citrate- (a) or EG_6OH- (b) coated AgNPs, citrate solution (c) or without any additions (d). PEDOT:PSS gates were employed as counter electrode and the complete DMEM medium as electrolyte.

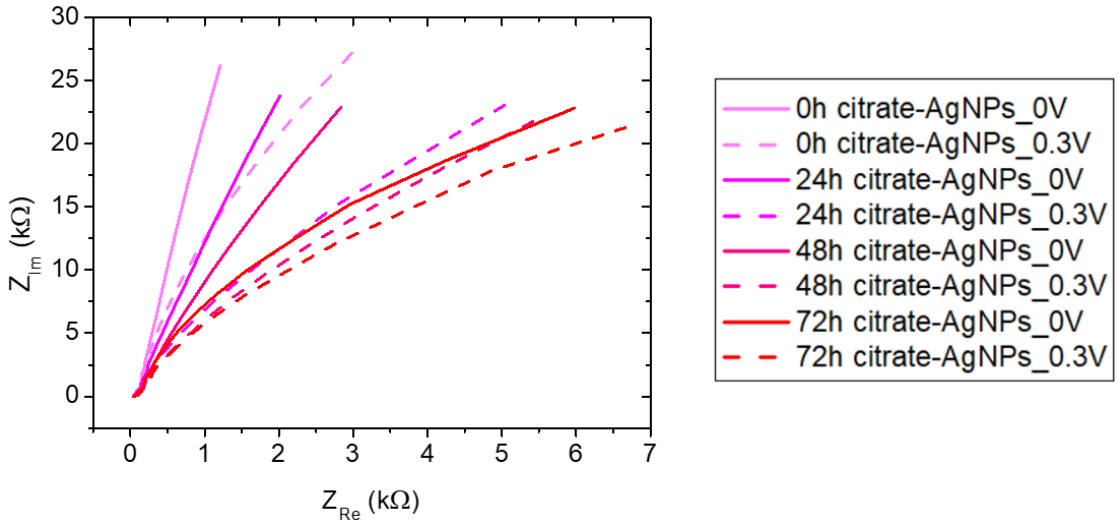

Figure 4.48: Nyquist plots of electrochemical impedance measurements on PEDOT:PSS electrodes upon the exposure to citrate-coated AgNPs, applying a bias on the working electrode of 0 V (solid lines) or 0.3 V (dashed lines).

4.4.2 Viability tests

In order to validate electrical data and assess the influence of nanoparticles on NIH-3T3 and Caco-2 cell lines, viability tests were performed using MTT assays, together with optical micrographs taken to investigate the layer integrity and fluorescent images to study cell morphology (which will be reported also in the following paragraphs).

MTT assay technique is explained in paragraph 3.4.2 and the results obtained over the two cell lines are shown in Figure 4.29a and 4.29b for Caco-2 and NIH-3T3, respectively. Here, the data are averaged over several measured and unmeasured devices after 72 hours of NPs treatment (since it was previously demonstrated in Figure 4.4 that the electrical measurements do not alter the cell viability), while the control value is taken for cells grown 96 h in a complete DMEM solution with a replacement of 200 µl with citrate solution, since fluorescent images shown that cell morphology is not affected from the diluted citrate solution in the DMEM medium (Figure 4.29c and Figure 4.29d for human colorectal epithelial and fibroblast cell lines, respectively). Indeed, actin cytoskeleton is not shrunk nor injured, but reports the standard integrity, as previously seen in Figure 4.7. Noteworthy, both cell lines grow healthy when treated with EG_6OH-coated AgNPs, with a slightly lower viability for NIH-3T3, which is still above the 80 %, chosen as ill/healthy cell culture threshold. On the opposite, citrate-coated AgNPs clearly introduce a toxic effect on cell lines with huge drops of the Caco-2 (value is halved compared to the control) and NIH-3T3 (only a third of the control) viabilities.

Moreover, optical images are reported in Figure 4.30: the first line show the destruction of the Caco-2 layer upon 72 hours of citrate-coated AgNPs treatment (Figure 4.30a), while Caco-2 growth results completely unaltered for EG_6OH-coated AgNPs (Figure 4.30b) and the addition of citrate solution (Figure 4.30c), forming a confluent, uniform layer without empty spaces. The same consequences are shown in Figure 4.30d, 4.30e and 4.30f for NIH-3T3 cell line, for citrate-, EG_6OH-coated AgNPs and only citrate additions, respectively, further confirming the previous fluorescent results and MTT assays.

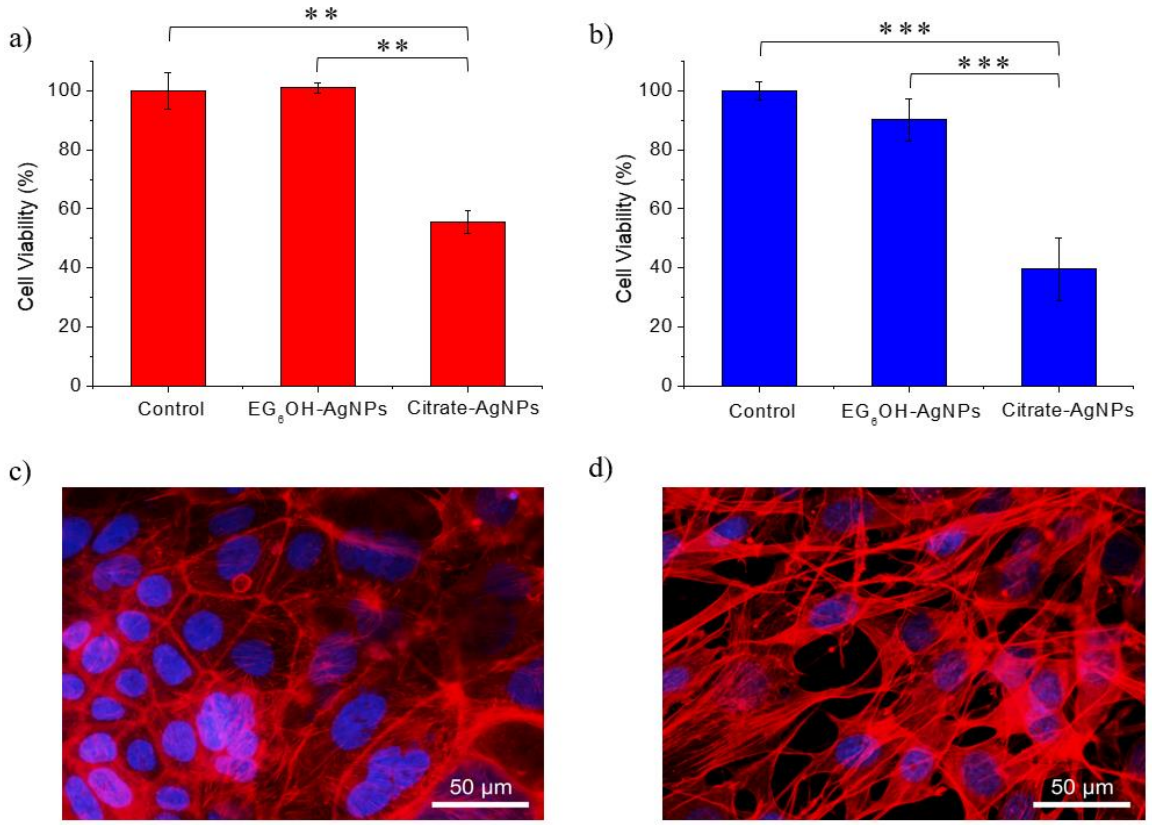

Figure 4.29: Cell viability of Caco-2 (a) and NIH-3T3 (b) cell lines after 72 hours of exposure to 40 µg/ml of citrate- or EG_6OH-coated AgNPs, with the control taken as a standard growth were 200 µl of medium were replaced with the same amount of citrate solution. Data are presented as mean ± standard deviation while the statistical analysis were performed with ANOVA followed by Turkey's test. **$p < 0.005$ and ***$p < 0.001$ denote significant differences with respect to the control.

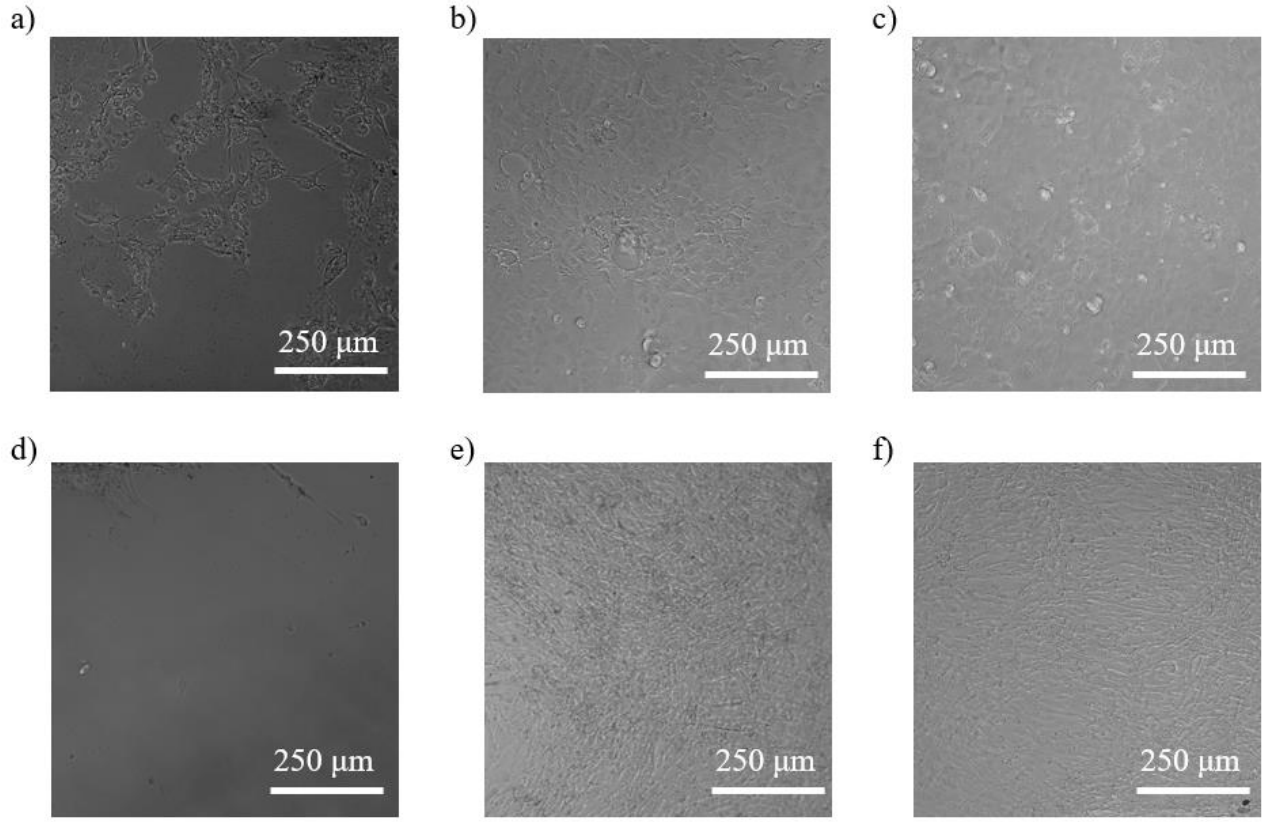

Figure 4.30: Optical micrographs of Caco-2 cells after 72 hours of citrate- (a), EG_6OH- (b) coated AgNPs and with citrate solution (c) addition, used as control. Optical micrographs of NIH-3T3 cells after 72 hours of citrate- (d), EG_6OH- (e) coated AgNPs and with citrate solution (f) addition, used as control.

4.4.3 Colorectal human epithelial cells (Caco-2)

Toxicity studies on Caco-2 cell line were performed with continuous monitoring of the time response variation of the current modulation upon the application of a square pulse on the gate, thus obtaining real-time information of the layer integrity and cell health, once exposed to the AgNPs with the two different coatings. Nanoparticles (as well as the citrate) were added after 24 hours from cell seeding, in order to assess how the growth was influenced once the cells were partially adhered and grown, as previously done for the fibroblast cell culture.

As shown in Figure 4.31a, the normalized time response of OECTs seeded with Caco-2 cells is strongly influenced by citrate-coated AgNPs treatment (black circle-line). In particular, the zoom in Figure 4.31b show that at the beginning the time response increases with increasing incubation time, due to cell adhesion and growth onto the PEDOT:PSS gate and channel. After AgNPs addition, the OECT time response continues to rise for 10 hours, when it slows down and start decreasing after 20 hours of NPs exposure (i.e. 44 h in the graph), reaching a final value that is comparable to the one before seeding (without cells). This response time trend differ significantly from the one for untreated cells (only citrate addition), that was employed as control (figure 4.31a and 4.31b): here, cell growth is unaltered from the citrate addition and the parameter τ increases during incubation time, reaching a final value 15 times higher than the pre-seeding one, thus revealing an healthy standard cell layer formation. Therefore, citrate-coated AgNPs clearly stress human colorectal epithelial layer formation, having a toxic activity on this cell line, as confirmed by optical images. Indeed, the optical analysis of the evolution upon citrate-coated AgNPs exposure shows Caco-2 cell healthy status, before the NPs addition, consisting in a mixture of small cells among areas covered with relatively large diameter cell clusters (Figure 4.31c). After 24 h from the NPs addition, cell density was still high, proving that the viability was not significantly affected yet. Noteworthy, after 48 h of exposure, the cytotoxic effect of AgNPs is clearly evident, since holes start forming in the cell layer, characterized also by an increased cell death (Figure 4.31e), both enhancing during the incubation time (Figure 4.31f). Studying the OECT response time trend, confirmed by optical images, it is possible to infer further details on NPs dynamics on cell growth. Noteworthy, immediately after AgNPs introduction in the system, cell growth and layer formation continue unaltered, since nanoparticles must be first taken up by the cell before causing toxicity. When a large enough number of silver nanoparticles has been taken up, revealed by the presence of dark spots due to fluorescence quenching by metal NPs in the actin cytoskeleton image (Figure 4.32a, white arrows highlight the NPs forming dark spots), cell death start to be relevant, as confirmed by the decrease in the time response slope and by the significant morphological alterations shown in Figure 4.32a, which are characteristic of cell death. Finally, the increasing NPs uptake leads to a drastic decrease of the time response, indicating that the cytotoxic effect of citrate-coated AgNPs overcomes cell growth and reproduction, leading to cell death.

On the other hand, devices seeded with Caco-2, treated with EG_6OH-coated AgNPs, show a response time trend (Figure 4.31a red square-line) similar to the one for untreated cells (Figure 4.31a blue triangle-line), increasing throughout the incubation period up to 19 times higher than the τ value before the seeding. This value thus confirms a healthy cell growth (as obtained in the previous Section in Figure 4.19 for Caco-2 on planar device, marked by a red dotted line) and the non-toxic effect of EG_6OH-coated AgNPs. In agreement with this result, fluorescence labelling of Caco-2 actin in Figure 4.32b showed the integrity of actin cytoskeleton and the absence of dark spots after the treatment with EG_6OH-coated AgNPs, proving that this surface passivated NPs were not taken up by Caco-2, thus without leading to cytotoxicity.

These results show a complete agreement between optical investigations and electrical measurements, further in accordance with optical images observed in Figure 4.30 and the MTT assays of Figure 4.29,

confirming the ability of OECTs to monitor the real-time evolution of Caco-2 cell line exposed to AgNPs, discriminating their toxic activity on the cell culture.

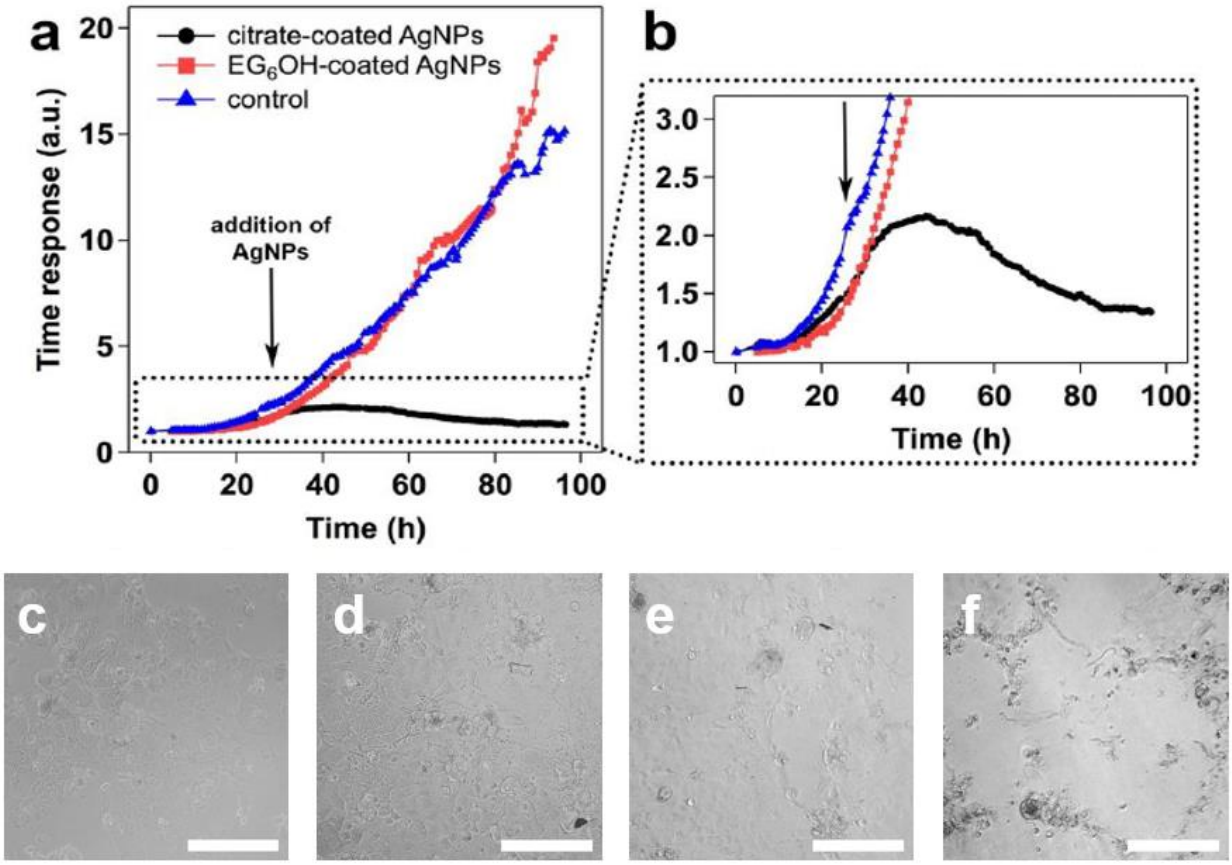

Figure 4.491: a) Real-time electrical monitoring of OECT time response variation during Caco-2 cell growth exposed to 40 μg/ml of citrate- (black circles), EG_6OH-coated AgNPs (red squares) and only citrate solution (control, blue triangles) treatments. The black arrows highlight the time of the addition (24 h after cell seeding). b) Zoom on OECT time response of Caco.2 cells treated with citrate-coated AgNPs. Optical micrographs of Caco-2 cells on the device before (c) and after 24 (d), 48 (e) and 72 (f) hours of exposure to citrate-coated AgNPs, with scale bar of 250 μm.

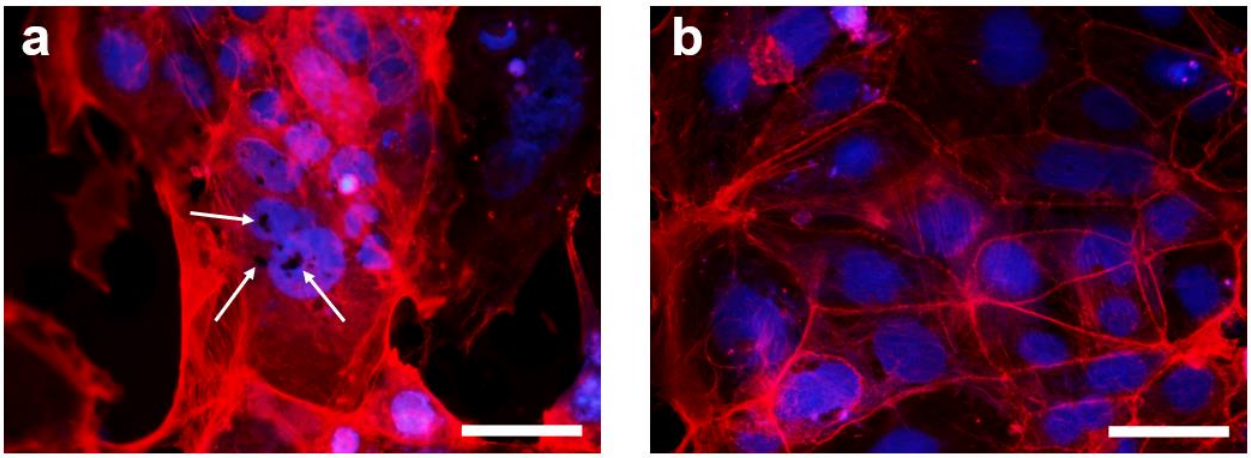

Figure 4.50: Fluorescence micrographs of Caco-2 cells labelled specifically for actin (red) and nucleus (blue), treated for 72 hours with 40 μg/ml of citrate- (a) and EG_6OH-coated (b) AgNPs. White arrows in (a) highlight the fluorescence quenching due to NPs clusters. The reported scale bar is 50 μm.

4.4.4 Mouse embryonic fibroblast (NIH-3T3)

To test the robustness of OECT capability to monitor the effect of AgNPs on cell lines, mouse embryonic fibroblast cells were used as they are adherent but non-barrier tissue cells, thus a more challenging system, as explained and demonstrated in the previous Section.
Similarly to the results achieved for Caco-2 cell line, the time response of OECTs, seeded with NIH-3T3 cells and treated with citrate-coated AgNPs, increases till 20-25 hours after the NPs addition, when reaches a steady-state (kept for less than 10 hours) and then decreases, as shown in Figure 4.33a (black circle-line). On the other hand, the addition of EG_6OH-coated AgNPs on fibroblast cells does not have toxic effect and the OECT response time trend is always increasing, mimicking the untreated control (Figure 4.33a, red square-line and blue triangle-line for the EG_6OH-coated AgNPs and the control, respectively).
Optical images of NIH-3T3 (grown on top of a planar measured OECT) treated with citrate-coated AgNPs are taken every 24 hours, proving the correct readout of the OECT: indeed, the cytotoxic activity of the NPs starts to be evident only after the 48 hours of exposure, developing holes in the cell layer due to cell death, as visible in Figure 4.33d and 4.33e.
All the obtained data agree with the fluorescent images (Figure 4.34), which show the citrate-coated AgNPs internalization by NIH-3T3 cells (white arrows in Figure 4.34a) and the subsequent cytoskeleton damages, while fibroblast treated with EG_6OH-coated AgNPs retain the integrity of their cytoskeleton and standard morphological structure (Figure 4.34b).
The OECTs are further revealed as powerful devices suitable to real-time monitor the AgNPs toxicity even for non-barrier cell lines.

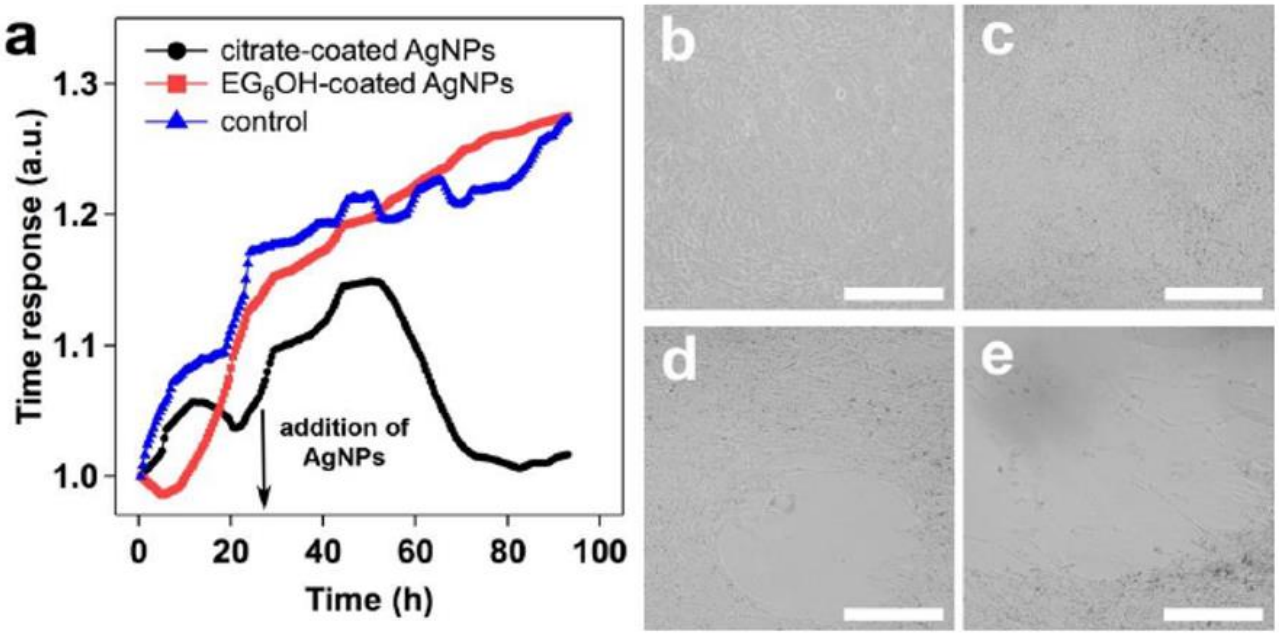

Figure 4.33: Real-time electrical monitoring of OECT time response variation during NIH-3T3 cell growth exposed to 40 μg/ml of citrate- (black circles), EG_6OH-coated AgNPs (red squares) and only citrate solution (control, blue triangles) treatments. The black arrow highlights the time of the addition (24 h after cell seeding). Optical micrographs on NIH-3T3 cells before (b) and after 24 (c), 48 (d) and 72 (e) hours of exposure to citrate-coated AgNPs, with scale bar of 250 μm.

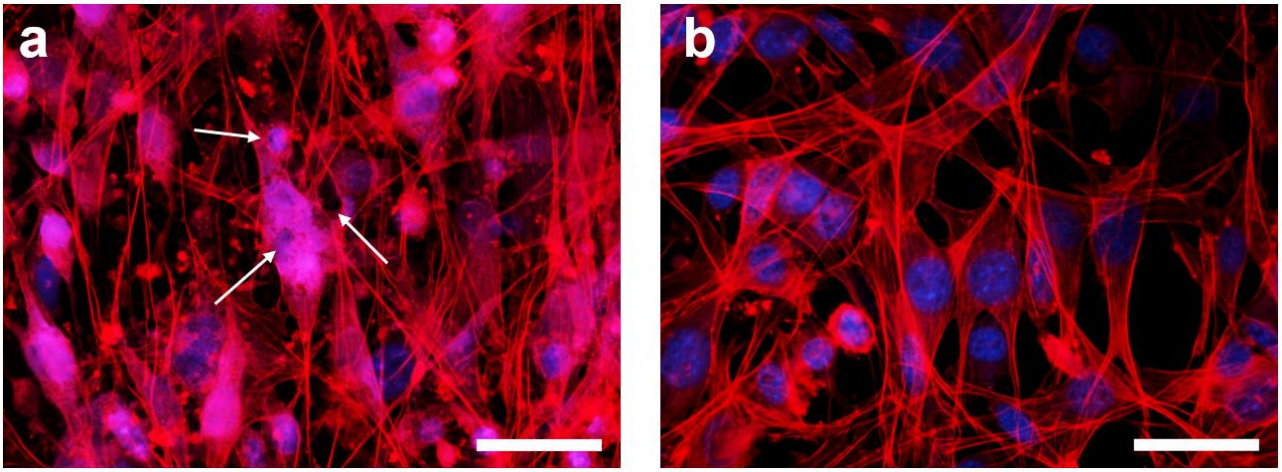

Figure 4.51: Fluorescence micrographs of NIH-3T3 cells labelled specifically for actin (red) and nucleus (blue), treated for 72 hours with 40 μg/ml of citrate- (a) and EG_6OH-coated (b) AgNPs. White arrows in (a) highlight the fluorescence quenching due to NPs clusters. The reported scale bar is 50 μm.

Major results

In this Chapter, PEDOT:PSS-based OECTs were employed for real-time monitoring of cell layer formation and disruption, achieving the following results:

1. The Tissue Engineering Cell Holder for Organic Electrochemical Transistor (TECH-OECT) was designed and realized, enabling the real-time, sequential monitoring of several devices even with diverse OECT configurations and with different cell seedings or stresses
2. Planar devices with active channel areas of 3 mm^2 proved to be able to study both barrier (human colorectal epithelial cells, i.e. Caco-2) and non-barrier (mouse embryonic fibroblasts, i.e. NIH-3T3) cell lines, owing to the double ion crossing of the cell layer (from the gate to the electrolyte and from the electrolyte to the channel) in the planar configuration
3. Vertical devices with active channel areas of 3 mm^2 failed to monitor non-barrier cell line (NIH-3T3), but were able to study only barrier cells (Caco-2), with lower (halved) sensitivity compared to planar OECTs

These results are summarized in Ref [385].

Planar OECTs were then employed to assess cell health under silver nanoparticles (AgNPs) toxicity, with the following main achievements:

4. The citrate-coated AgNPs proved to be cytotoxic to both cell lines, Caco-2 and NIH-3T3, while replacing (passivating) citrate molecules with (11-mercaptoundecyl)hexa(ethylene glycol) (EG_6OH) on the NP surface ensure a non-toxic activity
5. OECTs demonstrated to be reliable device to obtain further insights on the NPs cytotoxic effect on cells, performing a real-time monitoring of the cell layer health status upon NPs exposure

These data are reported in Ref [394].

Chapter 5
Electrodes for neural interfaces

Bioelectronic medicine envisions in the future minimally-invasive and bio-conformable interfaces merging with the neuronal tissue, thus enabling long-term and high quality recording and stimulation of signals both from the central and the peripheral nervous system.[395,396] The ability to access to such signals can develop novel therapeutic means to treat chronic or acute disease states, that are currently incurable.[397,398] In order to realize this vision, material scientists need to achieve mechanically compliant and low-impedance bioelectronic interfaces, replacing the currently used stiff metallic electrodes with micro- or nanostructured electronic materials. In this thesis work, the conducting polymer PEDOT:PSS was employed to fulfill both the requirements of low impedances and more elastic (stretchable) mechanical properties.

5.1 PEDOT:PSS vs PEDOT:PSS:PEG

With the aim to tune the mechanical properties of PEDOT:PSS microelectrodes the plasticizer polyethylene glycol (PEG) was added to the electropolymerization solution with the concentration of 5mM. Indeed, PEG or other plasticizers introduced in spin-coated PEDOT:PSS solution have been demonstrated to lead to softer polymeric thin films.[399]
In order to prove the enhancement of softness and stretchable features of PEDOT:PSS:PEG microelectrodes, the polymeric coating with and without the PEG introduction have been studied in this thesis work, characterizing their material properties. These experiments are reported in the next paragraphs of this Section.

5.1.1 Morphology and structural changes

The plasticizer introduction was assessed firstly by means of Attenuated Total Reflection Fourier Transform Infrared Spectroscopy (ATR-FTIR), previously described in the paragraph 3.1.6. Figure 5.1a reports the tip-enhanced PEDOT:PSS and PEDOT:PSS:PEG FTIR spectra with colour labelled functional groups and compounds to identify bands and fingerprints: in particular, the appearance of C-O stretching vibration at 1108 cm^{-1} together with other additional adsorption bands in the C-C fingerprint region can be assigned to the PEG presence, marked with green arrows.
Moreover, surface morphology was investigated performing atomic force microscopy measurements on 200 nm thick polymeric films, reported in Figure 5.1b and 5.1c for PEDOT:PSS and PEDOT:PSS:PEG, respectively. While PEDOT:PSS shows the characteristic cauliflower structures, associated to electropolymerized thiophene polymers, the PEDOT:PSS:PEG composites display smaller typical structure, ascribed to an altered growth mechanism during the electrodeposition procedure. Quantitative analysis on AFM maps, calculating and fitting the Height-Height Correlation function (*HHCF* is reported in Figure 5.1d, the fit is in accordance with Eq. 3.11), were developed to extract the surface roughness *S* and the characteristic autocorrelation length *T*. *S* and *T* are plotted as a function of the thickness of the deposited semiconducting polymers in Figure 5.1e and 5.1f, respectively. Figure 5.1d report a reduction for *S* and *T* for PEG introduction ($S_{PEDOT:PSS}$ = 10.0 ± 0.4 nm, $T_{PEDOT:PSS}$ = 120 ± 5 nm; $S_{PEDOT:PSS:PEG}$ = 4.2 ± 0.5 nm, $T_{PEDOT:PSS:PEG}$ = 88 ± 10 nm). Moreover, PEDOT:PSS films show a rise of both *S* and *T* for thicker electrodeposited films, while the thickness of films having PEG does not strongly impact the characteristic morphological parameters, that remain almost constant for 200 nm, 400 nm and 600 nm thick PEDOT:PSS:PEG composites.

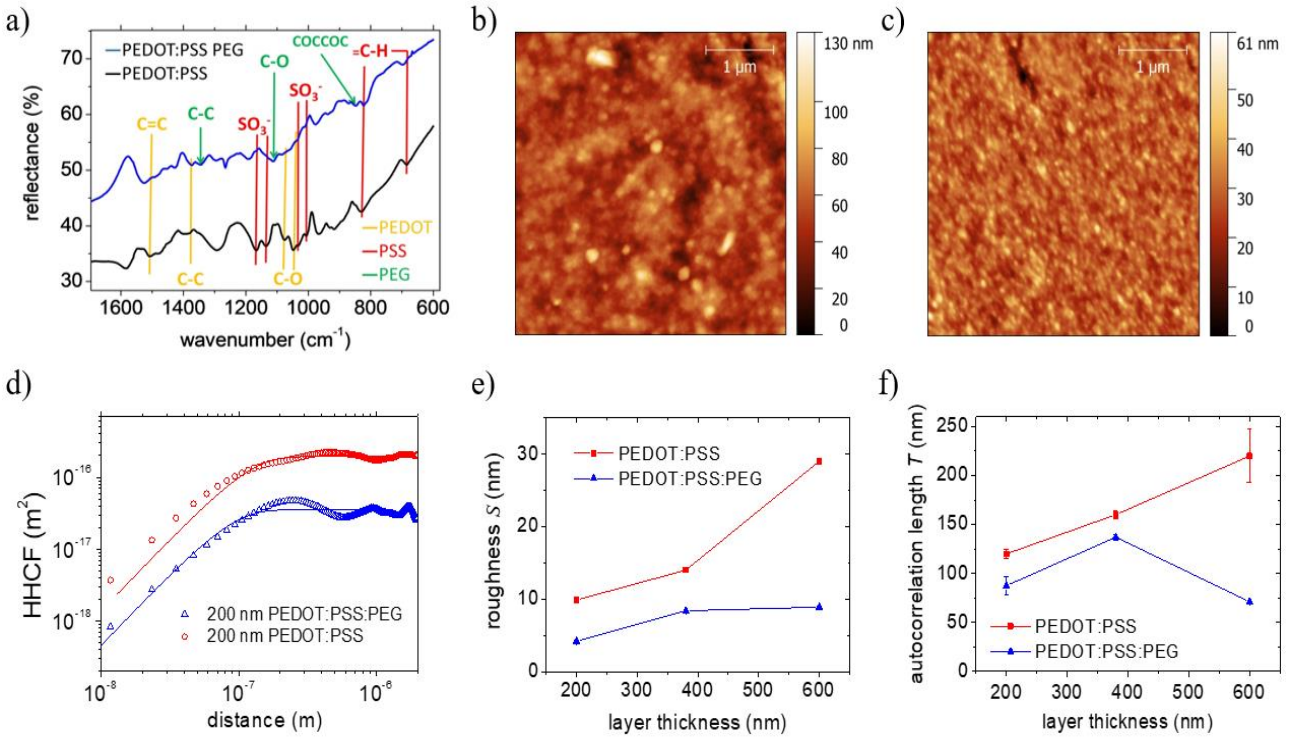

Figure 5.52: Comparison of the electropolymerized layer of PEDOT:PSS and PEDOT:PSS:PEG, focusing on bulk and surface properties. (a) Tip-enhanced FTIR spectra for PEDOT:PSS and PEDOT:PSS:PEG coatings. AFM images of PEDOT:PSS (b) and PEDOT:PSS:PEG (c) 200 nm thick films. d) Height.Height Correlation Function calculated and fitted, in order to obtain the sample roughness (e) and characteristic correlation length (f) for different polymeric layer thicknesses.

5.1.2 Electrochemical characterization

Crucial for bioelectronic operation is the electrochemical impedance of the electrode that records or stimulates. Figure 5.2a shows the electrochemical impedance spectra for Au, Au/PEDOT:PSS and Au/PEDOT:PSS:PEG electrode surfaces, fitted using a simple RC series equivalent circuit model. A flat impedance response (with phase 0) is observed in the high frequency range, which corresponds to the electrolyte resistance R. Moving towards lower impedances, $|Z|$ increases according to the capacitive behaviour of the electrode, that is determined by the ionic double layer at the interface. Upon the deposition of the conducting polymer layer, the impedance decreases more than an order of magnitude in the capacitive regime, thus leading to a wider frequency range for the flat impedance response. Noteworthy, a flat response is reached in the range 100 Hz – 3 kHz, which is interesting for bioelectronic recordings and stimulations. This impedance drop is related to the switching from a 2D metallic interface to a 3D polymeric one, together with the introduction of ionic conduction (in addition to the standard electronic one, present in metals), as clearly seen from the Figure 5.2b: this makes PEDOT:PSS covered electrodes display a higher capacitance value of 618 µF/cm^2, that is an order of magnitude higher than the bare gold electrode capacitance of 58 µF/cm^2. The addition of the plasticizer reduces slightly this specific capacitance per area of the layer ($C_{PEDOT:PSS:PEG}$ = 586 µF/cm^2) but has no significant effects on ion-to-electron exchange properties of the electrode. Indeed, the impedance spectra of PEDOT:PSS with or without PEG almost perfectly overlap in Figure 5.2a.

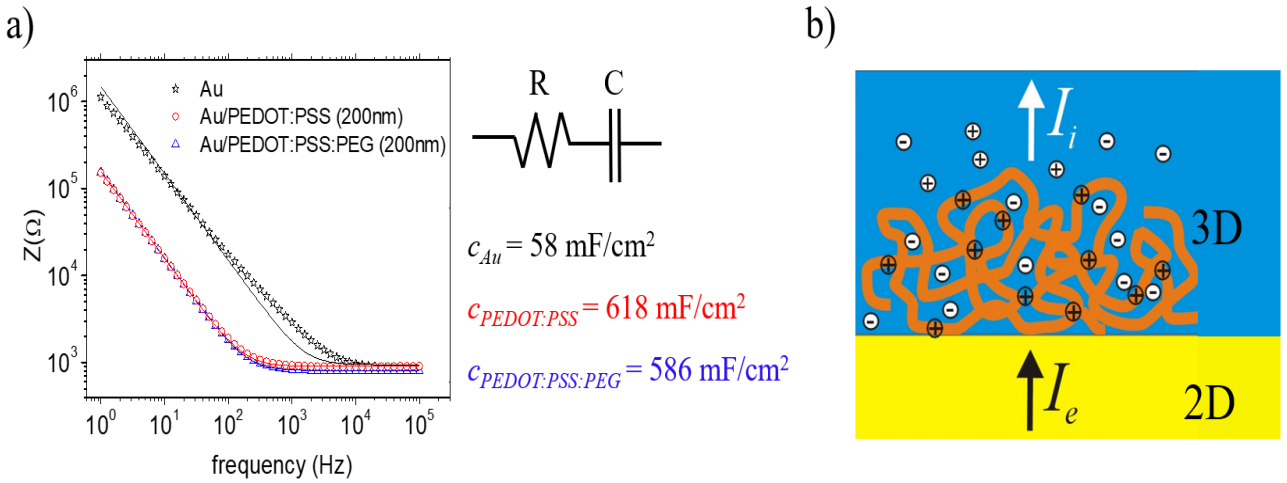

Figure 5.53: a) Electrochemical impedance spectra for bare gold, PEDOT:PSS and PEDOT:PSS:PEG coated electrodes. b) Schematic representation of the gold electrode coated with a polymeric layer, showing the introduced ionic conductivity and the 3D electrical interface with the medium.

To further confirm the similar electrochemical properties of PEDOT:PSS and PEDOT:PSS:PEG, CV and EIS measurements were taken for 200 nm and 400 nm thick polymeric electrodes with comparable areas. Data are reported in Figure 5.3 and 5.4 for cyclic voltammetry and impedance spectroscopy, respectively. These measurements clearly show that electrodes with the same volume give comparable voltammetry and impedance responses, thus confirming the unchanged ion-to-electron conversion properties at the electrolyte/polymer interface upon the addition of the plasticizer PEG (the only slight differences are present in the Nyquist plot, but they fall in the range of frequencies lower than 100 Hz, not used for bioelectronic recordings).

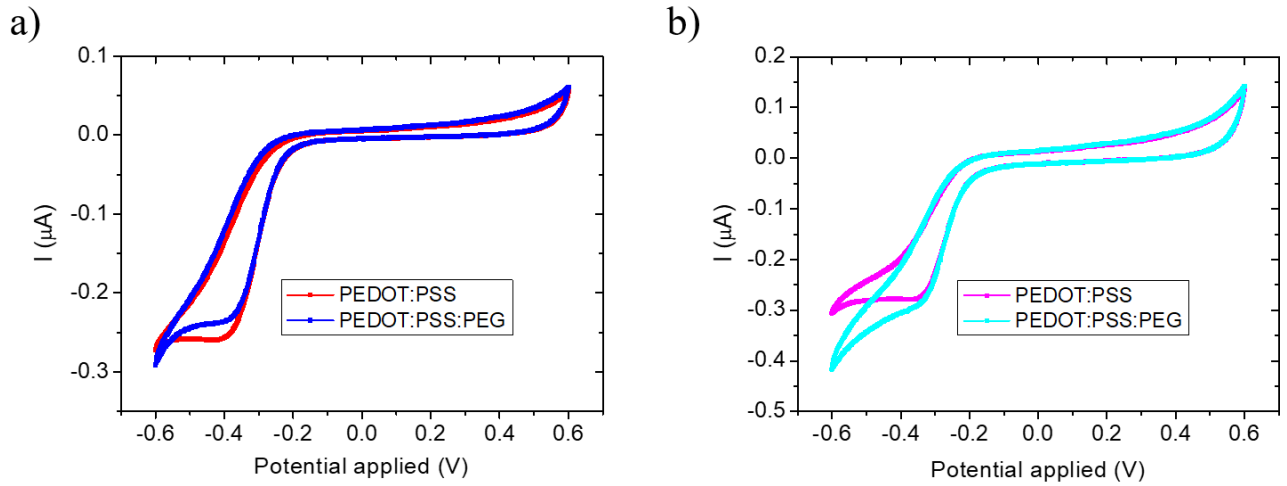

Figure 5.54: Cyclic voltammetry plots comparing the electrochemical response of 200nm (a) and 400 nm (b) thick PEDOT:PSS (red and magenta, respectively) and PEDOT:PSS:PEG (blue and cyan, respectively) coated electrode.

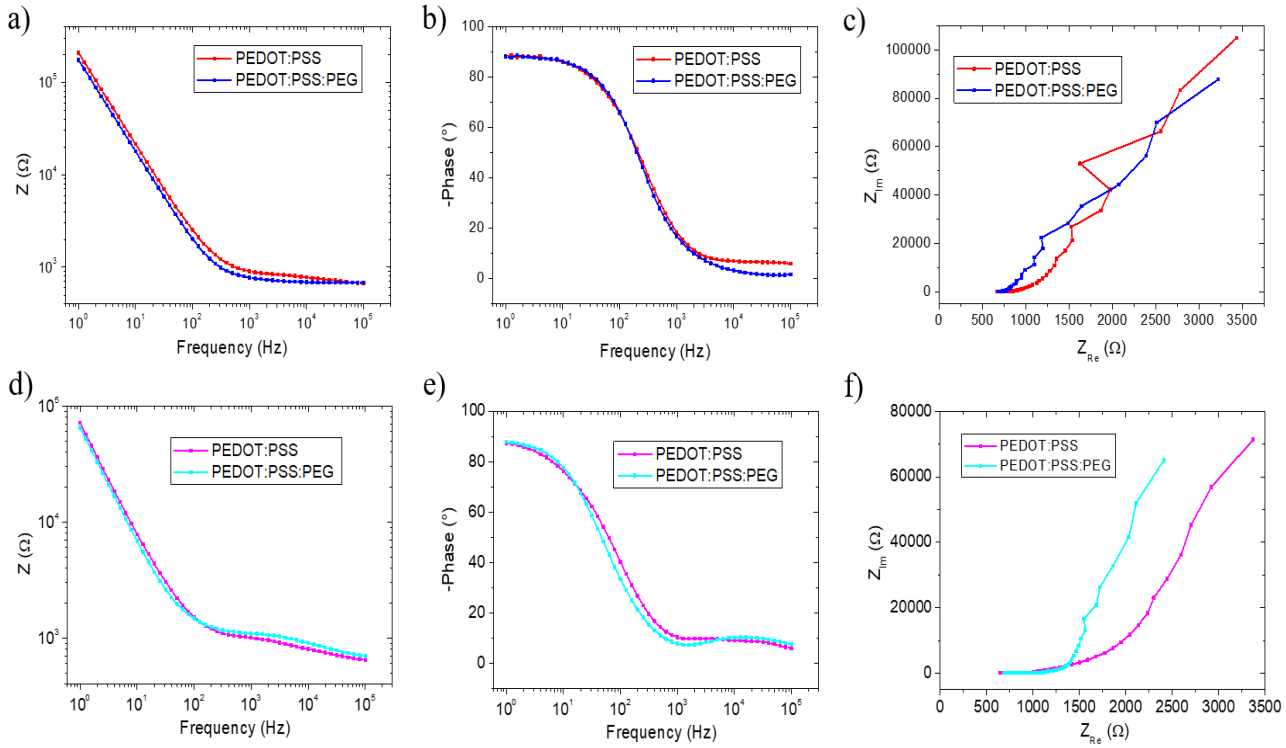

Figure 5.55: Electrical impedance spectroscopy plots comparing 200nm (a, b, c) and 400 nm (d, e, f) thick PEDOT:PSS (red and magenta, respectively) and PEDOT:PSS:PEG (blue and cyan, respectively) coated electrode.

5.1.3 Differences under strain

Since plasticizer was meant to improve the stretchability of the polymeric microelectrode, its important role can be assessed investigating the electrode performances under tensile strain with and without the PEG addition. In particular, electrochemical impedance at a frequency of 1 kHz can be studied for this purpose, as characteristic for bioelectronic signals. Figure 5.5a and Figure 5.5b show a schematic view and a picture, respectively, of the experimental setup developed for the realization of impedance measurements under strain. The setup consist of three main components: a mechanical holder fixed at the bottom of a glass rectangular bowl, filled with PBS 1X (used as electrolyte), that clamp the device on the PDMS interconnects at the electrode edges (outside the trench); the electrochemical impedance set up, previously described in 3.1.2; the optical microscope, taking the images from the top for the elongation (strain) calculations. Data are reported in Figure 5.5c as impedance at 1kHz values over strain percentage (where 0% means no strain is applied), for gold, PEDOT:PSS and PEDOT:PSS:PEG electrodes. The impedance of the uncovered Au electrode remains almost constant up to a strain of 60%: the microcracked gold film maintains also for high strain values a conductive percolating network contacting the different gold areas, thus keeping the full electrode area connected and avoiding variations in its overall capacitance. The small impedance increments can be ascribed to single gold islands which loose contact at the borders of the electrode. On the other hand, the excellent elasticity is lost once pure PEDOT:PSS is deposited on top of the gold electrode. The conducting polymer coating reduces the initial impedance of almost an order of magnitude, but already at small strain the electrode impedance undergoes to a steep increase that leads to a failure at strain above 20%. On the contrary, the addition of the PEG plasticizer carries out an electrode combining both the low impedance with the elastic stretchability. Indeed, an impedance comparable with the one obtained for the pure, unstrained PEDOT:PSS is kept for strain up to 40%. Noteworthy, a good overlap of the loading and unloading strain experiments is shown for all the electrodes, that seems to enable also a recovery of the starting impedance value before strain. Fatigue experiments, testing this assumption, are reported in paragraph 5.4.2.

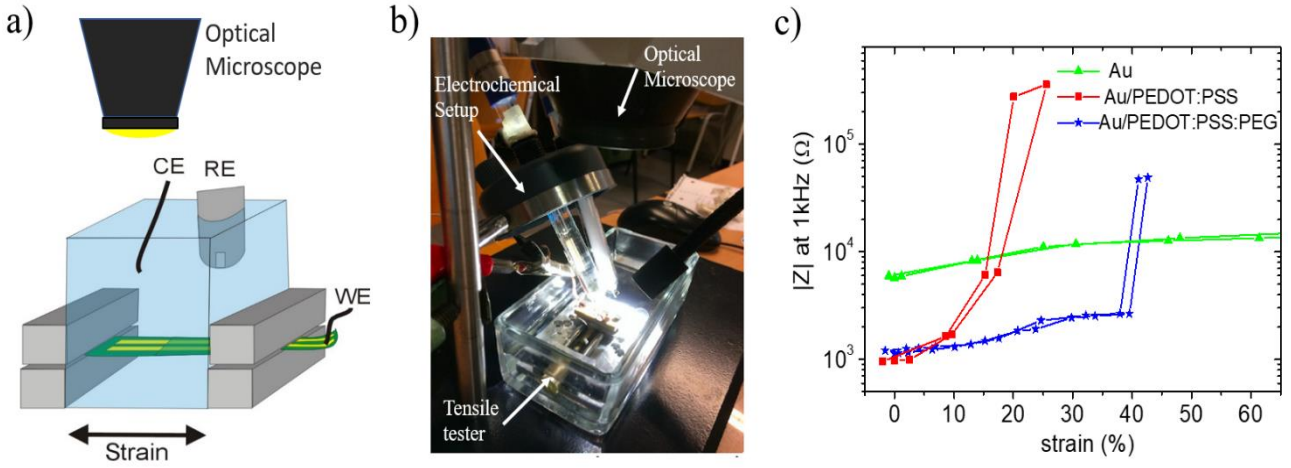

Figure 5.56: Schematic view (a) and picture (b) of the experimental setup for electrochemical measurements of the electrode under strain. c) Electrochemical impedance at the frequency of 1 kHz over strain, obtained for bare gold (green triangle-line), PEDOT:PSS (red square-line) and PEDOT:PSS:PEG (blue star-line) coated electrodes.

In order to understand the improved stretchability provided by the plasticizer addition, optical and AFM images of the different electrode surface under strain were analysed. Figure 5.6 shows the optical comparison between strained and unstrained electrodes. It can be noted that PEDOT:PSS electrode starts forming macroscopic cracks at a strain of 20%, which are orthogonal to the strain direction and cut the conducting pathway along the electrode: this leads to the formation of isolated, disconnected PEDOT:PSS conductive islands and explains the electrode failure, represented by the steep increase in the impedance (Figure 5.5c). Instead, pure gold and PEDOT:PSS:PEG coated electrodes do not show the formation of long cracks and only irregular microcracks appear along the thin film caused by the tensile strain. These findings are further validated by AFM maps, reported in Figure 5.7. In the resting position (absence of strain), all three maps contain variations in surface height that mark the position of microcracks, present in the gold layer underneath. Once the strain is applied (again around 20%), the images report differences regarding the absorption of the tensile deformation of the different materials. Indeed, Au film shows only microcracks under deformation that maintain a small extension of few micrometers in the direction orthogonal to the strain, as found in literature examples.[400,401] Thus, a conductive pathway is still present among the several metallic areas of the electrode surface. On the other hand, for polymeric coatings on the electrode, the crack formation is strongly modified due to the presence of additional forces, impacting on the crack opening kinetics: in particular, this drastically happens for PEDOT:PSS coating, where no microcrack openings are observed, but instead the strain is localized in fewer but wider cracks, that cause the complete loss of conductivity in the layer. These big cracks are coupled with significant holes in the electrode: the surface height reduction exceeds the thickness of pure PEDOT:PSS layer (200 nm), in order to keep the constant volume of the elongated elastic substrate. The introduction of the PEG plasticizer in the electrodeposited polymeric mixture allows for the restoration of microcrack openings under strain, thus having a topography under tensile strain that resembles the pure Au film. Only small differences, such as surface undulation and straighter crack border, are associated to the presence of the polymer coating in the AFM images. Therefore, the PEDOT:PSS:PEG electrodeposited layer permits up to 40% of tensile strain of the electrode, enabling the formation of microcracks that can contain a strain comparable to pure gold film, without the appearance of macroscopic cuts in the film that would interrupt the electrode conductivity.

In summary the PEG addition enables to retrieve the reversible stretchability of the gold microcracked films, which is due to the strong hydrophilic properties of PEG: the increase in water content in the electrode enhances the polymer chain mobility and reduces the dimensions of crystalline PEDOT rich

regions in the conducting polymer nano-composite, changing the material properties. Thus, the improved coating does not interfere with the gold microcrack network mechanics, allowing the film to elongate without interrupting its electrical conductivity.

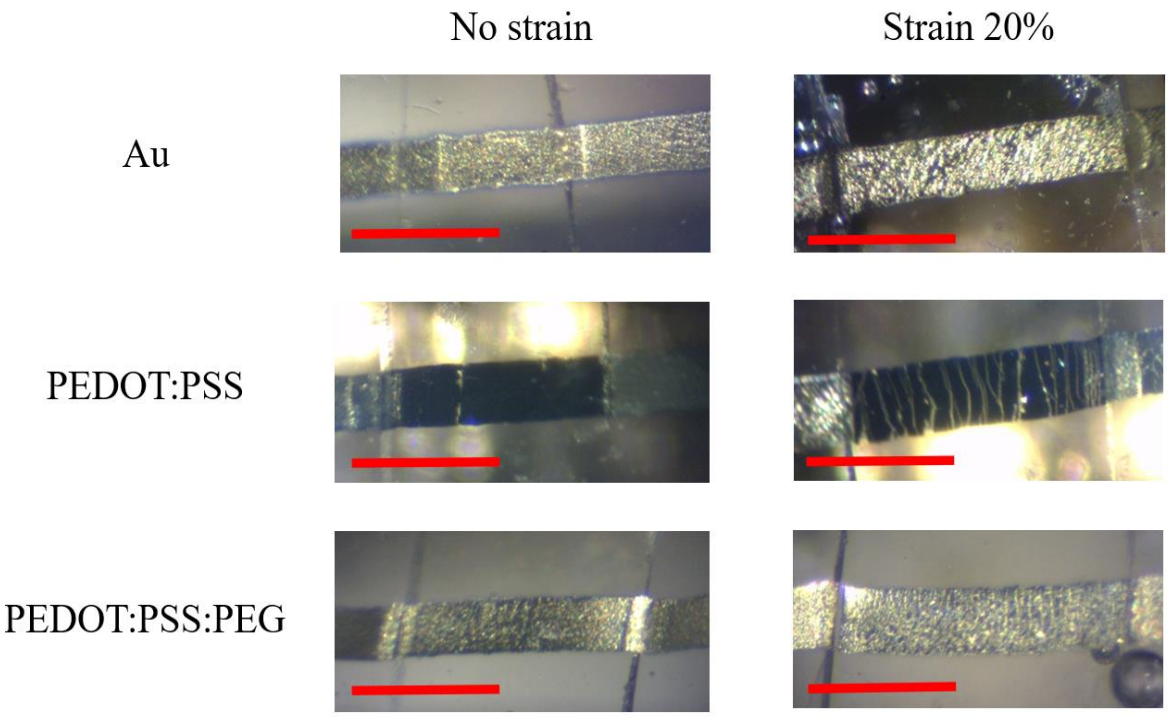

Figure 5.57: Optical microscopy of bare Au, PEDOT:PSS and PEDOT:PSS:PEG coated electrodes in resting position and under a tensile strain of 20%. The red scale bar is 500 μm.

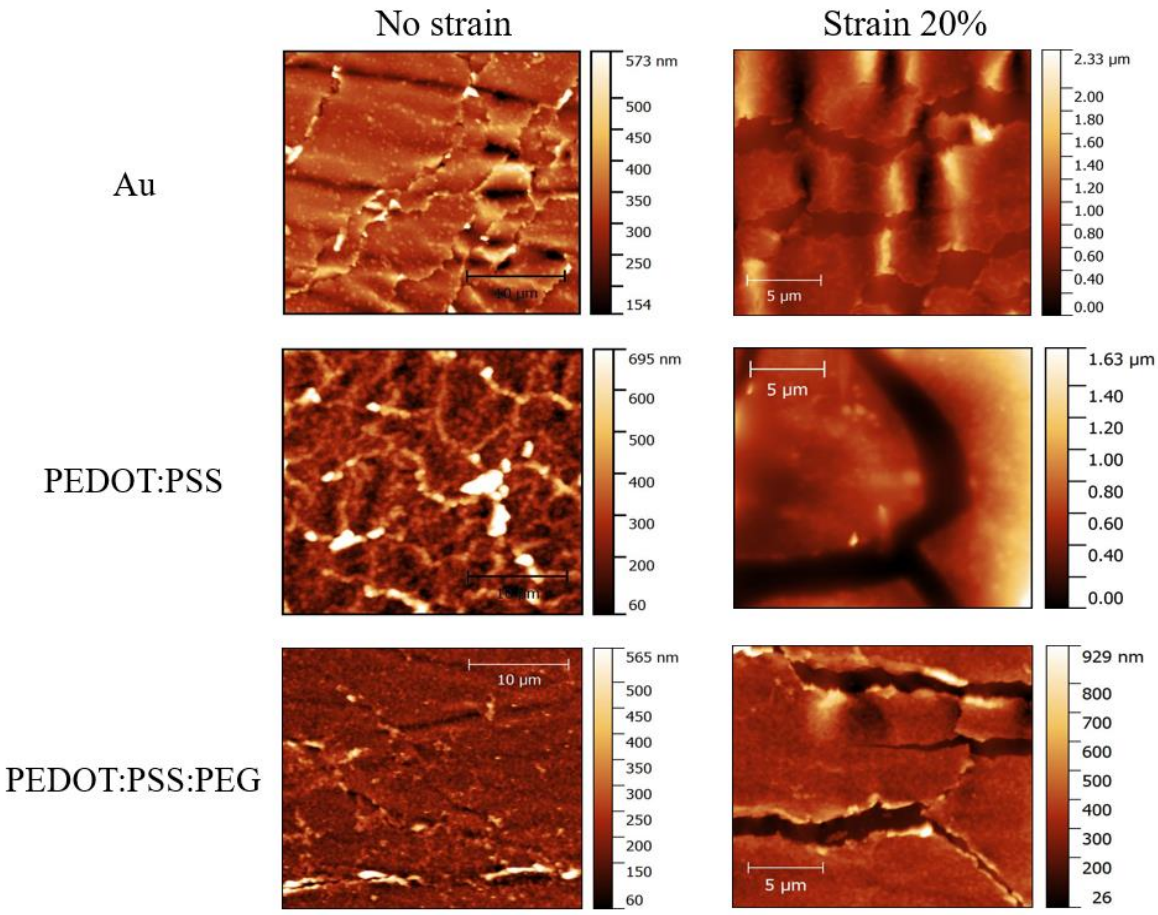

Figure 5.58: Atomic force microscopy topography maps of bare Au, PEDOT:PSS and PEDOT:PSS:PEG coated electrodes in resting position and under a tensile strain of 20%.

5.1.3 Mechanical indentation

Beside electrical measurements of the electrode, also mechanical investigations were performed on the electrode materials in isotonic solution, in order to mimic biological environment. Moreover, since materials properties may have significant differences from the macro to the micro-nanoscale, AFM indentation experiments (instead of the standard Dynamical Mechanical Analysis at the macro-level) were employed to study the micro-mechanical behavior of the electrode as should be experienced by the nerve. Indentation schematic and experimental data are reported in Figure 5.8a and 5.8b, respectively. As expected, thermally evaporated Au thin layer increases significantly the surface stiffness with respect to the bare PDMS elastomer substrate. Using the Hertzian Model (Eq. 3.13), briefly introduced in the paragraph 3.1.5, it was possible to compute the effective elastic modulus: Au deposition enhances Young's modulus from 0.81 ± 0.02 MPa (bare PDMS) to 32 ± 7 MPa (PDMS/Au substrate). In this case, the indentation of the AFM tip leads to the bending of the stiff but thin gold film (E ~ 80 GPa) under its load, combined with the deformation of the underlying soft PDMS layer. Upon the addition of the PEDOT:PSS surface coating, the effective modulus decreases to the value of 23 ± 3 MPa, quite similar to the PEDOT:PSS modulus when deposited on stiff substrates. The introduction of the PEG plasticizer in the polymeric mixture further reduces the Young's modulus of the electrode surface to 14 ± 2 MPa, thus rendering it more mechanically conformable towards soft neuronal tissue.

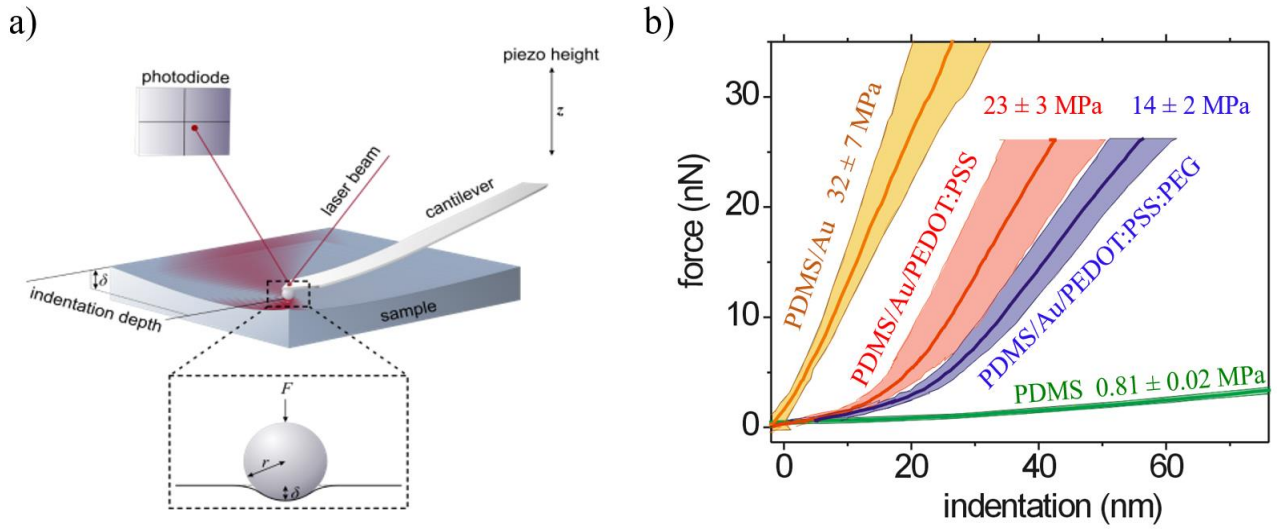

Figure 5.59: a) Schematic example of the AFM indentation experiment.[402] b) Force as a function of AFM tip indentation depth, measured in isotonic solution to extract the elastic modulus of the different materials employed for the electrode.

5.2 Controlled deposition: thickness evaluation

A particularly important step in the electrode fabrication procedure was the PEDOT:PSS or PEDOT:PSS:PEG deposition on uncovered gold films, exposed by the trench. The polymer was deposited using the electrochemical technique described in paragraph 3.1.1. Two main precautions were observed: i) the depositions were performed in inert atmosphere, fluxing nitrogen gas inside the electrochemical cell for over 10-15 minutes; ii) a thickness controlled chronoamperometric process was employed to define the amount of deposited polymer molecules. The former allowed for the reduction of oxygen related termination of the polymer that may lead to shorted PEDOT chains, easier to be subjected to delamination. This way a strong adhesion between the polymer and the microcracked gold layer was achieved. On the other hand, the latter was based on a potentiometric control of the deposition with the application of a positive constant potential of 1.2 V to the working electrode, while measuring the current flowing in it and integrating in order to continuously calculate the charge deposited on the working electrode, as reported in Figure 5.9a. According to the reaction in Figure 5.9b, the deposition of one molecular unit of PEDOT:PSS on the working electrode is driven by two electrons. Since the density of an organic layer can be estimated as 0.9 g/cm^3 and EDOT (PEDOT monomer) molar mass is 142 g/mol, a defined polymer thickness can be obtained if the area of the uncovered Au microelectrode is known, interrupting the electrochemical process once the charge reaches the corresponding amount, according to the following equation:

$$C = \frac{t \cdot A \cdot d}{MM} \cdot 2 \cdot C_{e^-} \cdot N_{Av} \tag{5.65}$$

where *t*, and *A* are the thickness and the area of the electrode, respectively, *d* is the polymer density, *MM* represents the EDOT molar mass, C_{e^-} the electron charge and N_{Av} the Avogadro number.
As an example, for a gold electrode with an area (calculated using the calibrated optical microscope) of $1.282 \cdot 10^5$ μm^2, the deposition of a 200 nm PEDOT:PSS layer required to stop the process at the charge amount of 0.031 mC.
Bare gold and PEDOT:PSS:PEG coated electrode optical images are reported in Figure 5.9c.

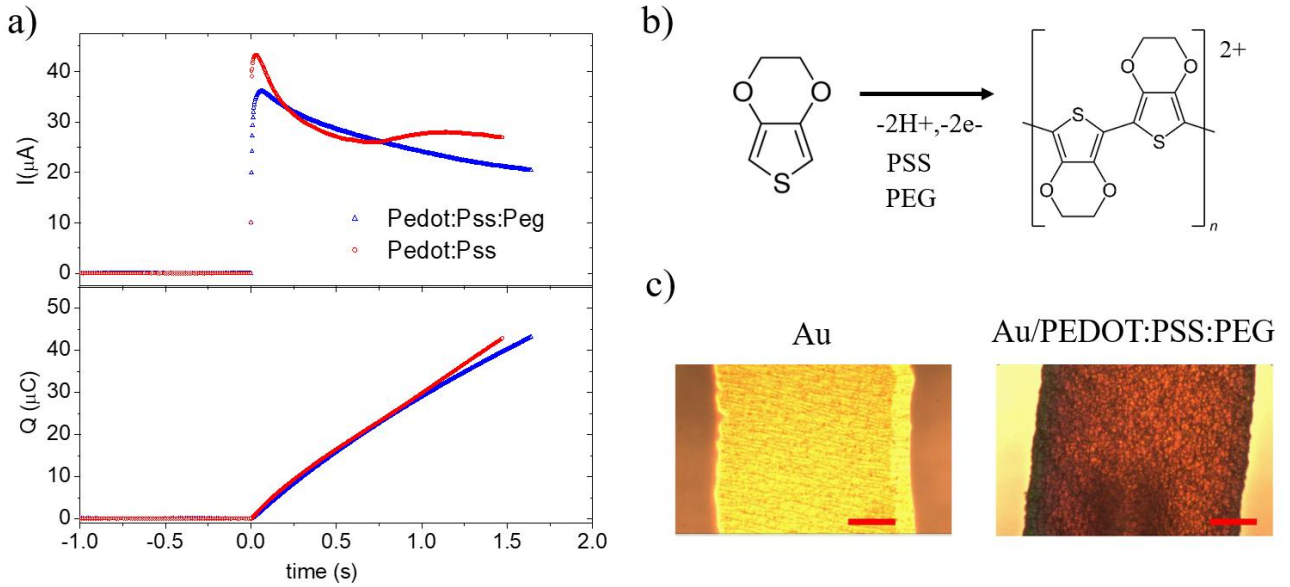

Figure 5.60: Electrodeposition of the semiconducting polymer composite. a) Current flowing (above) and charge deposited (below) on the working electrode (gold microelectrode) during the potentiometric controlled electrochemical polymer deposition. At t = 0, a voltage of *E* (vs SCE) = 1.2 V was applied. Once the needed amount of charge was deposited, the potential was set back to the ground and the deposition was stopped. b) Electrochemical reaction scheme where two electrons lead the deposition of a PEDOT:PSS or PEDOT:PSS:PEG molecular unit. c) Optical micrographs of bare gold (left) and PEDOT:PSS:PEG (right) coated electrodes. Scale bar of 50 μm.

5.3 Interconnects characterization

A fundamental part of the stretchable electrode is represented by the gold interconnects that are encapsulated between two layers of PDMS, in order to be protected, preserved and sheltered from external ion fluxes or contaminations. At the same time, the interconnects need to be stretchable as the electrode, in order to be able to follow the movements of the implanted animal without breaking. Their behaviour under mechanical strain was analysed in the following paragraph.

5.3.1 Resistance under stretch

Electromechanical tests were performed on the electrode interconnects, using the same tensile tester employed in the strain measurements on the electrode.

A simple mechanical characterization, shown in Figure 5.10a, was used at the beginning to assess the stress on the interconnects in function of the applied strain, extracting the elastic modulus from the slope of the resulting response. A value of E = 1.1 MPa was obtained, very close to the one obtained in the paragraph 5.1.3 from indentation experiment on bare PDMS, thus demonstrating a good mechanical stretchability.

However, particularly interesting was the ability to transport the recorded signal to the wireless transmitter connected to the "head" of the electrode, thus the resistance value of the interconnects under stretch. For this reason, the electrical resistance was measured while applying a tensile strain elongation of the electrode "body": a scheme of this experiment is reported in figure 5.10b. The electrical data underline step-by-step increase of electrical resistance upon the strain application that is almost symmetrical to the decrease steps during release (Figure 5.10c): during the strain, the stabilization of the resistance value is very fast and it is maintained while keeping a constant strain value. From the analysis of Figure 5.10d, that reports the extracted resistance for strain loading (black squares) and unloading (red circles) values, it can be noted that (i) the resistance is linear with the strain percentage, (ii) the hysteresis of the stretching process is almost zero, since the loading and unloading data are almost overlapping, and (iii) the resistance value triples for a strain of 35%, but

the electrical connection is not totally lost. In particular, a fit of the data highlights a resistance variation of ~ 54 ± 3 Ω each 1% of elongation.

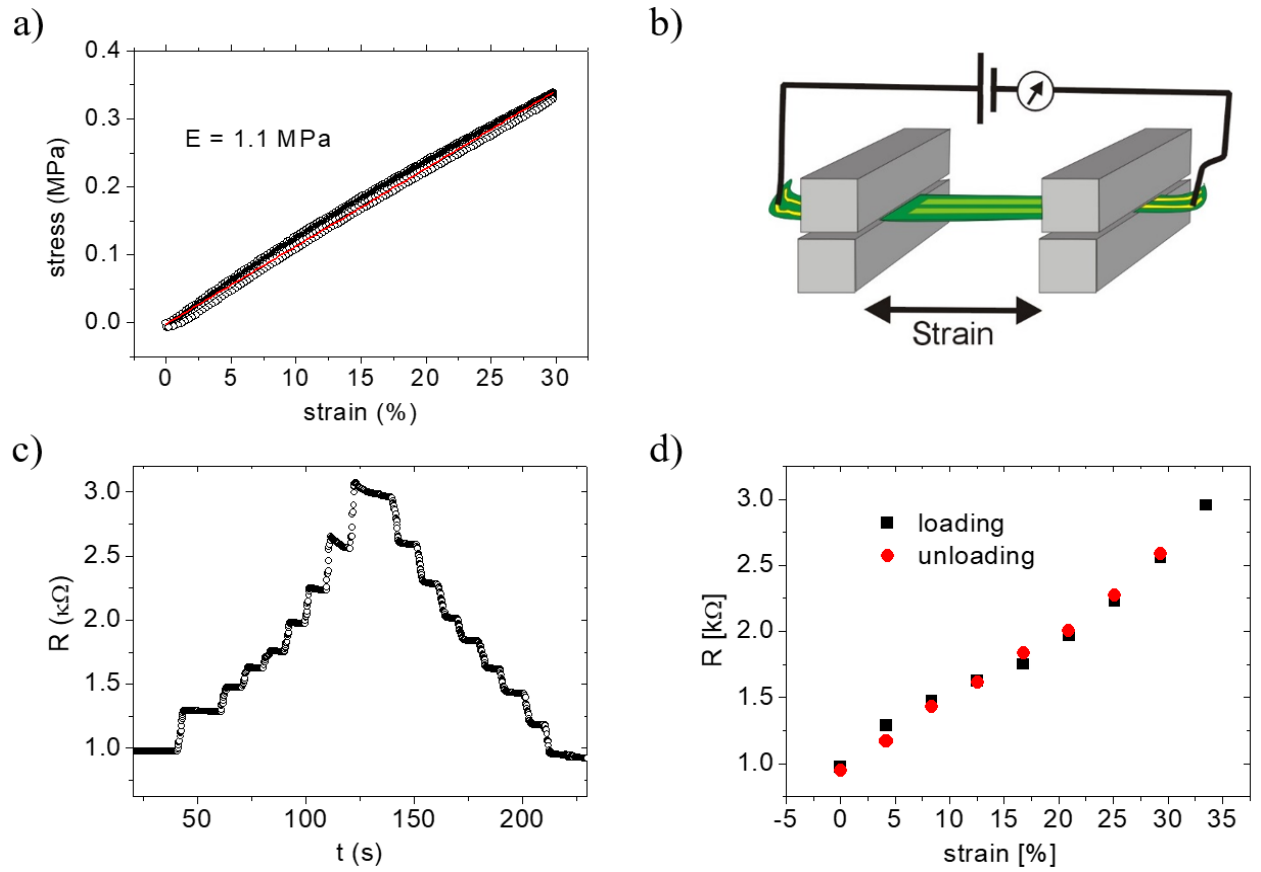

Figure 5.61: Electromechanical characterization of the electrode interconnects. a) Tensile stress of interconnect as a function of the elongation strain, giving an elastic modulus of 1.1 MPa. b) Schematic of the resistance versus strain experiments. c) Interconnect resistance R over time, during increasing and decreasing strain. d) Interconnect resistance value in function of strain, extracted from (c).

5.4 Electrode characterization

In this Section, lifetime and fatigue tests were performed on the electrode to assess its performances ,simulating the difficulties and problems arising from a real implant.

5.4.1 Lifetime test

In order to mimic the exposure of the microelectrode to the liquid biological environment of a real implant (thus the degradation deriving from being inside the body environment), the device was immersed in isotonic solution at 38 °C. Figure 5.11 presents the long-term stability data for the PEDOT:PSS:PEG electrode. The variation of the impedance of the electrode at the frequency of 1 kHz (as characteristic for bioelectronic signals) was evaluated over time of immersion in the solution. Indipendently from the polymer thickness (200 nm or 400 nm), the films show good stability over time and low impedance values are maintained for up to a month. Indeed, the impedance only doubles its starting value (measured at the end of the fabrication procedure) and the optical images in Figure 5.11b clearly show no delamination or disruption in the 200 nm (above) and 400 nm (below) PEDOT:PSS:PEG coatings, with the latter being darker due to the doubled thickness. Moreover, long-term immersion in water does not alter the chemical composition of the coatings, as demonstrated in the Figure 5.11c: here, an intense C-O stretching band at 1108 cm^{-1}, that can be uniquely attributed

to PEG molecules, is present even after two weeks of immersion in PBS. This proves that the plasticizer PEG does not leak out into the solvent, but remains entrapped in the polymeric film.

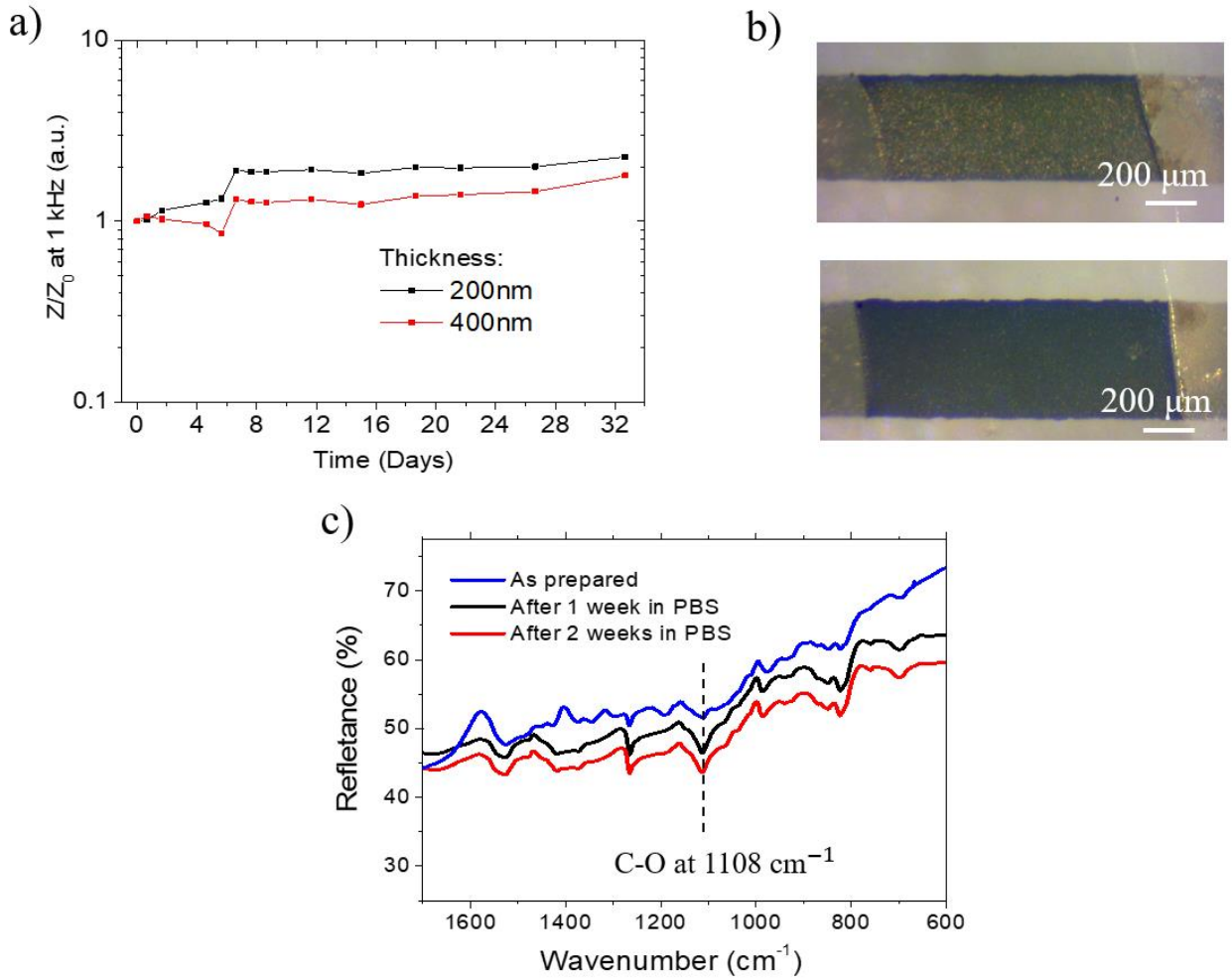

Figure 5.62: Stability of PEDOT:PSS:PEG electrodes immersed in an isotonic solution (PBS) over weeks. a) Normalized impedance at the frequency of 1 kHz as a function of the immersion time in 38° C isotonic PBS solution. b) Optical images of the electrodes measured in (a), at the end of the immersion experiment (over 1 month). c) Tip enhanced FTIR spectra of the PEDOT:PSS:PEG electrode after different immersion times in PBS, proving the chemical stability of the coating.

5.4.2 Fatigue experiments

To investigate the influence of the animal movements on the PEDOT:PSS:PEG electrode performance, the impedance at the frequency of 1 kHz was evaluated as a function of several stretching cycles. Electrical and optical data are reported in Figure 5.12a and 5.12b, respectively. It can be noted that the electrode is very stable for several cycles and no significant degradation occurs, except when stretching cycles up to 40% (forward and backward) exceed 50 repetitions. In this event, the electrode impedance increases also for low strain deformation (Figure 5.12a) : the explanation was hypothesized in the accumulation of defects at the electrode border, barely visible in Figure 5.12b, that causes an increase in the series resistance without affecting the overall volumetric capacitance of the polymeric film. Noteworthy, it was again demonstrated the adhesion of the polymeric film to the underneath gold substrate up to the 50th cycle, due to the nitrogen atmosphere fluxed in the electrochemical cell during the polymer deposition. Moreover, between the 5th and the 20th cycles, the impedance values seems to be almost constant at the different strain percentage, as if, after the starting cycles (where higher differences are present at different strain), the electrochemical performances of the electrode reached a stability, keeping a constant value in the strain range 0-20%.

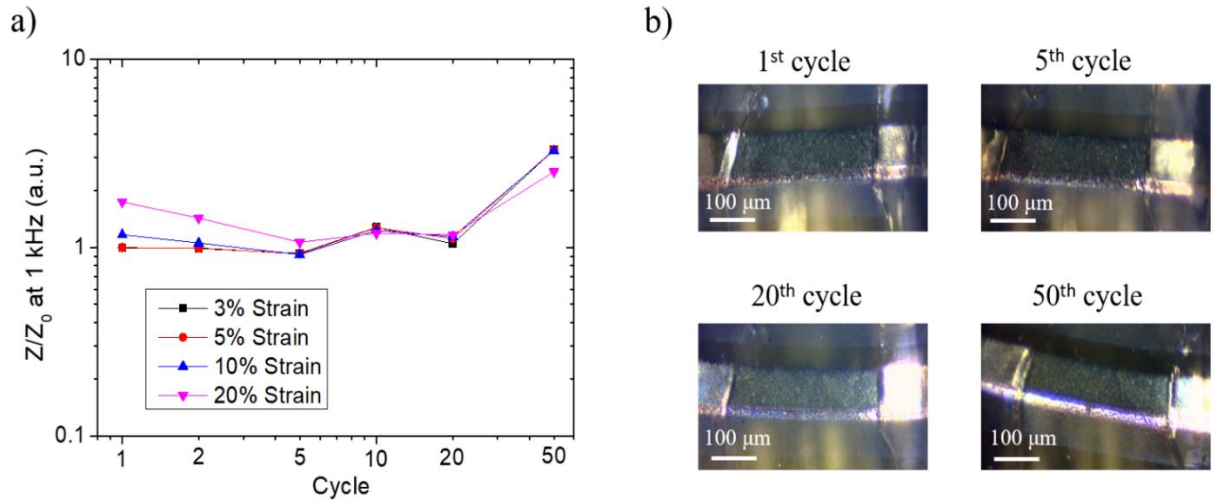

Figure 5.63: a) Normalized impedance at 1 kHz at 3%, 5%, 10% and 20% of strain as a function of the repetitive stretching cycles, performed up to a maximum strain of 40% while immersed in PBS solution. b) Optical images of the electrode under 10% of tensile strain at different cycles.

5.5 *In vivo* chronic recording

In order to demonstrate the facile handling, soft mechanical and low-impedance electrical properties, the device was implanted on the renal nerve of a Sprague-Dawley rat for acute and chronic *in vivo* recordings. The surgery implantation and the *in-vivo* recording procedures were performed in collaboration with the Department of Biomedical and Neuromotor Sciences in Bologna, by the group of Dr. Davide Martelli and Dr. Roberto Amici, and with the Florey Institute of Neuroscience and Mental Health of the University of Melbourne in Australia, by the group of William S. Korim and Song Yao.

The implantation different steps for the electrode insertion are shown in Figure 5.13, with the nerve highlighted by white arrow. Sprague-Dawley rats (with average weight of 350-450g) were anesthetized with 2% of isoflurane, keeping their body temperature at 37.0 ± 0.5 °C with a thermal blanket. The left femoral artery was then carefully dissected from the vein and nerve, for the implanting of the telemetry device (a PA-C40 telemetric transmitter, provided by Data Science International, MN) needed to monitor blood pressure. The animal was then placed prone and a left longitudinal incision was made on the left flank and the soft tissue was dissected, thus exposing the retroperitoneal cavity. Afterwards, the renal nerve was dissected from perineural connective tissue and positioned on the electrode (the kinked asymmetric shape allowing for facile insertion of the device into the surgical opening and manipulation with tweezers), using a drop of two component elastomer Kwik-Sil (World Precision Instruments, FL) to seal the nerve strand in the trench of the electrode. All the biological fluids around the nerve were meanwhile removed with small absorbed spears. The elastic interconnections were then sutured to neighbouring muscular tissue (Figure 5.13e) to keep the electrode in position while closing the abdominal muscle with absorbable suture (Figure 5.13f). Finally, the retroperitoneal cavity was closed and the transmitter (provided by Data Sciences International, MN) was secured subcutaneously on the back of the rat between the scapulae.

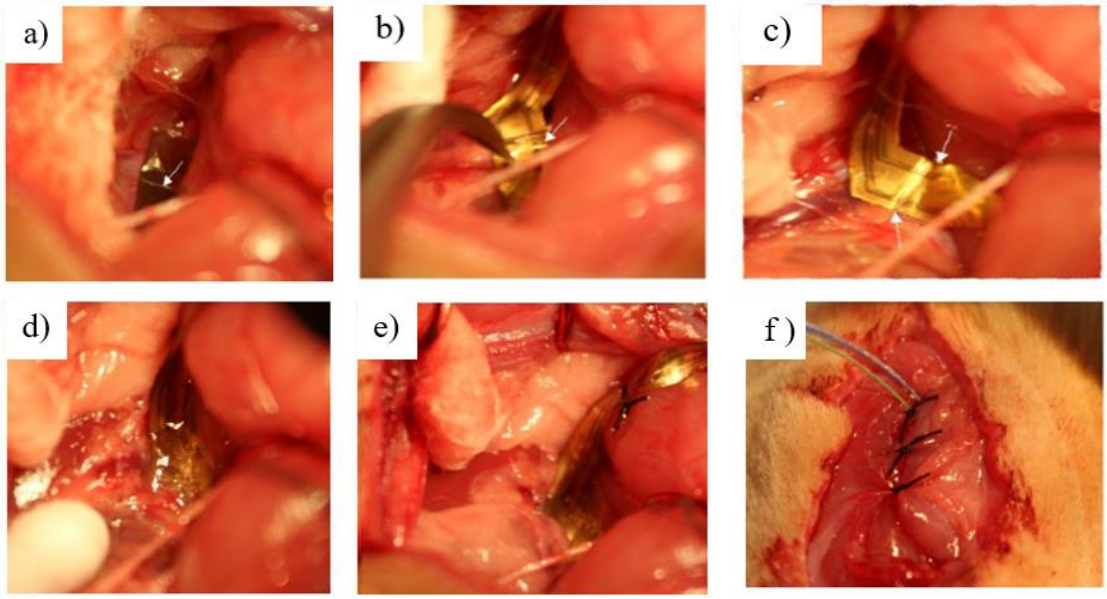

Figure 5.13: Optical images taken during the implantation of the stretchable microelectrode on renal nerve on a Sprague-Dawley rat. a) Isolation of the renal nerve. b) Microelectrode is positioned below the nerve and then (c) the nerve is inserted into the 400 μm wide trench. d) The trench with the nerve inside is sealed with self-curing silicone. e) The interconnects are sutured on the neighbouring muscles and (f) the tissue is closed.

The final device configuration and the implant components of the neural recording assembly are shown in Figure 5.14, comprising the wireless recording board (transmitter) that was placed subcutaneously in the animal. After the recovery of the animal from the surgery, it shows the normal behaviour with unrestrained motional activity and usual food uptake and no signs of distress or pain due to the implanted recording system.

Figure 5.15a reports signal traces recorded while the animal was awake but in resting position, acquired with the telemetry system after 14 days from surgery. Over the shown data trace of 80s a constant physiological arterial blood pressure (AP) of 85-120 mmHg and an heartrate (HR) of 330 beats per minute (bpm) were measured while the renal sympathetic neural activity (RSNA) presents spiking activity. This signal plotted on a shorter time scale (Figure 5.15b) shows a synchronization between the blood pressure and the spikes: several sympathetic burst of values around 10 μV, derived from compound action potentials, can be seen during diastolic blood pressure, while during pressure maxima (systole) only small random voltage fluctuations of 1.3 μVrms are shown, that are ascribed to the thermal amplifier noise. Moreover, there are no signs of interfering electrocardiogram (ECG) or electromyogram (EMG) signals due to the efficient shielding of the ground Ti/Au electrode evaporated on the back of the elastic electrode. The RSNA signal rhythmicity with the blood pressure was confirmed over longer recording periods and, in Figure 5.15c, the correlation between the time lag to the blood pressure maxima is reported, together with the counting of RSNA spikes recorded in a trace of 80 s. It can be clearly observed that maxima in the neural activity appear as multiples of the heartbeat interval of 180 ms: the pulse-synchronized activity is typical for sympathetic nerves, such as the splanchnic, lumbar or the observed renal nerve and is commonly employed as a method to evaluate recording quality under acute conditions. This ability to capture signal oscillations in chronic experiments confirms the quality of the developed stretchable and low-impedance electrode.

The proposed electrode allows for acute and chronic recordings, showing great stability in simulated biological environment and in real chronic experiments, together with the ability to dynamically adapt to the animal movement without being displaced or damaged. Moreover, the compact design and the possibility to adapt its shape to the neural implantation needs simplify the surgical procedure and the subsequent risk of mechanical failure and tissue bleeding/inflammations.

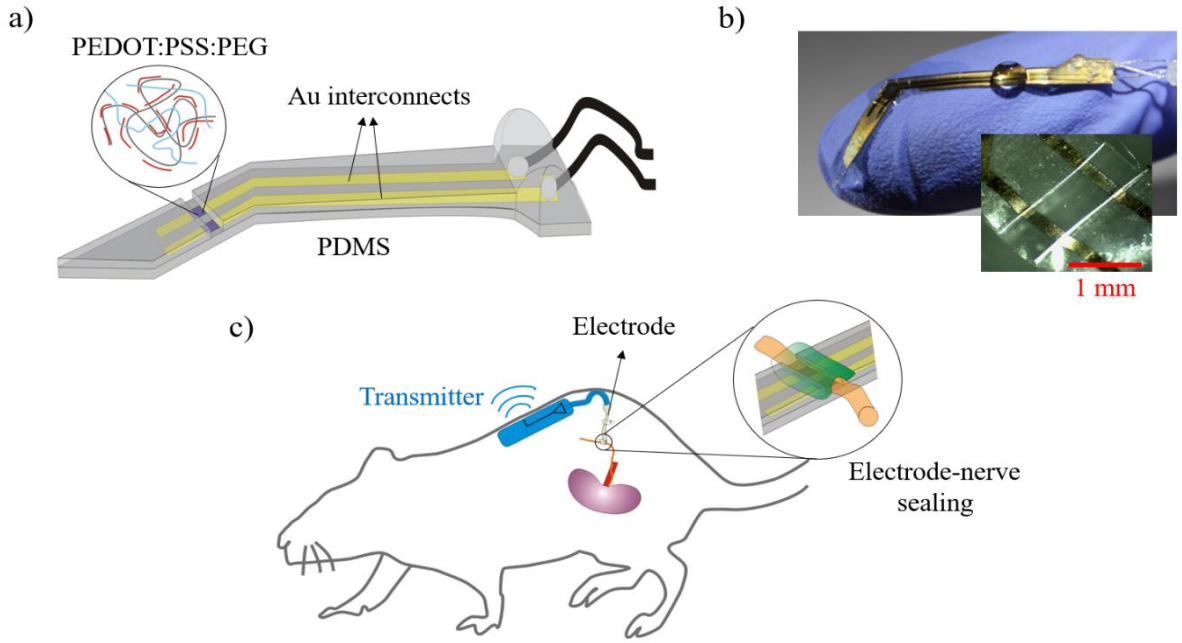

Figure 5.14: Schematic of the complete electrode structure with the PEDOT:PSS:PEG composite deposited on the exposed bipolar electrode to reduce its impedance and improve the stretchability. b) Optical images of the electrode with a zoom on the PDMS trench exposing the electrodes. c) Neural recording assembly, showing the different components (elastic electrode, subcutaneously-placed transmitter and silicone sealing).

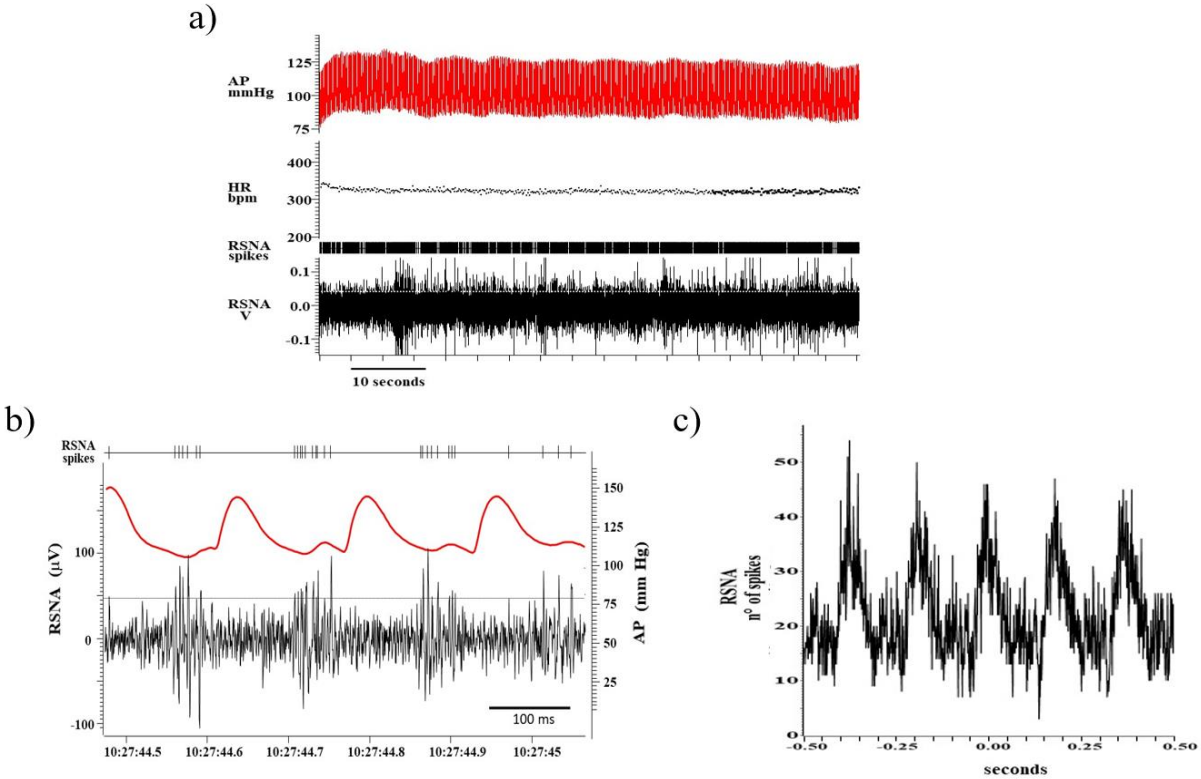

Figure 5.645: Chronic recording of rat renal sympathetic nerve activity (RSNA). a) Traces of RSNA, arterial pressure (AP) heart rate (HR) recorder signals with radiotelemetry. b) Zoom on RSNA (black) and AP (red) traces. c) Cross-correlation of RSNA spikes and AP, proving the good quality of the recorded signal.

Major results

PEDOT:PSS was deposited on gold electrodes, adding the plasticizer polyethylene glycol (PEG) to the composite, as biocompatible, low-impedance and stretchable interface towards a peripheral nerve, achieving the following results:

1. PEDOT:PSS:PEG coatings over Au electrode were able to maintain a low impedance up to 40% of strain, whereas pristine PEDOT:PSS ones lose the connection already at 20% of tensile strain
2. PEDOT:PSS:PEG electrodes showed high stability in simulated biologically environment, maintaining their electrochemical properties over several weeks of immersion in PBS solution and after up to 50 tensile strain cycles
3. The PEG addition to PEDOT:PSS composite enables to retrieve the crack opening kinetics typical of gold microcracked films, which permits reversible stretchability: due to the strong hydrophilic properties of PEG, the increase in water content in the electrode enhances the polymer chain mobility and reduces the dimensions of crystalline PEDOT rich regions in the conducting polymer nano-composite, promoting microcrack formation (avoiding macroscopic cracks that block conductivity)
4. The design of the proposed electrode simplifies the surgical procedure and reduce the risk of mechanical failure once implanted on peripheral nerves which are embedded in muscular tissue
5. The final device was implanted on the renal nerve of a Sprague-Dawley rat and used to record with success the spiking neural activity (synchronous to the blood pressure) of the nerve in *in vivo*, chronic conditions

This work is described in Ref [29].

Chapter 6
PEDOT:PSS Organic Electrochemical Transistor as sensors

6.1 Oxygen sensor

The fabrication of oxygen sensors, based on OECT geometry and using PEDOT:PSS as active layer, has been previously described in paragraph 3.2.1.
Cells are known to grow faster, live longer and with lower stress once cultured in low oxygen or even hypoxia condition.[403] Furthermore, hypoxia or low oxygen levels are often present in tumours and its level can vary in time and space:[404] standard physiological oxygen levels are found approximately around 10%,[405] while tumour masses can be either hypoxic or anoxic,[406] the level of which is associated with poor prognosis[407] and tumour aggressiveness. Evans *et al.* also studied the tissue oxygen partial pressure, presenting five categories of oxygen levels within gliomas: physiologic (10%), modest hypoxia (2.5%), moderate hypoxia (0.5%), sever hypoxia (0.1%) and anoxia (0%). Increased hypoxic levels are connected with more rapid tumour recurrence, since, for example, on average, grade 2, 3 and 4 tumours report modest, moderate and severe hypoxia, respectively.[404] Since the hypoxia levels can influence cancer prognosis or the efficacy of treatments, the monitoring and subsequent understanding of hypoxia during *in vitro* tests of cancer treatments can pave the way for the development of effective therapy.
The work described in this Chapter relies on this vision, thus the ability of PEDOT:PSS OECTs to detect especially low concentration of oxygen dissolved in solution, with partial pressure typically in the range 0-10% of the atmospheric pressure. In order to assess the device performances, the setup shown in Figure 6.1 was used: it consists in an electrochemical cell, filled with 25 ml of the selected electrolyte, where the OECT is partially immersed (only the active PEDOT:PSS areas). The lid of the cell is closed and the electrical connections, coming out from the cell, are sealed with parafilm to avoid gas exchanges between the inner and the outer part of the cell. The inner atmosphere and, subsequently, the oxygen dissolved in the solution are controlled by a two channels flowmeter, connected to a nitrogen cylinder and, depending on the range under investigation, oxygen or gas mixture (95% of N_2 and 5% of O_2) cylinder. Indeed, the mixture cylinder and the nitrogen one were used to flux 0-5% of O_2 in the cell, while for higher oxygen concentration the oxygen cylinder coupled with the nitrogen one were employed. The flowmeter outputs were connected to a gas bubbler to introduce the final calibrated gas mixture inside the cell, helping to homogeneously dissolve the O_2 in solution. A complete schematic of the developed setup and a picture of the electrochemical cell during an experiment are shown in Figure 6.1a and 6.1b, respectively.
I(t) measurements were performed keeping the valve on the bubbler “open”, waiting for the current to reach a stable value, while for output and transfer characteristic curves the target gas mixture was bubbled (with defined O_2 percentage) for 10-15 minutes, allowing for the proper dissolution of the gas in the solvent, then measurements were taken under oxygen:nitrogen (x% : y%) atmosphere.

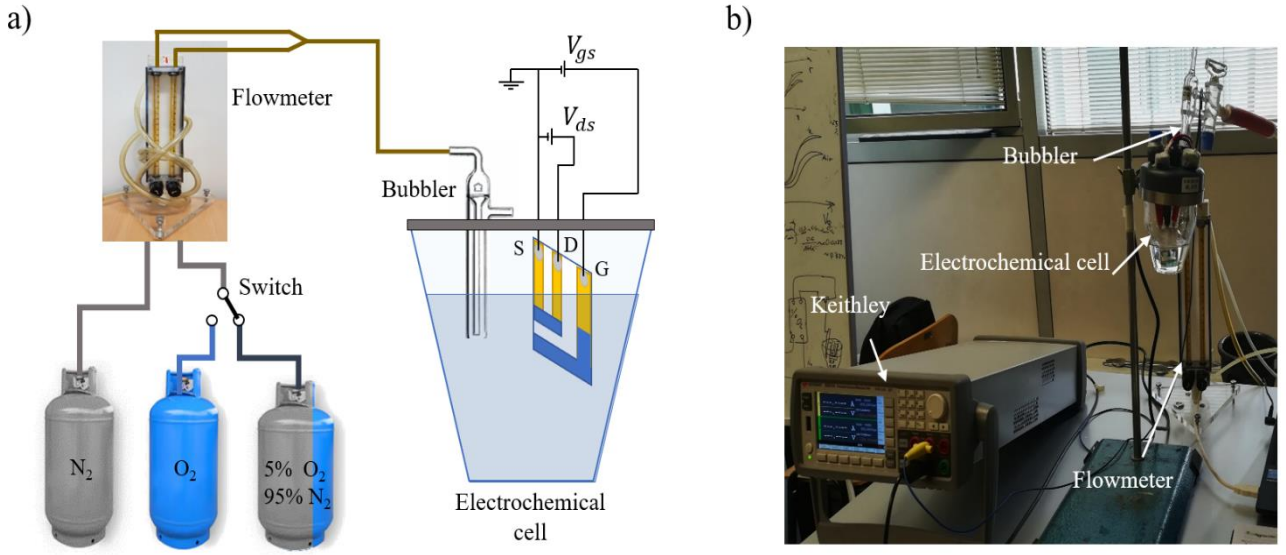

Figure 6.65: Schematic representation (a) and picture (b) of th oxygen experimental setup. The switch allows for the cylinder selection according to the oxygen range under investigation.

In order to correlate the oxygen partial pressure flushed by the flowmeter with the amount of oxygen dissolved in the solution (thus the real partial pressure above the solution), a titration, called Winkler method, was done, using KCl 0.1 M as solution. In detail, 2 ml of manganese sulfate were added to 25 ml of the sample solution and then other 2 ml of alkali-iodide-azide reagent were introduced in the solution, which was mixed carefully. Afterwards, 2 ml of concentrated sulfuric acid were added and the solution was mixed again. Titration with 2.5 mM sodium thiosulfate to a pale straw colour was done, adding after that the starch solution, in order to see a blue colour solution. Finally, a slowly titration was continued until the sample turned clear and the concentration of the oxygen dissolved is related to the number of millimetres of titrant used: each ml of sodium thiosulfate equals 2 mg/L of dissolved oxygen. Once the concentration of dissolved oxygen was known (C), it was possible to convert it in the resulting partial pressure above the solution (P), using the oxygen molecular weight (MW_{O2} = 31.999 g/mol) and the Henry law, $C = kP$, where k is the solubility constant. In this work, it was employed the oxygen solubility constant in water, k = 0.0013 mol/atm·L, as a first approximation.

Even though a proper calculation should be done for each electrolyte solution and, possibly, before every experiment, since oxygen solubility depends on salinity, temperature and pressure, keeping the laboratory temperature and pressure fixed, the following calibration was assumed to be suitable for all the measurements.

Table 6.2: Oxygen partial pressure, according to the flowmeter handling and the chemical calculation, and oxygen dissolved concentration. Errors associated to the flowmeter additions are around 10%, according to the precision that can be obtained from the visible scale on the columns, while errors around 1% are used for the chemical method. The nitrogen atmosphere was assumed with a negligible error, since N_2 was bubbled more than 20 minutes for the complete depletion of the oxygen in the solution.

Flowmeter O2	**Concentration**		**O_2 Partial Pressure calculated**
[%]	**[mg/L]**	**[µM]**	**[%]**
0	0	0	0
1.5 ± 0.1	0.760 ± 0.008	23.8 ± 0.2	1.827 ± 0.018
5.0 ± 0.5	1.96 ± 0.02	61.2 ± 0.6	4.71 ± 0.05
12 ± 1	3.72 ± 0.04	116.2 ± 1.2	8.94 ± 0.09

15.1 ± 1.5	4.72 ± 0.05	148 ± 0.1	11.35 ± 0.11
21 ± 2	7.28 ± 0.07	228 ± 2	17.50 ± 0.18

Table 6.1 reports the oxygen partial pressures, as introduced using the manual knobs of the two channels flowmeter, together with the oxygen dissolved concentration (calculated using the Winkler method) in the solvent and the resulting partial pressure of the oxygen above the solution. Data obtained by the chemical method allow for the proper calibration of the sensor, using the correct oxygen partial pressure: Figure 6.2a shows the overlap between the introduced and calculated oxygen percentage at low concentration, while the differences are more pronounced for high oxygen percentage. Nonetheless, the curve trends are quite similar, as evidenced by their slopes in Figure 6.2b, whose difference is contained in the error. However, Figure 6.2b shows that the linear fits for the low and high concentrations have different offsets, probably due to the need to switch the cylinders from one range to the other (as explained above). Thus, the two different calibration line were employed for the two different ranges to convert the "flowmeter data" into the "real", calculated ones, according to the following equations:

$$Calculated\ O_2 = 0.92\ x\ (Flowmeter\ O_2) + 0.2 \quad (0 - 10\%) \tag{6.1}$$

$$Calculated\ O_2 = 0.96\ x\ (Flowmeter\ O_2) - 2.8 \quad (10 - 22\%) \tag{6.266}$$

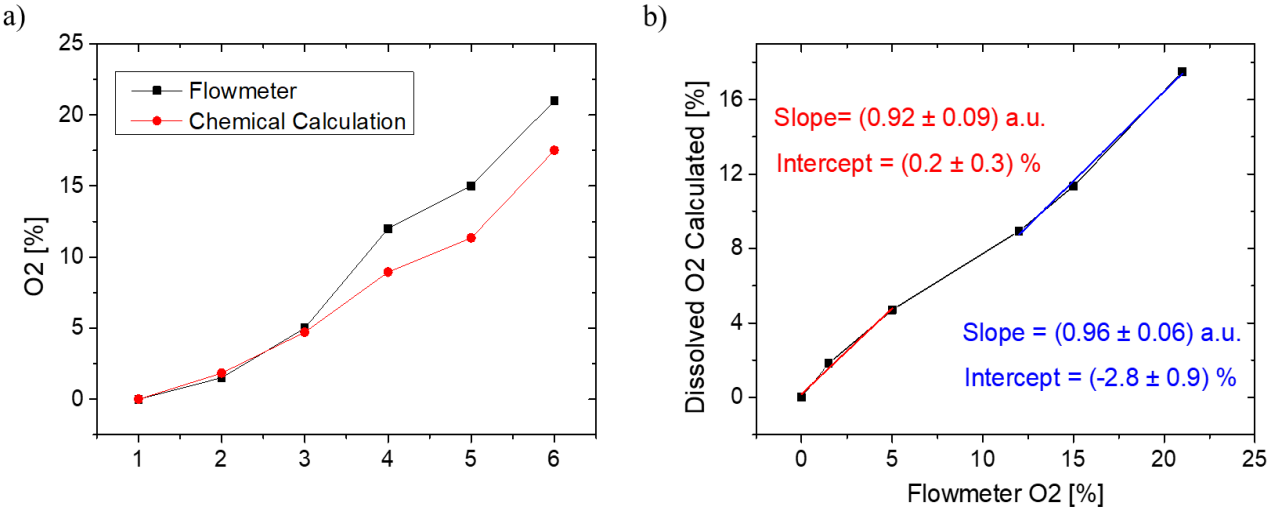

Figure 6.2: a) Oxygen partial pressure above the solution for the different additions, according to the flowmeter manual knobs (black squares) and the chemical calculations (red circles). b) Plot of the chemically calculated versus the flowmeter oxygen partial pressures. Two different linear trends are highlighted in the graphs, for low and high oxygen concentration, and slopes and intercepts are extracted to convert the O_2 concentrations in the respective ranges.

6.1.1 Sensors characterization in standard electrolyte (KCl 0.1M)

Firstly, OECTs were tested and characterized in a standard electrolyte solution, i.e. KCl 0.1 M, to assess the performance of the devices as oxygen sensor. Different amounts of oxygen were fluxed in the electrochemical cell using the flowmeter and, subsequently, converting the gas concentration according to the above reported Eq. 6.1 and 6.2.

6.1.1.1 Output and Transfer

Output

Output measurements were used to characterize the device steady-state response upon different oxygen partial pressure addition (thus upon different dissolved oxygen concentrations), exploring

also the possibility to extract current data to study the performance of the device as a sensor and, eventually, calibrate it. Data were collected sweeping the source-drain potential between 0 and -0.6 V, while V_g was fixed at a positive value of 0.2, 0.4, 0.6, 0.8, 1 and 1.2 V. These parameters were chosen in order to study the OECT under electrical dedoping upon different oxygen concentrations: indeed, as explained in the subparagraph 2.5.2.2, PEDOT:PSS catalytic properties allow it to undergo oxidizing redox reactions in presence of oxygen, thus changing $PEDOT^0$ (neutral state) into $PEDOT^+$ (conductive state), counteracting the electrical dedoping of the gate. Examples of the proposed measurements are reported in Figure 6.3 for different values of the applied potential on the gate and oxygen partial pressure ranging from 0% (completely nitrogen saturated atmosphere) up to 18.52% (a bit lower compared to the standard oxygen concentration in air of 21%). Oxygen was bubbled in the solution, thus partial pressure concentrations can be converted in oxygen dissolved in the solution using the solubility constant, as previously described. Figure 6.3b shows more distinct and separated curves in the interesting range 0-5%, together with the expected trend in which the rise of oxygen concentration leads to higher currents in the device due to the maintenance of the polymer in its conductive state ($PEDOT^+$). For these reasons, the output characteristic obtained for V_g = 0.8 V (OECT "off" state) were analysed, extracting I_d values at V_d = -0.3 V for the oxygen partial pressure range 0 to 5%. The calibration curve of the normalized current $(I_d - I_0)/ I_0$ versus the logarithm to the base 10 of the molar concentration (M) of dissolved O_2 in solution is shown in Figure 6.4, where I_0 is the current value for nitrogen saturated atmosphere (0% of oxygen).

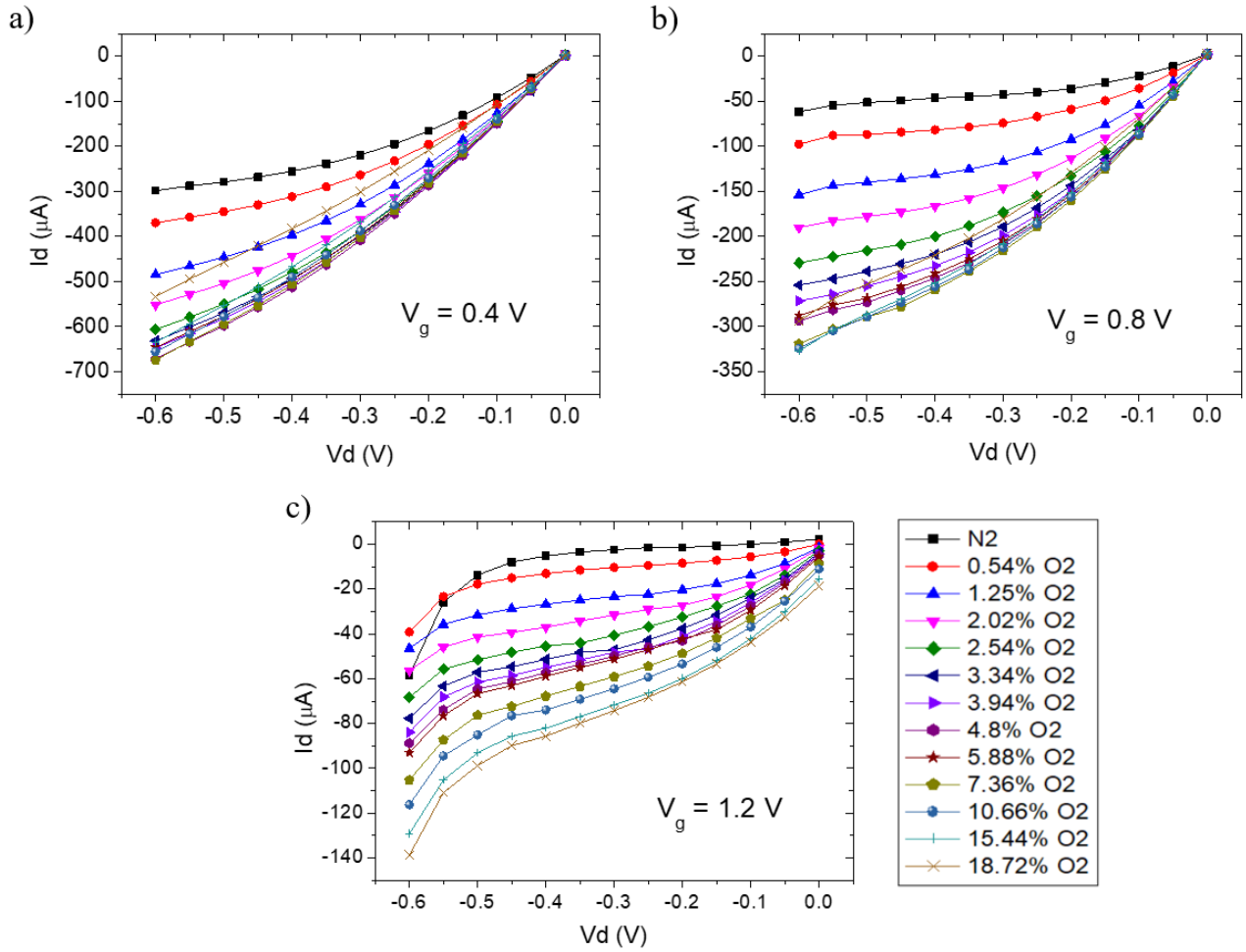

Figure 6.3: Output characteristic curves of PEDOT:PSS OECTs for different oxygen partial pressure in the atmosphere above the solution upon the application on a positive bias on the gate of 0.4 V (a), 0.8 V (b) or 1.2 V (c). The legend of the oxygen percentage is reported on the bottom right for all the graphs.

Figure 6.4 report the calibration curves described, highlighting a linear trend of the device normalized current modulation with respect to the logarithm to the base 10 of the dissolved oxygen. Thus, the sensitivity and limit of detection (LOD) of the sensor were calculated with a linear fit of the device response ($R^2 = 0.998$). In detail, the sensitivity was extracted as the slope of the linear fit, while the LOD was calculated adding the logarithm to the base 10 of the concentration of the blank signal (x_0) to the logarithm to the base 10 of the concentration leading to a signal 3 times higher compared to the experimental noise, which was evaluated as the standard deviation of the intercept of the fit, then converting the resulting value into a concentration one. The resulting equations resume the steps followed:

$$x_0 = -\frac{intercept}{slope} \quad (y = 0\,, blank\ signal) \tag{6.67}$$

$$Detectable\ signal = x_0 + 3 \cdot \Delta_{intercept}/slope \tag{6.68}$$

$$L.O.D.(M) = 10^{(Detectable\ signal)} \tag{6.69}$$

The calibration curve shows a sensitivity of the device of (4.17 ± 0.08) decade^{-1} and a limit of detection of 13 μM, which corresponds to a concentration of 0.41 mg/L, that means 1% of oxygen partial pressure above the solution. Even though the limit of detection is not under the 1%, the output characterization highlights the oxygen-dependent behaviour of the OECT and looks promising for the sensing of oxygen dissolved in solution, having above a partial pressure of this gas in the range 0-5%.

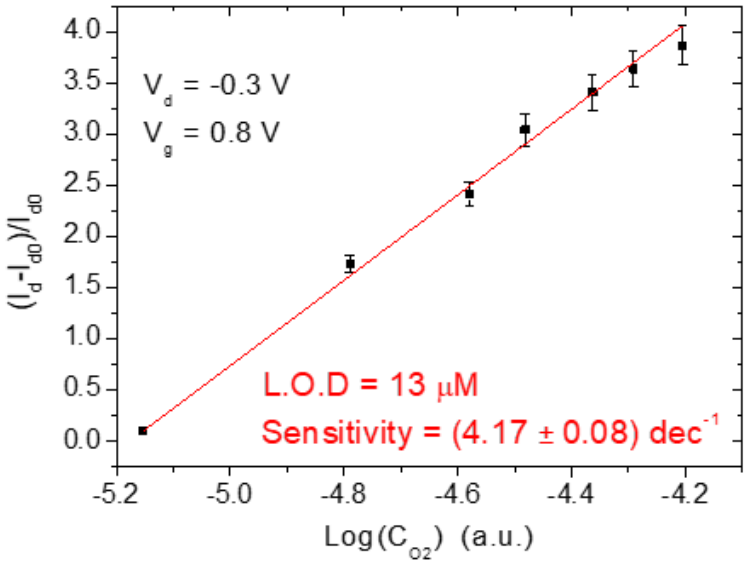

Figure 6.4: Normalized current ($I_d - I_0$)/ I_0 versus logarithm to the base 10 of the molar concentration of dissolved oxygen, employed as calibration curves for oxygen sensing. Data are taken from output characteristic curves in the oxygen range 0-5%.

Transfer

The second electrical method employed to study the OECTs as oxygen sensors was the transcharacteristic (transfer) curve, in which a fixed drain voltage of V_d = -0.3 V was applied, sweeping the gate bias from -0.2 V to 1.2 V. Data were collected after bubbling the oxygen in the solution at a certain concentration and acquired under a constant oxygen partial pressure.

Figures 6.5a and 6.5b report the measurements performed and the subsequent calibration curve ($I_d - I_0$)/ I_0 versus the logarithm of the molar concentration of dissolved oxygen in the solution.

The transcharacteristic curves show the typical shift towards higher current, upon the raising of the oxygen dissolved in the solution: compared to previous experiments, more oxygen concentration steps were fluxed to test the linearity in the small concentration range, resulting in closer (and nearly superimposed) electrical response. Current values were then extracted in the forward scan of the transfer curve at V_g = 0.8 V, according to the parameter used for output curves in the previous paragraph. The linear fit (R^2 = 0.998) reports a sensitivity of the oxygen sensor of (1.44 ± 0.04) decade^{-1}, which is almost 3 times lower compared to the one extracted from the output analysis, while the calculated limit of detection presented the same value of 13 µM (1%). Despite this result, the linear trend in Figure 6.5b highlights that a difference in initial (low) oxygen additions is detected by the sensor, revealing that the calculated LOD. represents an overestimation of the potential of the device.
Again, the OECT proves to be a valid oxygen sensor in the range between 0-5%, even with lower sensitivity.

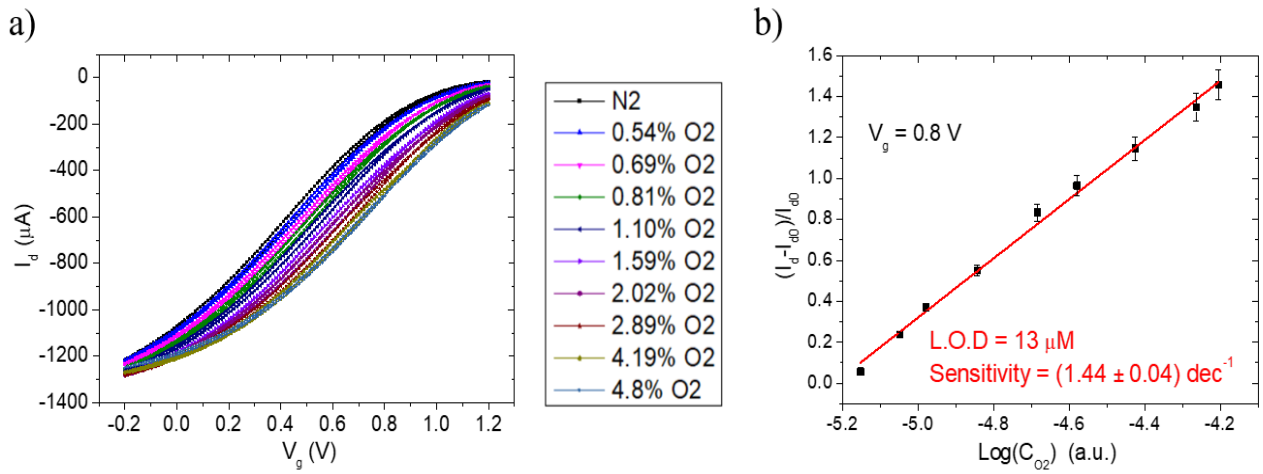

Figure 6.5: Transcharacteristic curves (a) and analysis (b) for OECT devices at different oxygen partial pressure above the solution, in the range 0-5%.

6.1.1.2 Current versus voltage

Once observed the device characterization at different oxygen concentration, OECT performances as oxygen sensors were evaluated using I_{ds}(t) measurements, with fixed potential on the gate and the channel (V_g = 0.8 V and V_d = -0.3 V, where higher curve separation were obtained from the previous studies), adding oxygen in the solution in the usual range 0-5% Figure 6.6a reports the performed measurement, together with the indication of the oxygen partial pressure additions, introduced with the flowmeter (bubbling in the electrolyte solution during the electrical data acquisition). The graph displays, as expected, increasing current upon the enhancement of the oxygen amount in the solution. After each addition, the stable current values were extracted and normalized with respect to the current extracted in nitrogen atmosphere, then plotted in function of the logarithm to the base 10 of the dissolved oxygen concentration (Figure 6.6b). Again, a linear correlation between these two parameters is present. In detail, the fitted sensitivity is (0.49 ± 0.01) decade^{-1}, almost an order of magnitude lower compared to the one extracted from the output characteristic curves. On the other hand, the achieved limit of detection of the sensor is 1 µM (0.03 mg/L), more than an order of magnitude lower than the previously calculated. Even though with lower sensitivity, this electrical monitoring of the oxygen amount shows a low oxygen detection limit, which corresponds to 0.08% of oxygen partial pressure, thus being suitable to study cells grown in hypoxia conditions or the tumour connection with the tissue oxygen partial pressure.

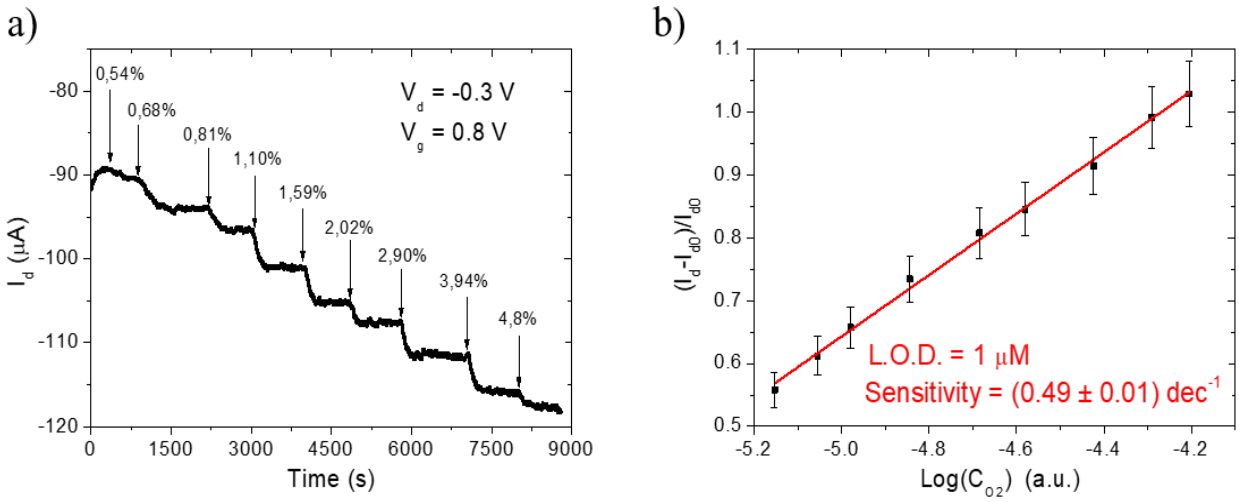

Figure 6.6: a) I_d (t) measurement of the PEDOT:PSS OECT with fixed V_d = -0.3 V and V_g = -0.8 V, during the bubbling of several oxygen partial pressure concentration in the electrolyte solution. b) Normalized current (I_d – I_0)/ I_0 versus logarithm to the base 10 of the molar concentration of dissolved oxygen, employed as calibration curves for oxygen sensing.

In order to study the hysteresis of the sensor, thus to understand its response to oxygen subtractions, a preliminary I_d(t) measurement was run, first raising the oxygen concentration up to 5%, then lowering it down, returning to a nitrogen saturated atmosphere with several intermediate steps. In order to limit the stress on the sensor, the applied gate potential was lowered to the value of V_g = 0.4 V, avoiding a strong reduction of the PEDOT:PSS channel, which can influence the OECT performances over long time. The obtained curves are reported in Figure 6.7a and 6.7b for the increasing and decreasing oxygen concentration, respectively. It can be noted that the initial low oxygen additions are not clearly detected by the OECT, probably due to a reduction of the gate potential or problems during the bubbling, but the standard current response is however displayed for the subsequent oxygen increasing amounts. Furthermore, the opposite behaviour, with current decrease upon oxygen reductions, is reported by the sensor, thus displaying that it can work in both directions (for raising or decreasing oxygen amounts). However, it is clearly visible that longer time should have been waited after each subtraction before the next, since the oxygen removal seems to need more time than its introduction and a defined current baseline was not reached yet.

Despite the small drawbacks, data analysis of the oxygen additions and for both oxygen introduction and removal were studied and are shown in Figure 6.7c and 6.7.d, respectively. Figure 6.7c displays a working sensor with slightly reduced sensitivity and a higher LOD. compared to the previously obtained, that can be ascribed to the reduced gate voltage used for the measurement. Importantly, the analysis for the oxygen introduction and removal (Figure 6.7d) highlights for the two directions a similar normalized current response in the range 1-5%. The extracted sensitivities result only slightly different, looking promising for a sensor whose response will not be influenced by the previously detected concentrations. Thus, further analyses will be performed on the sensor hysteresis, taking care of the time needed to remove the oxygen from the solution and trying to run measurements with the gate potential of V_g = 0.8 V using less intermediate steps in the range of 1-5% to prevent the polymer degradation.

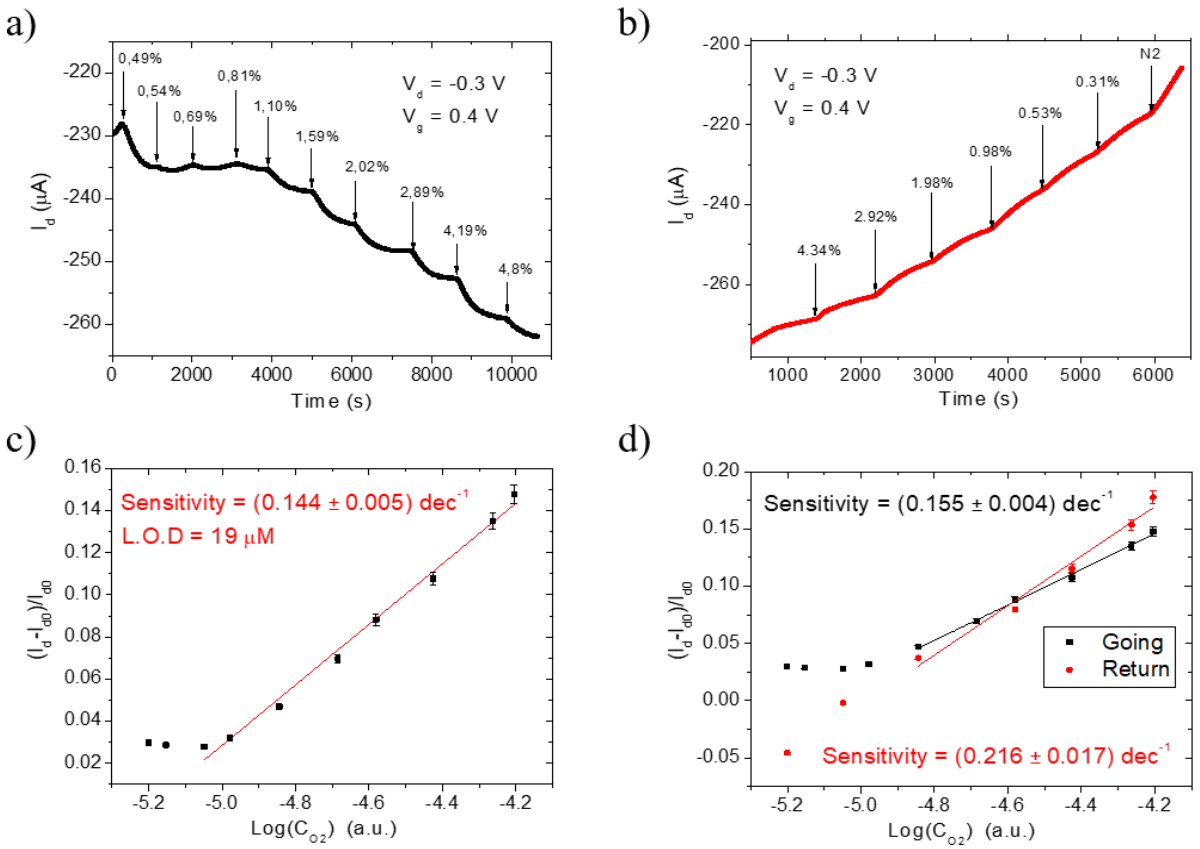

Figure 6.7: I_d (t) measurement of the PEDOT:PSS OECT with fixed V_d = -0.3 V and V_g = -0.4 V, during the bubbling of increasing (a) and decreasing (b) oxygen partial pressure concentration in the electrolyte solution. c) Data analysis for the increasing oxygen concentration curve (c) and for both increasing (going, black squares) and decreasing (return, red circle) oxygen amount to study the hysteresis of the sensor (d).

6.1.2 Experiments in cell culture medium

6.1.2.1 Output and transfer

The oxygen sensing OECTs were also investigated in a more complex and realistic cellular environment, namely the Dulbecco's Modified Eagle Medium (DMEM), that was previously employed as cell culture medium for fibroblast and Caco-2 in Chapter 4. However, the composition of the liquid induced several bubbles above the DMEM surface when gases were introduced in the solution, wetting and compromising the contacts and the sealing of the electrochemical cell. Thus, I_d(t) measurements were avoided keeping the flux of the flowmeter open only between the data acquisition to reduce the noise. Accordingly, only output and transfer characteristics were performed in the range of oxygen partial pressure above the solution between 0 and 5%, as in the previous paragraph. Output with fixed V_g = 0.8 V and transcharacteristic with fixed V_d = -0.3 V curves, showing the most distinct responses among the others, are reported in Figure 6.8a and 6.8b, respectively, together with a legend of the oxygen partial pressure additions. It can be noted that the separation between the curves is lower compared to their counterpart in KCl 0.1M solution, probably due to the higher ionic strength of the more complex medium that allows for a stronger electrochemical dedoping of the device, thus lowering down the current in the channel for positive gate bias. Nonetheless, the device displays correct curve trends, with higher the current in the channel upon the increasing of oxygen dissolved in the solution. However, fitting in the range where the normalized current and the logarithm to base 10 of the dissolved oxygen concentration are linearly correlated, the resulting sensitivities, analysed for output and transfer in Figure 6.8c and 6.8d, respectively, are basically halved compared to the ones of OECTs investigated in KCl. Accordingly,

the limits of detection calculated for the two electrical monitoring are doubled, obtaining 24 µM and 21 µM for output and transfer analysis, respectively, that correspond to 1.8% and 1.6% of oxygen partial pressure.
In conclusion, the OECT proved to be suitable for monitoring oxygen dissolved in solution, also in biological environment, such as cell culture medium. Even though the lower detectable amount has still to be improved, this study paves the way for investigating cell culture under hypoxia conditions and for further analysis on the correlation between tumour properties, such as aggressiveness, with the tissue oxygen partial pressure.

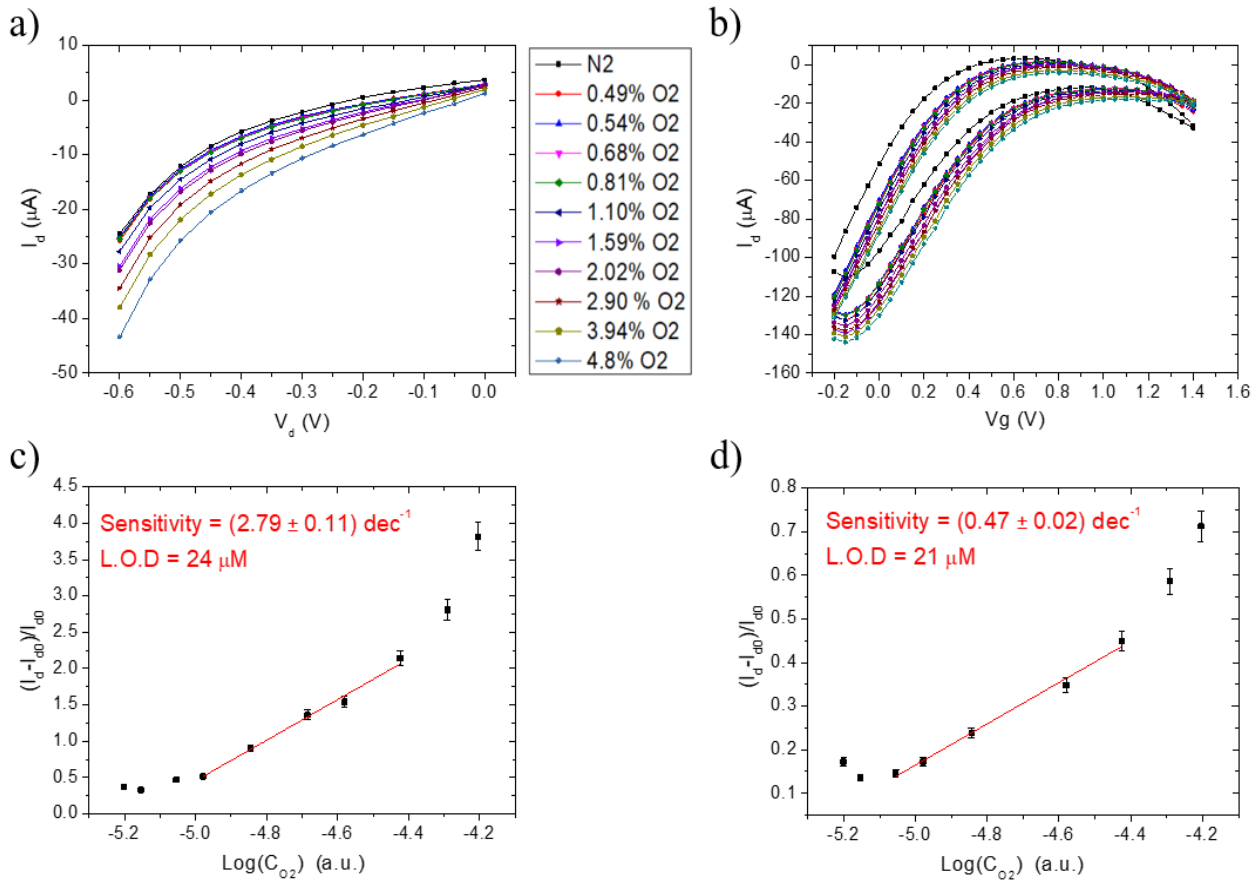

Figure 6.8: Output at V_g = 0.8 V (a) and transfer at $V_{d=}$ -0.3 V (b) characteristics for a PEDOT:PSS OECT, upon different dissolved oxygen concentration in DMEM solution (used as electrolyte). Data analysis of the output (c) and the transfer (d) curves.

Major results

PEDOT:PSS-based OECTs have been used in this Section as sensors for oxygen dissolved in solution, obtaining the following results:

1. Since the spontaneous reaction occurring between PEDOT:PSS and oxygen (due to PEDOT:PSS catalytic properties) keeps the polymer in its conducting (oxidized) state, the device response are shifted towards higher currents for increasing O_2 concentrations
2. A planar PEDOT:PSS OECT was characterized as an oxygen sensor in a solution of KCl 0.1M in the range of low oxygen concentration (0-5% of oxygen partial pressure above the solution), obtaining a low limit of detection of 1 μM (which means 0.03 mg/L, thus 0.08% of oxygen partial pressure above the solution)
3. A preliminary study on the sensor performances in a complete cell medium, proved the ability of OECTs to monitor oxygen dissolved in solution also in biological environment, paving the way towards investigations on cell culture grown in hypoxia conditions or on the correlation between tumour properties and tissue low oxygen partial pressure

The results are reported in Ref [408].

6.2 Cell differentiation sensor

Among several approaches, the use of stem cell to treat osteoporosis is lately a highly relevant and widespread method.[409,410] Stem cell osteogenic differentiation is a very complex process, articulated in a series of events such as the secretion of collagen type I, osteopontin, osteonectin and Bone Morphogenic Protein 2 (BMP-2), among others.[411] These molecules can be employed as markers to monitor stem cell fate, studying the effect of particularly differentiation techniques (such as the electrical stimulation with smart biocompatible material, which has lately developed as an innovative approach[90,412]). Currently available techniques to monitor these analytes or cytokines involve end-point enzymatic assays (i.e. Alkaline phosphate activity), enzyme-linked immunosorbent assay (ELISA) and gene expression profiling, that do not allow real-time monitoring, thus overlooking potentially interesting information.
In this thesis, in order to acquire more data and helpful informations of stem cells undergoing osteogenic differentiation, PEDOT:PSS organic electrochemical transistors have been explored as promising sensors for cell analytes and cytokines released during this process. In detail, a chemical-biological functionalization strategy has been developed with the aim to realize an on-line, electrical sensing device capable of being integrated within a cell culture chamber. In order to test the functionalization strategy and the device response to a target analyte, anti BMP-2 antibodies were used as last step to perform a proof of concept BMP-2 detection.
The work reported in this Section on the development of a cell differentiation sensor was done at the Department of Chemical Engineering and Biotechnology of the University of Cambridge (UK), led by the Prof. Roisin Owens and the Dr. Donata Iandolo, in a fruitful collaboration with the Department of Physics and centre for Plastic Electronics of the Imperial College in London (UK), working with Ellasia Tan and the Prof. Ji-Seong Kim, and the Biological and Environmental Science and Engineering Division of the King Abdullah University of Science and Technology in Thuwal (Saudi Arabia), collaborating with Dr. Achilleas Savva and Prof. Sahika Inal.

6.2.1 Functionalization strategy towards stem cell released cytokines detection

The functionalization process relies on the streptavidin-biotin chemistry towards a selected antibody, as a way to impart specificity to the biosensing element, and consists in 5 main steps, shown in Figure 6.9:

1. PEDOT:PSS thin films were treated with air plasma at low power intensity (20 Watt, 1 min) to introduce hydroxyl groups on the semiconducting polymer surface, without affecting its conductivity or etching it;[413]
2. (3-Aminopropyl)triethoxysilane (APTES) (from Sigma-Aldrich) was covalently bound to the activated surfaces, exploring two different techniques to deposit this layer;
3. Sulfo-NHS-Biotin (Abcam, UK) units were bound to the APTES-functionalized polymeric surfaces;
4. Streptavidin (Thermo Scientific) molecules were linked with great affinity with biotin;
5. A biotinylated, capture antibody was bound to streptavidin, in order to have the specificity towards the selected analyte/cytokine at the edge of the functionalization chain.

The plasma treatment induced a reduction in the contact angle of the PEDOT:PSS films from 41.9° ± 0.2° to 0° (a totally hydrophilic surface), upon the introduction of the hydroxyl groups, necessary for facilitating the APTES binding. Then, two methods were tested to functionalize PEDOT:PSS surfaces with APTES, namely a Chemical Vapor Deposition (CVD-APTES samples) technique and a Soaking one (S-APTES samples). Briefly, the former was performed inside a desiccator decreasing

the pressure down to ~35mbar and raising the temperature of the hotplate to heat the thermally conductive plate on which 500 µl of liquid APTES were placed. After 2 hours, the hotplate was turned off, the APTES exhaust vapor expelled and few drops of distilled water were introduced on the hot plate (pumping the vacuum), to allow the crosslinking of APTES molecules.[414] On the other hand, for the S-APTES samples, plasma treated PEDOT:PSS films were immersed in a 2% v/v APTES solution in a 95% ethanol acqueous solution overnight (~19 hours), then rinsed carefully with ethanol and distilled water. Finally, an annealing process at 65 °C for 5 hours was run to crosslink APTES molecules. These two different APTES-functionalization ways are investigated in the following paragraph.

Sulfo-NHS-Biotin and streptavidin functionalization were performed immersing the substrates in 4 mg/ml biotin acqueous and 200 µg/ml streptavidin in 1X PBS solutions, respectively, for 1 hour, then rinsed with distilled water. Additionally, streptavidin substrates were subsequently rinsed four times alternating a 0.05% solution of Tween® 20 in PBS (PBST) and PBS under constant agitation of 100 rpm to remove aspecific binding.

Anti BMP-2 antibodies (Abcam, UK9) were biotinylated using a biotinilation kit (ab201796-Biotin, Type B, Fast Conjugation Kit, Abcam, UK) and obtaining a 0.83 µg/ml in 1X PBS solution. Samples were incubated for 1 hour, then rinsed with PBS and Milli-Q water.

Finally, samples were incubated in 15 µl of 0.0016 µg/ml BMP-2 (Abcam, UK) in PBS solution for 1h, then rinsed with PBS and Milli-Q water.

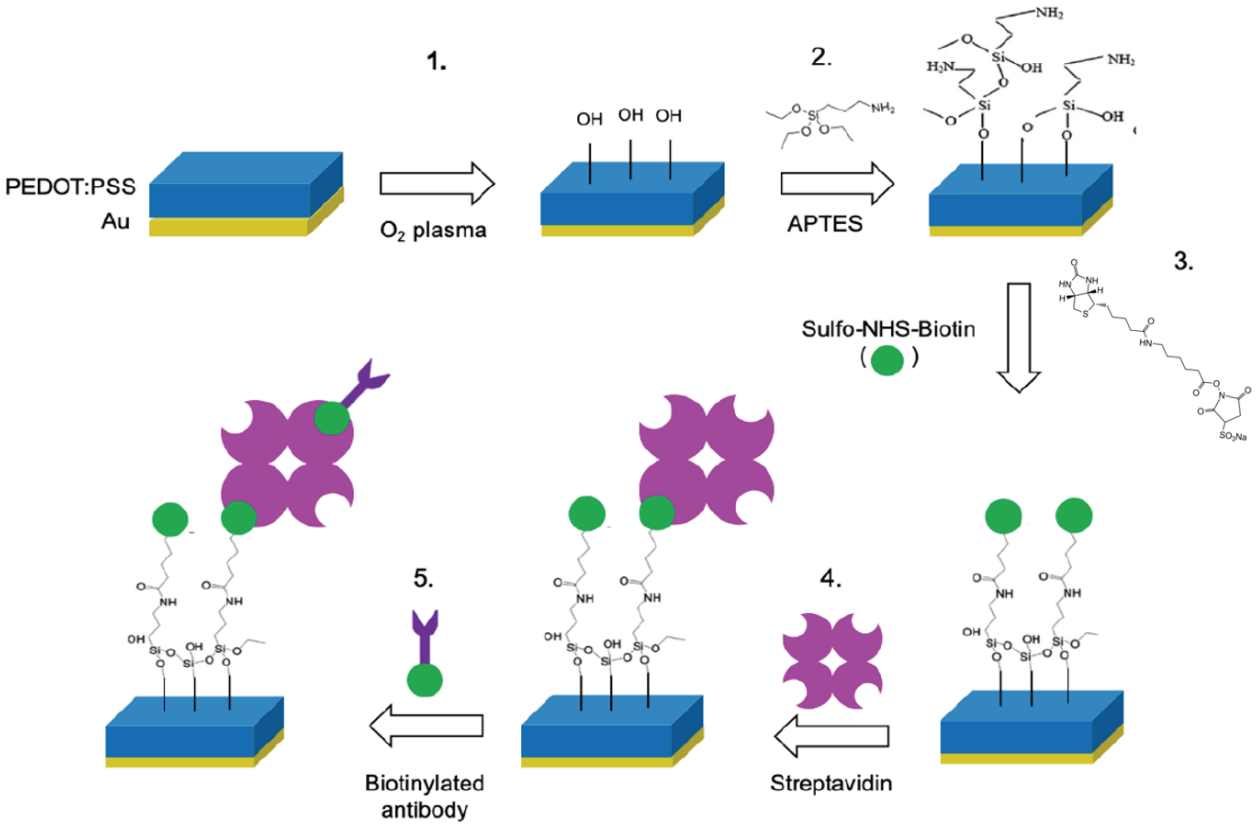

Figure 6.9: Functionalization strategy (in five sequential steps) employed on the PEDOT:PSS coated gold electrodes in order to impart selectivity to the device.

6.2.1.1 (3-Aminopropyl)triethoxysilane (APTES) deposition

Firstly, the properties of the two APTES-functionalized PEDOT:PSS films, compared to the pristine polymeric one, were properly investigated. In order to assess the presence of the APTES on the sample surfaces, contact angle measurements were employed dispensing a 5 µl drop of deionized

water onto the sample surface, as shown in Figure 6.10: compared to pristine PEDOT:PSS, having an average contact angle of 41.9° ± 0.3 (Figure 6.10a), higher values were obtained for APTES functionalized surface, i.e. 52° ± 1° (Figure 6.10b)) and 46.1 ± 0.4° for CVD- and S-APTES, respectively. These results represent the average values over five samples, each measured five times in a different surface position. The increased hydrophobicity of the surface once the silane is deposited, more pronounced for the CVD-APTES sample, proves the successful deposition, according to previous works in literature,[414–416] where contact angle values around 45° or higher are shown for hydrophilic surface functionalized with APTES.

Since the presence of the APTES would impart dielectric properties to the conducting PEDOT:PSS film, an electrical surface characterization was run using Conductive Atomic Force Microscopy (C-AFM). As expected, the C-AFM maps show a reduction in the surface conductivity after the silane deposition on top of the pristine conducting polymer map (Figure 6.10d). The drop in surface conductivity is accompanied by the appearance of conducting spots, more abundant in the case of CVD- (Figure 6.10e) than for S-APTES samples (Figure 6.10f). From a correlation between the morphology and the conductivity of the same scanned areas (Figure 6.11), conducting spots (highlighted by the white arrows) were ascribed to defects in the APTES deposition, their conductivity deriving from the underneath PEDOT:PSS layer. Thus, more homogeneous layers were deposited with the soaking process.

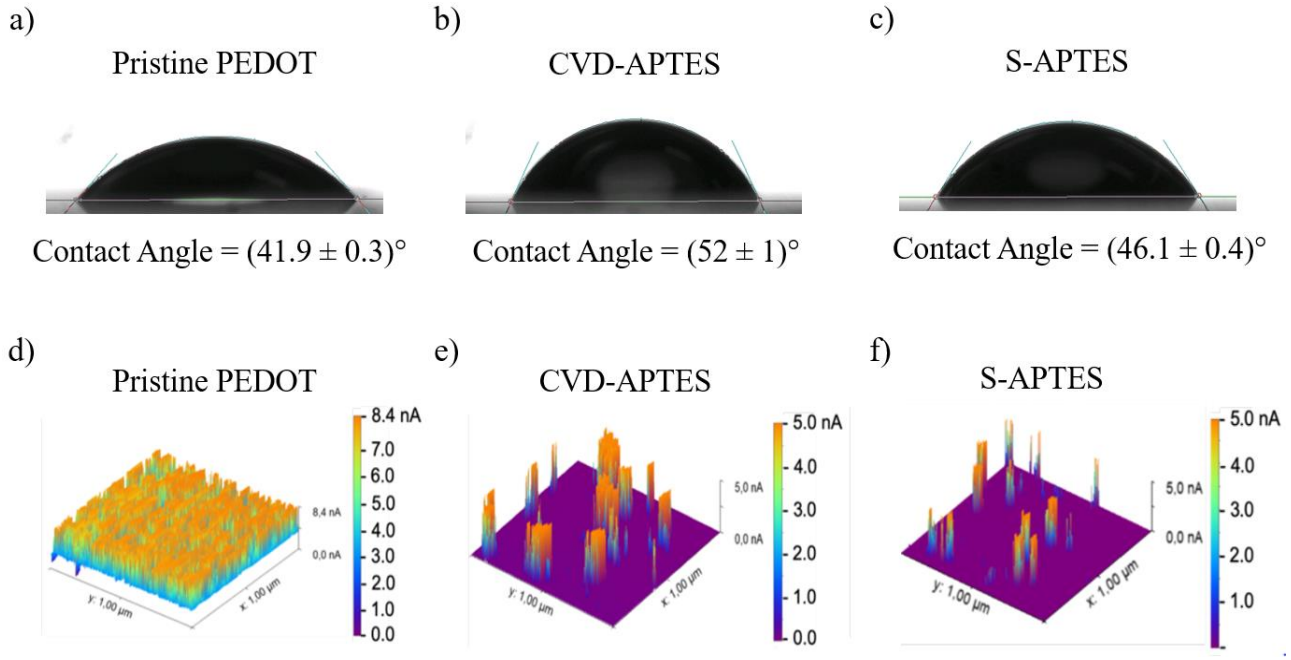

Figure 6.101: Samples surface characterization. Contact angle images of a 5 µl water drop on a pristine PEDOT:PSS surface (a), a CVD- (b) and S-APTES (c) functionalized ones. Conductive Atomic Force Microscopy maps of a pristine PEDOT:PSS surface (d), a CVD- (e) and S-APTES (f) functionalized ones.

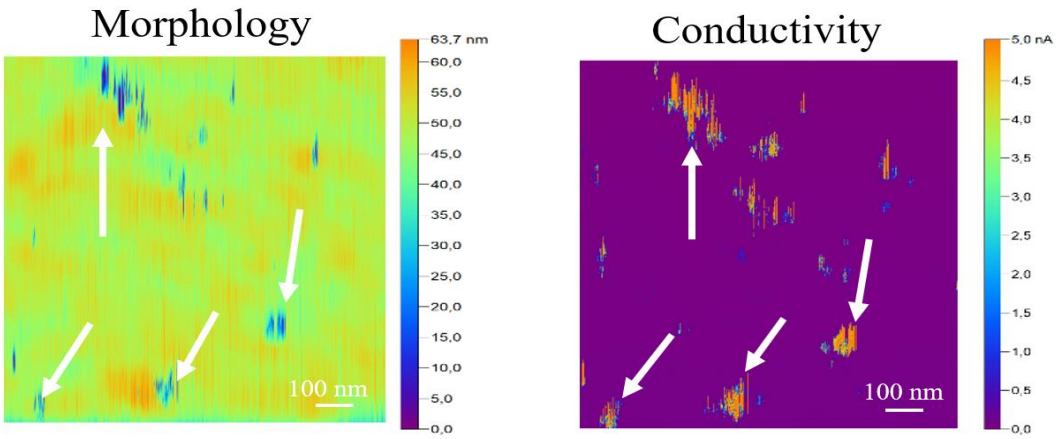

Figure 6.11: Topography (left) and Conductive (right) AFM maps of the same area of a CVD-APTES functionalized PEDOT:PSS samples. White arrows highlight the conducting spots representing holes in the morphology map of the APTES layer.

Afterwards, using *in-situ* electrochemical resonance Raman Spectroscopy, the bulk interaction between PEDOT:PSS and APTES was studied, both for the pristine (neutral) and the reduced films (negatively polarized samples), reported in Figure 6.12a and 6.12b, respectively. Since dedoped PEDOT is resonantly excited at 633 nm, this wavelength was used to excite the sample, providing higher sensitivity to structural changes in the reduction regime. When no bias was applied (Figure 6.12a), APTES effects on PEDOT vibrational states were similar for both the deposition techniques and resembled dedoping signatures (red and blue line for CVD- and S-APTES, respectively, compared to the black line for PEDOT:PSS,),[291,417] showing no other molecular structural changes resulting from the APTES deposition. For this reason, silane groups of APTES molecules can only interact with PSS-rich regions, as occurs for the crosslinking effect of GOPS on PEDOT:PSS.[418]

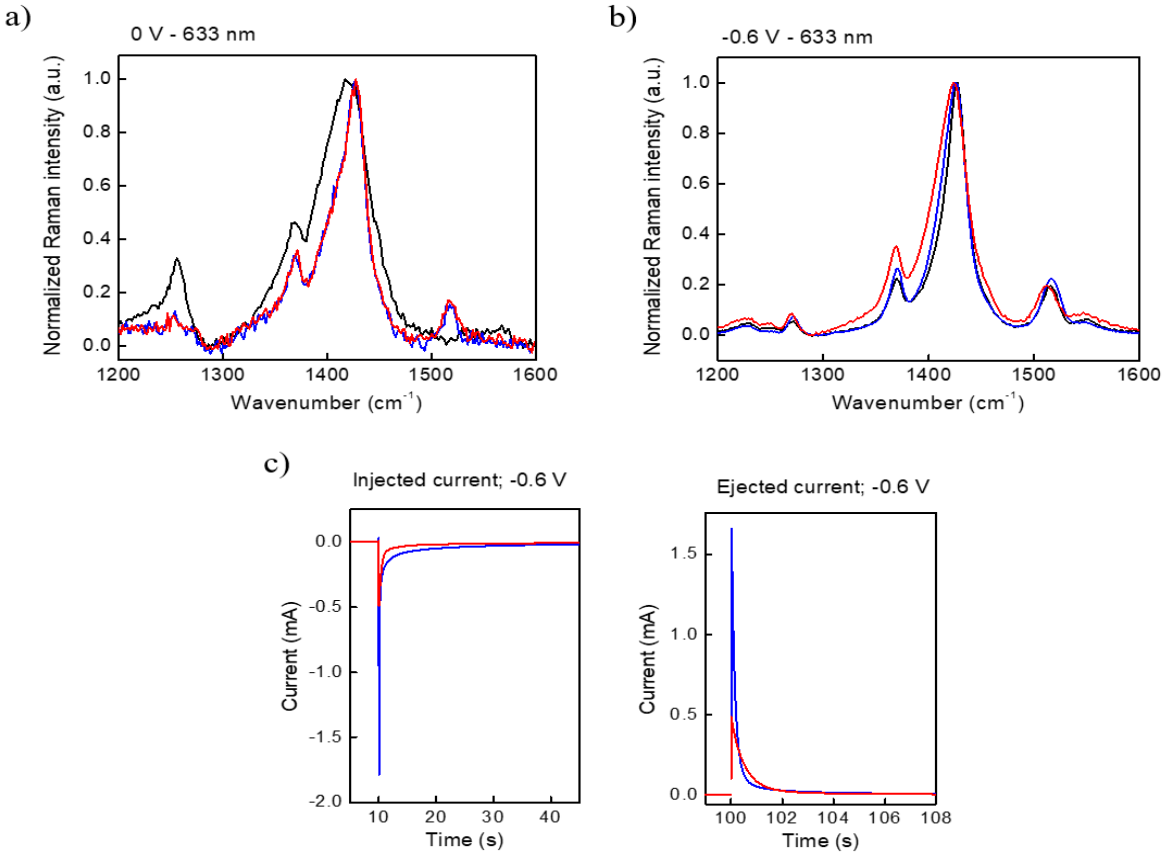

Figure 6.12: Studies on the bulk interaction between APTES layers deposited on PEDOT:PSS films. Electrochemical Raman Spectroscopy of pristine PEDOT:PSS thin films (black), CVD- (red) and S-APTES (blue) functionalized ones, in the neutral (a) and reduction (b) regimes, together with chronoamperometric measurements (c).

On the other hand, measuring CVD- (red line) and S-APTES (blue line) spectra in the reduction regime (under an applied bias of -0.6 V, as reported in Figure 6.12b), the latter spectra resulted closer to PEDOT:PSS (black line) ones at the same reduction potential. In order to further clarify this behaviour, chronoamperometry studies were run on both samples, obtaining lower injected and ejected currents for CVD samples under the applied bias of -0.6 V (Figure 6.12c), indicative of a reduced ion penetration into the polymeric film. As a consequence, this leads to a lower dedoping of the PEDOT:PSS film, being the CVD-APTES samples more difficult to reduce at the same potential, compared to the S-APTES one.
Furthermore, quartz crystal microbalance with dissipation monitoring (QCM-D) measurements were performed to investigate the effect of the silane on the swelling properties of PEDOT:PSS films in NaCl 0.1 M.[419] Gold was used as control, setting its thickness to zero. Figure 6.13 shows the results: APTES functionalization leads to a 5-fold drop of the film swelling capability (Table 6.2), compared to pristine PEDOT:PSS films, for both the employed deposition techniques. Since the same quantitative reduction in the swelling properties is present for CVD and S-APTES samples, the difference between them might be ascribed to the interaction between the PEDOT:PSS and the silane for the two processes.

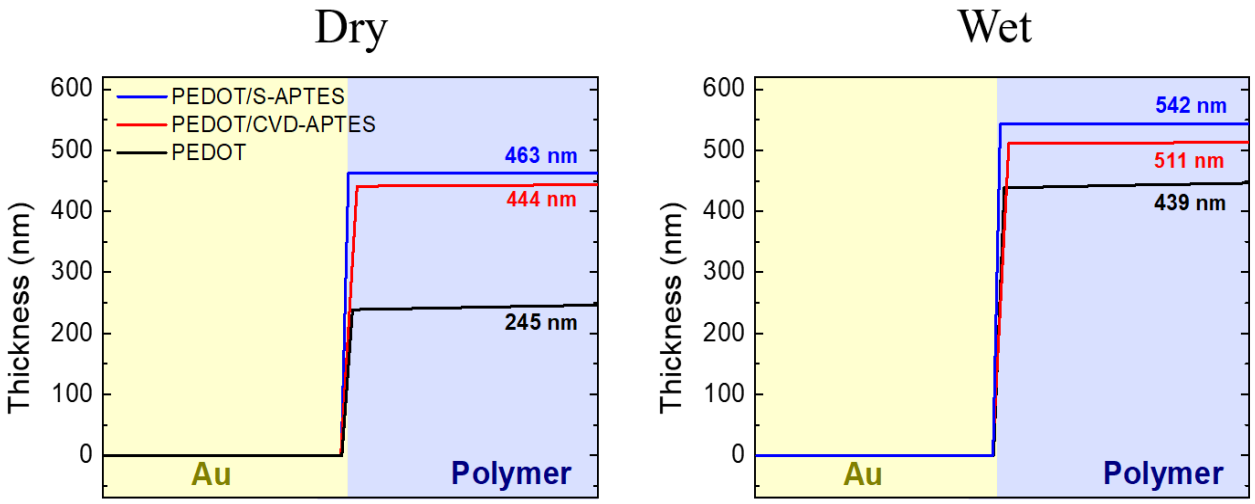

Figure 6.13: Swelling properties in 0.1 M $NaCl_{(ac)}$ solution for pristine PEDOT:PSS thin films (black), CVD- (red) and S-APTES (blue) functionalized films, obtained measuring the samples thickness *via* QCM-D.

In the end, the gate electrode of an all-PEDOT:PSS OECT was functionalized, testing its output characteristic curves before and after the APTES deposition to assess the influence of the two techniques over ion penetration and device performances, since this would be the final configuration for the monitoring. Output curves of an OECT with pristine PEDOT:PSS-coated Au gate electrode are reported in Figure 6.14a and 6.14b, used as control. Figure 6.14c shows that APTES layer deposited using the soaking technique still allows an efficient dedoping of the channel, turning off the device for the positive applied potential of 0.6 V on the gate. On the contrary, CVD-APTES sample displays no current modulation applying V_{gs} = 0.6 V (dedoping absence), with a linearly V_{ds}-dependent current (similarly to a standard resistance trend), as visible in Figure 6.14d. Indeed, this is further demonstrated by the comparison of the transistor output curves acquired for different V_{gs}, reported in Figure 6.14e and 6.14f, for S- and CVD-APTES functionalized PEDOT:PSS gates, respectively. S-APTES sample shows the standard OECT current modulation upon the increasing of the applied gate potential (from 0 to 0,6 V), while almost no modulation (but straight lines) are observed for the CVD-treated devices.

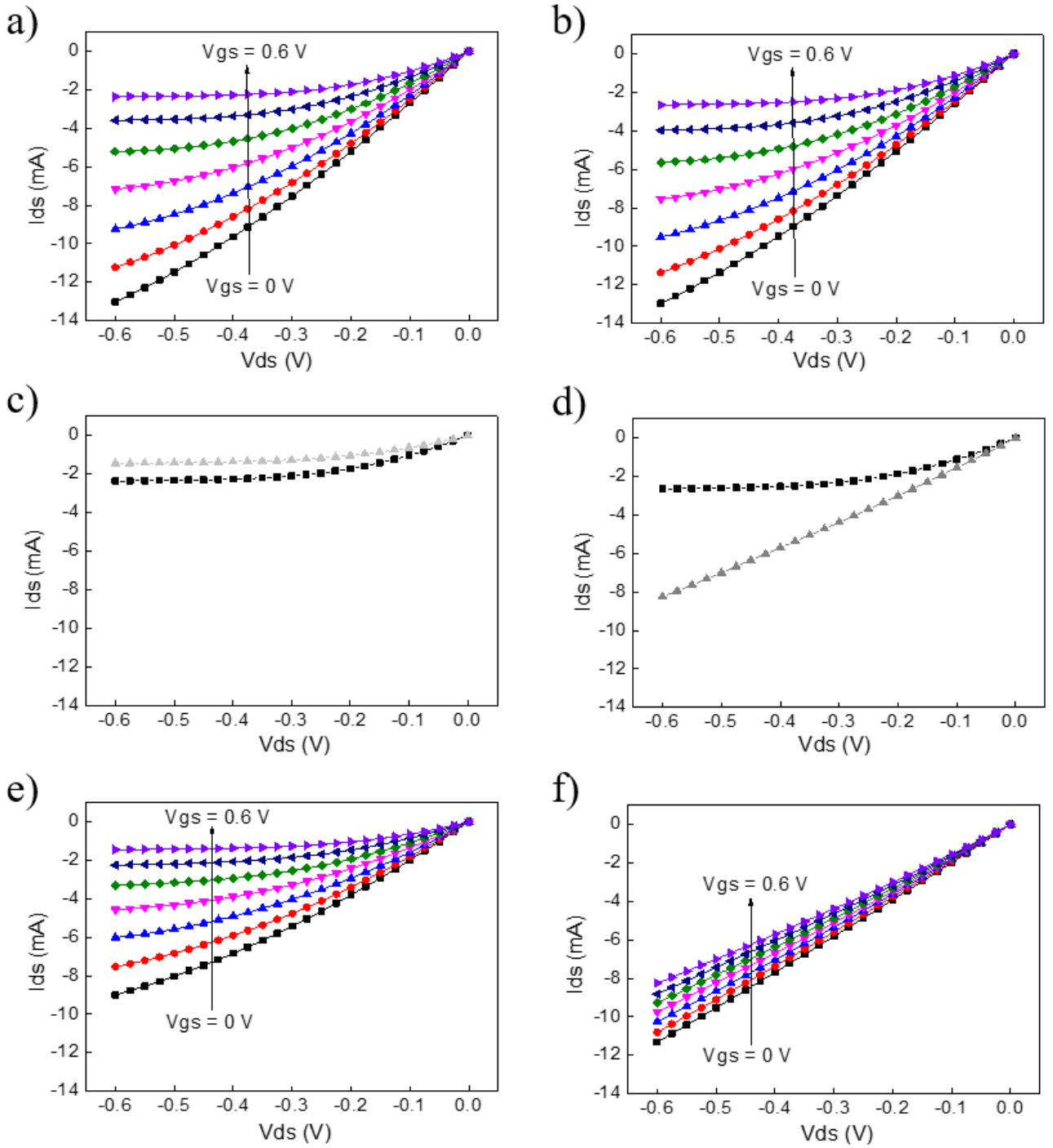

Figure 6.14: OECT output characteristic curves before and after the gate electrode functionalization with APTES. a,b) Output curves of two different devices with bare PEDOT:PSS gate, for V_{gs} values from 0 V (black squares) to 0.6 V (purple triangle). Comparison of output characteristics under an applied gate potential of 0.6 V for devices before (black squares) and after (light grey triangles) S- (c) and CVD- (d) APTES deposition over the PEDOT:PSS gate electrode. Output curves of OECTs with S- (e) and CVD- (f) APTES functionalized gate, for V_{gs} values from 0 V (black squares) to 0.6 V (purple triangle).

6.2.1.2 Biotin and streptavidin

After the corroboration of APTES presence and the analysis regarding its surface or bulk induced changes, biotin and streptavidin were the following layers deposited on the sample. QCM-D was then adopted to investigate these deposition yields, using Au, pristine PEDOT:PSS, CVD- and S-APTES functionalized samples as substrates. Distilled water and PBS were used to run baseline measurements before the biotin and streptavidin incubation, respectively. Figure 6.15a highlights that the non-specific adsorption of biotin onto Au or PEDOT:PSS is negligible: indeed, the excess of

biotin is easily removed even after the weak rinsing steps performed inside the QCM-D flowcell (Table 6.2). On the contrary, high levels of biotin adsorption are observed for the APTES functionalized samples, with the S-APTES (152 ng/cm^2) substrates having an order of magnitude higher yield compared to the CVD-APTES ones (23 ng/cm^2). Similar results are found for streptavidin deposition, even though in this case higher adsorption levels regardless of the functionalization approach are shown. It was hypothesized that the physisorption was responsible of the overall higher protein yields, allowed by the weak rinsing steps performed inside the QCM-D, that were not stringent enough to guarantee the aspecific bound removal. The confocal images, acquired at the edges of samples incubated with fluorescently labelled streptavidin deposited on top of biotin-coated or uncoated samples in a confined circular PDMS well (Figure 6.15b and 6.15c, respectively), confirm this idea. As can be clearly visible, fluorescent areas due to the dye-conjugated streptavidin are present only when biotin layer is deposited underneath, while the dark areas corresponds to sample areas where only the APTES is present, confirming that the standard washing steps have removed the physiosorbed streptavidin molecules. Thus, these images proved the need of biotin layer to chemically and stably bind the streptavidin molecules. Nonetheless, streptavidin levels for S-APTES/biotin samples reached already the highest value of 292 ng/cm^2 (compared to the 212 ng/cm^2 for CVD-APTES/biotin ones). For this reason and the possibility to better dedope S-APTES samples (shown in the previous paragraph), soaking technique was chosen for the functionalization strategy for the further characterization.

Table 6.2: Swelling percentage and amount of biotin and streptavidin adsorbed on Au, pristine PEDOT:PSS and CVD- and S-APTES functionalized substrates.

Substrate	Swelling	Bound Biotin	Bound Streptavidin
	(%)	(ng/cm^2)	(ng/cm^2)
Au	0	2	78
Au/PEDOT:PSS	80	2	190
Au/PEDOT:PSS/CVD	15	23	212
Au/PEDOT:PSS/S	17	152	292

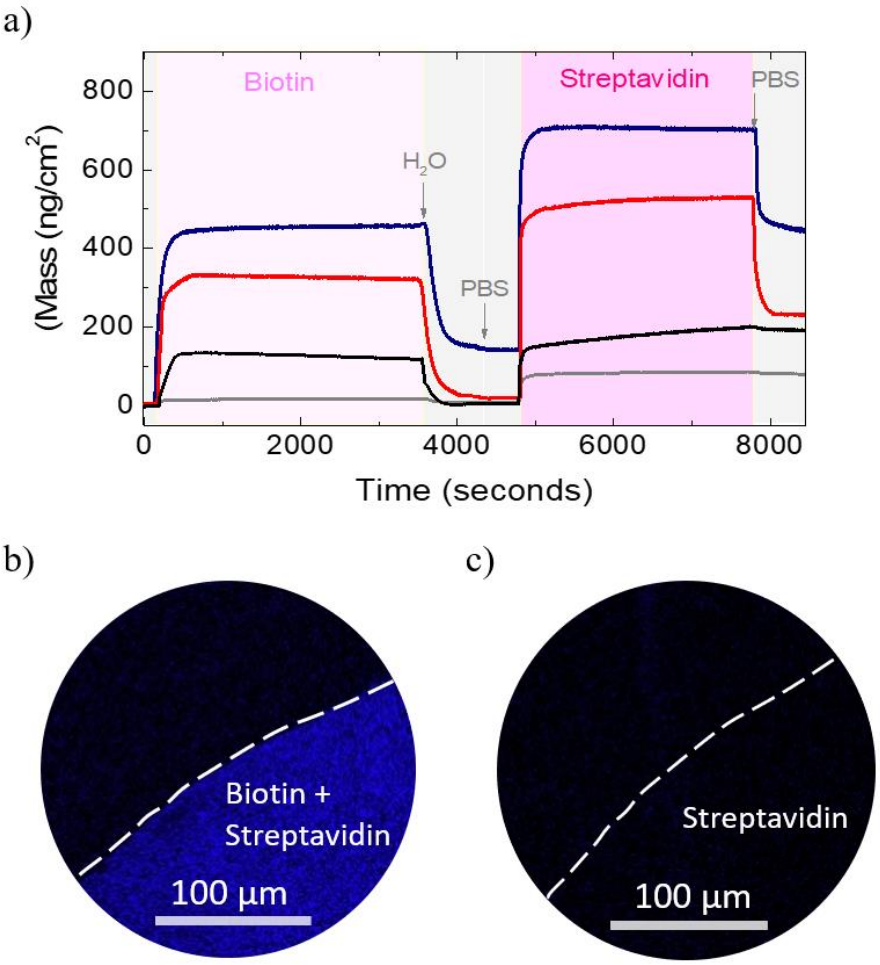

Figure 6.15: a) Quartz crystal microbalance with dissipation monitoring (QCM-D) analysis, reporting biotin and streptavidin mass adsorption on Au (grey), pristine PEDOT:PSS (black) and CVD- (red) and S- (blue) APTES functionalized films. Confocal Microscopy of PEDOT:PSS samples functionalized with (a) and without (b) biotin and then with a fluorescently labelled streptavidin (AlexaFluor 488). White dashed lines highlight the edge of the functionalized PDMS well.

6.2.1.3 Antibodies

Once the functionalization unit (APTES + biotin + streptavidin) was deposited and evaluated, biotinylated capture antibodies, directed towards the target analyte of interest (BMP-2), were introduced as a layer to impart specificity to the OECT devices. Confocal microscopy was then employed to assess the occurred binding of the antibody (Figure 6.16). Images were acquired at the edge of samples coated with fluorescently labelled antibody (FITC anti-BMP-2 antibodies) inside a confined PDMS well, in presence (Figure 6.16a) or absence (Figure 6.16b) of streptavidin molecules. As can be clearly understood from the reported images, the streptavidin is needed for the chemical binding of the detection antibody (bright green areas), and its absence leads to results similar to the antibody-unfunctionalized zones (dark areas).

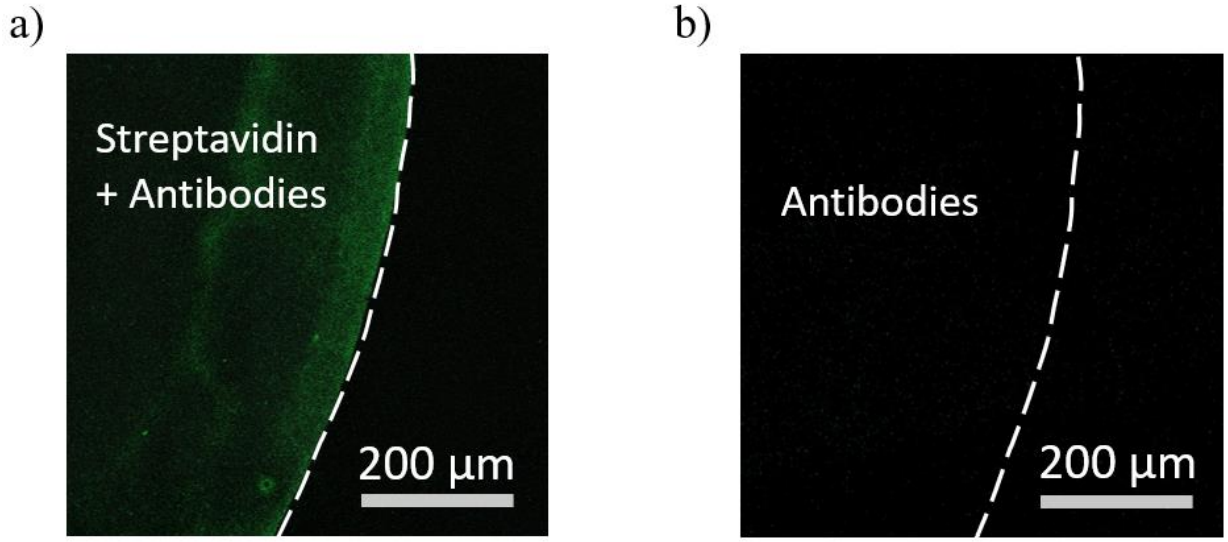

Figure 6.16: Confocal Microscopy images of PEDOT:PSS films functionalized using the developed strategy up to the antibody step using FITC-conjugated anti-BMP-2 antibodies, deposited on samples with (a) and without (b) streptavidin functionalization. White dashed lines show the edge of the PDMS well used for the functionalization.

6.2.1.4 Bone Morphogenic Protein 2 (BMP-2)

Finally, a BMP-2 solution was incubated with the functionalized PEDOT:PSS substrates to prove the efficiency of the strategy. BMP-2 was chosen since it is a key mediator for the stem cell differentiation process: indeed, it is crucial at the earlier stage of differentiation, as it is involved in increasing mineralization and in stimulating osteocalcin mRNA production.[6,420] This renders this cytokine suitable as a first marker to test the realized system.

Electrochemical impedance spectroscopy (EIS) was then used to check its presence and, in general, to assess the variations of the electrochemical properties upon the addition of each functionalization layer. The impedance and the phase spectra over frequency are reported in Figure 6.17a and 6.17b, respectively, after the addition of each layer. The overall impedance of the system increases with each functionalization, indicating the ion barrier formation at the electrolyte/surface (liquid/solid) interface, which is also confirmed by the shift of the phase away from the 90° and towards 0°.

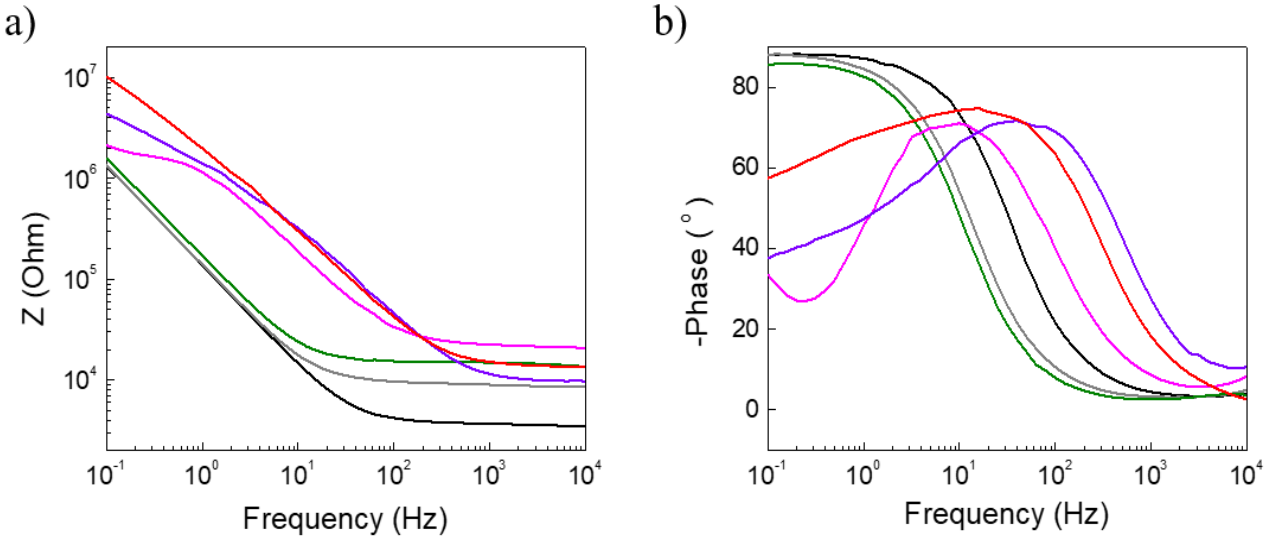

Figure 6.17: Electrochemical Impedance Spectroscopy (EIS), showing impedance (a) and phase (b) over frequency for pristine PEDOT:PSS (black), APTES (grey) biotin (green), streptavidin (magenta), biotinylated antibody (violet) and BMP-2 (red) functionalization layers. Measurements were performed on a functionalized gold electrode of (500 x 500) µm^2 with Pt and Ag/AgCl as counter and reference electrodes, respectively, using 1X PBS as electrolyte solution.

Nyquist plots (Figure 6.18a and 6.18b) and capacitance over frequency (Figure 6.18c and 6.18d) are shown, dividing the first four layers and the last four ones, in order to better appreciate the changes due to layer addition. Capacitance plots were constructed throughout the complex impedance equation:

$$Z = \sqrt{R^2 + \frac{1}{\omega^2 C^2}} \tag{6.6}$$

where R is the electrolyte resistance, ω the frequency and C the capacitance at the solid/liquid interface.

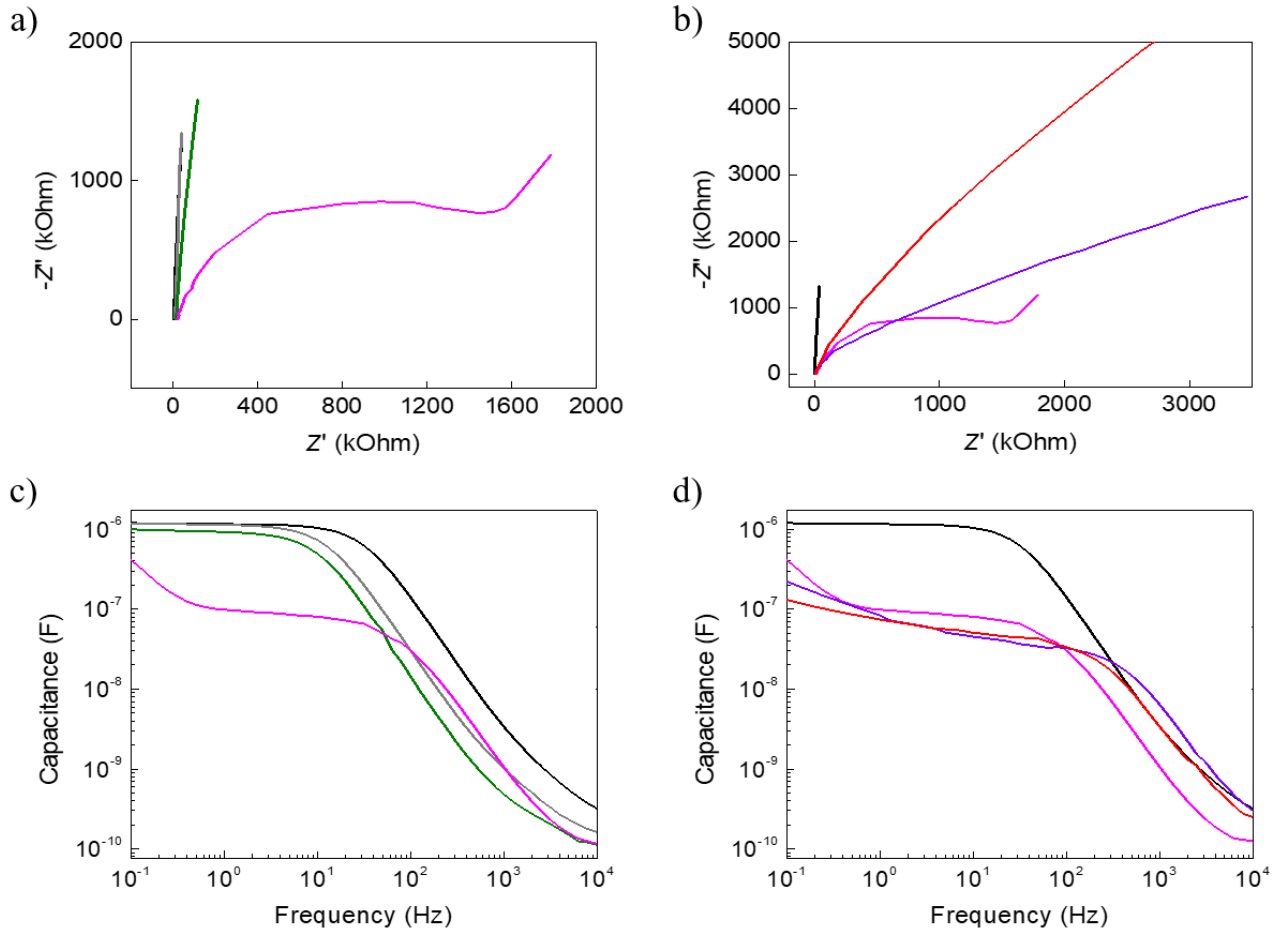

Figure 6.18: EIS measurements showing the Nyquist plots (a,b) and the capacitance over frequency (c,d) for pristine PEDOT:PSS (black), APTES (grey) biotin (green), streptavidin (magenta), biotinylated antibody (violet) and BMP-2 (red) functionalization layers. Measurements were performed on a functionalized gold electrode of (500 x 500) μm^2 with Pt and Ag/AgCl as counter and reference electrodes, respectively, using 1X PBS as electrolyte solution.

Importantly, Nyquist plot in Figure 6.18a clearly shows the shape differences after the incubation with the streptavidin proteins, and Figure 6.18b underlines the changes upon the antibody binding and, in particular, BMP-2 addition. On the other hand, the Nyquist plot recorded for the pristine PEDOT:PSS and, in general, for the other layers before streptavidin addition, depicts an overall impedance with linear-like trend, which stands for facile ion migration.[421,422] After the protein deposition, the Nyquist plot undergoes a clear change, displaying a shape with two distinguished regimes: a semi-circle behaviour at high frequencies and a linear behaviour with slope close to 45° at low frequencies, denoting delayed diffusion impedance. Noteworthy, as noted in the impedance and phase graphs, both for the addition of antibodies and BMP-2 the Nyquist plots report an increase in the impedance, showing only a large semi-circle trend and the absence of a linear regime. This change in the plot indicates that these bulky molecules impede the ion migration from the electrolyte into the

polymeric films, once bound to the electrode surface. The same observations can be done focusing on Figure 6.18c and 6.18d, reporting the capacitance spectra over frequency for the different functionalized layers. The capacitance slightly reduces with the addition of new layers on the semiconducting film till the streptavidin molecules are bound (Figure 6.18c), when a huge change and a high drop of the curve are reported. Then, as visible from Figure 6.18d, capacitance starts lowering down sequentially upon the antibody and BMP-2 additions, especially in the range between 100 and 0.1 Hz, where ionic charging takes place.[423] The effect can be ascribed to the impaired ion penetration into the PEDOT:PSS film caused by the addition of layers acting as ion injection barrier.

6.2.2 Proof of concept for BMP-2 detection

As previously reported, the gate electrode of a PEDOT:PSS-based OECT was then functionalized with the developed strategy, checking the device performances: Figure 6.19 shows the OECT output response having the gate in pristine PEDOT:PSS (Figure 6.19a), functionalized up to the antibody (Figure 6.19b) or BMP-2 layer (Figure 6.19c). Even though a reduction in the current modulated by the gate voltage is present (the transistor output curves look shrunk after the functionalization unit deposition on the gate, and also after the BMP-2 incubation, compared to the pristine PEDOT:PSS electrode), it can be noted that an efficient dedoping of the channel is still performed by V_{gs}, thus maintaining transistor features.

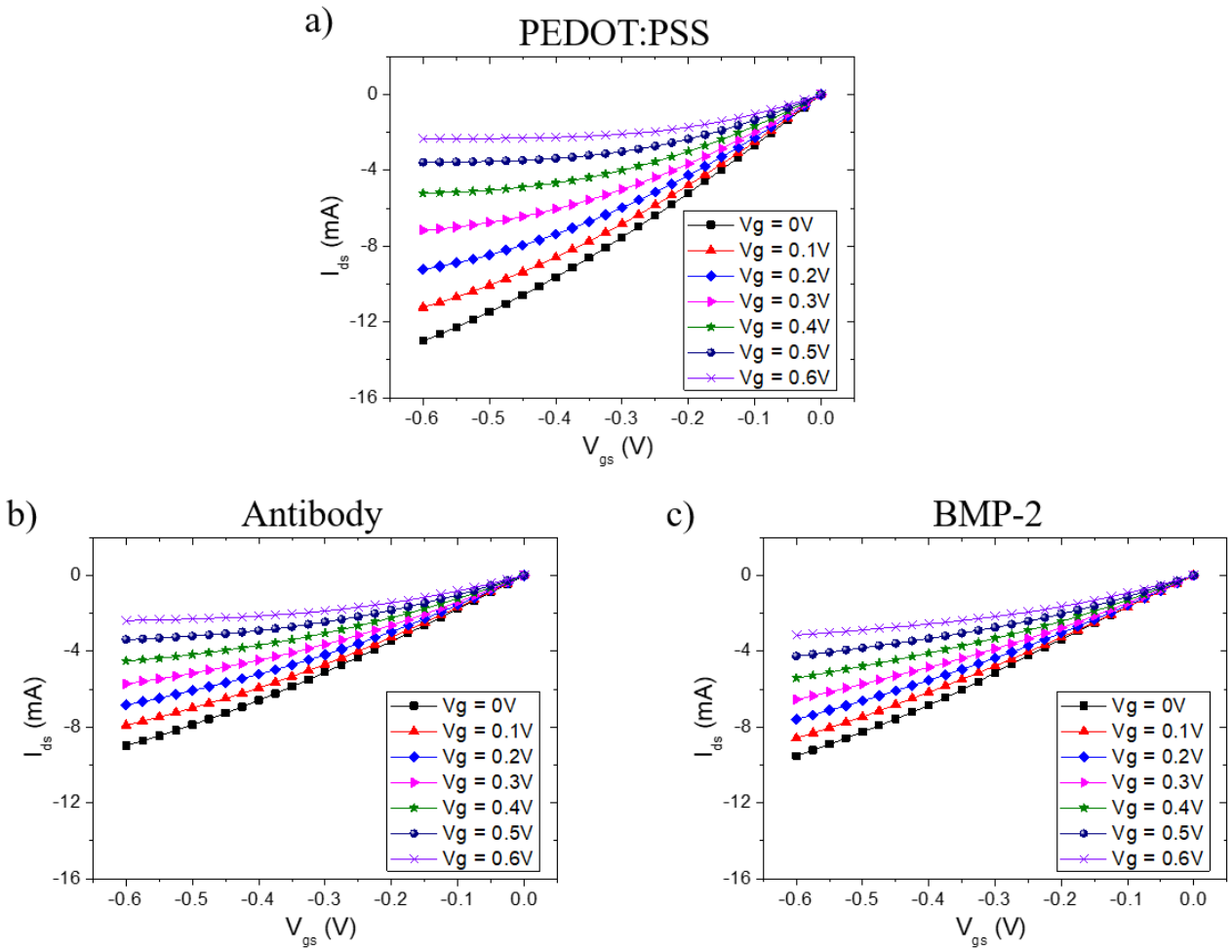

Figure 6.19: Output characteristic curves for OECT with the gate made in pristine PEDOT:PSS (a) and functionalized up to antibodies (b) and to BMP-2 (c), using different voltages on the gate.

In the end, this system was exploited to have a preliminary detection of the BMP-2 in a 0.01X PBS diluted solution, as a proof of concept experiment to prove the value of the functionalization strategy. OECT performances were monitored after each and every functionalization step, running alternating current (AC) measurements and studying the device transconductance over frequency ($g_m(f)$). As already reported, transconductance is the figure of merit of the OECT, reflecting the gain of the transistor ($g_m = \frac{\partial I_{ds}}{\partial V_{gs}}$). The device and measurement configurations, together with the functionalized gate, are reported in the schematic in Figure 6.20a. The semiconducting channel was biased at -0.6 V and a 0 V offset and10 mV amplitude sinusoidal wave was generated at the gate terminal, scanning the frequency range between 1 Hz and 20 kHz. A drop in the transconductance is observed upon the addition of each functionalization layer (Figure 6.20b), again as a result of an impaired gating due to the introductions of ion injection barriers. Normalized data for pristine PEDOT:PSS and for the last three deposited layers are summarized in the graph in Figure 6.20c and the g_m cut-off values (70% of the curve drop) are adopted as key parameter of the device to quantify the influence of each layer on the OECT response (reported in table 6.3). The ion penetration limitation due to additional layers reduces the values of this parameter. Starting from the bare PEDOT:PSS, the highest drop is obtained upon the addition of the streptavidin protein, then the incubation with antibodies and BMP-2 leads to g_m cut-off shifts towards lower frequencies. In detail, BMP-2 binding almost halves the device transconductance value, as it passes from 59 ± 6 Hz to 36 ± 2 Hz, highlighting the possibility to use g_m cut-off as key parameter to monitor BMP-2 presence in solution. This trend is well aligned with the outcomes obtained previously with impedance and capacitance value. As a matter of fact, the highest shifts were reported for the binding of the streptavidin protein and after BMP-2 incubation.
Importantly, depending on the selected capture element (aptamers, antibodies) added as final layer, the strategy can be employed for the detection of a wide range of biological analytes or cytokines (i.e. osteocalcin, osteopontin, osteonectin, collagene type I).
In conclusion, these results suggest that the proposed functionalization strategy imparts specificity towards BMP-2 on a PEDOT:PSS OECT, thus paving the way for its use as a monitor of stem cell undergoing osteogenic differentiation. Moreover, it can be foreseen that the real detection will be performed directly in the culture chamber and an accurate sample preparation and sensor calibration will proceed the actual measurement.

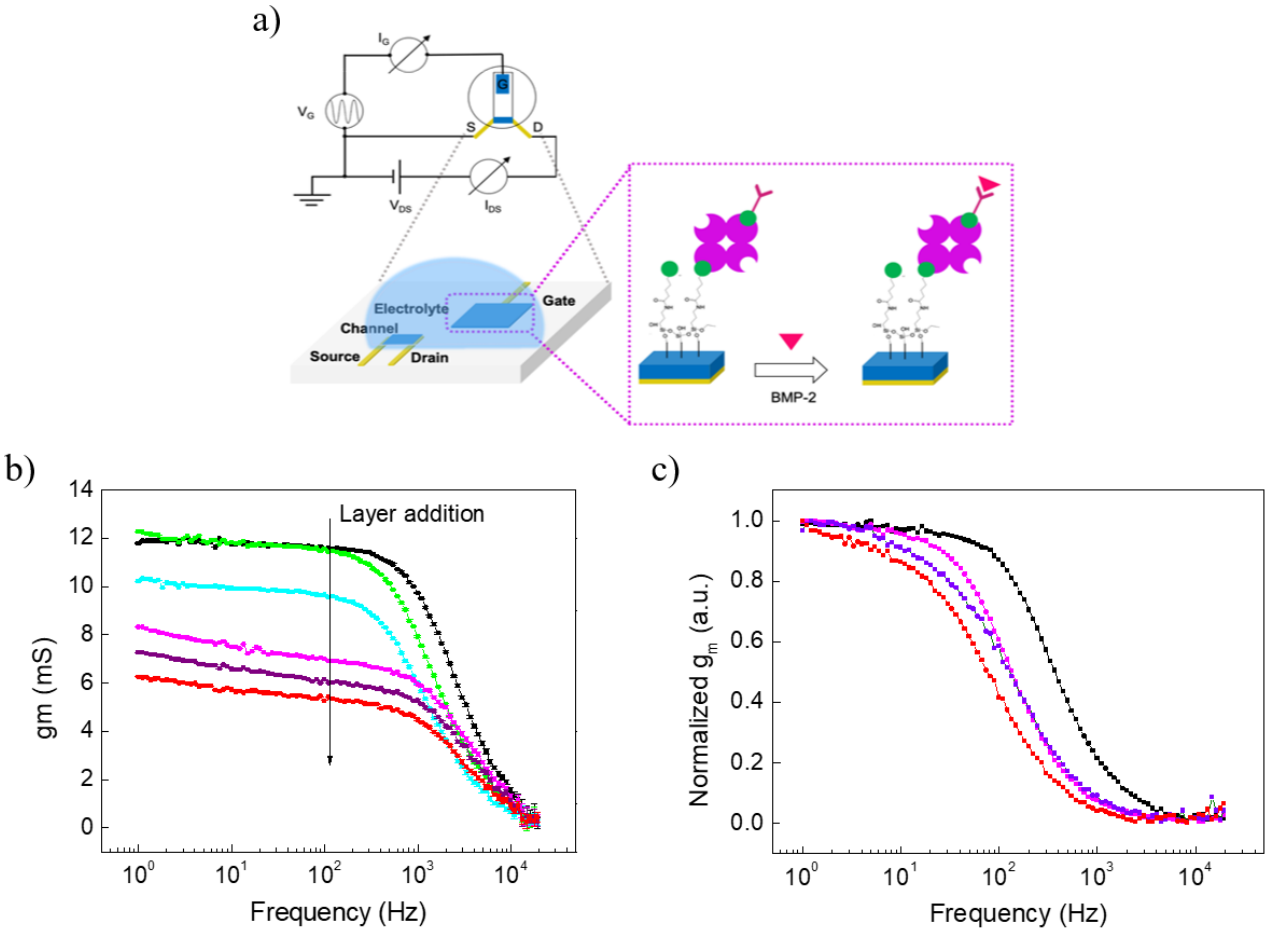

Figure 6.20: a) Schematic of the AC transconductance measurement and OECT circuit with the gate functionalized with antibodies towards BMP-2. b) Transconductance over frequency data for the subsequent layers deposited on top of PEDOT:PSS thin films (black squares). c) Normalized g_m over frequency for PEDOT:PSS (black), streptavidin (magenta), antibodies (violet) and BMP-2 (red).

Table 6.3: Transconductance cut-off values for OECT having the gate in pristine PEDOT:PSS or after its functionalization with streptavidin, anti-BMP-2 antibodies and BMP-2.

Layer	***g_m cut-off (Hz)***
PEDOT:PSS	200.8 ± 0.2
PEDOT:PSS/APTES/biotin/streptavidin	73.9 ± 0.1
PEDOT:PSS/APTES/biotin/streptavidin/Antibody	54.8 ± 0.2
PEDOT:PSS/APTES/biotin/streptavidin/Antibody/BMP-2	35.0 ± 2.0

Major results

A chemical functionalization strategy was developed in order to impart specificity to the gate of an all-PEDOT:PSS OECT using a monoclonal antibody towards the selected analyte/cytokine, with these final achievements:

1. (3-Aminopropyl)triethoxysilane (APTES), biotin, streptavidin and the capture antibody towards the selected analyte were the layers deposited on top of PEDOT:PSS thin films, in order to realize the biofunctionalization unit
2. Several experimental techniques were used to optimize the depositions and to guarantee the strong binding of each layer, allowing for the selection of the soaking process (over chemical vapour deposition) for the APTES, since less invasive on the electrical and electrochemical properties of the functionalized electrode
3. A preliminary detection of a fundamental cytokine (namely, Bone Morphogenic Protein 2, or BMP-2) was performed, suggesting that the proposed functionalization strategy paves the way for real-time stem cell undergoing osteogenic differentiation monitoring

This work is reported in Ref [424].

Conclusions

In this thesis, the semiconducting polymer poly(3,4-ethilenedioxithiophene) doped with poly(styrenesulfonate) (PEDOT:PSS) has been employed as smart interface and transducer between biological elements and electronic devices. In detail, PEDOT:PSS-based devices were fabricated and characterized: i) organic electrochemical transistors (OECTs) have been employed as tissue integrity and cell health real-time monitoring devices; ii) stretchable and low-impedance electrodes were fabricated and electrochemically characterized to record *in* vivo chronic peripheral nerve activity; iii) OECTs were demonstrated to be able to detect oxygen dissolved in solution and a biofunctionalization of the OECT gate has been introduced to realize a versatile sensing device towards cytokines released from stem cells undergoing differentiation.

Owing to the low-voltage of operation, the possibility to work in biological liquid environment, the good conductivity and their biocompatibility, together with their stability in liquid, OECTs are suitable devices for cell interfacing. In this thesis, in particular, OECTs have been fabricated and optimized in terms of the response to a pulse on the gate in order to be used as cell culture substrates able to monitor the tissue layer health. Firstly, a biocompatible sample holder, namely the Tissue Engineering Cell Holder - Organic Electrochemical Transistor (TECH-OECT), was designed mimicking cell culture petri dishes, with the addition of electrical connections for the sequential monitoring of the encapsulated devices. The aim of the TECH-OECT is to allow real-time monitoring of several devices (even with different cell seedings, OECT configurations or introduced stresses) inside the incubator, thus keeping the standard cell growth conditions (37°C and 5% of CO_2 atmosphere).

Then, the biocompatibility and cell correct growth on the OECT substrates in the TECH-OECT sample holder was proved using optical images and vitality test, that showed the healthy status of both human colorectal epithelial (Caco-2) and mouse embryonic fibroblast (NIH-3T3) cell lines grown on the devices, even with running electrical measurements.

In detail, cells grown onto the active area of OECTs introduce a resistance in series in the ionic circuit, enhancing the response time of the current modulation of the device to a voltage pulse on the gate. OECTs in vertical and planar configuration, having a designed channel area of 3 mm^2, were employed for real-time tissue integrity evaluations. The vertical configuration proved to be able to monitor only the Caco-2 layers, due to the high resistance of this cell layers to the passage of ions from the electrolyte to the semiconducting polymer and vice versa (barrier-like cells), compared to the one of NIH-3T3 (non-barrier cells). On the other hand, the planar configuration (where cells are grown both on the gate and the channels of the devices), was able to monitor the tissue layer formation and detachment of both cell lines, doubling the relative response time variations for the Caco-2 cells. This proves the hypothesis that the double ion crossing of the cell layer doubles the device sensitivity.[167]

Furthermore, a preliminary correlation between the response time of the device and the active surface covering of the cell layer was highlighted, with different detachments leading to different relative variation of the final response time. This paves the way for the calibration of tissue integrity sensors for different types of cell lines, patterning the dimensions of the active areas accordingly to the resistance (thus the nature) of the cell under study.

OECTs and the TECH-OECT system permit real-time and high temporal resolution (0.5 Hz) measurements of cell layer formation and disruption, enhancing the information currently provided by end-point assays or optical investigations. Noteworthy, a calibrated device geometry/patterning would allow for the monitoring of cells with lower TransEpithelial Electrical Resistances (TEERs) than the ones studied with the currently commercially available devices (such as epithelial voltohmmeter (EVOM)[425] or CellZscope of nanoAnalytics GmbH[426]).

Using planar geometry OECTs, Caco-2 and NIH-3T3 cell lines have been investigated under the exposure of silver nanoparticles (AgNPs) to assess their toxicity. For this purpose, citrate-coated AgNPs were used for their cytotoxic activity, while the replacement of citrate molecules with (11-mercaptoundecyl)hexa(ethylene glycol) (EG_6OH) on the NP surface, ensure a non-toxic activity. The real-time electrical data helped to obtain further insight on the NPs uptake and the incubation time needed to start cytotoxicity. In detail, citrate-coated AgNPs proved to be cytotoxic to both cell lines, Caco-2 and NIH-3T3: OECT response time (i.e. cell growth) started to be influenced after 20 hours from the exposure, since nanoparticles must be first taken up by the cells before causing toxicity; then, when a large enough number of silver nanoparticles had been taken up (after 40 hours from the exposure), cell death began to be relevant. On the contrary, replacing (passivating) citrate molecules with (11-mercaptoundecyl)hexa(ethylene glycol) (EG_6OH) on the NP surface, ensured a non-toxic activity on the cells.

AgNPs (and, nanomaterials in general) are often employed in consumer products (including bandages,[427] food packaging[428] and cosmetics[429]), even though their effect on human health is far from being completely understood. OECTs were demonstrated to be a real-time, *in vitro* platform for nanoparticles toxicity evaluation, strongly complementary to end-point and costly viability assay.

The same polymer, PEDOT:PSS, was then employed as biocompatible, soft and low-impedance interface for gold electrodes employed for nerve activity recording. The Polydimethylsiloxane (PDMS)-based device was fabricated and optimized according to the needs for the surgical procedures. Then, a deep study on the semiconducting material lead to the introduction of the plasticizer polyethylene glycol (PEG) in the polymeric composite, with the aim to enhance the elasticity of the final film, while keeping good conductivity and low-impedance.

The final proof of the successful improvement upon the plasticizer introduction was the characterization of the electrode impedance at 1 kHz in function of strain, highlighting that, without the PEG, the loss of the conductivity (electrical failure) is reached at strain of 20%, while for PEDOT:PSS:PEG-coated electrodes a combination of both low-impedance and elastic stretchability is reached. In detail, an impedance comparable to pure and unstrained PEDOT:PSS is maintained up to a strain of 40%. AFM images of strained and unstrained samples demonstrated that this behaviour is due to the ability of the PEDOT:PSS:PEG composite to form microcracks under tensile stretch that do not completely cut the percolating conductive network on the polymeric surface, resembling Au microcrack formation. On the other hand, PEDOT:PSS films showed much wider openings causing the complete loss of conductivity.

Optimized electrodes were implanted *in-vivo* on the renal nerve (in a Sprague-Dawley rat), showing that the low-impedance and elastic properties of the microelectrode enabled a stable recording of the sympathetic nerve activity for several weeks under acute and chronic conditions.

This work on a stretchable, low-impedance PEDOT:PSS:PEG-coated microelectrode aims at the realization of minimally-invasive and reliable interfaces for long-term and high quality recordings as well as stimulations. Indeed, so far, the best devices successfully employed for chronic stretchable implants were electrodeposited Pt black and Pt-nanoparticle silicone composites,[398,430] which, however, displayed high microscopic elastic modulus and low charge injection limits.[431] Instead, the proposed electrode benefits of two main advantages: the conducting polymer coating to reduce the impedance and improve charge injection, due to PEDOT:PSS ability to drive ionic currents as well as electronic ones; the enhanced softness and device conformability towards the nerve strand, thanks to the hydrogel-like properties of the polymer (increased by PEG addition), owing to the high ionic content which leads to water uptaking and subsequent swelling.[432]

OECTs were also used as molecule-sensing devices, for oxygen dissolved in solution and for analytes/cytokines released from stem cells undergoing osteogenic differentiation.

Oxygen sensing was tested and characterized in KCl 0.1M using standard output and transcharacteristic measurements in the range of low oxygen concentration (0-5% of oxygen partial pressure above the solution). Devices were optimized in terms of sensitivity and limit of detection (L.O.D.), working on the geometry of the OECT and having for the resulting planar configuration a low L.O.D. of 1 μM (which means 0.03 mg/L, thus 0.08% of oxygen partial pressure above the solution). The developed sensors thus proved to be able to study cell culture under hypoxia conditions and for further analysis on the tumour properties, such as aggressiveness, for different tissue oxygen partial pressures. Even though further optimization of the device geometry and features are mandatory for a commercial application, the proposed oxygen sensor has the potential to be easily miniaturized (without the stability problem occurring for Ag/AgCl electrode miniaturization), keeping currents in the range of mA and high signal-to-noise ratio, owing to the transistor amplification properties, emerging as a powerful alternative to the "gold standard" Clark electrode employed so far.

Finally, using PEDOT:PSS-based OECTs, a biofunctionalization strategy of the gate of a devices was developed in order to impart specificity to the device sensing, using a selected monoclonal antibody targeting the analyte of choice. In detail, the layer-by-layer deposition relies on 5 main steps: i) low intensity air plasma treatment of PEDOT:PSS surfaces to introduce hydroxyl groups on the semiconducting polymer; ii) (3-Aminopropyl)triethoxysilane (APTES) molecules were bound to the activated surfaces; iii) biotin units and then (iv) streptavidin proteins were linked with high affinity; v) a biotinylated capture antibody towards the selected analyte/cytokine was deposited. A proof of concept experiment was performed to prove the capability of the OECT to detect Bone Morphogenic Protein 2 (BMP-2), which is an interesting cytokine fundamental at the earlier stage of differentiation, through the screening of the transconductance over frequency (bandwidth) of the device. The results obtained allow to foresee a valuable functionalization strategy toward the realization of devices giving further insights on cells undergoing osteogenic differentiation. Noteworthy, changing the capture antibody, several interesting analytes/cytokines can be detected, with the final aim of real-time monitoring in the culture chamber of the osteogenic differentiation. Indeed, current methods used to study stem cell differentiation mainly involve end-point enzymatic and ELISA assays or gene expression profiling, that may overlook helpful and interesting informations. The driving force of this work, as well as of the previously reported OECTs for tissue integrity monitoring and oxygen dissolved in solution detection, was the bioelectronic trend to integrate real-time sensing units in culture chambers to continuously monitor the biological systems and environment.[35,433,434]

In conclusion, PEDOT:PSS demonstrated to be a biocompatible and smart material, suitable for bioelectronic applications, namely OECTs and electrodes. In the formers, PEDOT:PSS stability in water environment and ion-to-electron conversion ability were fundamental to monitor cell tissue layer formation and disruption for one week and detect oxygen dissolved in solution or cytokines released from stem cells undergoing osteogenic differentiation (for this purpose also the easiness of the polymer functionalization was of primary importance). Regarding the electrode, the material stretchability and low-impedance features allowed for the realization of a simple and compact device that succeeded in recording the neural spiking activity of peripheral nerves of rats in chronic, *in vivo* conditions. Owing to its properties and according to the work reported in this thesis, PEDOT:PSS was demonstrated to be a suitable and promising material for *in vitro*, as well as *in vivo*, biomedical applications, aiming at the improvement of human healthcare studies.

Bibliography

1. Simon, D. T., Gabrielsson, E. O., Tybrandt, K. & Berggren, M. Organic Bioelectronics: Bridging the Signaling Gap between Biology and Technology. *Chem. Rev.* **116**, 13009–13041 (2016).
2. *Smart Polymers and their Applications*. (Elsevier, 2019). doi:10.1016/C2017-0-00049-6
3. Inal, S. *et al.* Conjugated Polymers in Bioelectronics. (2018). doi:10.1021/acs.accounts.7b00624
4. Balint, R., Cassidy, N. J. & Cartmell, S. H. Conductive polymers: Towards a smart biomaterial for tissue engineering. *Acta Biomater.* **10**, 2341–2353 (2014).
5. Malliaras, G. & Abidian, M. R. Organic Bioelectronic Materials and Devices. *Advanced Materials* 7492 (2015). doi:10.1002/adma.201504783
6. Duplomb, L., Dagouassat, M., Jourdon, P. & Heymann, D. Concise Review: Embryonic Stem Cells: A New Tool to Study Osteoblast and Osteoclast Differentiation. *Stem Cells* **25**, 544–552 (2006).
7. Berggren, M. & Richter-Dahlfors, A. Organic Bioelectronics. *Adv. Mater.* **19**, 3201–3213 (2007).
8. Nagel, B., Dellweg, H. & Gierasch, L. M. Glossary for chemists of terms used in biotechnology (IUPAC Recommendations 1992). *Pure Appl. Chem.* **64**, 143–168 (1992).
9. Göpel, W. Bioelectronics and nanotechnologies. *Biosens. Bioelectron.* **13**, 723–728 (1998).
10. Carrara, S. *What is bioelectronics?* (2015).
11. Rivnay, J., Owens, R. M. & Malliaras, G. G. The Rise of Organic Bioelectronics. (2013). doi:10.1021/cm4022003
12. Malliaras, G. G. Organic bioelectronics: A new era for organic electronics. *Biochim. Biophys. Acta - Gen. Subj.* **1830**, 4286–4287 (2013).
13. Wallace, G. G., Moulton, S. E. & Clark, G. M. APPLIED PHYSICS: Electrode-Cellular Interface. *Science (80-.).* **324**, 185–186 (2009).
14. Malliaras, G. & Friend, R. An Organic Electronics Primer. *Phys. Today* **58**, 53–58 (2005).
15. Stojek, Z. The Electrical Double Layer and Its Structure. in *Electroanalytical Methods* 3–9 (Springer Berlin Heidelberg, 2010). doi:10.1007/978-3-642-02915-8_1
16. Ingebrandt, S. Sensing beyond the limit. *Nat. Nanotechnol.* **10**, 734–735 (2015).
17. Yang, J. & Martin, D. C. Impedance spectroscopy and nanoindentation of conducting poly(3,4-ethylenedioxythiophene) coatings on microfabricated neural prosthetic devices. *J. Mater. Res.* **21**, 1124–1132 (2006).
18. Zeglio, E., Rutz, A. L., Winkler, T. E., Malliaras, G. G. & Herland, A. Conjugated Polymers for Assessing and Controlling Biological Functions. *Adv. Mater.* **31**, 1806712 (2019).
19. Baleg, A. A. *et al.* Conducting Polymers and Composites. doi:10.1007/978-3-319-92067-2_17-1
20. Le, T.-H. *et al.* Electrical and Electrochemical Properties of Conducting Polymers. *Polymers (Basel).* **9**, 150 (2017).
21. Guo, B. & Ma, P. X. Conducting Polymers for Tissue Engineering. (2018). doi:10.1021/acs.biomac.8b00276
22. Ravichandran, R., Sundarrajan, S., Venugopal, J. R., Mukherjee, S. & Ramakrishna, S. Applications of conducting polymers and their issues in biomedical engineering. *J. R. Soc. Interface* **7**, (2010).
23. Guimard, N. K., Gomez, N. & Schmidt, C. E. Conducting polymers in biomedical engineering. *Prog. Polym. Sci.* **32**, 876–921 (2007).
24. Owens, R. M. & Malliaras, G. G. Organic Electronics at the Interface with Biology. *MRS Bull.* **35**, 449–456 (2010).
25. Ibanez, J. G. *et al.* Conducting Polymers in the Fields of Energy, Environmental Remediation,

and Chemical–Chiral Sensors. *Chem. Rev.* **118**, 4731–4816 (2018).
26. Das, T. K. & Prusty, S. Review on Conducting Polymers and Their Applications. *Polym. Plast. Technol. Eng.* **51**, 1487–1500 (2012).
27. Ludwig, K. A. *et al.* Poly(3,4-ethylenedioxythiophene) (PEDOT) polymer coatings facilitate smaller neural recording electrodes. *J. Neural Eng.* **8**, 014001 (2011).
28. Abidian, M. R., Ludwig, K. A., Marzullo, T. C., Martin, D. C. & Kipke, D. R. Interfacing Conducting Polymer Nanotubes with the Central Nervous System: Chronic Neural Recording using Poly(3,4-ethylenedioxythiophene) Nanotubes. *Adv. Mater.* **21**, 3764–3770 (2009).
29. Decataldo, F. *et al.* Stretchable Low Impedance Electrodes for Bioelectronic Recording from Small Peripheral Nerves. *Sci. Rep.* **9**, 10598 (2019).
30. Gualandi, I. *et al.* Selective detection of dopamine with an all PEDOT:PSS Organic Electrochemical Transistor. *Sci. Rep.* **6**, 35419 (2016).
31. Faria, G. C. *et al.* Organic electrochemical transistors as impedance biosensors. *MRS Commun.* **4**, 189–194 (2014).
32. Singh, S., Solanki, P. R., Pandey, M. K. & Malhotra, B. D. Cholesterol biosensor based on cholesterol esterase, cholesterol oxidase and peroxidase immobilized onto conducting polyaniline films. *Sensors Actuators B Chem.* **115**, 534–541 (2006).
33. Marzocchi, M. *et al.* Physical and Electrochemical Properties of PEDOT:PSS as a Tool for Controlling Cell Growth. *ACS Appl. Mater. Interfaces* **7**, 17993–18003 (2015).
34. Iandolo, D. *et al.* Electron Microscopy for 3D Scaffolds-Cell Biointerface Characterization. *Adv. Biosyst.* **3**, 1800103 (2019).
35. Pitsalidis, C. *et al.* Transistor in a tube: A route to three-dimensional bioelectronics. *Sci. Adv.* **4**, eaat4253 (2018).
36. Tandon, B., Magaz, A., Balint, R., Blaker, J. J. & Cartmell, S. H. Electroactive biomaterials: Vehicles for controlled delivery of therapeutic agents for drug delivery and tissue regeneration. *Adv. Drug Deliv. Rev.* **129**, 148–168 (2018).
37. Naveen, M. H., Gurudatt, N. G. & Shim, Y.-B. Applications of conducting polymer composites to electrochemical sensors: A review. *Appl. Mater. Today* **9**, 419–433 (2017).
38. Gualandi, I. *et al.* Selective detection of dopamine with an all PEDOT:PSS Organic Electrochemical Transistor. *Sci. Rep.* **6**, 35419 (2016).
39. Gualandi, I. *et al.* All poly(3,4-ethylenedioxythiophene) organic electrochemical transistor to amplify amperometric signals. *Electrochim. Acta* **268**, 476–483 (2018).
40. Wang, H., Barrett, M., Duane, B., Gu, J. & Zenhausern, F. Materials and processing of polymer-based electrochromic devices. *Mater. Sci. Eng. B* **228**, 167–174 (2018).
41. Mirvakili, S. M. & Hunter, I. W. Artificial Muscles: Mechanisms, Applications, and Challenges. *Adv. Mater.* **30**, 1704407 (2018).
42. Manoli, K. *et al.* Printable Bioelectronics To Investigate Functional Biological Interfaces. *Angew. Chemie Int. Ed.* **54**, 12562–12576 (2015).
43. Qi, D. *et al.* Highly Stretchable, Compliant, Polymeric Microelectrode Arrays for In Vivo Electrophysiological Interfacing. *Adv. Mater.* **29**, 1702800 (2017).
44. Wang, Y. *et al.* A highly stretchable, transparent, and conductive polymer. *Sci. Adv.* **3**, e1602076 (2017).
45. Andersson, A.-S. *et al.* Nanoscale features influence epithelial cell morphology and cytokine production. *Biomaterials* **24**, 3427–3436 (2003).
46. Luo, S.-C. *et al.* Poly(3,4-ethylenedioxythiophene) (PEDOT) Nanobiointerfaces: Thin, Ultrasmooth, and Functionalized PEDOT Films with in Vitro and in Vivo Biocompatibility. *Langmuir* **24**, 8071–8077 (2008).
47. Wang, X. *et al.* Evaluation of biocompatibility of polypyrrolein vitro andin vivo. *J. Biomed. Mater. Res.* **68A**, 411–422 (2004).
48. Kamalesh, S. *et al.* Biocompatibility of electroactive polymers in tissues. *J. Biomed. Mater. Res.* **52**, 467–478 (2000).

49. Wong, J. Y., Langer, R. & Ingber, D. E. Electrically conducting polymers can noninvasively control the shape and growth of mammalian cells. *Proc. Natl. Acad. Sci. U. S. A.* **91**, 3201–4 (1994).
50. Stevens, M. M. & George, J. H. Exploring and engineering the cell surface interface. *Science* **310**, 1135–8 (2005).
51. Åsberg, D. P. & Inganäs, O. PEDOT/PSS hydrogel networks as 3-D enzyme electrodes. *Synth. Met.* **137**, 1403–1404 (2003).
52. Vacanti, J. P. & Vacanti, C. A. The History and Scope of Tissue Engineering. *Princ. Tissue Eng.* 3–8 (2014). doi:10.1016/B978-0-12-398358-9.00001-X
53. Makris, E. A., Gomoll, A. H., Malizos, K. N., Hu, J. C. & Athanasiou, K. A. Repair and tissue engineering techniques for articular cartilage. *Nat. Rev. Rheumatol.* **11**, 21–34 (2015).
54. Schumann, D., Ekaputra, A. K., Lam, C. X. F. & Hutmacher, D. W. Biomaterials/Scaffolds. in 101–124 (Humana Press, 2007). doi:10.1007/978-1-59745-443-8_6
55. Castano, H., O'Rear, E. A., McFetridge, P. S. & Sikavitsas, V. I. Polypyrrole Thin Films Formed by Admicellar Polymerization Support the Osteogenic Differentiation of Mesenchymal Stem Cells. *Macromol. Biosci.* **4**, 785–794 (2004).
56. Li, M., Guo, Y., Wei, Y., MacDiarmid, A. G. & Lelkes, P. I. Electrospinning polyaniline-contained gelatin nanofibers for tissue engineering applications. *Biomaterials* **27**, 2705–2715 (2006).
57. Zhao, F., Shi, Y., Pan, L. & Yu, G. Multifunctional Nanostructured Conductive Polymer Gels: Synthesis, Properties, and Applications. *Acc. Chem. Res.* **50**, 1734–1743 (2017).
58. Zhang, Z., Roy, R., Dugr, F. J., Tessier, D. & Dao, L. H. In vitro biocompatibility study of electrically conductive polypyrrole-coated polyester fabrics. *J. Biomed. Mater. Res.* **57**, 63–71 (2001).
59. Ramanaviciene, A., Kausaite, A., Tautkus, S. & Ramanavicius, A. Biocompatibility of polypyrrole particles: an in-vivo study in mice. *J. Pharm. Pharmacol.* **59**, 311–315 (2007).
60. Humpolicek, P., Kasparkova, V., Saha, P. & Stejskal, J. Biocompatibility of polyaniline. *Synth. Met.* **162**, 722–727 (2012).
61. Liu, L. *et al.* Increased Proliferation and Differentiation of Pre-Osteoblasts MC3T3-E1 Cells on Nanostructured Polypyrrole Membrane Under Combined Electrical and Mechanical Stimulation. *J. Biomed. Nanotechnol.* **9**, 1532–1539 (2013).
62. Min, Y. *et al.* Self-doped polyaniline-based interdigitated electrodes for electrical stimulation of osteoblast cell lines. *Synth. Met.* **198**, 308–313 (2014).
63. Green, R. A., Lovell, N. H., Wallace, G. G. & Poole-Warren, L. A. Conducting polymers for neural interfaces: Challenges in developing an effective long-term implant. *Biomaterials* **29**, 3393–3399 (2008).
64. Xu, H. *et al.* Conductive PPY/PDLLA conduit for peripheral nerve regeneration. *Biomaterials* **35**, 225–235 (2014).
65. Guo, B., Glavas, L. & Albertsson, A.-C. Biodegradable and electrically conducting polymers for biomedical applications. *Prog. Polym. Sci.* **38**, 1263–1286 (2013).
66. Guimard, N. K. E., Sessler, J. L. & Schmidt, C. E. Toward a Biocompatible and Biodegradable Copolymer Incorporating Electroactive Oligothiophene Units. *Macromolecules* **42**, 502–511 (2009).
67. Gharibi, R., Yeganeh, H., Rezapour-Lactoee, A. & Hassan, Z. M. Stimulation of Wound Healing by Electroactive, Antibacterial, and Antioxidant Polyurethane/Siloxane Dressing Membranes: In Vitro and in Vivo Evaluations. *ACS Appl. Mater. Interfaces* **7**, 24296–24311 (2015).
68. Ma, P. X. Biomimetic materials for tissue engineering. *Adv. Drug Deliv. Rev.* **60**, 184–198 (2008).
69. Holzwarth, J. M. & Ma, P. X. Biomimetic nanofibrous scaffolds for bone tissue engineering. *Biomaterials* **32**, 9622–9629 (2011).

70. Sun, B. *et al.* Advances in three-dimensional nanofibrous macrostructures via electrospinning. *Prog. Polym. Sci.* **39**, 862–890 (2014).
71. Jiang, T., Carbone, E. J., Lo, K. W.-H. & Laurencin, C. T. Electrospinning of polymer nanofibers for tissue regeneration. *Prog. Polym. Sci.* **46**, 1–24 (2015).
72. Chen, M.-C., Sun, Y.-C. & Chen, Y.-H. Electrically conductive nanofibers with highly oriented structures and their potential application in skeletal muscle tissue engineering. *Acta Biomater.* **9**, 5562–5572 (2013).
73. Guiseppi-Elie, A. Electroconductive hydrogels: Synthesis, characterization and biomedical applications. *Biomaterials* **31**, 2701–2716 (2010).
74. Qu, J., Zhao, X., Ma, P. X. & Guo, B. Injectable antibacterial conductive hydrogels with dual response to an electric field and pH for localized "smart" drug release. *Acta Biomater.* **72**, 55–69 (2018).
75. Deng, Z., Guo, Y., Zhao, X., Ma, P. X. & Guo, B. Multifunctional Stimuli-Responsive Hydrogels with Self-Healing, High Conductivity, and Rapid Recovery through Host–Guest Interactions. *Chem. Mater.* **30**, 1729–1742 (2018).
76. Li, G. *et al.* Self-Healing Supramolecular Self-Assembled Hydrogels Based on Poly(l -glutamic acid). *Biomacromolecules* **16**, 3508–3518 (2015).
77. Lau, H. K. & Kiick, K. L. Opportunities for Multicomponent Hybrid Hydrogels in Biomedical Applications. *Biomacromolecules* **16**, 28–42 (2015).
78. Qu, J., Zhao, X., Ma, P. X. & Guo, B. pH-responsive self-healing injectable hydrogel based on N-carboxyethyl chitosan for hepatocellular carcinoma therapy. *Acta Biomater.* **58**, 168–180 (2017).
79. Li, L., Ge, J., Ma, P. X. & Guo, B. Injectable conducting interpenetrating polymer network hydrogels from gelatin-graft-polyaniline and oxidized dextran with enhanced mechanical properties. *RSC Adv.* **5**, 92490–92498 (2015).
80. Li, L., Ge, J., Guo, B. & Ma, P. X. In situ forming biodegradable electroactive hydrogels. *Polym. Chem.* **5**, 2880 (2014).
81. Mawad, D. *et al.* A Single Component Conducting Polymer Hydrogel as a Scaffold for Tissue Engineering. *Adv. Funct. Mater.* **22**, 2692–2699 (2012).
82. Jin, E. *et al.* Injectable electroactive hydrogels based on Pluronic® F127 and tetraaniline copolymer. *Eur. Polym. J.* **88**, 67–74 (2017).
83. Cui, H. *et al.* PLA-PEG-PLA and Its Electroactive Tetraaniline Copolymer as Multi-interactive Injectable Hydrogels for Tissue Engineering. *Biomacromolecules* **14**, 1904–1912 (2013).
84. Kashi, M., Baghbani, F., Moztarzadeh, F., Mobasheri, H. & Kowsari, E. Green synthesis of degradable conductive thermosensitive oligopyrrole/chitosan hydrogel intended for cartilage tissue engineering. *Int. J. Biol. Macromol.* **107**, 1567–1575 (2018).
85. Wang, L., Wu, Y., Guo, B. & Ma, P. X. Nanofiber Yarn/Hydrogel Core–Shell Scaffolds Mimicking Native Skeletal Muscle Tissue for Guiding 3D Myoblast Alignment, Elongation, and Differentiation. *ACS Nano* **9**, 9167–9179 (2015).
86. Li, L., Yu, M., Ma, P. X. & Guo, B. Electroactive degradable copolymers enhancing osteogenic differentiation from bone marrow derived mesenchymal stem cells. *J. Mater. Chem. B* **4**, 471–481 (2016).
87. Meng, S., Zhang, Z. & Rouabhia, M. Accelerated osteoblast mineralization on a conductive substrate by multiple electrical stimulation. *J. Bone Miner. Metab.* **29**, 535–544 (2011).
88. Wu, Y., Wang, L., Guo, B. & Ma, P. X. Interwoven Aligned Conductive Nanofiber Yarn/Hydrogel Composite Scaffolds for Engineered 3D Cardiac Anisotropy. *ACS Nano* **11**, 5646–5659 (2017).
89. Wang, L., Wu, Y., Hu, T., Guo, B. & Ma, P. X. Electrospun conductive nanofibrous scaffolds for engineering cardiac tissue and 3D bioactuators. *Acta Biomater.* **59**, 68–81 (2017).
90. Guex, A. G. *et al.* Highly porous scaffolds of PEDOT:PSS for bone tissue engineering. *Acta Biomater.* **62**, 91–101 (2017).

91. Mohamadali, M., Irani, S., Soleimani, M. & Hosseinzadeh, S. PANi/PAN copolymer as scaffolds for the muscle cell-like differentiation of mesenchymal stem cells. *Polym. Adv. Technol.* **28**, 1078–1087 (2017).
92. Wu, Y., Wang, L., Guo, B., Shao, Y. & Ma, P. X. Electroactive biodegradable polyurethane significantly enhanced Schwann cells myelin gene expression and neurotrophin secretion for peripheral nerve tissue engineering. *Biomaterials* **87**, 18–31 (2016).
93. Shi, Z. *et al.* In Situ Synthesis of Robust Conductive Cellulose/Polypyrrole Composite Aerogels and Their Potential Application in Nerve Regeneration. *Angew. Chemie Int. Ed.* **53**, 5380–5384 (2014).
94. Sun, B. *et al.* Polypyrrole-coated poly(l -lactic acid-co-ε-caprolactone)/silk fibroin nanofibrous membranes promoting neural cell proliferation and differentiation with electrical stimulation. *J. Mater. Chem. B* **4**, 6670–6679 (2016).
95. Zhang, Z. *et al.* Electrically Conductive Biodegradable Polymer Composite for Nerve Regeneration: Electricity-Stimulated Neurite Outgrowth and Axon Regeneration. *Artif. Organs* **31**, 13–22 (2007).
96. Lee, J. Y., Bashur, C. A., Goldstein, A. S. & Schmidt, C. E. Polypyrrole-coated electrospun PLGA nanofibers for neural tissue applications. *Biomaterials* **30**, 4325–4335 (2009).
97. Xie, J. *et al.* Conductive Core-Sheath Nanofibers and Their Potential Application in Neural Tissue Engineering. *Adv. Funct. Mater.* **19**, 2312–2318 (2009).
98. GhavamiNejad, A., Park, C. H. & Kim, C. S. In Situ Synthesis of Antimicrobial Silver Nanoparticles within Antifouling Zwitterionic Hydrogels by Catecholic Redox Chemistry for Wound Healing Application. *Biomacromolecules* **17**, 1213–1223 (2016).
99. Guo, B., Sun, Y., Finne-Wistrand, A., Mustafa, K. & Albertsson, A.-C. Electroactive porous tubular scaffolds with degradability and non-cytotoxicity for neural tissue regeneration. *Acta Biomater.* **8**, 144–153 (2012).
100. Zhao, X., Li, P., Guo, B. & Ma, P. X. Antibacterial and conductive injectable hydrogels based on quaternized chitosan-graft-polyaniline/oxidized dextran for tissue engineering. *Acta Biomater.* **26**, 236–248 (2015).
101. Nazarzadeh Zare, E., Mansour Lakouraj, M. & Mohseni, M. Biodegradable polypyrrole/dextrin conductive nanocomposite: Synthesis, characterization, antioxidant and antibacterial activity. *Synth. Met.* **187**, 9–16 (2014).
102. Zhao, X. *et al.* Antibacterial anti-oxidant electroactive injectable hydrogel as self-healing wound dressing with hemostasis and adhesiveness for cutaneous wound healing. *Biomaterials* **122**, 34–47 (2017).
103. Clark, L. C. & Lyons, C. ELECTRODE SYSTEMS FOR CONTINUOUS MONITORING IN CARDIOVASCULAR SURGERY. *Ann. N. Y. Acad. Sci.* **102**, 29–45 (1962).
104. Moon, J.-M., Thapliyal, N., Hussain, K. K., Goyal, R. N. & Shim, Y.-B. Conducting polymer-based electrochemical biosensors for neurotransmitters: A review. *Biosens. Bioelectron.* **102**, 540–552 (2018).
105. Gerard, M., Chaubey, A. & Malhotra, B. D. Application of conducting polymers to biosensors. *Biosens. Bioelectron.* **17**, 345–359 (2002).
106. Chaubey, A., Gerard, M., Singhal, R., Singh, V. . & Malhotra, B. . Immobilization of lactate dehydrogenase on electrochemically prepared polypyrrole–polyvinylsulphonate composite films for application to lactate biosensors. *Electrochim. Acta* **46**, 723–729 (2001).
107. Gambhir, A., Gerard, M., Mulchandani, A. K. & Malhotra, B. D. Coimmobilization of Urease and Glutamate Dehydrogenase in Electrochemically Prepared Polypyrrole - Polyvinyl Sulfonate Films. *Appl. Biochem. Biotechnol.* **96**, 249–258 (2001).
108. Ramanathan, K. *et al.* Covalent immobilization of glucose oxidase to poly(O-amino benzoic acid) for application to glucose biosensor. *J. Appl. Polym. Sci.* **78**, 662–667 (2000).
109. Ramanathan, K., Ram, M. K., Verghese, M. M. & Malhotra, B. D. Dielectric spectroscopic studies on polypyrrole glucose oxidase films. *J. Appl. Polym. Sci.* **60**, 2309–2316 (1996).

110. Ramanathan, K., Mehrotra, R., Jayaram, B., Murthy, A. S. N. & Malhotra, B. D. Simulation of Electrochemical Process for Glucose Oxidase Immobilized Conducting Polymer Electrodes. *Anal. Lett.* **29**, 1477–1484 (1996).
111. Jozef Švorc, †,‡, Stanislav Miertuš, *,†, Jaroslav Katrlík, †,‡ and & Miroslav Stred'anský†, ‡. Composite Transducers for Amperometric Biosensors. The Glucose Sensor. (1997). doi:10.1021/AC9609485
112. Urban, G. *et al.* High-resolution thin-film temperature sensor arrays for medical applications. *Sensors Actuators A Phys.* **22**, 650–654 (1990).
113. Aydemir, N., Malmström, J. & Travas-Sejdic, J. Conducting polymer based electrochemical biosensors. *Phys. Chem. Chem. Phys.* **18**, 8264–8277 (2016).
114. K. Peter R. Nilsson, *,‡, Anna Herland, ‡, Per Hammarström, § and & Inganäs‡, O. Conjugated Polyelectrolytes: Conformation-Sensitive Optical Probes for Detection of Amyloid Fibril Formation†. (2005). doi:10.1021/BI047402U
115. K. Peter R. Nilsson*, † and & Inganäs†, O. Optical Emission of a Conjugated Polyelectrolyte: Calcium-Induced Conformational Changes in Calmodulin and Calmodulin−Calcineurin Interactions. (2004). doi:10.1021/MA048605T
116. Trojanowicz, M. & Krawczy?ski vel Krawczyk, T. Electrochemical biosensors based on enzymes immobilized in electropolymerized films. *Mikrochim. Acta* **121**, 167–181 (1995).
117. Arslan, F., Yaşar, A. & Kılıç, E. An Amperometric Biosensor for Xanthine Determination Prepared from Xanthine Oxidase Immobilized in Polypyrrole Film. *Artif. Cells, Blood Substitutes, Biotechnol.* **34**, 113–128 (2006).
118. Fiorito, P. A., Brett, C. M. A. & Córdoba de Torresi, S. I. Polypyrrole/copper hexacyanoferrate hybrid as redox mediator for glucose biosensors. *Talanta* **69**, 403–408 (2006).
119. Cosnier, S., Dawod, M., Gorgy, K. & Da Silva, S. Synthesis and Electrochemical Characterization of a New Electropolymerizable Hydrophilic Viologen Designed for Enzyme Wiring. *Microchim. Acta* **143**, 139–145 (2003).
120. Arslan, F., Yaşar, A. & Kiliç, E. Preparation of Pt/polypyrrole-ferrocene hydrogen peroxide sensitive electrode for the use as a biosensor. *Russ. J. Electrochem.* **42**, 137–140 (2006).
121. Ronkainen, N. J., Halsall, H. B. & Heineman, W. R. Electrochemical biosensors. *Chem. Soc. Rev.* **39**, 1747 (2010).
122. Pandey, P. C. & Mishra, A. P. Conducting polymer-coated enzyme microsensor for urea. *Analyst* **113**, 329 (1988).
123. Nishizawa, M., Matsue, T. & Uchida, I. *Penicillin Sensor Based on a Microarray Electrode Coated with pH-Responsive Polypyrrole*. *Analytical Chemistry* **64**, (1992).
124. Contractor, A. Q. *et al.* Conducting polymer-based biosensors. *Electrochim. Acta* **39**, 1321–1324 (1994).
125. Brajter-Toth, A. & Chambers, J. Q. *Electroanalytical methods for biological materials*. (Marcel Dekker, 2002).
126. Singhal, R. *et al.* Immobilization of glucose oxidase onto Langmuir–Blodgett films of poly-3-hexylthiophene. *Curr. Appl. Phys.* **3**, 275–279 (2003).
127. Mosbach, K. & Danielsson, B. *Instrumentation Thermal Bioanalyzers in Flow Streams*.
128. Kergoat, L., Piro, B., Berggren, M., Horowitz, G. & Pham, M.-C. Advances in organic transistor-based biosensors: from organic electrochemical transistors to electrolyte-gated organic field-effect transistors. *Anal. Bioanal. Chem.* **402**, 1813–1826 (2012).
129. Bidan, G. Electroconducting conjugated polymers: New sensitive matrices to build up chemical or electrochemical sensors. A review. *Sensors Actuators B Chem.* **6**, 45–56 (1992).
130. Vázquez, M. *et al.* Potentiometric sensors based on poly(3,4-ethylenedioxythiophene) (PEDOT) doped with sulfonated calix[4]arene and calix[4]resorcarenes. *J. Solid State Electrochem.* **9**, 312–319 (2005).
131. Darain, F., Park, S.-U. & Shim, Y.-B. Disposable amperometric immunosensor system for rabbit IgG using a conducting polymer modified screen-printed electrode. *Biosens.*

Bioelectron. **18**, 773–780 (2003).
132. Ebisawa, F., Kurokawa, T. & Nara, S. Electrical properties of polyacetylene/polysiloxane interface. *J. Appl. Phys.* **54**, 3255–3259 (1983).
133. Torsi, L., Magliulo, M., Manoli, K. & Palazzo, G. Organic field-effect transistor sensors: a tutorial review. *Chem. Soc. Rev.* **42**, 8612 (2013).
134. Wang, C., Dong, H., Hu, W., Liu, Y. & Zhu, D. Semiconducting π-Conjugated Systems in Field-Effect Transistors: A Material Odyssey of Organic Electronics. *Chem. Rev.* **112**, 2208–2267 (2012).
135. Garnier, F., Hajlaoui, R., Yassar, A. & Srivastava, P. All-polymer field-effect transistor realized by printing techniques. *Science* **265**, 1684–6 (1994).
136. Ortiz, R. P., Facchetti, A. & Marks, T. J. High- *k* Organic, Inorganic, and Hybrid Dielectrics for Low-Voltage Organic Field-Effect Transistors. *Chem. Rev.* **110**, 205–239 (2010).
137. Tiwari, S. *et al.* Poly-3-hexylthiophene based organic field-effect transistor: Detection of low concentration of ammonia. *Sensors Actuators B Chem.* **171**–**172**, 962–968 (2012).
138. Royer, J. E. *et al.* Organic Thin-Film Transistors for Selective Hydrogen Peroxide and Organic Peroxide Vapor Detection. *J. Phys. Chem. C* **116**, 24566–24572 (2012).
139. Bergveld, P. Development of an Ion-Sensitive Solid-State Device for Neurophysiological Measurements. *IEEE Trans. Biomed. Eng.* **BME-17**, 70–71 (1970).
140. Bartic, C., Palan, B., Campitelli, A. & Borghs, G. Monitoring pH with organic-based field-effect transistors. *Sensors Actuators B Chem.* **83**, 115–122 (2002).
141. Bartic, C., Campitelli, A. & Borghs, S. Field-effect detection of chemical species with hybrid organic/inorganic transistors. *Appl. Phys. Lett.* **82**, 475–477 (2003).
142. Lai, S. *et al.* Ultralow Voltage, OTFT-Based Sensor for Label-Free DNA Detection. *Adv. Mater.* **25**, 103–107 (2013).
143. Panzer, M. J., Newman, C. R. & Frisbie, C. D. Low-voltage operation of a pentacene field-effect transistor with a polymer electrolyte gate dielectric. *Appl. Phys. Lett.* **86**, 103503 (2005).
144. Kergoat, L. *et al.* A Water-Gate Organic Field-Effect Transistor. *Adv. Mater.* **22**, 2565–2569 (2010).
145. Shimotani, H., Asanuma, H., Takeya, J. & Iwasa, Y. Electrolyte-gated charge accumulation in organic single crystals. *Appl. Phys. Lett.* **89**, 203501 (2006).
146. Hamedi, M. *et al.* Fiber-Embedded Electrolyte-Gated Field-Effect Transistors for e-Textiles. *Adv. Mater.* **21**, 573–577 (2009).
147. Said, E., Larsson, O., Berggren, M. & Crispin, X. Effects of the Ionic Currents in Electrolyte-gated Organic Field-Effect Transistors. *Adv. Funct. Mater.* **18**, 3529–3536 (2008).
148. Cho, J. H. *et al.* High-Capacitance Ion Gel Gate Dielectrics with Faster Polarization Response Times for Organic Thin Film Transistors. *Adv. Mater.* **20**, 686–690 (2008).
149. Tarabella, G. *et al.* New opportunities for organic electronics and bioelectronics: ions in action. *Chem. Sci.* **4**, 1395 (2013).
150. Jonathan D. Yuen, † *et al.* Electrochemical Doping in Electrolyte-Gated Polymer Transistors. (2007). doi:10.1021/JA0749845
151. Said, E. *et al.* Polymer field-effect transistor gated via a poly(styrenesulfonic acid) thin film. *Appl. Phys. Lett.* **89**, 143507 (2006).
152. White, H. S., Kittlesen, G. P. & Wrighton, M. S. Chemical derivatization of an array of three gold microelectrodes with polypyrrole: fabrication of a molecule-based transistor. *J. Am. Chem. Soc.* **106**, 5375–5377 (1984).
153. Khodagholy, D. *et al.* High transconductance organic electrochemical transistors. *Nat. Commun.* **4**, 2133 (2013).
154. Rivnay, J. *et al.* Organic electrochemical transistors. *Nat. Rev. Mater.* **3**, 17086 (2018).
155. Bernards, D. A. & Malliaras, G. G. Steady-State and Transient Behavior of Organic Electrochemical Transistors. *Adv. Funct. Mater.* **17**, 3538–3544 (2007).
156. Proctor, C. M., Rivnay, J. & Malliaras, G. G. Understanding volumetric capacitance in

conducting polymers. *J. Polym. Sci. Part B Polym. Phys.* **54**, 1433–1436 (2016).
157. Lin, F. & Lonergan, M. C. Gate electrode processes in an electrolyte-gated transistor: Non-Faradaically versus Faradaically coupled conductivity modulation of a polyacetylene ionomer. *Appl. Phys. Lett.* **88**, 133507 (2006).
158. Lin, P., Yan, F. & Chan, H. L. W. Ion-Sensitive Properties of Organic Electrochemical Transistors. *ACS Appl. Mater. Interfaces* **2**, 1637–1641 (2010).
159. Cicoira, F. *et al.* Influence of Device Geometry on Sensor Characteristics of Planar Organic Electrochemical Transistors. *Adv. Mater.* **22**, 1012–1016 (2010).
160. Gualandi, I. *et al.* A simple all-PEDOT:PSS electrochemical transistor for ascorbic acid sensing. *J. Mater. Chem. B* **3**, 6753–6762 (2015).
161. Rivnay, J. *et al.* High-performance transistors for bioelectronics through tuning of channel thickness. *Sci. Adv.* **1**, e1400251 (2015).
162. Basiricò, L., Cosseddu, P., Fraboni, B. & Bonfiglio, A. Inkjet printing of transparent, flexible, organic transistors. *Thin Solid Films* **520**, 1291–1294 (2011).
163. Zhang, L. *et al.* Highly selective and sensitive sensor based on an organic electrochemical transistor for the detection of ascorbic acid. *Biosens. Bioelectron.* **100**, 235–241 (2018).
164. Coppedè, N. *et al.* Human stress monitoring through an organic cotton-fiber biosensor. *J. Mater. Chem. B* **2**, 5620–5626 (2014).
165. Khodagholy, D. *et al.* Organic electrochemical transistor incorporating an ionogel as a solid state electrolyte for lactate sensing. *J. Mater. Chem.* **22**, 4440 (2012).
166. Rivnay, J. *et al.* Organic electrochemical transistors for cell-based impedance sensing. *Appl. Phys. Lett.* **106**, 043301 (2015).
167. Ramuz, M. *et al.* Combined Optical and Electronic Sensing of Epithelial Cells Using Planar Organic Transistors. *Adv. Mater.* **26**, 7083–7090 (2014).
168. Curto, V. F. *et al.* Organic transistor platform with integrated microfluidics for in-line multi-parametric in vitro cell monitoring. *Microsystems Nanoeng.* **3**, 17028 (2017).
169. Ramuz, M., Hama, A., Rivnay, J., Leleux, P. & Owens, R. M. Monitoring of cell layer coverage and differentiation with the organic electrochemical transistor. *J. Mater. Chem. B* **3**, 5971–5977 (2015).
170. Khodagholy, D. *et al.* In vivo recordings of brain activity using organic transistors. *Nat. Commun.* **4**, 1575 (2013).
171. van de Burgt, Y. *et al.* A non-volatile organic electrochemical device as a low-voltage artificial synapse for neuromorphic computing. *Nat. Mater.* **16**, 414–418 (2017).
172. Gualandi, I. *et al.* Textile Organic Electrochemical Transistors as a Platform for Wearable Biosensors. *Sci. Rep.* **6**, 33637 (2016).
173. Tessarolo, M., Gualandi, I. & Fraboni, B. Recent Progress in Wearable Fully Textile Chemical Sensors. *Adv. Mater. Technol.* **3**, 1700310 (2018).
174. Acarón Ledesma, H. *et al.* An atlas of nano-enabled neural interfaces. *Nat. Nanotechnol.* **14**, 645–657 (2019).
175. Boyden, E. S., Zhang, F., Bamberg, E., Nagel, G. & Deisseroth, K. Millisecond-timescale, genetically targeted optical control of neural activity. *Nat. Neurosci.* **8**, 1263–1268 (2005).
176. Testerman, R. L., Rise, M. T. & Stypulkowski, P. H. Electrical stimulation as therapy for neurological disorders. *IEEE Eng. Med. Biol. Mag.* **25**, 74–78 (2006).
177. Fisher, R. S. & Velasco, A. L. Electrical brain stimulation for epilepsy. *Nat. Rev. Neurol.* **10**, 261–270 (2014).
178. Insel, T. R., Landis, S. C. & Collins, F. S. The NIH BRAIN Initiative. *Science (80-.).* **340**, 687–688 (2013).
179. Poo, M. *et al.* China Brain Project: Basic Neuroscience, Brain Diseases, and Brain-Inspired Computing. *Neuron* **92**, 591–596 (2016).
180. Amunts, K. *et al.* The Human Brain Project: Creating a European Research Infrastructure to Decode the Human Brain. *Neuron* **92**, 574–581 (2016).

181. Abidian, M. R. & Martin, D. C. Experimental and theoretical characterization of implantable neural microelectrodes modified with conducting polymer nanotubes. *Biomaterials* **29**, 1273–1283 (2008).
182. Baranauskas, G. *et al.* Carbon nanotube composite coating of neural microelectrodes preferentially improves the multiunit signal-to-noise ratio. *J. Neural Eng.* **8**, 066013 (2011).
183. Thaning, E. M., Asplund, M. L. M., Nyberg, T. A., Inganäs, O. W. & von Holst, H. Stability of poly(3,4-ethylene dioxythiophene) materials intended for implants. *J. Biomed. Mater. Res. Part B Appl. Biomater.* **93B**, 407–415 (2010).
184. Merrill, D. R., Bikson, M. & Jefferys, J. G. R. Electrical stimulation of excitable tissue: design of efficacious and safe protocols. *J. Neurosci. Methods* **141**, 171–198 (2005).
185. Asplund, M., Nyberg, T. & Inganäs, O. Electroactive polymers for neural interfaces. *Polym. Chem.* **1**, 1374 (2010).
186. Cui, X., Hetke, J. F., Wiler, J. A., Anderson, D. J. & Martin, D. C. Electrochemical deposition and characterization of conducting polymer polypyrrole/PSS on multichannel neural probes. *Sensors Actuators A Phys.* **93**, 8–18 (2001).
187. Cui, X. *et al.* Surface modification of neural recording electrodes with conducting polymer/biomolecule blends. *J. Biomed. Mater. Res.* **56**, 261–272 (2001).
188. Kim, D.-H., Abidian, M. & Martin, D. C. Conducting polymers grown in hydrogel scaffolds coated on neural prosthetic devices. *J. Biomed. Mater. Res.* **71A**, 577–585 (2004).
189. Cui, X. & Martin, D. C. Electrochemical deposition and characterization of poly(3,4-ethylenedioxythiophene) on neural microelectrode arrays. *Sensors Actuators B Chem.* **89**, 92–102 (2003).
190. George, P. M. *et al.* Fabrication and biocompatibility of polypyrrole implants suitable for neural prosthetics. *Biomaterials* **26**, 3511–3519 (2005).
191. Stauffer, W. R. & Cui, X. T. Polypyrrole doped with 2 peptide sequences from laminin. *Biomaterials* **27**, 2405–2413 (2006).
192. Rogers, J. A., Someya, T. & Huang, Y. Materials and mechanics for stretchable electronics. *Science* **327**, 1603–7 (2010).
193. Sekine, S., Ido, Y., Miyake, T., Nagamine, K. & Nishizawa, M. Conducting Polymer Electrodes Printed on Hydrogel. *J. Am. Chem. Soc.* **132**, 13174–13175 (2010).
194. Guo, L., Ma, M., Zhang, N., Langer, R. & Anderson, D. G. Stretchable Polymeric Multielectrode Array for Conformal Neural Interfacing. *Adv. Mater.* **26**, 1427–1433 (2014).
195. Shirakawa, H., Louis, E. J., MacDiarmid, A. G., Chiang, C. K. & Heeger, A. J. Synthesis of electrically conducting organic polymers: halogen derivatives of polyacetylene, (CH) x. *J. Chem. Soc. Chem. Commun.* **0**, 578 (1977).
196. *Advanced Information - The Nobel Prize in Chemistry 2000*.
197. Elschner, A., Kirchmeyer, S., Lövenich, W., Merker, U. & Reuter, K. *PEDOT: Principles and applications of an intrinsically conductive polyme*. *PEDOT: Principles and Applications of an Intrinsically Conductive Polymer* (CRC Press, 2010). doi:10.1201/b10318
198. Reddinger, J. L. & Reynolds, J. R. Molecular Engineering of π-Conjugated Polymers. in *Radical Polymerisation Polyelectrolytes* 57–122 (Springer Berlin Heidelberg, 1999). doi:10.1007/3-540-70733-6_2
199. Nalwa, H. S. *Handbook of organic conductive molecules and polymers. Vol. 2*. (Wiley, 1997).
200. Miillen, K., Wegner, / G & Roth, S. *Handbook of Oligo- and Polythiophenes*.
201. Roncali, J. Electrogenerated functional conjugated polymers as advanced electrode materials. *J. Mater. Chem.* **9**, 1875–1893 (1999).
202. Heeger, A. J. Semiconducting and metallic polymers: The fourth generation of polymeric materials. *Curr. Appl. Phys.* **1**, 247–267 (2001).
203. Hoffmann, R., Janiak, C. & Kollmar, C. *Macromolecules Reviews A Chemical Approach to the Orbitals of Organic Polymers A/* \. (1991).
204. Davies, J. H. (John H. . *The physics of low-dimensional semiconductors : an introduction*.

(Cambridge University Press, 1998).
205. Grundmann, M. *The physics of semiconductors : an introduction including devices and nanophysics*. (Springer, 2006).
206. Inzelt, G. *Conducting polymers : a new era in electrochemistry*. (Springer, 2012).
207. Bredas, J. L. & Street, G. B. Polarons, bipolarons, and solitons in conducting polymers. *Acc. Chem. Res.* **18**, 309–315 (1985).
208. Handbook of Organic Conductive Molecules and Polymers, Volume 4, Conductive Polymers: Transport, Photophysics and Applications | Polymer Science & Technology General | Subjects | Wiley. Available at: https://www.wiley.com/en-ai/Handbook+of+Organic+Conductive+Molecules+and+Polymers%2C+Volume+4%2C+Conductive+Polymers%3A+Transport%2C+Photophysics+and+Applications-p-9780470859452. (Accessed: 26th August 2019)
209. Camurlu, P. Polypyrrole derivatives for electrochromic applications. *RSC Adv.* **4**, 55832–55845 (2014).
210. Brédas, J. E., Chance, R. R. & Silbey, R. Theoretical Studies of Charged Defect States in Doped Polyacetylene and Polyparaphenylene. *Mol. Cryst. Liq. Cryst.* **77**, 319–332 (1981).
211. Brédas, J. L., Scott, J. C., Yakushi, K. & Street, G. B. Polarons and bipolarons in polypyrrole: Evolution of the band structure and optical spectrum upon doing. *Phys. Rev. B* **30**, 1023–1025 (1984).
212. Scott, J. C., Pfluger, P., Krounbi, M. T. & Street, G. B. Electron-spin-resonance studies of pyrrole polymers: Evidence for bipolarons. *Phys. Rev. B* **28**, 2140–2145 (1983).
213. Su, W. P., Schrieffer, J. R. & Heeger, A. J. Solitons in Polyacetylene. *Phys. Rev. Lett.* **42**, 1698–1701 (1979).
214. Kivelson, S. Electron Hopping Conduction in the Soliton Model of Polyacetylene. *Mol. Cryst. Liq. Cryst.* **77**, 65–79 (1981).
215. Chiang, C. K. *et al.* Polyacetylene, $(CH)_x$: *n* -type and *p* -type doping and compensation. *Appl. Phys. Lett.* **33**, 18–20 (1978).
216. Chiang, C. K. *et al.* Electrical Conductivity in Doped Polyacetylene. *Phys. Rev. Lett.* **39**, 1098–1101 (1977).
217. Nigrey, P. J., MacDiarmid, A. G. & Heeger, A. J. Electrochemistry of polyacetylene, (CH) x : electrochemical doping of (CH) x films to the metallic state. *J. Chem. Soc. Chem. Commun.* 594 (1979). doi:10.1039/c39790000594
218. Heeger, A. J., Kivelson, S., Schrieffer, J. R. & Su, W.-P. Solitons in conducting polymers. *Rev. Mod. Phys.* **60**, 781–850 (1988).
219. Rothberg, L. J. *et al.* Photophysics of phenylenevinylene polymers. *Synth. Met.* **80**, 41–58 (1996).
220. J. Cornil, †,‡,§, D. A. dos Santos, †, X. Crispin, †, R. Silbey, ‡ and & J. L. Brédas*, †,§. Influence of Interchain Interactions on the Absorption and Luminescence of Conjugated Oligomers and Polymers: A Quantum-Chemical Characterization. (1998). doi:10.1021/JA973761J
221. Müller, H. K., Hocker, J., Menke, K., Ehinger, K. & Roth, S. Long-term conductivity decrease in polyacetylene samples. *Synth. Met.* **10**, 273–280 (1985).
222. H. Kondo, S. Ono, S. I. Pyrrole derivatives. IV. Condensation of β-bromolevulinic ester with acetoacetic ester and ammonia. *Yakugaku Zasshi* **57**, 404–406 (1937).
223. P.C. Guha, B. H. I. Attempts towards the synthesis of cantharidin- partII. *J. Indian Inst Sci* **21A**, 115–118 (1938).
224. Gogte, V. N., Shah, L. G., Tilak, B. D., Gadekar, K. N. & Sahasrabudhe, M. B. Synthesis of potential anticancer agents—I: Synthesis of substituted thiophenes. *Tetrahedron* **23**, 2437–2441 (1967).
225. Heywang, G. & Jonas, F. Poly(alkylenedioxythiophene)s—new, very stable conducting polymers. *Adv. Mater.* **4**, 116–118 (1992).

226. Coffey, M., McKellar, B. R., Reinhardt, B. A., Nijakowski, T. & Feld, W. A. A Facile Synthesis of 3,4-Dialkoxythiophenes. *Synth. Commun.* **26**, 2205–2212 (1996).
227. Groenendaal, L., Jonas, F., Freitag, D., Pielartzik, H. & Reynolds, J. R. Poly(3,4-ethylenedioxythiophene) and Its Derivatives: Past, Present, and Future. *Adv. Mater.* **12**, 481–494 (2000).
228. Pei, Q., Zuccarello, G., Ahlskog, M. & Inganäs, O. Electrochromic and highly stable poly(3,4-ethylenedioxythiophene) switches between opaque blue-black and transparent sky blue. *Polymer (Guildf).* **35**, 1347–1351 (1994).
229. Corradi, R. & Armes, S. P. Chemical synthesis of poly(3,4-ethylenedioxythiophene). *Synth. Met.* **84**, 453–454 (1997).
230. Dietrich, M., Heinze, J., Heywang, G. & Jonas, F. Electrochemical and spectroscopic characterization of polyalkylenedioxythiophenes. *J. Electroanal. Chem.* **369**, 87–92 (1994).
231. Jonas, F., Krafft, W. & Muys, B. Poly(3, 4-ethylenedioxythiophene): Conductive coatings, technical applications and properties. *Macromol. Symp.* **100**, 169–173 (1995).
232. de Leeuw, D. M., Kraakman, P. A., Bongaerts, P. F. G., Mutsaers, C. M. J. & Klaassen, D. B. M. Electroplating of conductive polymers for the metallization of insulators. *Synth. Met.* **66**, 263–273 (1994).
233. Pettersson, L. A. A., Johansson, T., Carlsson, F., Arwin, H. & Inganäs, O. Anisotropic optical properties of doped poly(3,4-ethylenedioxythiophene). *Synth. Met.* **101**, 198–199 (1999).
234. Pettersson, L. A. A., Carlsson, F., Inganäs, O. & Arwin, H. Spectroscopic ellipsometry studies of the optical properties of doped poly(3,4-ethylenedioxythiophene): an anisotropic metal. *Thin Solid Films* **313**–**314**, 356–361 (1998).
235. Jonas, F. & Heywang, G. Technical applications for conductive polymers. *Electrochim. Acta* **39**, 1345–1347 (1994).
236. Xiwen Chen, Ke-Zhao Xing, and & Inganäs*, O. Electrochemically Induced Volume Changes in Poly(3,4-ethylenedioxythiophene). (1996). doi:10.1021/CM9600034
237. Randriamahazaka, H., Noël, V. & Chevrot, C. Nucleation and growth of poly(3,4-ethylenedioxythiophene) in acetonitrile on platinum under potentiostatic conditions. *J. Electroanal. Chem.* **472**, 103–111 (1999).
238. Yamato, H., Kai, K., Ohwa, M., Wernet, W. & Matsumura, M. Mechanical, electrochemical and optical properties of poly(3,4-ethylenedioxythiophene)/sulfated poly(β-hydroxyethers) composite films. *Electrochim. Acta* **42**, 2517–2523 (1997).
239. Yamato, H. *et al.* Synthesis of free-standing poly(3,4-ethylenedioxythiophene) conducting polymer films on a pilot scale. *Synth. Met.* **83**, 125–130 (1996).
240. Yamato, H., Ohwa, M. & Wernet, W. Stability of polypyrrole and poly(3,4-ethylenedioxythiophene) for biosensor application. *J. Electroanal. Chem.* **397**, 163–170 (1995).
241. Sakmeche, N. *et al.* Application of sodium dodecylsulfate (SDS) micellar solution as an organized medium for electropolymerization of thiophene derivatives in water. *Synth. Met.* **84**, 191–192 (1997).
242. Sakmeche, N. *et al.* Anionic micelles; a new aqueous medium for electropolymerization of poly(3,4-ethylenedioxythiophene) films on Pt electrodes. *Chem. Commun.* 2723 (1996). doi:10.1039/cc9960002723
243. Lima, A., Schottland, P., Sadki, S. & Chevrot, C. Electropolymerization of 3,4-ethylenedioxythiophene and 3,4-ethylenedioxythiophene methanol in the presence of dodecylbenzenesulfonate. *Synth. Met.* **93**, 33–41 (1998).
244. Sotzing, G. A., Reynolds, J. R. & Steel, P. J. Poly(3,4-ethylenedioxythiophene) (PEDOT) prepared via electrochemical polymerization of EDOT, 2,2?-Bis(3,4-ethylenedioxythiophene) (BiEDOT), and their TMS derivatives. *Adv. Mater.* **9**, 795–798 (1997).
245. Yamamoto, T. π-Conjugated Polymers Bearing Electronic and Optical Functionalities. Preparation by Organometallic Polycondensations, Properties, and Their Applications. *Bull.*

Chem. Soc. Jpn. **72**, 621–638 (1999).
246. Yamamoto, T. *et al.* Temperature dependent electrical conductivity of p -doped poly(3,4-ethylenedioxythiophene) and poly(3-alkylthiophene)s. *Polym. Bull.* **42**, 321–327 (1999).
247. Yamamoto, T. & Abla, M. Synthesis of non-doped poly(3,4-ethylenedioxythiophene) and its spectroscopic data. *Synth. Met.* **100**, 237–239 (1999).
248. Wang, Y. Research progress on a novel conductive polymer–poly(3,4-ethylenedioxythiophene) (PEDOT). *J. Phys. Conf. Ser.* **152**, 012023 (2009).
249. Reynolds, J. R. *et al.* Unique variable-gap polyheterocycles for high-contrast dual polymer electrochromic devices. *Synth. Met.* **85**, 1295–1298 (1997).
250. R. Kiebooms, A. Aleshin, K. Hutchison, and & Wudl*, F. Thermal and Electromagnetic Behavior of Doped Poly(3,4-ethylenedioxythiophene) Films. (1997). doi:10.1021/JP9720101
251. Harri J. Ahonen, *, Jukka Lukkari, and & Kankare, J. n- and p-Doped Poly(3,4-ethylenedioxythiophene): Two Electronically Conducting States of the Polymer. (2000). doi:10.1021/MA0004312
252. Cornil, J., Dos Santos, D. A., Beljonne, D. & Bredas, J. L. Electronic Structure of Phenylene Vinylene Oligomers: Influence of Donor/Acceptor Substitutions. *J. Phys. Chem.* **99**, 5604–5611 (1995).
253. Kvarnström, C. *et al.* In situ ftir spectroelectrochemical characterization of poly(3,4-ethylenedioxythiophene) films. *Synth. Met.* **101**, 66 (1999).
254. Kirchmeyer, S. & Reuter, K. Scientific importance, properties and growing applications of poly(3,4-ethylenedioxythiophene). *J. Mater. Chem.* **15**, 2077 (2005).
255. Poly(styrenesulfonate) (PSS) and Copolymers - Polyelectrolytes | Sigma-Aldrich. Available at: https://www.sigmaaldrich.com/materials-science/material-science-products.html?TablePage=112436131. (Accessed: 28th August 2019)
256. Groenendaal, L., Jonas, F., Freitag, D., Pielartzik, H. & Reynolds, J. R. Poly(3,4-ethylenedioxythiophene) and Its Derivatives: Past, Present, and Future. *Adv. Mater.* **12**, 481–494 (2000).
257. Hwang, J., Tanner, D. B., Schwendeman, I. & Reynolds, J. R. Optical properties of nondegenerate ground-state polymers: Three dioxythiophene-based conjugated polymers. *Phys. Rev. B* **67**, 115205 (2003).
258. Aasmundtveit, K. E. *et al.* Structure of thin films of poly(3,4-ethylenedioxythiophene). *Synth. Met.* **101**, 561–564 (1999).
259. G. Zotti, * *et al.* Electrochemical and XPS Studies toward the Role of Monomeric and Polymeric Sulfonate Counterions in the Synthesis, Composition, and Properties of Poly(3,4-ethylenedioxythiophene). (2003). doi:10.1021/MA021715K
260. Rivnay, J. *et al.* Structural control of mixed ionic and electronic transport in conducting polymers. *Nat. Commun.* **7**, 11287 (2016).
261. Ouyang, J. *et al.* On the mechanism of conductivity enhancement in poly(3,4-ethylenedioxythiophene):poly(styrene sulfonate) film through solvent treatment. *Polymer (Guildf).* **45**, 8443–8450 (2004).
262. Jönsson, S. K. . *et al.* The effects of solvents on the morphology and sheet resistance in poly(3,4-ethylenedioxythiophene)–polystyrenesulfonic acid (PEDOT–PSS) films. *Synth. Met.* **139**, 1–10 (2003).
263. Pingree, L. S. C., MacLeod, B. A. & Ginger, D. S. The Changing Face of PEDOT:PSS Films: Substrate, Bias, and Processing Effects on Vertical Charge Transport. *J. Phys. Chem. C* **112**, 7922–7927 (2008).
264. Krebs, F. C. Fabrication and processing of polymer solar cells: A review of printing and coating techniques. *Sol. Energy Mater. Sol. Cells* **93**, 394–412 (2009).
265. HOHNHOLZ & D. Line patterning of conducting polymers : New horizons for inexpensive, disposable electronic devices. *Synth. Met.* **121**, 1327 (2001).
266. Tachikawa, T., Itoh, N., Handa, S., Aoki, D. & Miyake, T. 34.3: High-Resolution Full-Color

Polymer Light-Emitting Devices Using Photolithography. *SID Symp. Dig. Tech. Pap.* **36**, 1280 (2005).
267. Elschner, A. & Kirchmeyer, S. PEDOT-Type Materials in Organic Solar Cells. in *Organic Photovoltaics* 211–242 (Wiley-VCH Verlag GmbH & Co. KGaA). doi:10.1002/9783527623198.ch7
268. Jonda, C., Mayer, A. B. R., Stolz, U., Elschner, A. & Karbach, A. Surface roughness effects and their influence on the degradation of organic light emitting devices. *J. Mater. Sci.* **35**, 5645–5651 (2000).
269. F Diaz, B. A., Keiji Kanazawa, K. & Piero Gardini, G. *Electrochemical Polymerization of Pyrrole*. (1979).
270. Scavetta, E. *et al.* Dopamine amperometric detection at a ferrocene clicked PEDOT:PSS coated electrode. *J. Mater. Chem. B* **2**, 2861–2867 (2014).
271. Han, D., Yang, G., Song, J., Niu, L. & Ivaska, A. Morphology of electrodeposited poly(3,4-ethylenedioxythiophene)/poly(4-styrene sulfonate) films. *J. Electroanal. Chem.* **602**, 24–28 (2007).
272. Bobacka, J., Lewenstam, A. & Ivaska, A. Electrochemical impedance spectroscopy of oxidized poly(3,4-ethylenedioxythiophene) film electrodes in aqueous solutions. *J. Electroanal. Chem.* **489**, 17–27 (2000).
273. Li, G. & Pickup, P. G. Ion transport in poly(3,4-ethylenedioxythiophene)–poly(styrene-4-sulfonate) composites. *Phys. Chem. Chem. Phys.* **2**, 1255–1260 (2000).
274. Jeuris, K., Groenendaal, L., Verheyen, H., Louwet, F. & De Schryver, F. . Light stability of 3,4-ethylenedioxythiophene-based derivatives. *Synth. Met.* **132**, 289–295 (2003).
275. Norrman, K. & Krebs, F. C. Lifetimes of organic photovoltaics: Using TOF-SIMS and 18O2 isotopic labelling to characterise chemical degradation mechanisms. *Sol. Energy Mater. Sol. Cells* **90**, 213–227 (2006).
276. Kawano, K. *et al.* Degradation of organic solar cells due to air exposure. *Sol. Energy Mater. Sol. Cells* **90**, 3520–3530 (2006).
277. Paetzold, R. *et al.* Performance of flexible polymeric light-emitting diodes under bending conditions. *Appl. Phys. Lett.* **82**, 3342–3344 (2003).
278. Lang, U., Naujoks, N. & Dual, J. Mechanical characterization of PEDOT:PSS thin films. *Synth. Met.* **159**, 473–479 (2009).
279. Aleshin, A. N., Williams, S. R. & Heeger, A. J. Transport properties of poly(3,4-ethylenedioxythiophene)/poly(styrenesulfonate). *Synth. Met.* **94**, 173–177 (1998).
280. Martin, B. D. *et al.* Hydroxylated secondary dopants for surface resistance enhancement in transparent poly(3,4-ethylenedioxythiophene)–poly(styrenesulfonate) thin films. *Synth. Met.* **142**, 187–193 (2004).
281. Su, K. *et al.* Fast Conductance Switching in Single-Crystal Organic Nanoneedles Prepared from an Interfacial Polymerization-Crystallization of 3,4-Ethylenedioxythiophene. *Adv. Mater.* **19**, 669–672 (2007).
282. Greczynski, G., Kugler, T. & Salaneck, W. . Characterization of the PEDOT-PSS system by means of X-ray and ultraviolet photoelectron spectroscopy. *Thin Solid Films* **354**, 129–135 (1999).
283. Nardes, A. M. *et al.* Microscopic Understanding of the Anisotropic Conductivity of PEDOT:PSS Thin Films. *Adv. Mater.* **19**, 1196–1200 (2007).
284. Pettersson, L. A. ., Ghosh, S. & Inganäs, O. Optical anisotropy in thin films of poly(3,4-ethylenedioxythiophene)–poly(4-styrenesulfonate). *Org. Electron.* **3**, 143–148 (2002).
285. Gustafsson, J. C., Liedberg, B. & Inganäs, O. In situ spectroscopic investigations of electrochromism and ion transport in a poly (3,4-ethylenedioxythiophene) electrode in a solid state electrochemical cell. *Solid State Ionics* **69**, 145–152 (1994).
286. Heuer, H. W., Wehrmann, R. & Kirchmeyer, S. Electrochromic Window Based on Conducting Poly(3,4-ethylenedioxythiophene)-Poly(styrene sulfonate). *Adv. Funct. Mater.* **12**, 89–94

(2002).
287. Nalwa, H. S. *Handbook of organic conductive molecules and polymers. Vol. 3*. (Wiley, 1997).
288. Patil, A. O., Heeger, A. J. & Wudl, F. Optical properties of conducting polymers. *Chem. Rev.* **88**, 183–200 (1988).
289. Cornil, J. & Brédas, J.-L. Nature of the optical transitions in charged oligothiophenes. *Adv. Mater.* **7**, 295–297 (1995).
290. Garreau, S., Louam, G., Lefrant, S., Buisson, J. P. & Froyer, G. Optical study and vibrational analysis of the poly (3,4-ethylenedioxythiophene) (PEDT). *Synth. Met.* **101**, 312–313 (1999).
291. S. Garreau, *, G. Louarn, J. P. Buisson, G. Froyer, and & Lefrant, S. In Situ Spectroelectrochemical Raman Studies of Poly(3,4-ethylenedioxythiophene) (PEDT). (1999). doi:10.1021/MA9905674
292. Winther-Jensen, B. *et al.* High current density and drift velocity in templated conducting polymers. *Org. Electron.* **8**, 796–800 (2007).
293. Prigodin, V. N. & Epstein, A. J. Quantum hopping in metallic polymers. *Phys. B Condens. Matter* **338**, 310–317 (2003).
294. Drummond, J. P., Clarson, S. J., Zetts, J. S., Hopkins, F. K. & Caracci, S. J. Enhanced electro-optic poling in guest–host systems using conductive polymer-based cladding layers. *Appl. Phys. Lett.* **74**, 368–370 (1999).
295. Borsenberger, P. M. & Weiss, D. S. *Organic photoreceptors for imaging systems*. (M. Dekker, 1993).
296. Mott, N. F. (Nevill F. & Davis, E. A. (Edward A. *Electronic processes in non-crystalline materials*. (Oxford University Press, 2012).
297. Ashcroft, N. W. & Mermin, N. D. *Solid state physics*. (Holt, Rinehart and Winston, 1976).
298. MacDiarmid, A. G. & Epstein, A. J. The concept of secondary doping as applied to polyaniline. *Synth. Met.* **65**, 103–116 (1994).
299. Elschner, A. & Lövenich, W. Solution-deposited PEDOT for transparent conductive applications. *MRS Bull.* **36**, 794–798 (2011).
300. Kim, N. *et al.* Highly Conductive PEDOT:PSS Nanofibrils Induced by Solution-Processed Crystallization. *Adv. Mater.* **26**, 2268–2272 (2014).
301. X. Crispin, *,† *et al.* The Origin of the High Conductivity of Poly(3,4-ethylenedioxythiophene)−Poly(styrenesulfonate) (PEDOT−PSS) Plastic Electrodes. (2006). doi:10.1021/CM061032+
302. Zhang, S. *et al.* Solvent-induced changes in PEDOT:PSS films for organic electrochemical transistors. *APL Mater.* **3**, 014911 (2015).
303. Timpanaro, S., Kemerink, M., Touwslager, F. J., De Kok, M. M. & Schrader, S. Morphology and conductivity of PEDOT/PSS films studied by scanning–tunneling microscopy. *Chem. Phys. Lett.* **394**, 339–343 (2004).
304. Nardes, A. M., Janssen, R. A. J. & Kemerink, M. A Morphological Model for the Solvent-Enhanced Conductivity of PEDOT:PSS Thin Films. *Adv. Funct. Mater.* **18**, 865–871 (2008).
305. Ghosh, S. & Inganäs, O. Nano-structured conducting polymer network based on PEDOT-PSS. *Synth. Met.* **121**, 1321–1322 (2001).
306. Kim, J. Y., Jung, J. H., Lee, D. E. & Joo, J. Enhancement of electrical conductivity of poly(3,4-ethylenedioxythiophene)/poly(4-styrenesulfonate) by a change of solvents. *Synth. Met.* **126**, 311–316 (2002).
307. Ouyang, J., Chu, C.-W., Chen, F.-C., Xu, Q. & Yang, Y. High-Conductivity Poly(3,4-ethylenedioxythiophene):Poly(styrene sulfonate) Film and Its Application in Polymer Optoelectronic Devices. *Adv. Funct. Mater.* **15**, 203–208 (2005).
308. Kergoat, L. *et al.* Detection of Glutamate and Acetylcholine with Organic Electrochemical Transistors Based on Conducting Polymer/Platinum Nanoparticle Composites. *Adv. Mater.* **26**, 5658–5664 (2014).
309. Nardes, A. M. *et al.* Conductivity, work function, and environmental stability of PEDOT:PSS

thin films treated with sorbitol. *Org. Electron.* **9**, 727–734 (2008).
310. Shen, Y. *et al.* Charge transport in doped organic semiconductors. *Phys. Rev. B* **68**, 081204 (2003).
311. Blom, P. W. M., de Jong, M. J. M. & van Munster, M. G. Electric-field and temperature dependence of the hole mobility in poly(p-phenylene vinylene). *Phys. Rev. B* **55**, R656–R659 (1997).
312. Bard, A. J. & Faulkner, L. R. *Electrochemical methods : fundamentals and applications*. (Wiley, 2001).
313. Stenger-Smith, J. D. *et al.* Poly(3,4-alkylenedioxythiophene)-Based Supercapacitors Using Ionic Liquids as Supporting Electrolytes. *J. Electrochem. Soc.* **149**, A973 (2002).
314. Bernards, D. A. & Malliaras, G. G. Steady-state and transient behavior of organic electrochemical transistors. *Adv. Funct. Mater.* **17**, 3538–3544 (2007).
315. Sangodkar, H., Sukeerthi, S., Srinivasa, R. S., Lal, R. & Contractor, A. Q. A Biosensor Array Based on Polyaniline. *Anal. Chem.* **68**, 779–783 (1996).
316. Battaglini, F., and, P. N. B. & Wang, J. H. Covalent Attachment of Osmium Complexes to Glucose Oxidase and the Application of the Resulting Modified Enzyme in an Enzyme Switch Responsive to Glucose. (1999). doi:10.1021/AC990321X
317. Saxena, V., Shirodkar, V. & Prakash, R. Copper(II) ion-selective microelectrochemical transistor. *J. Solid State Electrochem.* **4**, 234–236 (2000).
318. Kanungo, M., Srivastava, D. N., Kumar, A. & Contractor, A. Q. Conductimetric immunosensor based on poly(3,4-ethylenedioxythiophene). *Chem. Commun.* 680–681 (2002). doi:10.1039/b111728a
319. Krishnamoorthy, K., Gokhale, R. S., Contractor, A. Q. & Kumar, A. Novel label-free DNA sensors based on poly(3,4-ethylenedioxythiophene)Electronic Supplementary Information (ESI) available: Experimental details and sensor response for various sensors listed in Table 2. Cyclic voltammograms confirming the increase in resistance due to the duplex formation between the probe and target DNA in conducting polymer matrix. See http://www.rsc.org/suppdata/cc/b3/b316794a/. *Chem. Commun.* 820 (2004). doi:10.1039/b316794a
320. Mabeck, J. T. & Malliaras, G. G. Chemical and biological sensors based on organic thin-film transistors. *Anal. Bioanal. Chem.* **384**, 343–353 (2005).
321. Nikolou, M. & Malliaras, G. G. Applications of poly(3,4-ethylenedioxythiophene) doped with poly(styrene sulfonic acid) transistors in chemical and biological sensors. *Chem. Rec.* **8**, 13–22 (2008).
322. Epstein, A. J., Hsu, F.-C., Chiou, N.-R. & Prigodin, V. N. Electric-field induced ion-leveraged metal–insulator transition in conducting polymer-based field effect devices. *Curr. Appl. Phys.* **2**, 339–343 (2002).
323. Nilsson, D. *et al.* Bi-stable dynamic current modulation in electrochemical organic transistors. *Adv. Mater.* **14**, 51–54 (2002).
324. Lisdat, F. & Schäfer, D. The use of electrochemical impedance spectroscopy for biosensing. *Anal. Bioanal. Chem.* **391**, 1555–1567 (2008).
325. Ramuz, M. *et al.* Optimization of a planar all-polymer transistor for characterization of barrier tissue. *ChemPhysChem* **16**, 1210–1216 (2015).
326. Yeung, S. Y., Gu, X., Tsang, C. M., Tsao, S. W. & Hsing, I. Engineering organic electrochemical transistor (OECT) to be sensitive cell-based biosensor through tuning of channel area. *Sensors Actuators A Phys.* **287**, 185–193 (2019).
327. Jimison, L. H. *et al.* Measurement of Barrier Tissue Integrity with an Organic Electrochemical Transistor. *Adv. Mater.* **24**, 5919–5923 (2012).
328. Tria, S. A., Jimison, L. H., Hama, A., Bongo, M. & Owens, R. M. Validation of the organic electrochemical transistor for in vitro toxicology. *Biochim. Biophys. Acta - Gen. Subj.* **1830**, 4381–4390 (2013).

329. Tria, S. A., Ramuz, M., Jimison, L. H., Hama, A. & Owens, R. M. Sensing of Barrier Tissue Disruption with an Organic Electrochemical Transistor. *J. Vis. Exp.* e51102 (2014). doi:10.3791/51102
330. Lin, P., Yan, F., Yu, J., Chan, H. L. W. & Yang, M. The Application of Organic Electrochemical Transistors in Cell-Based Biosensors. *Adv. Mater.* **22**, 3655–3660 (2010).
331. Faria, G. C., Duong, D. T. & Salleo, A. On the transient response of organic electrochemical transistors. *Org. Electron.* **45**, 215–221 (2017).
332. Shim, N. Y. *et al.* All-Plastic Electrochemical Transistor for Glucose Sensing Using a Ferrocene Mediator. *Sensors* **9**, 9896–9902 (2009).
333. Zhu, Z.-T. *et al.* A simple poly(3,4-ethylene dioxythiophene)/poly(styrene sulfonic acid) transistor for glucose sensing at neutral pH. *Chem. Commun.* 1556 (2004). doi:10.1039/b403327m
334. Gualandi, I. *et al.* All poly(3,4-ethylenedioxythiophene) organic electrochemical transistor to amplify amperometric signals. *Electrochim. Acta* **268**, 476–483 (2018).
335. Tang, H., Lin, P., Chan, H. L. W. & Yan, F. Highly sensitive dopamine biosensors based on organic electrochemical transistors. *Biosens. Bioelectron.* **26**, 4559–4563 (2011).
336. Contractor, A. Q. *et al.* Conducting polymer-based biosensors. *Electrochim. Acta* **39**, 1321–1324 (1994).
337. Strakosas, X., Bongo, M. & Owens, R. M. The organic electrochemical transistor for biological applications. *J. Appl. Polym. Sci.* **132**, n/a-n/a (2015).
338. Bernards, D. A. *et al.* Enzymatic sensing with organic electrochemical transistors. *J. Mater. Chem.* **18**, 116–120 (2008).
339. Yaghmazadeh, O. *et al.* Optimization of organic electrochemical transistors for sensor applications. *J. Polym. Sci. Part B Polym. Phys.* **49**, 34–39 (2011).
340. Zanardi, C., Terzi, F. & Seeber, R. Polythiophenes and polythiophene-based composites in amperometric sensing. *Anal. Bioanal. Chem.* **405**, 509–531 (2013).
341. Singh, S. K., Crispin, X. & Zozoulenko, I. V. Oxygen Reduction Reaction in Conducting Polymer PEDOT: Density Functional Theory Study. *J. Phys. Chem. C* **121**, 12270–12277 (2017).
342. Lin, P., Yan, F. & Chan, H. L. W. Ion-Sensitive Properties of Organic Electrochemical Transistors. *ACS Appl. Mater. Interfaces* **2**, 1637–1641 (2010).
343. Volkov, A. V. *et al.* Understanding the Capacitance of PEDOT:PSS. *Adv. Funct. Mater.* **27**, 1700329 (2017).
344. Ghosh, S. & Inganäs, O. Electrochemical Characterization of Poly(3,4-ethylene dioxythiophene) Based Conducting Hydrogel Networks. *J. Electrochem. Soc.* **147**, 1872 (2000).
345. Kurra, N., Park, J. & Alshareef, H. N. A conducting polymer nucleation scheme for efficient solid-state supercapacitors on paper. *J. Mater. Chem. A* **2**, 17058–17065 (2014).
346. Kozai, T. D. Y. *et al.* Ultrasmall implantable composite microelectrodes with bioactive surfaces for chronic neural interfaces. *Nat. Mater.* **11**, 1065–1073 (2012).
347. Williamson, A. *et al.* Localized Neuron Stimulation with Organic Electrochemical Transistors on Delaminating Depth Probes. *Adv. Mater.* **27**, 4405–4410 (2015).
348. Khodagholy, D. *et al.* NeuroGrid: recording action potentials from the surface of the brain. *Nat. Neurosci.* **18**, 310–315 (2015).
349. Blau, A. *et al.* Flexible, all-polymer microelectrode arrays for the capture of cardiac and neuronal signals. *Biomaterials* **32**, 1778–1786 (2011).
350. Guex, A. A. *et al.* Conducting polymer electrodes for auditory brainstem implants. *J. Mater. Chem. B* **3**, 5021–5027 (2015).
351. Raghunandhan, S. & Kameswaran, M. Audiitory Brainstem Implants. *Otorhinolaryngol. Clin.* **2**, 151–155 (2010).
352. Zhang, S. *et al.* Water stability and orthogonal patterning of flexible micro-electrochemical

transistors on plastic. *J. Mater. Chem. C* **4**, 1382–1385 (2016).
353. Scholz, F. *Electroanalytical Methods Guide to Experiments and Applications*. (Springer Berlin, 2014).
354. Oldham, K. B. & Myland, J. C. *Fundamentals of electrochemical science*. (Academic Press, 1994).
355. Bard, A. J. & Stratmann, M. *Encyclopedia of electrochemistry*. (Wiley-VCH, 2001).
356. Rubinstein, I. *Physical electrochemistry : principles, methods, and applications*. (M. Dekker, 1995).
357. Victor L. Mironov. *Fundamentals of scanning probe microscopy*. (Nizhniy Novgorod, 2004).
358. García, R., Magerle, R. & Perez, R. Nanoscale compositional mapping with gentle forces. *Nat. Mater.* **6**, 405–411 (2007).
359. Klapetek, P. *Quantitative Data Processing in Scanning Probe Microscopy : SPM Applications for Nanometrology.* (Elsevier Science, 2012).
360. Lanza, M. *Conductive atomic force microscopy : applications in nanomaterials*. (Wiley-VCH, 2017).
361. Yanev, V., Erlbacher, T., Rommel, M., Bauer, A. J. & Frey, L. Comparative study between conventional macroscopic IV techniques and advanced AFM based methods for electrical characterization of dielectrics at the nanoscale. *Microelectron. Eng.* **86**, 1911–1914 (2009).
362. Rommel, M. *et al.* Influence of parasitic capacitances on conductive AFM *I-V* measurements and approaches for its reduction. *J. Vac. Sci. Technol. B, Nanotechnol. Microelectron. Mater. Process. Meas. Phenom.* **31**, 01A108 (2013).
363. Stuart, B. (Barbara H. . *Infrared spectroscopy : fundamentals and applications*. (J. Wiley, 2004).
364. Pappa, A.-M. *et al.* Organic Transistor Arrays Integrated with Finger-Powered Microfluidics for Multianalyte Saliva Testing. *Adv. Healthc. Mater.* **5**, 2295–2302 (2016).
365. Caco-2 [Caco2] ATCC ® HTB-37™ Homo sapiens Colon Colorectal. Available at: https://www.lgcstandards-atcc.org/Products/All/HTB-37.aspx. (Accessed: 17th September 2019)
366. NIH/3T3 ATCC® CRL-1658™. Available at: https://www.lgcstandards-atcc.org/Products/All/CRL-1658.aspx. (Accessed: 17th September 2019)
367. Echegoyen, Y. & Nerín, C. Nanoparticle release from nano-silver antimicrobial food containers. *Food Chem. Toxicol.* **62**, 16–22 (2013).
368. Furuse, M. *et al.* Occludin: a novel integral membrane protein localizing at tight junctions. *J. Cell Biol.* **123**, 1777–88 (1993).
369. Colegio, O. R., Van Itallie, C. M., McCrea, H. J., Rahner, C. & Anderson, J. M. Claudins create charge-selective channels in the paracellular pathway between epithelial cells. *Am. J. Physiol. Physiol.* **283**, C142–C147 (2002).
370. Fanning, A. S., Van Itallie, C. M. & Anderson, J. M. Zonula occludens-1 and -2 regulate apical cell structure and the zonula adherens cytoskeleton in polarized epithelia. *Mol. Biol. Cell* **23**, 577–590 (2012).
371. Gajbhiye, S. & Sakharwade, S. Silver nanoparticles in cosmetics. *J. Cosmet. dermatological Sci. Appl.* **6**, 48–53 (2016).
372. Introduction to Fluorescence Microscopy | MicroscopyU. Available at: https://www.microscopyu.com/techniques/fluorescence/introduction-to-fluorescence-microscopy. (Accessed: 17th September 2019)
373. Roco, M. C. Nanotechnology: convergence with modern biology and medicine. *Curr. Opin. Biotechnol.* **14**, 337–346 (2003).
374. What It Is and How It Works | Nano. Available at: https://www.nano.gov/nanotech-101/what#content. (Accessed: 17th September 2019)
375. García-Barrasa, J., López-de-Luzuriaga, J. & Monge, M. Silver nanoparticles: synthesis through chemical methods in solution and biomedical applications. *Open Chem.* **9**, 7–19

(2011).
376. Kim, S. & Ryu, D.-Y. Silver nanoparticle-induced oxidative stress, genotoxicity and apoptosis in cultured cells and animal tissues. *J. Appl. Toxicol.* **33**, 78–89 (2013).
377. Bastús, N. G., Merkoçi, F., Piella, J. & Puntes, V. Synthesis of Highly Monodisperse Citrate-Stabilized Silver Nanoparticles of up to 200 nm: Kinetic Control and Catalytic Properties. *Chem. Mater.* **26**, 2836–2846 (2014).
378. La spettrofotometria visibile e ultravioletta | Chimicamo.org. Available at: https://www.chimicamo.org/chimica-analitica/la-spettrofotometria-visibile-e-ultravioletta.html. (Accessed: 18th September 2019)
379. Hirao, M., Ogi, H. & Fukuoka, H. Resonance EMAT system for acoustoelastic stress measurement in sheet metals. *Rev. Sci. Instrum.* **64**, 3198–3205 (1993).
380. Rodahl, M. & Kasemo, B. A simple setup to simultaneously measure the resonant frequency and the absolute dissipation factor of a quartz crystal microbalance. *Rev. Sci. Instrum.* **67**, 3238–3241 (1996).
381. Johannsmann, D. Viscoelastic, mechanical, and dielectric measurements on complex samples with the quartz crystal microbalance. *Physical Chemistry Chemical Physics* **10**, 4516–4534 (2008).
382. Nightingale, J., Wade, J., Moia, D., Nelson, J. & Kim, J. S. Impact of Molecular Order on Polaron Formation in Conjugated Polymers. *J. Phys. Chem. C* **122**, 29129–29140 (2018).
383. Wood, S., Hollis, J. R. & Kim, J.-S. Raman spectroscopy as an advanced structural nanoprobe for conjugated molecular semiconductors. 1–32 (2017). doi:10.1088/1361-6463/50/7/073001
384. Afzal, A. *et al.* Gravimetric Viral Diagnostics: QCM Based Biosensors for Early Detection of Viruses. (2017). doi:10.3390/chemosensors5010007
385. Decataldo, F. *et al.* Organic Electrochemical Transistors: Smart Devices for Real-Time Monitoring of Cellular Vitality. *Adv. Mater. Technol.* 1900207 (2019). doi:10.1002/admt.201900207
386. KiCad EDA. Available at: http://kicad-pcb.org/. (Accessed: 20th September 2019)
387. MD Srl - Circuiti Stampati di Qualità Servizio rapido in 24 ore. Available at: https://www.mdsrl.it/. (Accessed: 20th September 2019)
388. Pernodet, N. *et al.* Adverse Effects of Citrate/Gold Nanoparticles on Human Dermal Fibroblasts. *Small* **2**, 766–773 (2006).
389. Moore, E. R., Fischer, E. R., Mead, D. J. & Hackstadt, T. The Chlamydial Inclusion Preferentially Intercepts Basolaterally Directed Sphingomyelin-Containing Exocytic Vacuoles. *Traffic* **9**, 2130–2140 (2008).
390. Arthur, J. M. The MDCK cell line is made up of populations of cells with diverse resistive and transport properties. *Tissue Cell* **32**, 446–450 (2000).
391. Ashraf, S. *et al.* Protein-mediated synthesis, pH-induced reversible agglomeration, toxicity and cellular interaction of silver nanoparticles. *Colloids Surfaces B Biointerfaces* **102**, 511–518 (2013).
392. Monopoli, M. P., Bombelli, F. B. & Dawson, K. A. Nanoparticle coronas take shape. *Nat. Nanotechnol.* **6**, 11–12 (2011).
393. Barbalinardo, M., Caicci, F., Cavallini, M. & Gentili, D. Protein Corona Mediated Uptake and Cytotoxicity of Silver Nanoparticles in Mouse Embryonic Fibroblast. *Small* **14**, 1801219 (2018).
394. Decataldo, F. *et al.* Organic Electrochemical Transistors for Real-Time Monitoring of In-Vitro Silver Nanoparticle Toxicity. Manuscript in Publication (2019).
395. Olofsson, P. S. & Tracey, K. J. Bioelectronic medicine: technology targeting molecular mechanisms for therapy. *J. Intern. Med.* **282**, 3 (2017).
396. Famm, K., Litt, B., Tracey, K. J., Boyden, E. S. & Slaoui, M. A jump-start for electroceuticals. *Nature* **496**, 159–161 (2013).
397. Chew, D. J. *et al.* A microchannel neuroprosthesis for bladder control after spinal cord injury

in rat. *Sci. Transl. Med.* **5**, 210ra155 (2013).
398. Minev, I. R. *et al.* Electronic dura mater for long-term multimodal neural interfaces. *Science (80-.).* **347**, (2015).
399. Savagatrup, S. *et al.* Plasticization of PEDOT:PSS by Common Additives for Mechanically Robust Organic Solar Cells and Wearable Sensors. *Adv. Funct. Mater.* **25**, 427–436 (2015).
400. Vandeparre, H., Liu, Q., Minev, I. R., Suo, Z. & Lacour, S. P. Localization of Folds and Cracks in Thin Metal Films Coated on Flexible Elastomer Foams. *Adv. Mater.* **25**, 3117–3121 (2013).
401. Lacour, S. P., Chan, D., Wagner, S., Li, T. & Suo, Z. Mechanisms of reversible stretchability of thin metal films on elastomeric substrates. *Appl. Phys. Lett.* **88**, 204103 (2006).
402. AFM – GuckLab. Available at: https://gucklab.com/?page_id=38. (Accessed: 5th October 2019)
403. Bates Mary Kay. Culturing Cells Under Hypoxic Conditions for Biologically Relevant Results. *Am. Lab.* 1–3 (2012).
404. Grist, S., Schmok, J., Liu, M.-C., Chrostowski, L. & Cheung, K. Designing a Microfluidic Device with Integrated Ratiometric Oxygen Sensors for the Long-Term Control and Monitoring of Chronic and Cyclic Hypoxia. *Sensors* **15**, 20030–20052 (2015).
405. Amberger-Murphy, V. Hypoxia Helps Glioma to Fight Therapy. *Curr. Cancer Drug Targets* **9**, 381–390 (2009).
406. Favaro, E., Lord, S., Harris, A. L. & Buffa, F. M. Gene expression and hypoxia in breast cancer. *Genome Med.* **3**, 55 (2011).
407. Brizel, D. M., Sibley, G. S., Prosnitz, L. R., Scher, R. L. & Dewhirst, M. W. Tumor hypoxia adversely affects the prognosis of carcinoma of the head and neck. *Int. J. Radiat. Oncol.* **38**, 285–289 (1997).
408. Decataldo, F., Gualandi, I., Tessarolo, M., Scavetta, E. & Fraboni, B. Organic Electrochemical Transistors as sensing devices for oxygen dissolved in solution. Submitted
409. Kiernan, J., Hu, S., Grynpas, M. D., Davies, J. E. & Stanford, W. L. Systemic Mesenchymal Stromal Cell Transplantation Prevents Functional Bone Loss in a Mouse Model of Age-Related Osteoporosis. *Stem Cells Transl. Med.* **5**, 683–693 (2016).
410. Saito, A. *et al.* Umbilical cord extracts improve osteoporotic abnormalities of bone marrow-derived mesenchymal stem cells and promote their therapeutic effects on ovariectomised rats. *Sci. Rep.* **8**, 1161 (2018).
411. Rutkovskiy, A., Stensløkken, K.-O. & Vaage, I. J. Osteoblast Differentiation at a Glance. *Med. Sci. Monit. Basic Res.* **22**, 95–106 (2016).
412. Iandolo, D. *et al.* Development and Characterization of Organic Electronic Scaffolds for Bone Tissue Engineering. *Adv. Healthc. Mater.* **5**, 1505–1512 (2016).
413. Ohayon, D. *et al.* Laser Patterning of Self-Assembled Monolayers on PEDOT:PSS Films for Controlled Cell Adhesion. *Adv. Mater. Interfaces* **4**, 1700191 (2017).
414. Fiorilli, S. *et al.* Vapor-phase self-assembled monolayers of aminosilane on plasma-activated silicon substrates. *J. Colloid Interface Sci.* **321**, 235–241 (2008).
415. Zeng, X., Xu, G., Gao, Y. & An, Y. Surface Wettability of (3-Aminopropyl)triethoxysilane Self-Assembled Monolayers. *J. Phys. Chem. B* **115**, 450–454 (2011).
416. Zhang, F. *et al.* Chemical Vapor Deposition of Three Aminosilanes on Silicon Dioxide: Surface Characterization, Stability, Effects of Silane Concentration, and Cyanine Dye Adsorption. *Langmuir* **26**, 14648–14654 (2010).
417. Chia, P.-J. *et al.* Injection-induced De-doping in a Conducting Polymer during Device Operation: Asymmetry in the Hole Injection and Extraction Rates. *Adv. Mater.* **19**, 4202–4207 (2007).
418. Håkansson, A. *et al.* Effect of (3-glycidyloxypropyl)trimethoxysilane (GOPS) on the electrical properties of PEDOT:PSS films. *J. Polym. Sci. Part B Polym. Phys.* **55**, 814–820 (2017).
419. Savva, A., Wustoni, S. & Inal, S. Ionic-to-electronic coupling efficiency in PEDOT:PSS films operated in aqueous electrolytes. *J. Mater. Chem. C* **6**, 12023–12030 (2018).

420. Wozney, J. M. Overview of Bone Morphogenetic Proteins. *Spine (Phila. Pa. 1976).* **27**, S2–S8 (2002).
421. Bard, A. J. & Faulkner, L. R. *Electrochemical methods : fundamentals and applications*. (Wiley, 2001).
422. Southampton Electrochemistry Group. *Instrumental methods in electrochemistry*.
423. Savva, A. *et al.* Influence of Water on the Performance of Organic Electrochemical Transistors. *Chem. Mater.* **31**, 927–937 (2019).
424. Decataldo, F. *et al.* Biofunctionalized PEDOT:PSS-based OECTs for stem cell osteogenic differentiation monitoring. Manuscript in Publication (2019).
425. World Precision Instruments | Cell & Tissue | TEER Measurement | EVOM2. Available at: https://www.wpi-europe.com/products/cell-and-tissue/ teer-measurement/evom2.aspx. (Accessed: 5th February 2020)
426. cellZscope - nanoAnalytics - service laboratory specialized in materials characterization and manufacturer of scientific instruments. Available at: https://www.nanoanalytics.com/en/products/cellzscope.html. (Accessed: 5th February 2020)
427. García-Barrasa, J., López-De-luzuriaga, J. M. & Monge, M. Silver nanoparticles: Synthesis through chemical methods in solution and biomedical applications. *Cent. Eur. J. Chem.* **9**, 7–19 (2011).
428. Echegoyen, Y. & Nerín, C. Nanoparticle release from nano-silver antimicrobial food containers. *Food Chem. Toxicol.* **62**, 16–22 (2013).
429. Gajbhiye, S. & Sakharwade, S. Silver Nanoparticles in Cosmetics. *J. Cosmet. Dermatological Sci. Appl.* **06**, 48–53 (2016).
430. Tybrandt, K. *et al.* High-Density Stretchable Electrode Grids for Chronic Neural Recording. *Adv. Mater.* **30**, 1706520 (2018).
431. Lee, Y. J., Kim, H. J., Do, S. H., Kang, J. Y. & Lee, S. H. Characterization of nerve-cuff electrode interface for biocompatible and chronic stimulating application. *Sensors Actuators, B Chem.* **237**, 924–934 (2016).
432. Amorini, F. *et al.* Electrically Controlled "Sponge Effect" of PEDOT:PSS Governs Membrane Potential and Cellular Growth. *ACS Appl. Mater. Interfaces* **9**, 6679–6689 (2017).
433. Shin, S. R. *et al.* Label-Free and Regenerative Electrochemical Microfluidic Biosensors for Continual Monitoring of Cell Secretomes. *Adv. Sci.* **4**, 1600522 (2017).
434. Song, J. H., Lee, S. M. & Yoo, K. H. Label-free and real-time monitoring of human mesenchymal stem cell differentiation in 2D and 3D cell culture systems using impedance cell sensors. *RSC Adv.* **8**, 31246–31254 (2018).

Acknowledgements

The realization of this thesis would not have been possible without the help and support given by several people that I have worked and lived with in these years.
First of all, I would like to thank my tutor, the Prof. Beatrice Fraboni, for giving me the opportunity to start the PhD programme (this job strongly increase my researcher skills and life experiences) and for her leadership and advices, provided during these three years: her guide was fundamental to coordinate and carry on the several projects and experiments that I have done in this work.
Bioelectronics is an extremely interdisciplinary research field, where physics, chemistry, biology, medicine and other scientific branches merge and overlaps: thus, the contributions of many researchers having diverse backgrounds are of primary importance. For this reason, I acknowledge all the collaborators that contributed to the development of this work, starting from my colleagues at the Department of Physics and Astronomy at the University of Bologna. In particular, I thank Prof. Tobias Cramer, who led the work on the stretchable and low-impedance electrode for bioelectronic recordings, and Dr. Marta Tessarolo, who guided and helped me during the PhD. I would also thank the people I have worked with during these three years in Bologna, namely Nicola, Luca, Tommaso, Ilaria, Alberto, Sara, Giacomo, Matteo, Maria Antonietta, Marco, Dario, Vito, Laura, Andrea, together with the guests, coming from other labs and Universities. Moreover, I would like to thank all the bachelor and master students that collaborated in these projects for their contribution. I am very grateful to Dr. Filippo Maria Giorgi and Maria Calienni, our laboratory technicians, for helping in the technical/electronical realization of the TECH-OECT and the important suggestions and contributions regarding the biological investigations, respectively.
I acknowledge the group of Prof. Erika Scavetta from the Department of Industrial Chemistry of the University of Bologna for the strong and fruitfull collaboration (still going on) regarding the electrochemical sensors and the wearable electronics. In particular, I really enjoyed working with Isacco Gualandi and Federica Mariani and benefitted from their help and suggestions.
Moreover, I warmly thank the group of Dr. Massimiliano Cavallini of the Institute for the Study of Nanostructure Materials of the National Centre of Research (CNR-ISMN). In particular, Marianna Barbalinardo and Denis Gentili strongly helped me on all aspects regarding the cell culture and the nanoparticles, respectively, Dr. Francesco Valle provided good contributions in the meetings, and Mauro Murgia helped in the fabrication process optimization and final configuration of the stretchable electrode.
I would like to thank also Dr. Roberto Amici of the Department of Biomedical and Neuromotor Sciences in Bologna and William S. Korim and Song Yao of the Florey Institute of Neuroscience and Mental Health of the University of Melbourne in Australia for the collaborations on the stretchable electrode project. I gratefully thank especially Dr. Davide Martelli who surgically implanted the electrode and recorded and analyzed the nerve spiking activity.
I really thank Prof. Roisin Owens, from the Department of Chemical Engineering and Biotechnology at the University of Cambridge, for giving me the opportunity to do my secondment in her group, working in her laboratories as a visiting PhD student. These six months improved my abilities as a researcher, learning new experimental techniques and fabrication methods, together with my English language as well. I also thank the amazing people I have met there, especially Donata (who coordinate my work), Victor, Magali, Anna-Maria, Babis, Janire, Anthie, Aimee Pavia and Aimee Withers, for their kindness and help.
I acknowledge the Marco Polo project of the Department of Physics and Astronomy of the University of Bologna for the financial support given for my research period abroad during the 2nd year.

Finally, I warmly thank my family, who always believed in me, for their constant support and help and Arianna, for her kindness, love and support in this study and working path.